

Microfluidic devices to facilitate in-flow medium exchange, and tuneable size-based sorting, of microspheres

A thesis submitted to Cardiff University in accordance with the requirements for the degree of

DOCTOR OF PHILOSOPHY
BY EXAMINATION AND THESIS

By

Alex John Lewis Morgan MEng

Cardiff School of Engineering



2014

DECLARATION

This work has not been submitted in substance for any other degree or award at this or any other university or place of learning, nor is being submitted concurrently in candidature for any degree or other award.

Signed (candidate) Date

STATEMENT 1

This thesis is being submitted in partial fulfillment of the requirements for the degree of(insert MCh, MD, MPhil, PhD etc, as appropriate)

Signed (candidate) Date

STATEMENT 2

This thesis is the result of my own independent work/investigation, except where otherwise stated.
Other sources are acknowledged by explicit references. The views expressed are my own.

Signed (candidate) Date

STATEMENT 3

I hereby give consent for my thesis, if accepted, to be available for photocopying and for inter-library loan, and for the title and summary to be made available to outside organisations.

Signed (candidate) Date

STATEMENT 4: PREVIOUSLY APPROVED BAR ON ACCESS

I hereby give consent for my thesis, if accepted, to be available for photocopying and for inter-library loans after expiry of a bar on access previously approved by the Academic Standards & Quality Committee.

Signed (candidate) Date

Acknowledgments

I would like to thank Professor David Barrow for all the help and guidance he provided throughout my PhD research. I'd also like to thank Neil Sykes and Dr. Nazeem Rizvi for their help with laser machining and Dr. Angela Sobierski and Dr. Chris Dunscombe for their assistance in the clean room.

I must also thank my friends and colleagues for helping to keep me sane over the last few years particularly Dave, Hannah, Adam and Beth who have had to put up with me much more than most others could probably manage. Also all my team mates at Shamilton who have kept our football as a great stress reliever by not taking our successes or failures too seriously.

Finally, I would like to thank my family for their constant love and support and Martha moo for being the cutest thing ever.

Contents

Abstract	1
Project Aim.....	2
1 Introduction to Microfluidics	4
1.1 History of Microfluidics	4
1.2 Why Microfluidics?	6
1.3 Fluid Flow	7
1.4 Flow Characteristics.....	8
1.5 Channel Material	12
2 Sphere Manipulation	13
2.1 Active Control	13
2.1.1 Acoustophoresis	14
2.1.2 Dielectrophoresis (DEP)	21
2.1.3 Magnetophoresis	26
2.1.4 Optical Methods	27
2.1.5 Gravitational.....	29
2.2 Passive Control.....	30
2.2.1 Obstacle Induced Separation	30
2.2.2 Hydrodynamic Filtration.....	34
2.2.3 Pinched Flow Fractionation (PFF).....	38
2.2.4 Inertial Focusing.....	42

2.3	Conclusion.....	51
3	Phase Exchanger Concept.....	53
3.1	Objective.....	53
3.2	Introduction to the Phase Separator	53
3.3	Exchanger Design.....	57
3.3.1	Design One	57
3.3.2	Design two.....	58
3.4	Exchanger Chip One	60
3.4.1	Experimental.....	60
3.4.2	Results and Discussion.....	62
3.5	Exchanger Chip Two	64
3.5.1	Experimental.....	64
3.5.2	Results and Discussion.....	65
3.6	Exchanger Chip Three	68
3.6.1	Experimental.....	68
3.6.2	Results and Discussion.....	68
3.7	Sphere Production	69
3.7.1	Sphere Production Chip One.....	70
3.7.2	Sphere Production Chip Two.....	72
3.7.3	UV dispersion test.....	74
3.7.4	Sphere Production Chip Three.....	77

3.7.5	Sphere Production Chip Four	81
3.8	Sphere Exchange	85
3.9	Conclusion.....	89
3.10	Appendix - Device Fabrication.....	90
4	Phase Exchanger Development	94
4.1	Development Simulations.....	95
4.1.1	Model Parameters	96
4.1.2	The Pressure Problem	97
4.1.3	Flow Rate Differential.....	102
4.1.4	Shallower Exchanger	104
4.1.5	Separator Channel Length	106
4.1.6	Number of Separator Channels.....	108
4.1.7	Exchanger Architecture	111
4.3	Testing the Exchanger	121
4.3.1	Quantitative analysis using a spectrometer.....	121
4.3.2	Spectrometer Calibration.....	128
4.3.3	500 μ m Square Cross-section Exchanger.....	131
4.3.4	150 μ m x 500 μ m Cross-section Channels.....	136
4.3.5	Deeper Outlet.....	140
4.3.6	Impact of Temperature on Exchange	145
4.3.7	Outlet Channel Length.....	150

4.3.8	Separator Channel Size	153
4.4	Overview.....	157
4.5	Buffer Region	158
4.5.1	Method.....	158
4.5.2	Results and Discussion.....	160
4.6	Sphere Cleaning.....	162
4.6.1	Method.....	162
4.6.2	Results and Discussion.....	163
4.7	Future Work.....	165
4.8	Conclusion.....	165
5	Inertial Sorting of Microspheres	169
5.1	Why does size matter?	169
5.2	Current Size Analysis Techniques	170
5.3	Tuneable Inertial Sorting.....	171
5.4	Device Design.....	176
5.5	Deformation Modelling.....	177
5.5.1	Parallel Stretching.....	178
5.5.2	Perpendicular Stretching	186
5.5.3	Compression.....	192
5.6	Modelling Sphere Focusing.....	196
5.6.1	Model Parameters.....	196

5.6.2	Results and Discussion.....	201
5.7	Device Testing.....	209
5.7.1	Methods.....	209
5.7.2	80µm Wide Channel Results and Discussion.....	211
5.7.3	Image Analysis.....	213
5.7.4	200µm Wide Channel Results and Discussion.....	215
5.8	Future Work.....	223
5.9	Conclusion.....	224
5.10	Appendix - Device Fabrication	225
5.10.1	80µm Wide Channels.....	225
5.10.2	200µm Wide Channel	229
6	Conclusion.....	231
7	References.....	235
8	APPENDIX A - Laser Machining Study	247
8.1	Experimental.....	247
8.2	Results	249
8.2.1	Number of loops	249
8.2.2	Machining Speed.....	252
8.3	Conclusion.....	255

List of Abbreviations

APFF	Asymmetric pinched flow fractionation
DEP	Dielectrophoresis
DI	Deionised
DLD	Deterministic lateral displacement
FFF	Field flow fractionation
HPLC	High performance liquid chromatography
LED	Light emitting diode
PDMS	Polydimethylsiloxane
PEEK	Poly ether ketone
PEG	Polyethylene glycol dimethacrylate
PFF	Pinched flow fractionation
PTFE	Polytetrafluoroethylene
SPLITT	Split-flow lateral transport thin
TEOS	Tetraethyl orthosilicate
TMPTA	Trimethylolpropane triacrylate
UV	Ultraviolet

List of Symbols

α	Thermal expansion coefficient
β_c	Sphere compressibility
β_w	Medium compressibility
γ_v	Liquid-vapour tension
γ_{sl}	Solid-vapour tension
γ_{sv}	Liquid-vapour tension
ϵ_m	Medium permittivity
ϵ_p	Particle permittivity
θ	Contact angle
λ	Wavelength
μ	Dynamic viscosity
ρ	Density
ρ_c	Sphere density
ρ_w	Medium density
ϕ	Contrast factor
χ	Magnetic susceptibility
a	Particle diameter
A	Cross-sectional area of channel
A_0	Original area
A_l	Light absorption
B	Magnetic flux density
C_{one}	Concentration of phase one

c_{two}	Concentration of phase two
d	Peak to valley difference (y-plane)
D	Diffusion coefficient
De	Dean number
D_h	Hydraulic diameter
E	Electric field strength
F_{Ax}	Axial Force
F_B	Bjerknes force
f_c	Lift coefficient
f_{CM}	Clausius-Mossotti factor
F_{DEP}	Dielectrophoretic force
F_{drag}	Drag force
F_{mag}	Magnetic force
F_s	Stokes drag force
F_{Tr}	Transverse force
F_z	Inertial lift force
g	Acceleration due to gravity
I	Intensity of measured light
I_0	Intensity of light when no absorption occurs
k	Wave number
L	Length
l	Path length
L_0	Original Length
L_p	Maximum migration distance

L_{sep}	Length of separator channels
n	Number
P	Pressure
p	Wetting perimeter of channel
p_0	Pressure amplitude
Pe	Peclet number
Q	Volumetric flow rate
r	Sphere radius
$\langle r \rangle^2$	Mean square displacement
R	Fluidic resistance
Ra	Average roughness
$Ra(x)$	Average roughness in the x-direction
$Ra(y)$	Average roughness in the y-direction
Re	Reynolds number
Re_c	Channel Reynolds number
Re_p	Particle Reynolds number
R_q	Root-mean-squared roughness
R_t	Peak to valley difference (x-plane)
t	Time
T	Light transmittance
U_1	Main channel flow speed
U_2	Separator channel flow speed
U_{avg}	Average flow velocity
U_{defl}	Deflection velocity

U_{hyd}	Hydrodynamic flow velocity
U_m	Maximum flow velocity
U_{mag}	Magnetic deflection velocity
U_p	Migration velocity
U_{sed}	Sedimentation velocity
V	Voltage
V_p	Sphere volume
w	Channel width
w_1	Width of channel containing flow that will travel past a perpendicular branch channel
w_2	Width of channel containing flow that will not travel past a perpendicular branch channel
x	Distance

Abstract

This thesis is focused on the manipulation of solid spheres and droplets with a particular focus on medium exchange and size based sorting. Two novel microfluidic devices are demonstrated. Firstly, a medium exchanger capable of transferring spheres and droplets between two miscible liquids was developed. The primary phase was extracted via a series of narrow perpendicular channels using a pressure differential created by mismatched input flow rates. Complete exchange of mineral oil phases has been demonstrated along with the use of the device to create a buffer region for chemical sphere curing of alginate droplets for use in stem cell encapsulation. This device offers simple passive exchange at greater throughput than previously demonstrated.

The second device is a tuneable sphere focusing device that focuses spheres via inertial lift forces. Through the compression of the device the channel width is reduced such that the spheres are moved from an unfocused state into two focused streams. Focusing of 12 μ m spheres into two streams is achieved through channel dimension deformation. The device is shown to be capable of up to 88% \pm 1.1% focusing when compressed whilst the uncompressed device only focuses 51.4% \pm 2.1% of the spheres. The deformation of the device offers the potential for a greater range of tuning than previously possible with inertial lift based sorting.

Project Aim

This project was initially funded by ThermoFisher Scientific Ltd and as a result the original aim of this project was to use microfluidics to improve the manufacture of silica spheres for use in high performance liquid chromatography (HPLC) columns. In collaboration with ThermoFisher two main avenues for improvement were identified. Firstly, it was decided that finding some way to perform in flow medium exchange would be advantageous. When silica spheres are manufactured by ThermoFisher they are produced in a large tank where tetraethyl orthosilicate (TEOS) is mixed with acid, water and a surfactant for several hours. Following this they are left to settle to the bottom of the tank and then transferred to another large tank to clean them in acetone. This process is extremely time consuming and also involves large quantities of chemicals and therefore some way to transfer spheres from one solution to the other, in flow, on a microfluidic scale would offer advantages in terms of safety, speed and waste reduction.

The second area identified was sphere sizing. The spheres created by ThermoFisher using the two-tank technique have a normal diameter distribution and therefore often cover a wider range of diameters than desired. Monodispersity is advantageous in spheres used in chromatographic columns as it allows the spheres to be packed more tightly. Packing the spheres more tightly allows a greater number of spheres to be packed into the column, which in turn provides a greater silica surface area. A greater surface area means better chromatographic performance as there is a greater area available for bonding [1]. The distribution of sizes created

during manufacture means that size sorting is necessary. Currently this is performed based on the mass of the spheres but this can prove problematic as the density typically ranges from 1800-2200 kg/m³ [2]. Inconsistent density can lead to spheres of different sizes having the same mass. Thus a simple microfluidic sorting technique capable of density independent sorting of silica spheres was identified as a project goal.

1 Introduction to Microfluidics

Fluids behave differently at the micro-scale compared to how we perceive fluids, more generally, on an everyday basis. This is due to the increased influence of forces, such as interfacial tension, and the viscous force of a fluid at this scale, as opposed to the dominance of inertial forces at the macro-scale [3]. Microfluidics attempts to exploit this different behaviour by creating chips, that comprise of channels with at least one dimension that is in the micrometre scale, to manipulate the behaviour of liquids and gases [4, 5]. An example of this 'different' behaviour is shown in Figure 1-1.

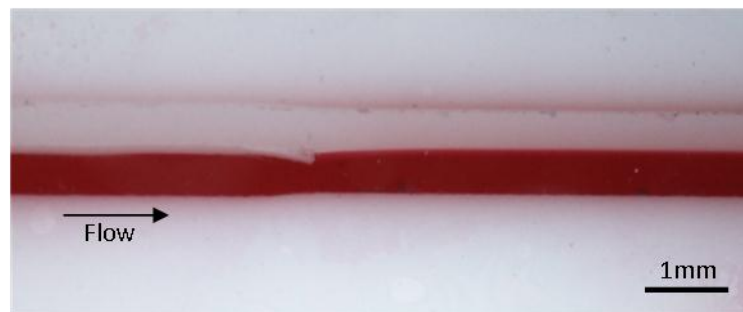


Figure 1-1: An example of the behaviour of fluids at a micrometre scale. Two fluids are introduced to each other within an enclosed $500\mu\text{m} \times 1\text{mm}$ cross-section channel (in this case the fluids are chloroform and chloroform coloured with Sudan red dye). On a macroscopic scale, the liquids would be expected to mix together through turbulence. However, at the micro-scale the two streams flow alongside each other with mixing only occurring through diffusion.

1.1 History of Microfluidics

In 1883, Osborne Reynolds performed a study into the flow of fluids in glass pipes [6]. By adding streams of coloured water to fluid flowing through these glass pipes, he was able to observe that by varying flow velocity, pipe

diameter and fluid temperature, it was possible to alter the manner of flow within the pipes. He discovered that there was a transition from 'streamline' to 'sinuous' flow; what we now know as laminar and turbulent flow respectively. This discovery laid the foundation of modern microfluidics.

Despite this early discovery the first true step on the path to microfluidics has been cited as Richard Feynman's seminal 1959 lecture "There's Plenty of Room at the Bottom" [5, 7]. In this lecture, Feynman championed the potential of miniaturisation and challenged the scientific community to push the limits of technology into the micro- and nano-scale. This strive for miniaturisation led to the emergence of the field of microelectromechanical systems (MEMS) through the 1970s and 1980s [8, 9]. There were also examples of microfluidic technology during this time [10-12]. However, due to manufacturing difficulties, these remained largely isolated instances until the 1990s. During this decade there were advances in MEMS technology that allowed microfluidics to begin to emerge as a promising research field. The microfluidic technologies developed in the 1990s covered a diverse range of topics such as electrophoretic separation [13-15], electro-osmotic pumping [16], diffusive separation [17], micromixers [18], DNA analysis [19-21], cytometers [22] and chemical microreactors [23].

Many of the early microfluidic devices were manufactured with silicon and glass. The use of silicon was found to have some limitations as it is expensive, opaque to visible light and impermeable to gases [24]. Moving into the 21st century devices manufactured out of polymers such as polydimethyl siloxane (PDMS) were developed. These polymer devices were

quicker and easier to manufacture, and provided additional advantages such as permeability to gases, such as oxygen and carbon dioxide, meaning that the use of living cells in such environments became more viable [24]. This development helped the field of microfluidics to continue to expand into areas such as chemical synthesis [25, 26], bioanalyses [4, 27], drug screening [4], separations [28, 29], cell analysis and manipulation [4, 30] and multiphase flows to generate droplets and bubbles [31-33].

1.2 Why Microfluidics?

The diversity of microfluidic technology is a result of the many advantages associated with the use of fluids at such a small scale. The laws of scale dictate that heat transfer and chemical reactions occur much more rapidly at the micro-, rather than macro-scale, meaning that throughput can be dramatically increased [4]. Additionally, the small quantities used mean that strongly endo- or exo-thermic reactions, that are difficult to control on the large scale, are more easily controlled [5]. The faster reactions are a result of reduced diffusion times and also the increase in surface to volume ratio that results from a reduction in size [3].

Reducing the quantities of chemicals used, offers potential cost reductions and, also a lowers the risk of chemical contamination of the surrounding environment. When combined with the reduced footprint of microfluidic devices, it is potentially possible to produce microfluidic devices close to potential users and therefore also reduce transportation costs [5].

Another advantage of microfluidics is the potential to integrate numerous processes onto one device. These devices are known as micro total analysis systems (microTAS) or as a lab-on-a-chip [5]. Integrated devices allow many stages of analysis or synthesis to be carried out within an enclosed device. This reduces the time taken to perform the task and also reduces the risk of contamination occurring between stages [5]. As long ago as 1998, a device was demonstrated that was capable of measuring an aqueous reagent and DNA solution and then mix the two, amplify or digest the DNA and finally separate and detect the result, all on one chip [34].

Using such small volumes creates a challenge to ensure that sufficient quantities are used to make microfluidics commercially viable. Thanks to the small footprint of the devices it is possible to employ massive parallelisation [5], this increases the overall throughput to the point that it is possible for them to be viable. Parallelisation also provides another potential advantage as it offers the potential to test many different reactions at the same time making microfluidics useful in areas such as drug development [5].

1.3 Fluid Flow

Fluid behaviour can be completely different at the microscale to what is seen at the macroscale [35]. To understand this difference we must first consider the characteristics of fluids.

Liquids are generally characterised by three parameters: density, ρ ; pressure, P ; and dynamic viscosity, μ .

Pressure in a liquid depends on the depth within the liquid; on the micro-scale of microfluidics this pressure differential can be considered to be negligible. Pressure applied externally, such as from an inlet or outlet will induce the liquid to flow.

A liquid in motion will resist the force applied to it due to its internal friction. This internal friction is the viscosity of the liquid. It is a measurement of the relationship of shear stress created by the applied force and the resultant velocity this force induces. A fluid is considered Newtonian if the shear stress is directly proportional to the velocity gradient. Otherwise, the liquid is non-Newtonian [35]. Whilst non-Newtonian fluids encompasses any fluid with flow properties that differ from Newtonians fluids, many people will be most familiar with the non-Newtonian behaviour of a cornflour in water mixture whereby the viscosity increases when the fluid is put under stress.

1.4 Flow Characteristics

Flow conditions are determined by the magnitudes of inertial and viscous forces as expressed by the dimensionless Reynolds number, Re , as given by the equation 1.1 for an enclosed channel:

$$Re = \frac{\textit{inertial forces}}{\textit{viscous forces}} = \frac{\rho D_h U_{avg}}{\mu} \quad (1-1)$$

where D_h is the hydraulic diameter, ρ is the fluid density, μ is the dynamic viscosity and U_{avg} is the average velocity of the moving liquid. The transition between laminar and turbulent flow is dependent on the channel geometry but in a straight channel it typically occurs at around $Re = 2000-2500$ [35-37]. Below 2000 viscous forces dominate and the flow is laminar. Above this value, inertial forces are dominant.

It is clear from equation 1-1 that low Re can be achieved with a low velocity, small dimensions or low density, as well as with high viscosity [36]. Therefore, it is clear that with the small dimensions of microchannels, the laminar flow regime will likely be dominant. This can be demonstrated if water flowing in a square $500\mu\text{m}$ channel is considered. To obtain a Re that equals or exceeds even the lowest end of the transition zone ($Re=2000$) the water must flow at 90mph [35].

To understand fluid flow, a set of equations that have been created based on the fundamental laws of conservation of mass, momentum and energy can be considered. These laws are combined with fluid equations governing viscosity and thermal conductivity to create the equations known as the Navier-Stokes equations [38]. The equations themselves are not solvable as there are fewer Navier-Stokes equations than there are unknown parameters within said equations. This means that several conditions have to be adopted to solve them based on the given circumstance. Most often a no-slip boundary condition is adopted [35]. The velocities at phase boundaries (i.e. the boundary created by a channel wall and liquid) must be

equal, therefore, with the no-slip condition, the fluid velocity must be zero at the walls [35]. This type of flow is known as Poiseuille flow, which is characterised by the faster flow in the centre of the channel [39].

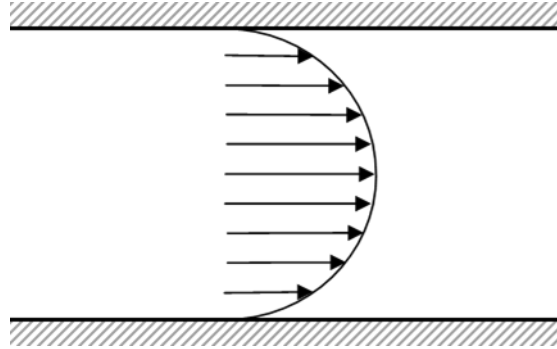


Figure 1-2: Illustration of Poiseuille Flow. Fluid is introduced to an empty channel. Arrows placed at the fluid boundary indicate the direction of flow and their length indicates the magnitude of flow rate. Flow is faster at the centre of the channel than at the edges.

In microfluidic systems there are generally two types of flow mechanisms; directed transport and statistical transport. Directed transport is a result of work being exerted on the fluid, for example by a mechanical pump, and leads to volume flow of the fluid. Statistical transport is entropy driven; for example, diffusive mixing. Robert Brown investigated diffusion in 1827 when he observed the erratic behaviour of pollen on the surface of water [40] but it was Einstein *et al.* that established the role of molecules in the mechanisms of diffusion [41]. Diffusion occurs when there is a concentration gradient of one kind of molecule within a fluid leading to a net movement of molecules from an area of high concentration to one of lower concentration [35]. This occurs as a result of probability; with more molecules in the higher concentration area it is more likely that a molecule will move randomly away from this area than towards it. Diffusive mixing demonstrates one of the advantages of the small-scale found in

microfluidics. Molecular movement by diffusion can be characterised by the root mean square displacement as given by [35, 42]:

$$\langle r \rangle^2 = qDt \quad (1-2)$$

where, D is the diffusion constant (also known as the diffusion coefficient), q is a numerical constant that depends on the number of dimensions considered (for 1, 2 and 3 dimensions $q= 2, 4$ and 6 respectively) and t is the time taken. If we consider the average diffusion distance in just one dimension, for example x , then $x^2=2Dt$ (similarly y^2 and z^2 are also equal to $2Dt$)[42]. This means that diffusion time is related to the distance squared and, therefore, the diffusion time can be drastically cut down. For example, by making the diffusion distance 100 times smaller, the time taken is 10,000 times shorter.

In reality, fluid flow is usually some mixture of these two types of transport mechanism. To understand which type is dominant the Peclet number can be used [43]. This number is a measure of the importance of advection in relation to diffusion. As the Peclet number increases so does the dominance of flow forces over that of molecular diffusion with regards to mixing. This number is, therefore, important in determining the conditions in which diffusion is the primary mixing method:

$$Pe = \frac{U_{avg}L}{D} \quad (1-3)$$

where, L is the characteristic length. If the Peclet number is less than 1, then diffusion dominates. Where it is above 1, then directed flow is dominant.

1.5 Channel Material

Aside from the fluid, it is also important to consider the material that the microfluidic channel is made from [35]. The relationship between the fluid and the material can be analysed by measuring the contact angle. This measurement can be used to find the surface energy of the material. In 1805 Thomas Young established the relationship between the contact angle of a liquid drop on a solid surface and the mechanical equilibrium of the drop that is subjected to three measures of interfacial tensions [44]. This relationship is given by Young's equation:

$$\gamma_{lv}\cos\theta = \gamma_{sv} - \gamma_{sl} \quad (1-4)$$

where, θ is the contact angle, γ_{sv} is the solid-vapour interfacial tension, γ_{sl} the solid-liquid tension and γ_{lv} the liquid-vapour tension. The contact angle demonstrates the attraction of the liquid molecules to the surface. At the solid-liquid interface, if the liquid molecules are more attracted to the solid than to each other, then surface wetting occurs, meaning the contact angle is obtuse. This type of surface is referred to as hydrophilic and will have a higher surface energy. If the molecules are more attracted to each other the droplet will 'bead up' to reduce the wetting of the surface, giving an acute contact angle. This is a hydrophobic surface.

2 Sphere Manipulation

In recent years the control and manipulation of solid spheres and liquid droplets has become a fundamental application of microfluidics. Henceforth the term spheres will be used to refer to solid spheres such as particles or cells whilst the term droplets will be used for liquid spheres. This control and manipulation covers areas such as cell enrichment and purification [45, 46], droplet or bubble generation and control [47, 48] and sample preparation [49, 50]. Techniques to achieve this have varied widely and are discussed here. As this thesis deals primarily with sphere exchange and continuous sphere sorting, each technique will be assessed based on its merits for these processes.

There are two categories of sphere control, namely active and passive. Active control involves the application of some external force, whereas, passive control uses the inherent microfluidic forces to control the spheres [51].

2.1 Active Control

Particle separation through active control was first introduced by Giddings in 1966 in his paper developing the technology of field flow fractionation (FFF) [52]. FFF is the use of an external field applied perpendicular to the channel flow allowing the sorting of spheres based on some physical

property of the sphere (e.g. size). Originally the external force was gravity but alternative forces were used later as will be detailed in this section. This gravity driven technique was further developed by Giddings [53] by adding a secondary inlet to control the sphere position prior to entering the field. This is called Split-Flow Lateral Transport Thin (SPLITT) separation as illustrated in Figure 2-1. Most microfluidic active sorters use some variation of FFF or SPLITT [51].

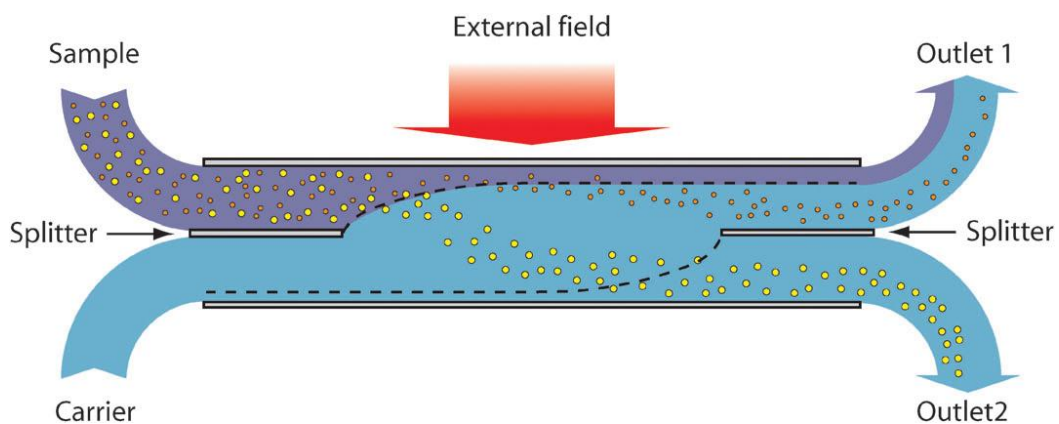


Figure 2-1: Split-Flow Lateral Transport Thin (SPLITT) separation. Channel is viewed side-on as fluid flows from left to right. A primary inlet carries spheres into the device (sample) whilst a secondary inlet introduces a sphere-less carrier liquid. An external field imparts a greater force on one type of sphere than the other (in this case the yellow spheres) causing them to be diverted more and therefore exit through a different outlet to the less affected spheres. Image from article by Lenshof and Laurell [51].

2.1.1 Acoustophoresis

Acoustophoresis in microfluidics refers to the use of acoustic fields, usually ultrasonic, to apply a force to either a fluid or a sphere in a device. Typically, the wavelength is set to twice the width of the microfluidic channel ensuring that a standing wave is setup. If a sphere is introduced into this acoustic field it is subjected to a radiation force that moves the sphere towards either

a pressure node or anti-node [51, 54]. The acoustic field is usually created by a piezoelectric plate attached to the microfluidic device close to, or as part of, the microfluidic channel.

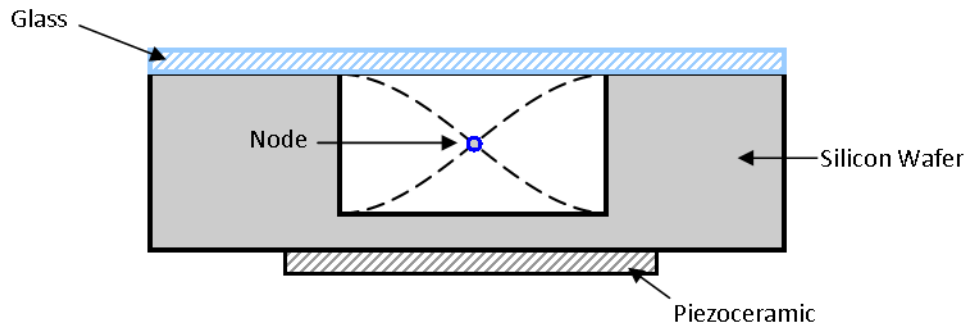


Figure 2-2: Cross-section of a microfluidic device that employs acoustophoresis to deflect spheres. An acoustic standing wave (indicated by a dashed line) is induced in the microfluidic channel by a piezoceramic plate. The standing wave creates a node at the centre of the channel that is able to deflect passing spheres as they flow through the channel and past the node. The amount of deflection is volume dependent meaning sorting can be achieved by placing outlets such that the amount of deflection will determine which outlet the spheres exit through.

A micro-sphere travelling through an acoustic field within a carrier fluid is subjected to primary and secondary radiation forces. Primary forces are further split into axial (F_{Ax}) and transverse forces (F_{Tr}). The acoustic field causes axial forces; they act in the direction of propagation moving the sphere towards, or away from, a node. Axial forces are stronger than transverse forces, which pack particles closer together and are a result of the flow of fluid [55].

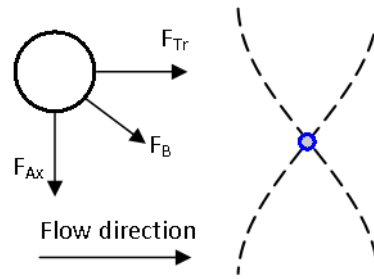


Figure 2-3: Radiation forces on a particle flowing through an acoustic field showing transverse (F_{Tr}), axial (F_{Ax}) and Bjerknes forces (F_B).

The magnitude of the primary radiation force can be expressed as:

$$F_r = \left(\frac{\pi p_0 V_p \beta_w}{2\lambda} \right) \phi(\beta, \rho) \sin(kx) \quad (2-1)$$

where the pressure amplitude, p_0 , is proportional to the piezoelectric supply voltage; V_p is the sphere volume; β_w is the medium compressibility; and λ is the wavelength. The wave number, k , is equal to $2\pi/\lambda$ and x is the distance from a node. The contrast factor, ϕ , can be defined by:

$$\phi = \frac{5\rho_c - 2\rho_w}{2\rho_c + \rho_w} - \frac{\beta_c}{\beta_w} \quad (2-2)$$

where ρ_c and ρ_w are the sphere and medium density respectively. β_c is the sphere compressibility [54, 56]. The contrast factor determines whether a sphere moves towards a node or an anti-node. A positive contrast factor results in the sphere moving towards a node whilst a negative contrast factor will lead to the sphere moving towards an anti-node. Generally solid particles move towards nodes whilst gas bubbles move towards anti-nodes [55].

From equation 2-1 it is clear that the radiation force scales with the volume, therefore, the force scales with the cube of sphere radius. This means the force is highly size dependent making acoustophoresis very useful in the field of sphere size sorting. Due to the force also featuring a density element, it is possible, however, that spheres of different sizes and densities could be subject to the same force creating sorting errors.

The secondary radiation force is a result of inter-sphere, or 'Bjerknes', forces (F_B) caused by the waves that are created by the movement of other spheres. These forces are usually very weak and are only effective when the spheres are very close together.

Multiple harmonics can also be achieved by adjusting the frequency of the acoustic wave or the geometry of the microfluidic channel. This means there are a multiple nodes across the width of the microfluidic channel [57].

Table 2-1: Summary of size sorting devices using acoustophoresis.

Ref.	Chip	Fluid	Spheres	Quality	Notes
[58]	Silicon wafer, 3mm wide main channel, 70+mm long	Glycerin, water mixture. 1068ml/hr - 1884ml/hr	100 μ m blue polystyrene, 170 μ m red polystyrene	Outlet One: 99-85% of red spheres, 0-9% of blue. Outlet Two: 1-15% of red, 100-91% of blue spheres.	Not strictly speaking a microfluidic device.
[59]	Polyacrylamide & Teflon, 3mm wide main channel adjustable, 70+mm long	Cell media	Lactobacilli cells (4.8×10^7 per ml), Hybridomas cells (1.2×10^6 per ml)	Ratio of hybridomas to lactobacilli at side outlet: $6.9 \pm 1.8 : 0.39 \pm 0.01$ (~95% sorting)	From same group as ref [58] so very similar design.
[60]	PDMS, 100-160 μ m wide and 120-150 μ m	Solution, 0.1944ml/hr- 0.684ml/hr	5 μ m polyamide 12 particles, red blood cells	Maximum of 99.975% sorting efficiency.	Three-stage device, flow rate reduced by a third at each stage.
[61]	PDMS bonded to lithium niobate wafer, 150 μ m wide, 80 μ m deep	DI water, 0.036- 0.12ml/hr	Fluorescent polystyrene beads, 4.17 μ m (2.53×10^7 per ml), 0.87 μ m (2.76×10^7 per ml)	Side outlets: ~90% of smaller beads, ~20% of larger. Central outlet: ~10% of smaller, ~80% of larger beads.	
[62]	Silicon wafer, 52-400 μ m wide channels, 200 μ m deep	Sample: 2ml/hr Buffer: 14 ml/hr	3, 5 and 10 μ m polystyrene (~ 10^7 per ml)	Average sorting efficiency: $98\% \pm 0.4\%$	Multi-size sorting
[57]	Silicon wafer, 400 μ m wide, 50 μ m deep	0.012ml/hr	Polystyrene spheres, 5 μ m (600/1000 per μ l), 10 μ m (70/10 per μ l)	Centre outlet: 100% of 10 μ m Side outlets: 86-98% of 5 μ m	Number of nodes changes along the length of the device. Low concentration of 10 μ m spheres, quality of sorting reduces as concentration increases.
[63]	Silicon wafer, 370 μ m wide, 125 μ m deep. 3 inlets, 11 outlets (5 pairs and a central outlet)	Distilled water, Outlet flow ~6ml/hr	2 μ m (~0.5% vol), 3 μ m, 5 μ m, 8 μ m and 10 μ m (~1% vol) polystyrene spheres	Out 1: 94% of 10 μ m, out 2: 62% of 8 μ m, out 3: 66% of 5 μ m, out 4: 88% of 2 μ m. 3 μ m could not be separated	Multi-size sorting

Table 2-1 gives a summary of recent research in the field of acoustophoretic sorting by sphere size. It is clear from this that acoustophoresis is a promising technique however there are drawbacks. The reliance on contrast factor to determine sphere behaviour means that acoustophoretic sorting is not density independent, which may lead to potential sorting errors when attempting to select exclusively for size. Additionally there is potentially an issue that pressure fluctuations created by the acoustic field could distort and possibly damage cells. Another possible problem is that it has been found that at high voltages cells can begin to clump together leading to gravitational forces influencing the behaviour of the spheres [59]. The addition of a piezoelectric device also adds a level of complexity to the device.

The most promising devices appear to be the device created by Adams and Soh [62] and Petersson *et al.* [63] as they demonstrate reasonably high sorting quality and are capable of sorting more than two sizes. All the other techniques can only consistently differentiate between two different spheres. Whilst Kapishnikov *et al.* [60] claim a maximum sorting efficiency of 99.975% it is not clear from the publication how consistently this level can be achieved.

Table 2-2: Summary of current research into using acoustophoresis to perform medium exchanges.

Ref.	Microchannel material	Size	Fluid	Spheres	Quality	Notes
[64]	PDMS	250 μ m wide, 10mm deep, 5mm long	Water and sodium fluorescein, Flows vertically upwards at 612ml/hr	Yeast cells (\sim 2.5 μ m), 1.53×10^7 per ml	\sim 91% fluid exchange (9% contamination) w/out spheres. Drops to \sim 72% when cells introduced. \sim 70% of cells are transferred.	Increasing flow rate improves fluid exchange but cell exchange is worse.
[65]	Silicon	350 μ m wide, 125 μ m deep, 30mm long	Distilled water, up to 16.2ml/hr, Blood plasma.	5 μ m polyamide spheres (1.5%vol), bovine blood cells	Medium exchange: 80-65%, up to \sim 95% if buffer zone introduced. 95% sphere transfer, 98% cell transfer	Medium exchange quality effected by the applied voltage
[66]	Silicon	375 μ m wide, 150 μ m deep. Side channels are 150 μ m square. 60mm long	Doppler fluid in milli Q water, washing buffer 3-7.2ml/hr for main channel. Side channels flow at 25-40% of the main channel.	Polyamide 5 μ m (2%vol), red blood cells (0.2%vol)	Medium exchange: 96% w/out spheres. Sphere transfer: 94% with medium exchange of 19%	Increasing flow rate of washing buffer through side flows improves the medium exchange but fewer spheres are transferred.
[67]	Silicon	375 μ m wide, 150 μ m deep. Side channels are 150 μ m square. 60mm long	3ml/hr (sample fluid), 6ml/hr (wash fluid 1), 12ml/hr (wash fluid 2)	Polystyrene 5 μ m (6×10^6 per ml)	Medium exchange: 99.995% (sphere con. 0.01%w)-95% (2%w). \sim 75% sphere transfer	Development of [66]. Throughput of $\sim 5 \times 10^5$ spheres per second.

Table 2-2 provides a brief summary of recent research in the field of acoustophoretic medium exchange. It is clear that in every medium exchanger there is a balance to be struck between the amount of contamination and the number of spheres transferred. Improving the medium exchange has a cost; either in the percentage of spheres transferred, as in the cases where exchange is improved by increasing flow rate [64, 66], or in the initial sphere concentration [65, 67]. It is also clear, however, that using acoustophoresis for medium exchange is a promising area.

Acoustophoresis is, in theory, a very encouraging technique for sphere manipulation offering high levels of control and throughput. The problem with it is that the need to apply an external force makes manufacture more costly and complex, requiring connections to external equipment to supply a voltage. Also, expensive high precision silicon wafer manufacture is often required.

2.1.2 Dielectrophoresis (DEP)

Particles in a non-uniform electric field may be subjected to a dielectrophoretic force. This force occurs due to a reaction with a particle dipole. There are two types of dipole, namely a permanent dipole, caused by the orientation of the atoms, or an induced dipole, created by a reorientation of charges on to a particle surface. The strength of the force is dependent on a number of characteristics. Among them are the electrical properties of both the carrier medium and the sphere and also the shape and size of the

sphere [51, 68]. The electric field created for DEP can be applied using either DC or AC current. The required non-uniformity of the field is created through the use of electrodes of various shapes and size or by putting insulating obstacles into the microfluidic channels.

Dielectrophoresis is one of the most popular methods of sphere manipulation for a number of reasons, amongst them are:

- It can sort spheres or cells without the need of labels
- It has favourable scaling effects
- It is capable of inducing both positive and negative forces.

The favourable scaling effects can be demonstrated by examining the following equation for dielectrophoretic force, F_{DEP} , acting on a homogenous isotropic sphere[69]:

$$F_{DEP} = 2\pi f_{CM} r^3 \nabla(E \cdot E) = 2\pi \epsilon_m \text{Re}[f_{CM}] r^3 \nabla |E|^2 \quad (2-3)$$

where ϵ_m is the medium permittivity, r is the sphere radius and E is the electric field strength. $\text{Re}[f_{CM}]$ is the real part of the Clausius-Mossotti factor, which is a measure of the difference in polarisation between the sphere and the carrier medium [70]. The Clausius-Mossotti factor is given by the equation [69, 71]:

$$f_{CM} = \frac{\epsilon_p^* - \epsilon_m^*}{\epsilon_p^* + 2\epsilon_m^*} \quad (2-4)$$

where ϵ_p^* is the complex particle permittivity and ϵ_m^* is the complex medium permittivity. When dealing with AC DEP, complex permittivity must be used

as the permittivity varies with frequency. From equation (2-3) it is possible to derive the following approximate equation [46]:

$$F_{DEP} \approx \frac{V^2}{x^3} \quad (2-5)$$

where V is the applied voltage and x is the distance from the DEP electrode. This means that reducing the scale by 100 times will reduce the required voltage by 1000 to achieve the same force, making DEP a much more attractive technique on the micro-scale. It should also be noted that DEP can be used for size-based sorting as a result of the r^3 parameter in equation 2-3. This means that the force is greater on larger particles. The magnitude of this force is vital as F_{DEP} must dominate over the other forces in the microchannel (e.g. the drag force induced by the flow of fluid) for dielectrophoresis to work. The direction of F_{DEP} is dependent of the value of f_{CM} ; above 0 the sphere will be attracted to electric field maxima. Below 0 spheres are attracted to the minimum.

These principles of DEP can be applied to field flow fractionation (FFF) devices by using the combination of sphere buoyancy (or gravitational force downwards) and F_{DEP} to position spheres at different equilibrium positions as they flow past DEP electrodes. These equilibrium positions cause the spheres to exit at different rates due to the parabolic flow profile within a microfluidic channel. Alternatively the dielectric force can be used to deflect spheres by differing degrees depending on their size as they pass the electrodes before being collected at well placed outlets [69].

Table 2-3: A selection of recent DEP based sphere-sorting research.

Ref.	Chip	DEP Type	Fluid	Spheres	Quality	Notes
[72]	Channels made with SU-8, 1mm wide x 25 μ m deep	AC	Flow rate: 0.24 or 0.36ml/hr	Lipisode vesicles, 100nm-4.7 μ m	At 0.24ml/hr sorted 2.1-4.6 μ m to outlet 1, 0.7-1.8 μ m to outlet 2. At 0.36ml/hr sorted 2.3-4.7 μ m (out 1) and 1.5-2.7 μ m (out 2)	Cannot sort any spheres below 700nm. At 0.36ml/hr there is some crossover between the size ranges.
[73]	PDMS channels, 515 μ m x 40 μ m. Oil droplet used to restrict channel width	DC	DI water	1, 5.7 and 15.7 μ m carboxylate-modified fluorescent polystyrene particles	Shifted spheres along y-axis. Prior to DEP: 15.7 μ m y=13 μ m, 5.7 μ m y=3 μ m. Post DEP: 15.7 μ m y=338 μ m, 5.7 μ m y=98 μ m	A larger oil droplet gives better separation.
[74]	PDMS, 300 μ m x 90 μ m channels	DC	Water and Sodium carbonate	5.7, 10.35 and 15.7 μ m carboxylate-modified fluorescent polystyrene particles ~10 ⁵ per ml	Two sizes can be separated from each other at any one time	The sizes that are sorted can be chosen by varying the voltage
[75]	PDMS, Channels width varies 50-100 μ m, 25 μ m depth	DC	Phosphate buffer	3, 5 and 10 μ m polystyrene spheres, ~10 ⁷ per ml	100% separation of 5 and 10 μ m at 600V DC.	3 and 5 μ m could also be separated but not 100% even at 1500V DC. Enough to damage cells.
[76]	PDMS mixed with silver, Main channel 200 μ m x 40 μ m. Side channels 50-115 μ m wide	AC	NaHCO ₃ buffer, 0-3 μ l/hr	5, 10 and 15 μ m latex polystyrene spheres, 10 ⁶ -10 ⁷ per ml	5 and 10 μ m, 87.7% of 5 μ m at outlet C, 100% of 10 μ m spheres at outlet D (55V AC). 10 and 15 μ m sorted 100% (50V)	Only two sizes at once.
[77]	Dry film resist, 500 μ m x 40 μ m	AC	Flow rate: ~36 μ l/hr	500nm, 1 μ m and 2 μ m fluorescent carboxylate-modified latex spheres	Separates two sizes at 99.9% efficiency	
[78]	PDMS, channel 300 μ m wide narrowing to 40-60 μ m, 40 μ m deep	DC	NaCl diluted in DI water	10 and 15 μ m polystyrene spheres	~95% separation efficiency	

A review of the research shown in Table 2-3 highlights many of the advantages of DEP but also some of the problems. It is clear that highly efficient sorting can be achieved, however, the throughput of the devices appears to be relatively low. The potential issue of Joule heating caused by the voltage through the electrodes is highlighted through the work by Zhu *et al.* where 1500V DC is required to sort 5 μm spheres from 10 μm spheres. This voltage is sufficient to heat the surrounding carrier solution to the point where it would be harmful to any cells that were sorted using such a device [75]. These papers also highlight the issue that fabricating the electrodes into the device often seems to be a complex, time-consuming, and somewhat expensive process. It is also clear that spheres often require functionalisation in order for dielectrophoresis to be effective, often with carboxylate.

There appears to be little research into medium or phase exchange using DEP although Tornay *et al.* have undertaken work in this field [50, 79]. In spite of the capability of this exchanger to achieve high quality exchange it also has limitations in terms of throughput with 90% of 1 μm spheres being exchanged with a just a 7.2 $\mu\text{l/hr}$ flow rate. There is a balance to be struck between contamination level and sphere exchange. Faster flow rates lower the contamination between phases but also reduce the number of spheres that are exchanged. Seger *et al.* developed a technique in 2004 that 'dipped' spheres into another medium by transferring them into a second medium and then transferring them back afterwards. This technique also has a low throughput with a the flow-rate similar to that employed by Tornay *et al.* (approximately 10.8 $\mu\text{l/hr}$) [80].

2.1.3 Magnetophoresis

Much like DEP, magnetophoresis exploits the properties of the spheres to cause a deviation in their path allowing for sphere manipulation. To achieve this on a microfluidic chip a magnetic field is applied perpendicular to the flow of fluid creating a magnetic field gradient across the channel [81, 82]. This magnetic field can be created using either permanent magnets or electromagnets [82, 83]. The degree of deflection of the sphere (U_{defl}), given as a velocity (m/s), can be determined using the following equation [82]:

$$U_{defl} = U_{mag} + U_{hyd} \quad (2-6)$$

Where U_{mag} is magnetic deflection and U_{hyd} is the deflection due to hydrodynamic flow. The magnetic deflection being the ratio of magnetic force and viscous drag force as given by following equation:

$$U_{mag} = \frac{F_{mag}}{F_{drag}} = \frac{F_{mag}}{6\pi\mu r} \quad (2-7)$$

with μ representing the fluid viscosity and r the sphere radius. The magnetic force in this equation is given by [84]:

$$F_{mag} = \frac{\Delta\chi V_p}{\mu} (\nabla B \cdot B) \quad (2-8)$$

where, V_p is the volume of the sphere, $\Delta\chi$ represents the difference in magnetic susceptibility between the carrier fluid and the sphere, and B is the magnetic flux density. It can be seen that both equation 2-7 and 2-8 have a sphere radius component (with the sphere volume representing r^3). Therefore, it is clear that the magnitude of deflection is proportional to r^2 and also the magnetic susceptibility, χ_p , of the sphere (assuming the carrier liquid remains constant) as shown in equation 2-9.

$$U_{mag} \propto r^2 \chi_p \quad (2-9)$$

There has not been a great deal of work done in the field of sphere sorting with magnetophoresis, even though this technique is not subject to one of the main problems with DEP, that being Joule heating. In fact there is generally no heat generation caused by magnetophoresis. Aside from this advantage there are many disadvantages to be considered. Firstly, most cells or spheres require labelling, usually with a superparamagnetic material such as iron oxide [85-89], in order for the magnetic field to have an effect. Superparamagnetic labels are typically used, rather than ferromagnetic labels, as they become magnetised only in the presence of a magnetic field making homogenous suspensions more easily obtainable [90]. Another disadvantage is that what work there has been has typically achieved relatively poor sorting efficiencies, in the range of only 70-80% [82, 83]. This has been slightly improved by passing the solution through the device multiple times, achieving an efficiency of ~95% [86]. Another problem is that throughput is generally very low, in the 10s or 100s of spheres sorted per minute [82, 83]. Magnetic hysteresis can also be troublesome as it can lead to spheres clumping together after they have exited the applied magnetic field [51]. For these reasons magnetophoresis has not yet emerged as a truly viable sphere manipulation technique.

2.1.4 Optical Methods

In 1970 Ashkin established that light beams could be used to manipulate microspheres [91]. A light beam with a Gaussian profile will have a very strong electric field gradient in the narrowest part of a focused beam. A dielectric particle entering this beam will experience a force towards the

centre of the beam where there is an equilibrium position that can trap a sphere. This was further developed by Ashkin *et al* to show a single tightly focused laser beam can trap a particle allowing it to be moved in three dimensions [92]. This was the foundation of what is known as ‘optical tweezers,’ which have historically been the primary micro-object manipulation tool in the scientific community [93]. Its use in continuous microfluidic sorting, however, is a relatively new development with work only emerging in the last decade [94-103]. Most of the continuous optical sorting techniques use active sorting which involves a decision making step, commonly using a camera to make a decision based on some properties of the sphere such as its size or fluorescence intensity [95, 96, 101]. Passive optical sphere sorting is the alternative technique. This relies on a difference in the magnitude of the force on a sphere due to some properties of said sphere (e.g. size, material etc.) [97, 99, 100]. Both techniques have been shown to be capable of relatively high resolution sorting in comparison to other sorting techniques, differentiating spheres that are less than 500nm different in diameter. Despite this high resolution this technique is not particularly well suited to microfluidic chip sorting as the equipment necessary to perform optical sorting is both complex and bulky. It is also relatively expensive to implement [93]. Additionally, much like with dielectrophoresis, there is the potential for cell damage as the laser beam will raise the temperature. In order to negate this problem the power has to be limited thus lowering the potential force that can be applied to a cell and potentially also lowering the quality of the sorting. Although there has been

no reported work on an optical microfluidic medium exchanger the sorting techniques could be easily adapted to behave as such.

2.1.5 Gravitational

The main limitation of gravitational separation is summed up by Kumar *et al.* in that “processing rates are limited by the response of particles to gravity that, owing to their small size, is often very slow”[59]. This can be shown by the following equation that expresses the sedimentation velocity, U_{sed} [104, 105]:

$$U_{sed} = \frac{2r^2 g \Delta\rho}{9\mu} \quad (2-10)$$

where r is the radius of the sphere, g is the acceleration due to gravity, $\Delta\rho$ is the difference in density between sphere and carrier liquid and μ is the viscosity of the carrier liquid. The r^2 term ensures that as the sedimentation speed drops drastically with the size of the sphere. As such, there is little microfluidic work that relies on gravity to separate particles. What work there is, tends to involve small ($\sim 1-2\mu\text{m}$) particles being unaffected whilst larger particles ($20+\mu\text{m}$) sink to a lower outlet. The quality of separation tends to be poor at this lower outlet, with a great deal of crossover between target and non-target particles [106, 107]. Other work has reported a separation yield of $\sim 73\%$ [104]. This slow response and reasonably poor quality exchange makes gravitational sorting an unappealing technique. Additionally, there is a limitation in that only spheres denser than the carrier liquid will settle to the bottom of the channel.

It should be noted that gravity based separation is more common outside of the microfluidic environment where the principal of sedimentation can be

used to separate larger numbers of spheres based on size, shape and density within large vessels [105]. Gravitational sedimentation techniques have little worth for spheres below approximately $5\mu\text{m}$ due to the long settling times plus the greater impact of convection diffusion and Brownian motion causes problems with sedimentation. This is often overcome by using a centrifuge to speed up the settling process [108]. The centrifugal force is greater on larger spheres hence they travel through a centrifuged medium at a faster velocity allowing for separation into distinct size bands. This separation can be poor if the spheres sizes are similar meaning density gradient separation is often used. This is achieved by carefully layering different concentration liquids on top of one another to ensure the density increases from the top to the bottom layer. These density layers make the size bands more distinct [109].

2.2 Passive Control

Passive control does not rely on any external force, instead it works purely on microfluidic forces created by the interaction of the fluid and the geometry of the chip [51].

2.2.1 Obstacle Induced Separation

Obstacle induced separation uses obstacles within a microchannel such as pinches, weirs and posts [51]. One common technique is deterministic lateral displacement (DLD), which uses an array of micropillars to sort particles of differing sizes [110-117]. Fluid flows through the micropillar array in a laminar fashion passing through many rows of pillars with each row shifted laterally from the one preceding it. This laminar flow creates

'zig-zag' streamlines through the array that spheres will follow if they are smaller than a critical diameter. If, however, the spheres are larger than this critical diameter they will not fit into the streamlines and will be displaced laterally into an adjacent streamline. The critical diameter is defined by the centre of the sphere and its position relative to streamlines passing the micropillars. The centre of smaller spheres can get closer to the pillars and therefore can follow alternative flow routes through the pillars than large spheres. By varying the shift of micropillars it is possible to sort different sizes.

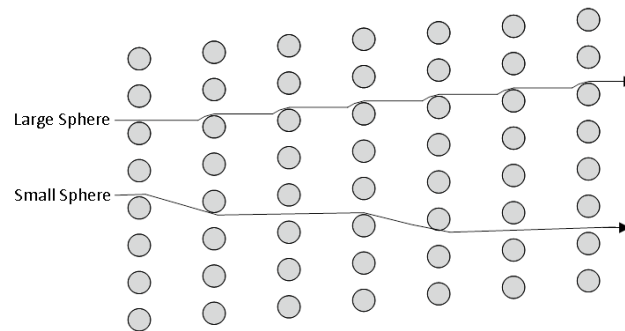


Figure 2-4: Deterministic Lateral Displacement. The positioning of the pillars determines the path of different sized spheres. The position of the centre of the sphere relative to the streamlines passing through the micropillar structure determines the route the spheres take. Smaller spheres can get closer to the pillars and therefore be carried by different streamline routes than the larger spheres [115].

The key parameters determining the path of the spheres through a micropillar array are [112]:

- The lateral shift between adjacent rows
- The distance between adjacent rows
- The size of the gap between micropillars.
- The diameter of the sphere.

Separation of particles has been demonstrated over a wide range of sizes with Lubbersen *et al.* separating particles as large as 309-532 μm [111] and Huang *et al.* separating particles as small as 0.8 μm [117]. This paper also demonstrates a high sorting resolution as three polystyrene particle sizes that differ by just 0.1 μm are separated (0.8 μm , 0.9 μm and 1 μm). A way of increasing throughput has also been demonstrated by employing parallelisation [114] which is a fairly common technique for improving volume throughput in microfluidics [5].

Brownian ratchets can also be used for obstacle induced separation. Brownian ratchets are similar to DLD but with asymmetric posts in a symmetric array. Brownian motion is a result of sphere surface being bombarded by the molecules of the liquid in which they are suspended. Each of these collisions impart a small force on the sphere. If the sphere is large then enough collisions will happen in all directions to ensure that the net effect of these impacts is zero. As the spheres get smaller, however, the net impact of these impacts is less likely to sum to zero meaning there is an increased chance of movement being induced in the sphere [69]. This Brownian motion can cause some problems in that it can, to some degree, prevent the spheres from following the flow and therefore cause errors in the measurement of flow velocity and also uncertainty in the sphere location within a flow profile. Brownian motion can be exploited though by using Brownian ratchets [118]. Using the previously mentioned asymmetric posts Brownian diffusion can be selectively blocked in one direction causing particles to drift laterally [111, 119-121]. As Brownian diffusion has a greater impact on smaller spheres they will drift farther across the post

array than larger spheres allowing them to be separated based on their size [118].

Slanted obstacles along the top and bottom of microchannels can be used to focus particles to one side of a microchannel due to pressure fields induced by the microstructures [122]. These slanted obstacles reach all the way across the channels leaving a gap, either above or below, which allows the obstacles to deflect but not block the particles. Filtration objects have a gap above them that is large enough for smaller particles to pass through but small enough that it blocks the large particles. Unlike the slanted obstacles, filtration objects do not reach all the way across. There is a gap down one side of the channel (the opposite side to the focal position created by the slanted obstacles) that allows the larger spheres past. Thus, two particle sizes can be separated into different streamlines. This technique has been demonstrated with polystyrene spheres ranging from 8-12 μm , with complete separation of 9 μm spheres from 12 μm spheres [123]. This technique is called hydrophoretic filtration.

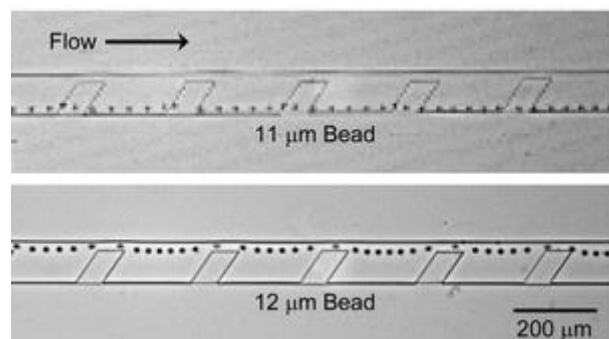


Figure 2-5: Hydrophoretic filtration of 11 μm and 12 μm spheres. Top-down view of flow through a hydrophoretic filtration channel showing spheres travelling past filtration obstacles. These filtration obstacles are not as tall as the channel is deep leaving a narrow space above them. Smaller spheres are able to pass over the slanted obstacles (top image)

whilst larger ones must go round them (bottom image). Image reprinted from the Lab-on-a-Chip journal [123].

Microfluidic sieves or filters are also a type of obstacle induced separation although they are not very common [124-126]. This is partly due to their propensity to become clogged; this is a common problem with many obstacle induced separation techniques particularly as particle density increases [51, 123]. Another problem with obstacle induced separation devices is that they are not very adaptable as tuning them to separate new particles sizes often requires a complete rebuild with different channel geometries. Some devices have attempted to overcome this, either by making the chip elastic, meaning the chip can be stretched to separate different sphere sizes [127] or by adding an element of active control by introducing an applied field across the device [120].

2.2.2 Hydrodynamic Filtration

Hydrodynamic filtration employs side channels to remove the carrier fluid and also selectively remove particles. The flow rate and channel width determine whether a sphere will travel down these side channels or continue onwards. However, unlike in a traditional filter, the spheres are all small enough to fit down these side channels. The filtration works due to the Zweifach-Fung effect, a.k.a the bifurcation law, first described in the late 1960s and early 1970s [128, 129].

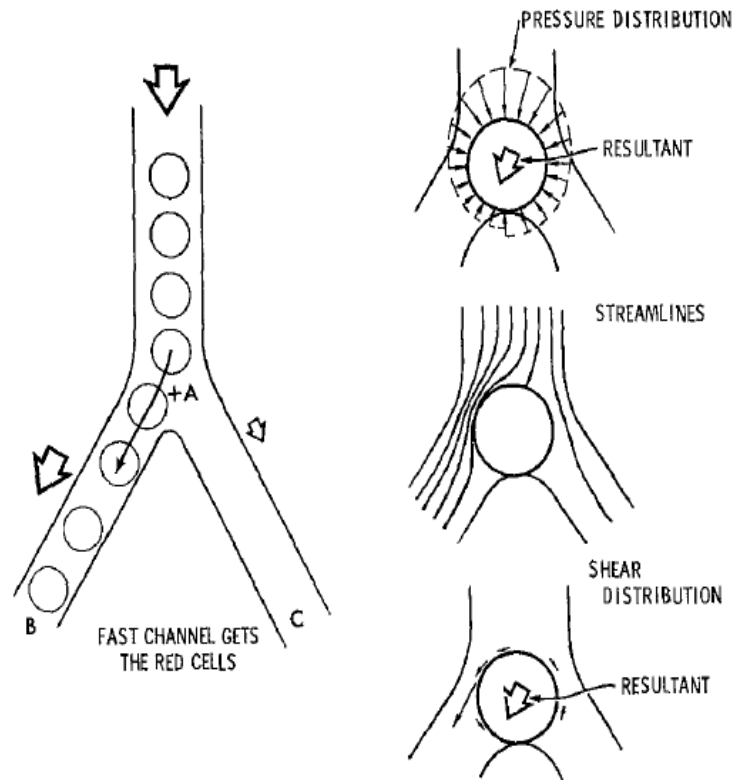


Figure 2-6: Illustration of the Zweifach-Fung effect on a red blood cell in a capillary. The faster flow through the right hand channel causes a shear force acting on the spheres towards the channel with the faster flow. Image from publication by Fung [128].

This effect, shown in Figure 2-6, describes the behaviour of a sphere at a bifurcation that will preferentially travel into the daughter channel with the higher flow rate due to the higher pressure gradient caused by this faster flow [130]. The critical flow ratio of these daughter channels has been found to be $\sim 2.5:1$ when the sphere diameter is similar to the channel width [131].

This principle can be adapted for use in either a size sorter or in a medium exchanger by adjusting the flow rates and channel geometries. If the flow rate down the side channels is low then particles larger than a specific value will never go down the side channels as the centre position of the sphere cannot get within a certain distance of the side walls. This is because flow

forces on the sphere are not great enough to overcome the wall interaction force, thus this distance, approximately equal to the particle radius, is never overcome. The faster the flow rate through these side channels, then the larger the flow forces, and therefore, the larger the particles that will go down the channels [132]. This is illustrated in Figure 2-7.

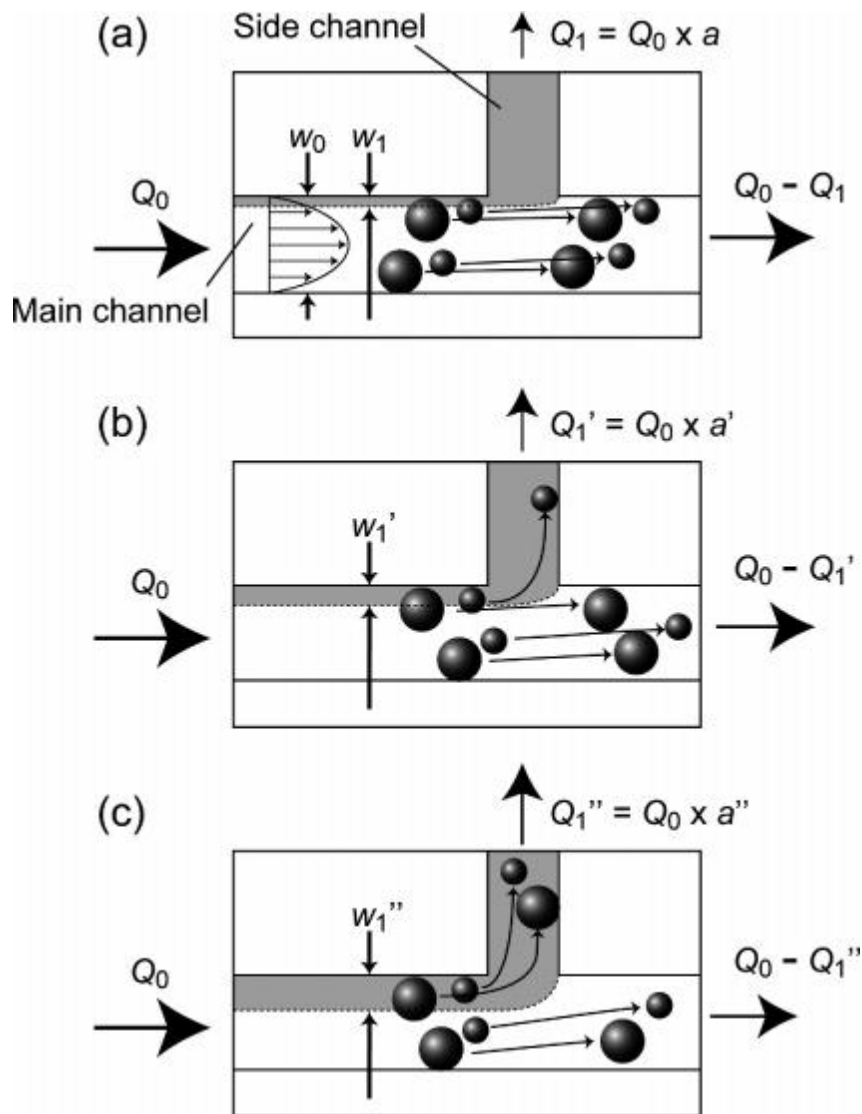


Figure 2-7: Relation between particle behaviour and relative flow rate distributed into a side channel at a branch point. The relative flow rate into the side channel is (a) small, (b) medium, and (c) large, i.e., $a < a' < a''$. The virtual region of the flow distributed into the side channel is dark-coloured. Image from reference [133].

By keeping the flow rate low enough it is possible to perform a medium exchange by removing the medium without any of the spheres going down the side channels as was demonstrated by Yamada *et al.* [134] where $9.9\mu\text{m}$ polystyrene microspheres were exchanged twice by passing channels that were $20\text{-}35\mu\text{m}$ wide. This exchanger is shown in Figure 2-8. The inlet one and two flow rates were both held at 1.8ml/hr . With the inlet three flow rate below 0.6ml/hr it was possible to recover 99% of the particles, however, once this flow rate exceeded 0.84ml/hr , this dropped to almost 0%. In a further experiment using cells, the throughput was demonstrated to be 1000 cells/s.

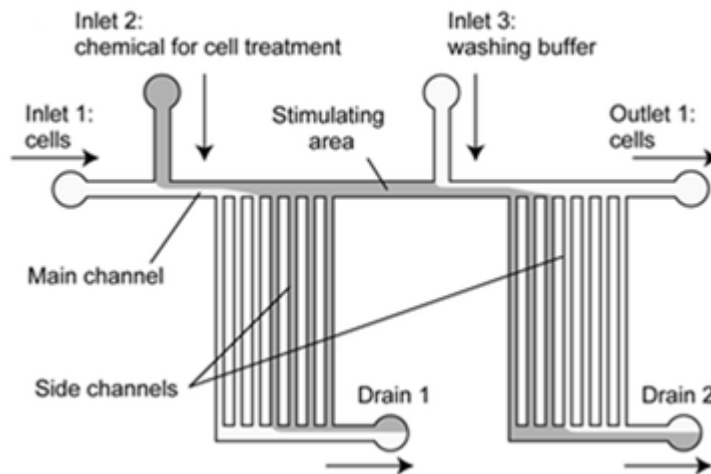


Figure 2-8: Hydrodynamic medium exchange as demonstrated by Yamada *et al.* Two exchanges occur in this device [134].

Size based sorting has also been demonstrated [132, 133, 135] with the best results also achieved by Yamada *et al.* who demonstrated the ability to sort particles of $1\mu\text{m}$, $2.1\mu\text{m}$ and $3\mu\text{m}$ into three separate outlets ($\sim 90\%$ of the $3\mu\text{m}$ particles through outlet 3, $\sim 67\%$ of the $2.1\mu\text{m}$ particles through outlet 4 and $\sim 69\%$ of $1\mu\text{m}$ particles through outlet 5) [133].

Hydrodynamic filtration appears to be a promising technique as it has been demonstrated to have the capability of sorting multiple different sizes at a relatively low resolution, showing sorting, for example, of three sizes with a range of only 2 μm . It has also been shown to be an effective tool for medium exchange.

2.2.3 Pinched Flow Fractionation (PFF)

Pinched flow fractionation is a technique first developed by Yamada *et al.* [136]. The technique employs two inlet channels that meet at a narrow channel known as the 'pinched' region. The flow through one inlet contains a particle suspension whilst the other inlet contains a suspension-less buffer flow. By ensuring the buffer flow is faster than the suspension flow, it is possible to align the particles, regardless of size, to one sidewall. A broadened region where the channel is much wider follows this pinched region. The alignment creates a difference in the particle centre position that is then amplified when the particles enter the expansion region meaning smaller particles are closer to the side walls and larger particles closer to the centre [137].

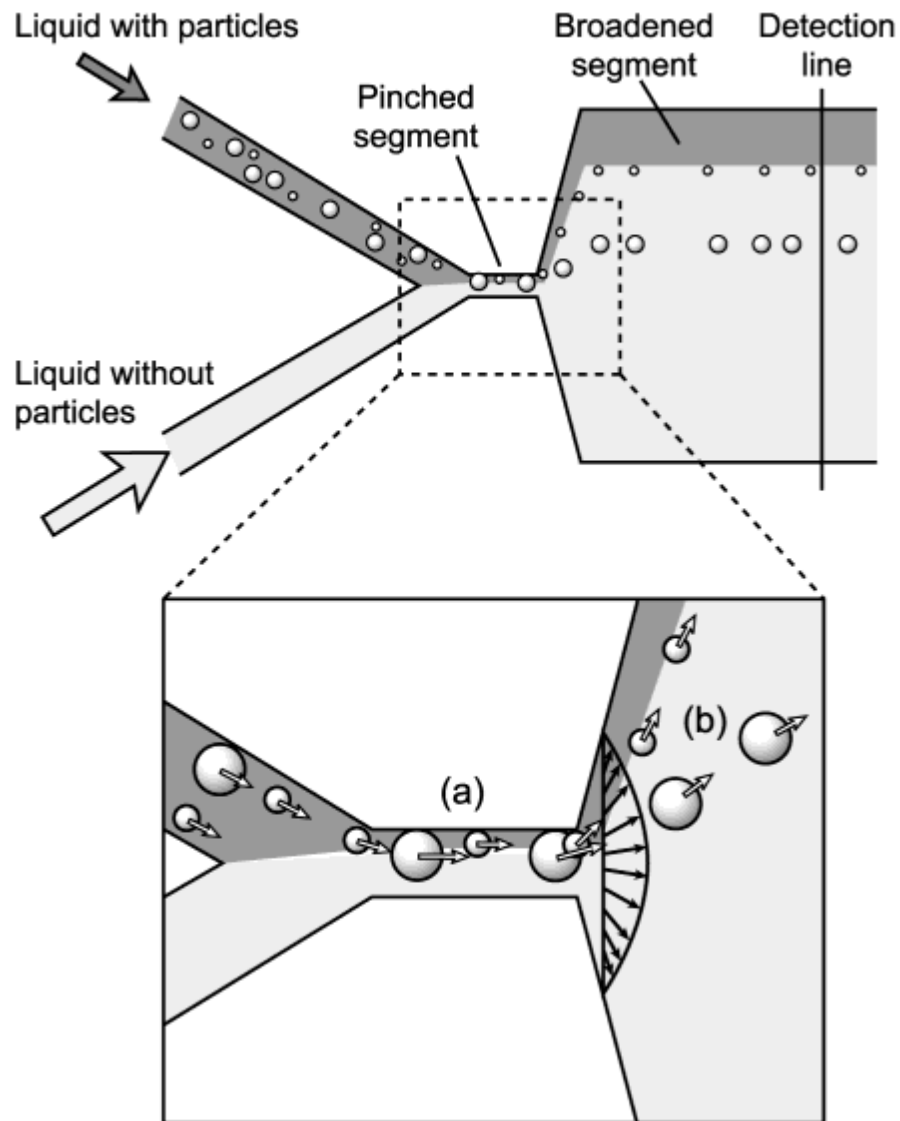


Figure 2-9: Principle of pinched flow fractionation. (a) In the pinched segment, particles are aligned to one sidewall regardless of their sizes by controlling the flow rates from two inlets; (b) particles are separated according to their sizes by the spreading flow profile at the boundary of the pinched and the broadened segments. The liquid containing particles is dark-coloured. Image from reference [136].

The initial work by Yamada *et al.* demonstrated the separation of 15 μm and 30 μm polystyrene spheres. They also demonstrated that there are three main factors that influence the extent of separation. The ratio of the two inlet flow rates must be sufficient to align the particles as the better the

alignment, the better the separation. Additionally, it was found that a narrower pinched region lead to better separation, and that the angle between the two regions had an impact, with a larger angle offering better separation [136].

Various adaptations have been made to this technique to improve the quality of separation. The first adaptation demonstrated was asymmetric PFF (APFF) that employed branched asymmetric channels to collect the particle streams. One of these channels was shorter and/or broader than the others. This channel acted as a drain channel as the bulk of the liquid flowed into it. This drain channel reduced the flow resistance leading to improved separation [138]. APFF was further adapted, with the addition of a curved channel [139] or by adding valves to the outlets allowing control of the outlet flow rates, and therefore, the flow resistance and separation [140]. Another technique used to adapt PFF was to introduce an additional force such as an electro-osmotic force [141] or an optical force [142]. The addition of a 'snakelike' structure in the broadening segment has also been demonstrated to enhance PFF [143].

As can be seen from Table 2-4, pinched flow fractionation is an effective technique for particle separation, demonstrating the high quality separation of multiple particle sizes with reasonably high resolution. The main drawback of this technique is that the throughput is generally quite low with the flow rate typically in the range of $\mu\text{l/hr}$ [139-141]. Parallelisation could possibly be used to improve this throughput but it would always be fundamentally lower than other techniques if they were also parallelised.

Additionally, the width of the broadened region means that the device footprint is larger than many other microfluidic techniques therefore reducing the potential for parallelisation.

Table 2-4: Summary of published pinched flow fractionation results.

Ref	Type	Separation quality
[136]	Pinched Flow Fractionation (PFF)	Outlet 1: 99% of 15 μ m, 8.4% of 30 μ m Outlet 2: 1% of 15 μ m, 91.6% of 30 μ m
[138]	Asymmetric Pinched Flow Fractionation (APFF)	Outlet 1: 99% 1 μ m, 23.6% 2.1 μ m Outlet 2: 1% 1 μ m, 76.4% 2.1 μ m, 49.5% 3 μ m Outlet 3: 50.5% 3 μ m Outlet 4: 85.7% 5 μ m Outlet 5: 14.3% 5 μ m
[139]	Curved channel APFF	Separation of 10 μ m and 25 μ m spheres measured at reference line. \sim 201 μ m apart.
[140]	Tunable APFF	Flow through outlet 1 reduced. Outlet 1: 100% 1 μ m Outlet 2: 98.5% 2.1 μ m Flow through outlets 1 and 2 reduced Outlet 1: 100% 1 μ m, 1.1% 2.1 μ m Outlet 2: 97.3% 2.1 μ m, 0.6% 3 μ m Outlet 3: 1.6% 2.1 μ m, 99.4% 3 μ m
[141]	Electroosmotic PFF	1 μ m and 2.1 μ m separation Outlet 1: 96.8% 1 μ m, 6.6% 2.1 μ m Outlet 2: 3.2% 1 μ m, 93.4% 2.1 μ m 0.5 μ m and 0.86 μ m separation Outlet 1: 91.3% 0.5 μ m Outlet 2: 91.5% 0.86 μ m 1 μ m, 2.1 μ m and 3 μ m separation Outlet 1: 91.3% 1 μ m, 2.4% 2.1 μ m Outlet 2: 8.7% 1 μ m, 88.2% 2.1 μ m, 12.3% 3 μ m Outlet 3: 9.4% 2.1 μ m, 87.7% 3 μ m
[143]	Enhanced PFF	Separation of 7 particle sizes (0.25 μ m-2.5 μ m). Clear separation of 0.5 μ m and 1.5 μ m particles demonstrated.
[144]	PFF	Separation of particles with particle radius between 0-0.97 μ m in 16 outlet channels.

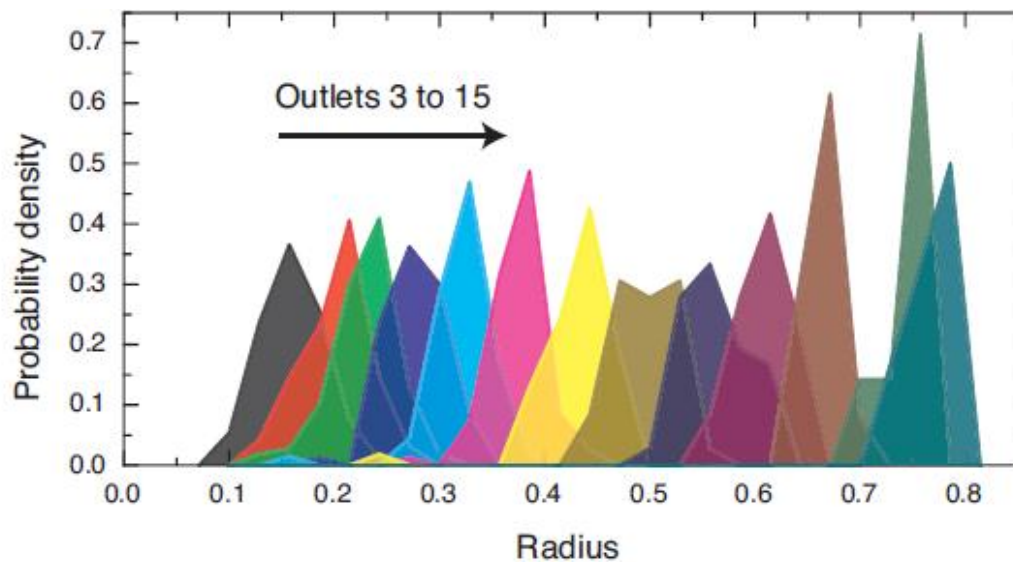


Figure 2-10: Probability density of particle radius at each outlet of a pinched flow fractionation device. Each colour denotes a different outlet. Shows many different sizes have been distributed although there is significant overlap between the particle sizes in adjacent channels. Image from reference [144].

Although this technique has never been investigated to determine its suitability as a medium exchanger it appears that this technique could be easily adapted to be used as a medium exchanger by ensuring the centre line of the particle to be exchanged is forced into the secondary phase at the pinched region.

2.2.4 Inertial Focusing

The parabolic nature of Poiseuille flow in an enclosed microfluidic channel causes a differential in fluid velocity from one side of the sphere to the other. Relative to the sphere, fluid flows over the surface of the sphere faster on the side of the sphere that is closest to the wall, this is illustrated in Figure 2-11. The velocity gradient causes a pressure gradient across the sphere meaning the pressure is lower on the side of the sphere closest to the wall

leading to a migration of the sphere away from the centre and towards the channel wall [145]. This is known as the inertial lift force.

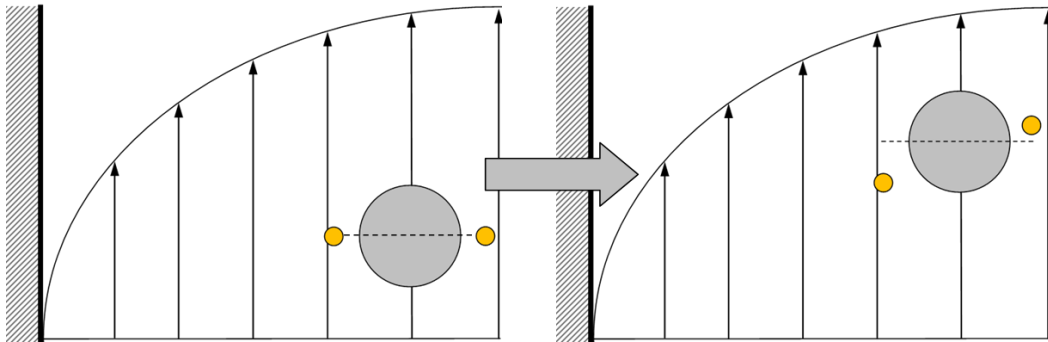


Figure 2-11: Illustration of the mechanism of inertial lift in a microfluidic channel (half of the channel width is shown here) showing a sphere in flow at time= t , and then at time $=t+\Delta t$. Flow through a channel induces a parabolic flow as indicated here by a series of arrows. Arrow length relates to speed of flow. The grey circle is a neutrally buoyant sphere being carried by the fluid flow. The orange spheres highlight a point in space on either side of the sphere (left) with a dashed line to indicate the centre of the sphere. As the sphere is carried along the channel (right) the points beside the sphere move at different velocities relative to the sphere. The difference in velocity is greater on the side closer to the wall and therefore the pressure is lower on the side closer to the wall, which induces a lift force causing lateral movement of the sphere towards the wall.

As the sphere approaches the channel wall it is subject to an extra drag force created by the wall causing the sphere to lag behind the fluid causing the relative flow velocity to be slower on the wall side of the sphere and thus cause a pressure gradient that pushes the sphere away from the wall. This pressure gradient is further enhanced by the dissymmetry of the sphere's wake vortices caused by the presence of a channel wall [145, 146]. This force away from the channel wall is known as the wall effect induced force. These two opposing forces create an equilibrium position where particles can be focused.

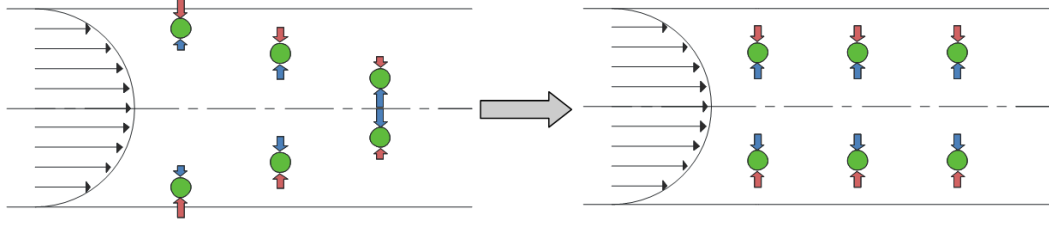


Figure 2-12: Illustration of the two forces that influence a sphere that is carried by a fluid in a straight microfluidic channel. The red arrows represent the wall induced forces. The blue arrows are the inertial lift force. The size of the arrows indicates the magnitude of the force. It can be seen that farther down the channel the spheres are in their equilibrium positions [146].

The inertial lift force dominates when the particle Reynolds number, Re_p , is greater than or equal to one [147]. The particle Reynolds number characterises the flow around a sphere suspended in a flowing fluid. It is given by [148]:

$$Re_p = \frac{U_m a^2 \rho}{D_h \mu} \quad (2-11)$$

where U_m is the maximum flow velocity, a is the particle diameter, ρ is the fluid density and D_h is the channel hydraulic diameter. The scale of the lift force on a sphere is given by the following equation [147]:

$$F_z = \frac{\rho U_m^2 a^4}{D_h^2} f_c(Re_c, w) = \frac{\mu^2}{\rho} Re_p^2 f_c(Re_c, w) \quad (2-12)$$

where f_c is the lift coefficient which varies with the channel Reynolds number, Re_c , and the position of the sphere across the channel width (w). The lift coefficient is 0 at the channel centreline and increases in magnitude as the distance towards the wall decreases until it reaches a maximum before dropping to zero again at the equilibrium position ($\sim 0.2 w$ from the wall). Further movement towards the channel walls leads to a negative lift coefficient to indicate that the force now acts towards the channel centre

rather than away from it [149]. Equation 2-12 can be adapted, so that it is possible to determine the speed at which the sphere will migrate laterally across the channel, U_p :

$$U_p = \frac{\rho U_m^2 a^3}{3\pi\mu D_h^2} f_c(R_c, w) \quad (2-13)$$

From this equation, it is clear that migration velocity is highly dependent on the particle diameter meaning that, by designing channels with appropriate geometries and outlet positions, it should be possible to use inertial lift forces to separate spheres based on their size.

In square microchannels the spheres equilibrate to all four channel walls. This is problematic as collecting the focused particles from all four sides creates manufacturing difficulties. Hence many techniques have been considered to reduce the number of equilibrium positions. One possible technique is to employ curved microchannels to introduce an additional force known as the Dean force [147]. As fluid flows round a curved microfluidic channel, a secondary rotational flow is created by the fluids inertia out towards the outer wall. This creates two vortices known as Dean vortices, one above the other, across the width of the channel [150].

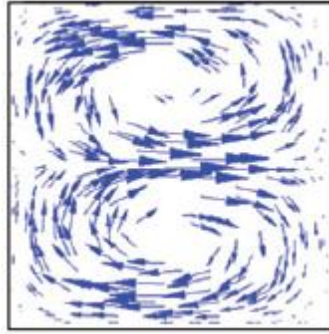


Figure 2-13: Two-dimensional vector fields in a curved square microchannel demonstrating Dean vortices. The inner wall of the curve is on the left hand side. Image from reference [150].

These vortices provide an additional Dean drag force that can reduce the number of equilibrium positions to one. This is possible as the Dean drag force only counters the inertial lift force at the inner wall, at all other positions it breaks the equilibrium previously created by the inertial lift force. There are three possible cases to consider:

- Inertial lift force \approx Dean drag force
 - Concentration of spheres to one equilibrium position
- Inertial lift force \gg Dean drag force
 - Inertial focusing only
- Dean drag force \gg Inertial lift force
 - No sphere focusing occurs.

These cases relate to a number of parameters, such as flow rate and the radius of the curve. The channel dimensions are one of the major controlling parameters and must fulfil the following criteria for focusing to occur in curved channel: $\frac{a}{D_h} \geq 0.07$. Below 0.07 the inertial lift force is not of a sufficient magnitude to focus the particles. If this value is greater than 0.5

there is a chance particle obstruction may occur due to the size of the sphere relative to the channel. Another limit is found with the Dean number, a dimensionless number that characterises the Dean vortices [151]. If the Dean number, De , exceeds 20 the magnitude of Dean drag becomes too great and there will be no equilibrium positions [147, 152].

Di Carlo *et al.* used meandering curved microchannels to investigate this principal. Using a symmetric curving geometry they demonstrated a reduction to two equilibrium positions along the side walls. This was further reduced to one equilibrium position by employing asymmetric curved channels [147].

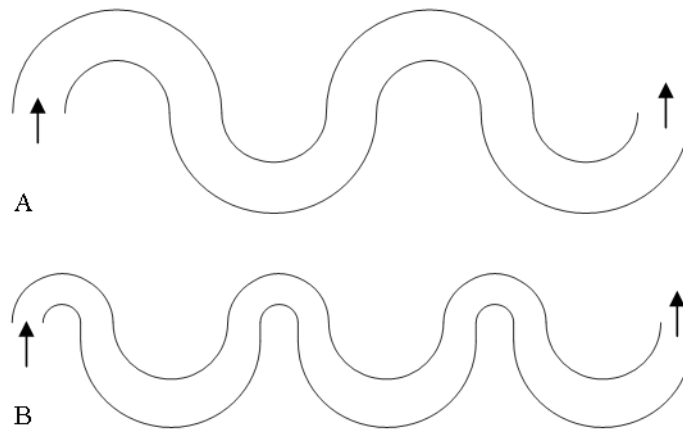


Figure 2-14: Meandering channels used for sphere focusing. A) Symmetric channels - Two equilibrium positions. B) Asymmetric Channels - One equilibrium position. Arrows indicate flow direction [147].

The use of Dean flow to sort spheres has been further expanded upon through the use of a longer curved channel in the form of a spiral. This technique has been shown to be capable of sorting multiple sphere sizes at once [153-158]. It has been demonstrated that spiral microchannels will focus different sized particles into distinct equilibrium positions. This is a result of the inertial lift force scaling with a^4 whilst the Dean drag force

scales with just a thus larger spheres will equilibrate closer to the inner wall than smaller spheres.

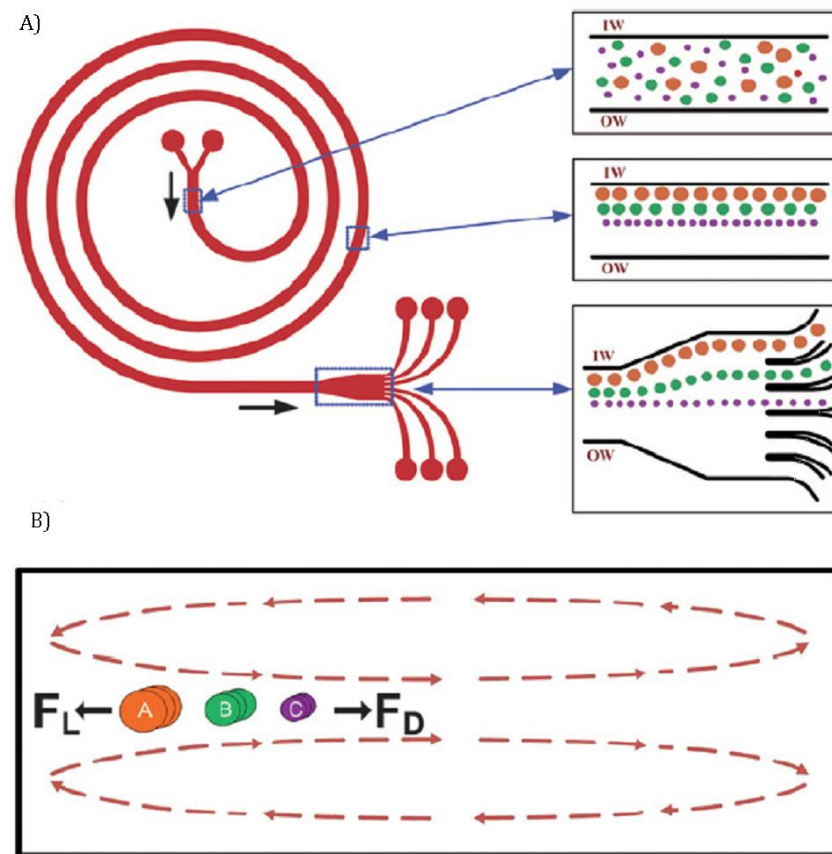


Figure 2-15: A) Illustrations of the principle of sorting using Dean forces in a spiral. Larger spheres are focused closer to the inner wall allowing different sized spheres to be collected from well-placed outlets. B) Channel cross section. Larger sphere equilibrate to inner wall due to the ratios of inertial lift and Dean drag force for the different sphere sizes i.e. $[F_L/F_D]_A > [F_L/F_D]_B > [F_L/F_D]_C$. Image from reference [156].

Another technique that can be used to reduce the number of equilibrium positions is to increase the aspect ratio of the channels, i.e. make the height divided by the width of the channel greater than one. This causes the shear rate created by the parabolic flow to be greater across the narrower channel dimension therefore spheres will equilibrate more readily along the side walls than at the top or bottom wall [159]. This has been demonstrated with

straight high aspect ratio channels and via a series of narrowing and widening channels that work in a similar fashion to straight microchannels, with the advantage of reducing the pressure needed to drive the fluids through the device [146].

Whilst the majority of sorting devices use Newtonian fluids it has been demonstrated that inertial focusing can be achieved using non-Newtonian liquids. When using non-Newtonian liquids the direction of the inertial lift force acts in the opposite direction i.e. the sphere moves towards the centre of the channel rather than towards the channel wall [160].

It is clear from Table 2-5 that the use of inertial lift and Dean drag forces is a promising technique for sphere separation by size. One of the main advantages of these devices is the relatively high throughput achievable along with the ability to sort multiple sizes at once. The high throughputs and sorting efficiencies achieved by Hansson *et al.* [161] and Kuntaegowdanahalli *et al.* [156] are particularly encouraging.

The use of inertial lift and Dean drag forces to achieve medium exchange has been demonstrated by Lee *et al.* via the use of expansion and contraction channels to force spheres to one side of a channel and a medium to the other [162]. It has also been used to enhance existing phase partitioning which exploits the different charges between spheres and carrier liquids to move spheres to a particular medium [163].

Table 2-5: Summary of inertial and Dean based separation techniques. High throughput is achievable along with the ability to sort multiple sizes simultaneously.

Ref	Type	Channel dimensions	Sphere Size	Quality	Notes
[147]	Asymmetric curved channel	$D_h = 10-87\mu\text{m}$	2-17 μm	Sorting of 4 and 7 μm spheres at slightly less than 1g/hr (~90ml/hr)	Focusing of 9 μm spheres in straight square microchannel is also demonstrated.
[160]	Non-newtonian fluid	$D_h = 50\mu\text{m}$	1 and 5 μm	Central outlet: 99.9% of 5 μm spheres Side outlets: 99.1% of 1 μm spheres Flow rate: 0.27ml/hr	
[149]	Asymmetric curved channel	50 μm deep	3.1 and 9 μm	3.1 μm to all outlets, 5 μm to outlet 5	There is a trade of between throughput and separation purity.
[152]	Spiral	500x220 μm	40 and 60 μm	Demonstration of two distinct focused streams at 180ml/hr	
[154]	Spiral	50 μm deep	7 and 10 μm	10 μm focused at 193 μm from inner wall. 7 μm focused at 275 μm from inner wall.	Channel width gets wider as spiral radius increases.
[164]	Straight channel	100x230 μm	3 and 10.2 μm	Central outlet: 69% 3 μm , 22% 10.2 μm Side Outlets: 31% 3 μm , 78% 10.2 μm	Additional inlets are used to initially focus all the spheres into the centre of the channel.
[159]	Straight channel	20x50 μm	590nm and 1.9 μm	1.9 μm spheres focused, collected at side outlets. 590nm spheres remain unfocused.	
[161]	Straight channel	50 μm wide, 50-250 μm deep	2 and 10 μm	4 parallel channels - 97% efficient - 48ml/hr 16 parallel channels - 95% efficient - 192ml/hr	Two-level parallelised device. Focused spheres go to one layer, unfocused spheres remain
[156]	Spiral	500 μm wide, 90-140 μm deep	10, 15 and 20 μm	Separation efficiency of ~90%. 20, 15 and 10 μm spheres sorted to outlets 1, 2 and 3 respectively. Flow rate ~180ml/hr	
[157]	Spiral	250x50 μm	1.9 and 7.32 μm	Complete separation of 1.9 and 7.32 μm spheres at flow rate of up to 1.2ml/hr	
[162]	Expansion Contraction channel	350x38 μm (expansion), 50x38 μm	4, 10 and 15 μm	Complete separation of 4 and 10 μm spheres	Medium exchange also demonstrated.
[165]	Spiral	20x20 μm	1, 2.1 and 3.2 μm	87 % of 2.1 μm and 93% of 3.2 μm spheres through outlets A, B and C, majority of spheres through outlet D 1 μm	Aimed to isolate spheres below a certain size by focusing only spheres above that size.

2.3 Conclusion

It is clear that there are many techniques that can be employed in combination with microfluidics to sort spheres based on their size. When selecting which technique to use it was important to consider the design criteria put forwards by Thermofisher, namely that the sorting technique be density independent and simple. These two considerations rule out all of the active control techniques as acoustophoresis, dielectrophoresis and gravity based methods are all density dependent whilst optical methods and magnetophoresis are not simple; requiring complex equipment or, in the case of magnetophoresis, sphere labelling. This leaves passive techniques and it was decided that inertial focusing techniques were the most promising as they offer relatively high throughput and sorting accuracy whilst they are also comparatively simple to design and manufacture.

There has not been a great deal of work carried out in the field of microfluidic medium exchange however there are a few instances showing that it is clearly possible to continuously transfer spheres between mediums within microfluidic channels. It was decided that the medium exchanger would be a development of a phase separator device that was previously invented by a colleague within the laboratory as this appeared to be a promising technique for selectively extracting mediums. Clearly this capability could be useful when trying to perform an exchange. An adaptation of the phase separator should allow for medium exchange based on hydrodynamic filtration but with the aim of achieving greater throughput

than has been previously demonstrated [134]. The principles behind the phase separator are introduced in the next chapter.

3 Phase Exchanger Concept

3.1 Objective

Multi-stage chemical processes, such as the manufacture of silica spheres, often require the transfer of the product from one reagent or solvent to another to facilitate the next stage of a process. Typically, in industry, separation is performed via a gravimetric approach which can take several hours. As such, a technique for separating and exchanging liquid phases in flow, on a microfluidic chip, is an attractive prospect as it could drastically reduce production times. This chapter presents work to develop a phase exchanger for this purpose. The exchanger will be based on a previously developed phase separator. As such the phase separator concept will also be introduced in this chapter.

3.2 Introduction to the Phase Separator

In recent years there have been many studies performed to achieve liquid-liquid phase separation. In many cases, particularly in industry, a gravimetric technique is employed for phase separation as it is simple and requires little maintenance [166-168]. This approach, along with centrifugal techniques, relies on a density difference between the liquid phases [167, 169, 170] and as such, these approaches are less appropriate, or, sometimes completely ineffective on a microfluidic scale [171]. Microextractors (microfluidic phase separators) can possess advantages over macro-scale approaches as they tend to be safer, cleaner and smaller [167] with much lower solvent use and waste.

The majority of microfluidic phase separation techniques exploit differences in the wetting characteristics of the liquids to be separated, typically via a membrane [172-174], microchannels [168, 174, 175] or junction splitting [167, 171, 176-179]. This section focuses on a microchannel approach based on the work by Castell *et al.* [168]. The microchannel technique was selected as it is more durable [180] and easier to manufacture than a membrane based design, and is potentially more adaptable than a junction splitter based device. It was also selected as it works for segmented flow regimes which allow greater mixing than is possible with side by side laminar flow where mixing occurs via diffusion [181].

The *Castell* phase separator works by exploiting the different wetting characteristics of the aqueous phase (water) and the organic phase (chloroform) in a Polytetrafluoroethylene (PTFE) device. PTFE is hydrophobic so the aqueous phase is repelled whereas the organic phase wets the surface.

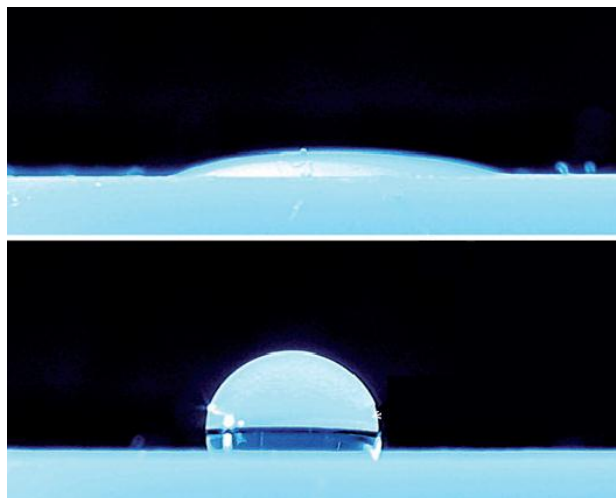


Figure 3-1: Demonstration of the PTFE wettability of chloroform (upper image) and water (lower) image. Drop volume 10 μ L. Image from reference [168].

Several narrow ($\approx 30\mu\text{m}$ wide) separator channels were machined perpendicular to the main microfluidic channel with a pressure differential exerted across them. This pressure differential encourages the wetting (organic) phase to travel down the separator channels whilst the non-wetting (aqueous) phase cannot [168].

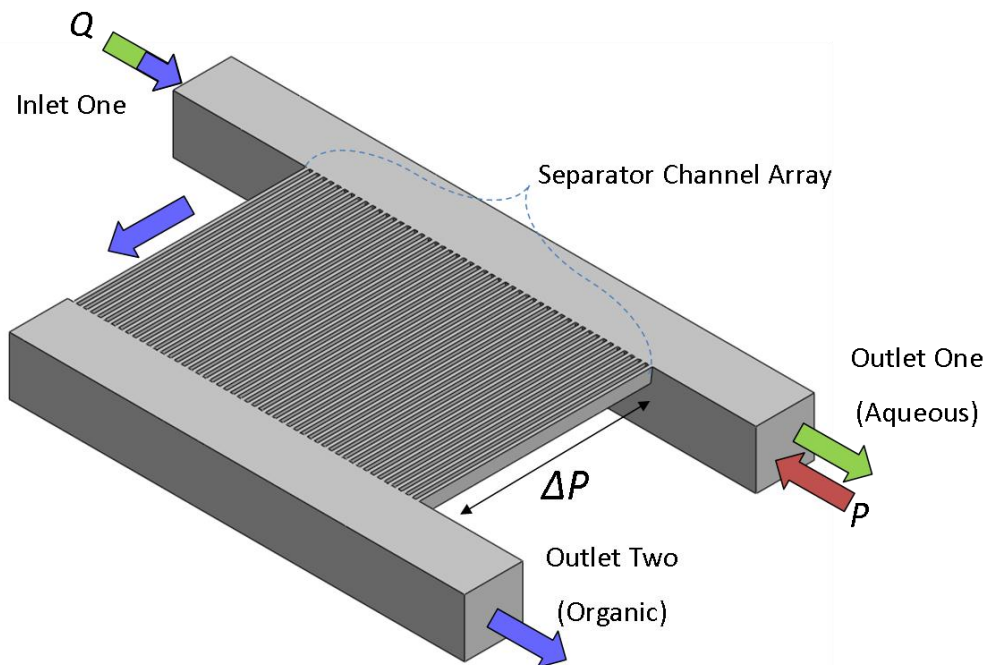


Figure 3-2: Phase Separator showing two main channels with an array of narrow separator channels running perpendicular to connect the two channels. Green arrows indicate aqueous flow through the device whilst blue arrows indicate organic phase flow. The aqueous and organic phases enter in a segmented flow pattern through inlet one at a fixed flow rate, Q , whilst a pressure, P , is applied to outlet one (as indicated by the red arrow) via an air filled syringe. This applied pressure creates a pressure differential, ΔP , across the length of the separator channels inducing the organic phase (that has a lower contact angle) to travel down these channels and exit through outlet two whilst the aqueous phase exits through outlet one.

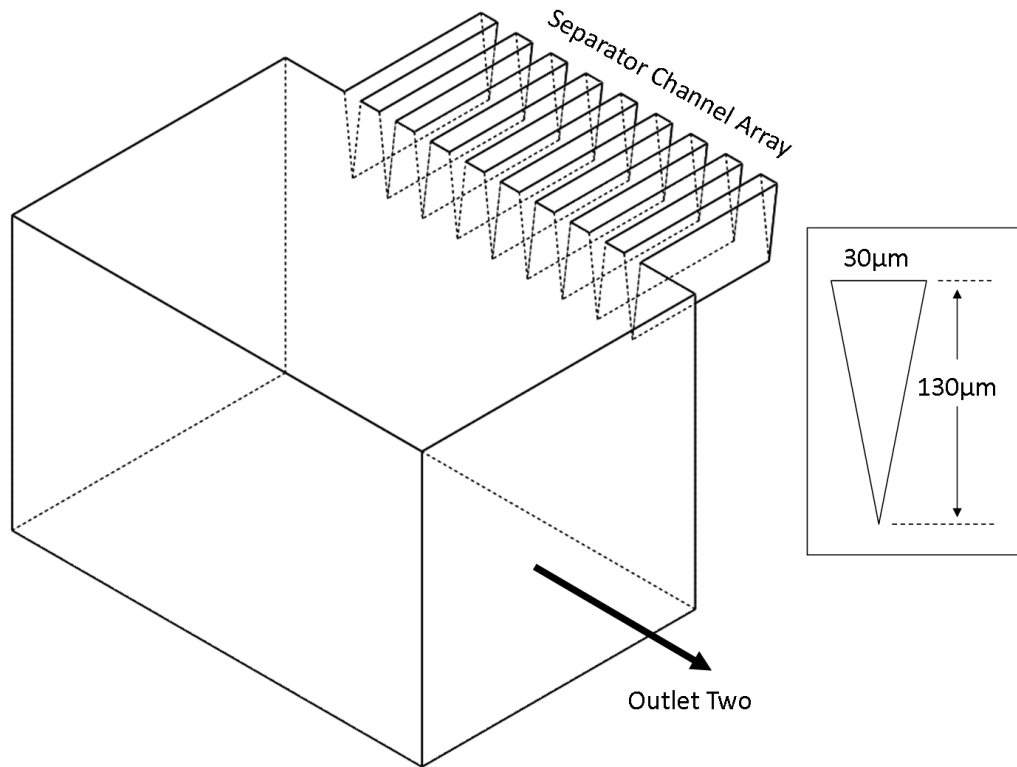


Figure 3-3: Illustration of the separator channel position in relation to the main (500x500μm) microfluidic channels. A series of narrow channels running perpendicular between the outlet one and outlet two channels positioned at the top of the main channels. Inset: The separator channel cross-sectional dimensions. They have an approximately triangular cross section with a maximum width of 30μm and are ablated to a depth of 130μm.

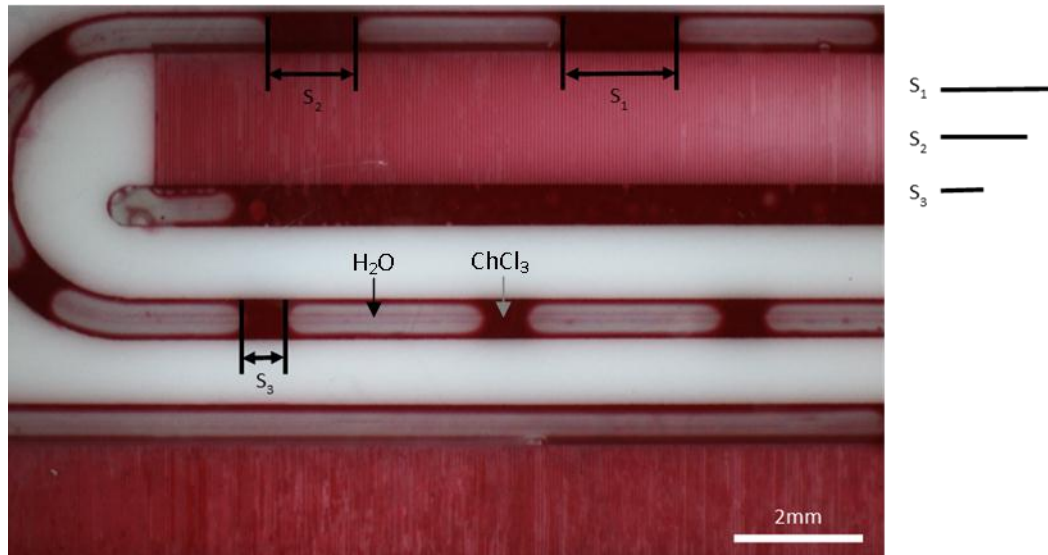


Figure 3-4: Photomicrograph of the phase separator in action showing chloroform being extracted. The segments of chloroform (red) are shrinking as they pass the separator array showing they are being extracted. Three segments are highlighted (S_1 , S_2 and S_3) and their respective lengths are compared alongside the image using three scale bars that are equal to the lengths of the three segments. The decreasing length of three highlighted segments illustrates that chloroform is being extracted as the segments pass the separator arrays. Although complete separation is not shown in this figure it has been demonstrated many times.

3.3 Exchanger Design

Two initial designs were tested. The principles of these designs are laid out below.

3.3.1 Design One

The principle behind this design is that phase two is supplied to the main channel via four thin channels (approximately $\frac{1}{4}$ the width of the main channels) as phase one is extracted through a phase separator. It was expected that the silica spheres would transfer from phase one to phase two, where the phases meet.

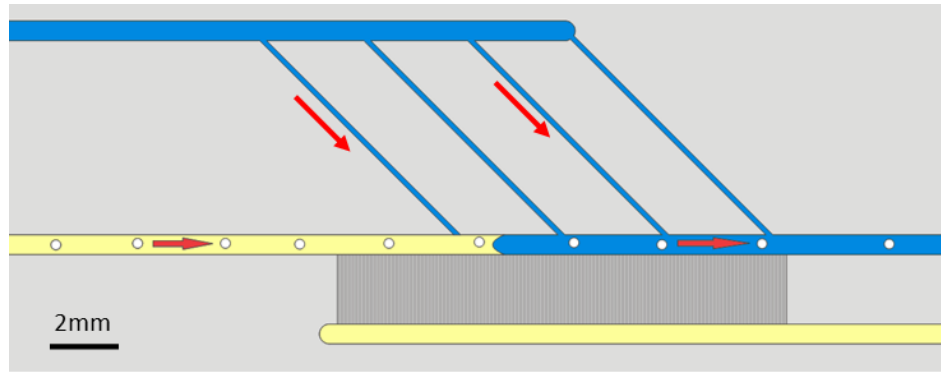


Figure 3-5: Phase exchanger design one. Thin channels supply phase two (blue), as phase one (yellow) is extracted via the separator channels.

3.3.2 Design two

The concept behind this design is that phases one and two are brought together into a side-by-side parallel flow pattern. Then, phase one is extracted via the separator channels.

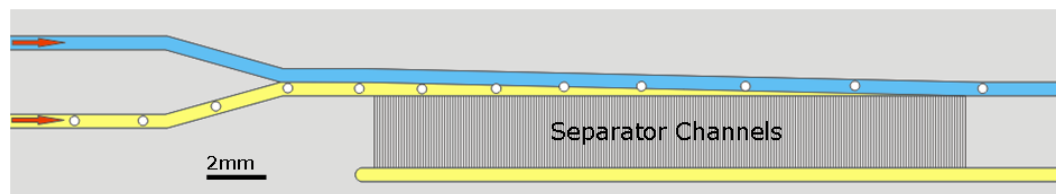


Figure 3-6: Design two, phase one (yellow) is extracted via the phase separator, whilst the main channel narrows, allowing phase two (blue) to fill the channel.

Channel narrowing brings phase two down to fill the space created by phase one, being extracted at which point the particles are collected by phase two. This design maintains the flow-rate of phase two due to the reduction in channel width during phase extraction. This means the stream width of phase two should be maintained throughout and hence the flow rate.

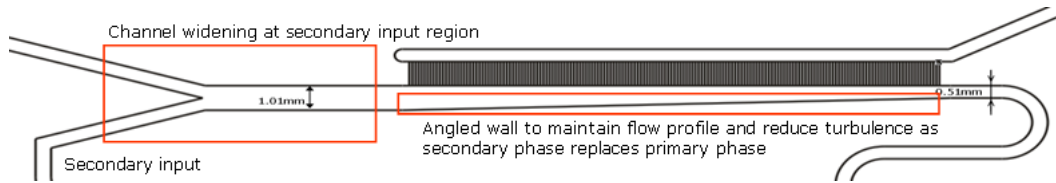


Figure 3-7: Key features of exchanger design two. Two inlet channels join together to form one channel with the same width as the two channels combined allowing two phases to flow in parallel to each other whilst maintaining the flow rates that were present in the two inlet channels. An array of separator channels then extracts the phase that is positioned closest to the separator array. To keep the flow rate as consistent as possible the channel width is reduced over the length of the separator array.

When the spheres are close to the separator channels, both these designs are, in effect, a form of hydrodynamic filtration. As such, it should be possible to exchange spheres that are smaller than the separator channel width due to the Zweifach-Fung effect, as described in section 2.2.2.

3.4 Exchanger Chip One

3.4.1 Experimental

The first chip was manufactured with two possible exchanger designs allowing both to be tested in a short time period. The main features of design one are the four 150 μm channels that introduce the secondary phase, as the primary phase is extracted. All other channels in design one have a cross-section of 500 μm x 500 μm . The fabrication technique for this, and all subsequent chips, is as described in section 3.10, unless stated otherwise.

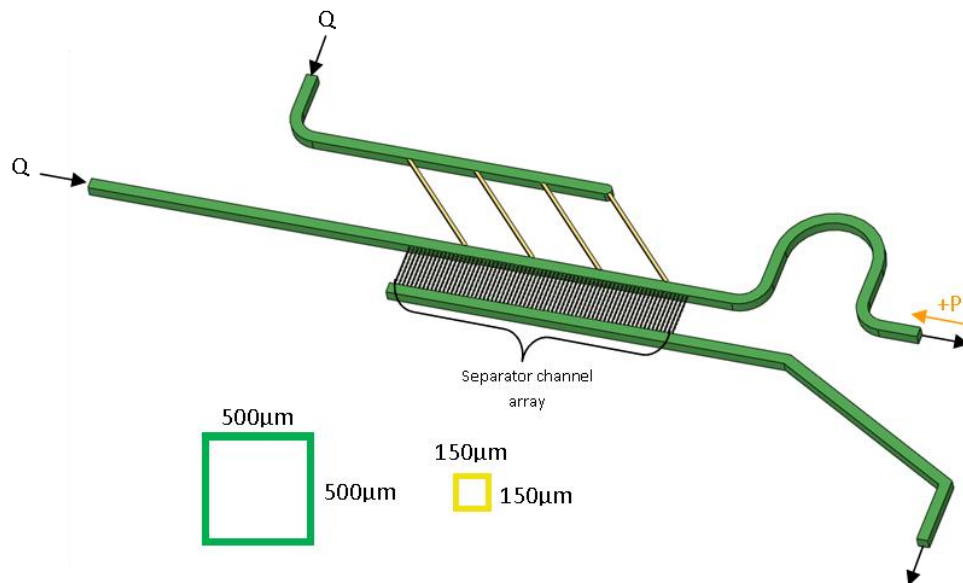


Figure 3-8: Channel cross-sectional dimensions of phase exchanger design one. Main channels (green) are created by removing material via milling a 50mm diameter PTFE chip. Exchanger channels (yellow) are ablated using a femtosecond laser. The separator channels are also ablated such that they are 30 μm wide and approximately 130 μm deep, they have a triangular cross section as described in Figure 3-3. A pressure differential is created across the separator channels by applying pressure as indicated by an orange arrow. Black arrows indicate the direction of flow. Flow through the inlets was supplied at a constant flow rate, Q , by syringe pump.

The four 150 μm channels in exchanger design one are created by using laser ablation due to the unavailability at the time of manufacture of a small enough milling tool. Using laser ablation to effectively clear a reasonably large area in PTFE was investigated in chapter 8 (Appendix A).

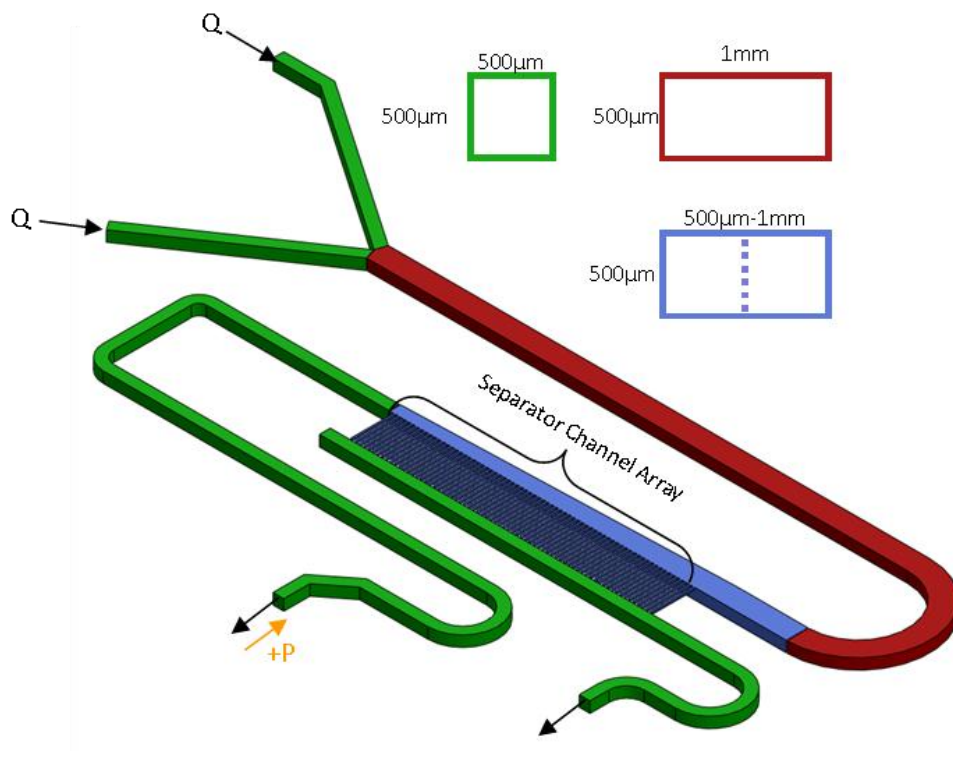


Figure 3-9: Channel cross-sectional dimensions of phase exchanger design two. The two-phase flow channel (red) and the inlet and outlet channels (green) are created by removing material via milling a 50mm diameter PTFE chip. Transition region (blue) features a milled channel that narrows from 1mm to 500 μm wide along the length of the separator channel array. The separator channels are also ablated such that they are 30 μm wide and approximately 130 μm deep, they have a triangular cross section as described in Figure 3-3. Black arrows indicate the direction of flow. Flow through the inlets was supplied at a constant flow rate, Q , via a syringe pump. A pressure differential is created across the separator channels by applying pressure as indicated by an orange arrow.

The separator arrays were made of 225 channels for design one and 290 channels for design two. The number of channels was selected such that there were more channels than in previous phase separator work but without taking up too much room on the chip. In both cases the separator channels were 2.05mm long. Chloroform (coloured with Sudan Red IV) and water (coloured with Green Silver Spoon food colouring) were used as phases one and two respectively.

3.4.2 Results and Discussion

Whilst an exchange did occur with exchanger design one, a problem was identified in that the boundary between the two phases is stationary. As such, there is no flow across the barrier, and therefore, the solid particles may not be encouraged to cross between phases one and two.

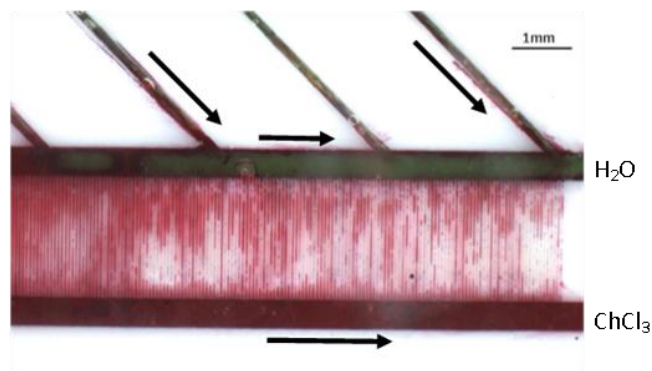


Figure 3-10: Exchanger design one showing an exchange of chloroform (red) for water (green). Chloroform is extracted via the separator channel array whilst water is introduced through the 4 narrow channels. Arrows indicate the direction of flow.

The creation of the narrow 150 μ m channels via laser ablation caused the channels to be rough and, therefore, highly liable to contamination and the collection of dirt. The nature of these channels can be seen in Figure 3-11.

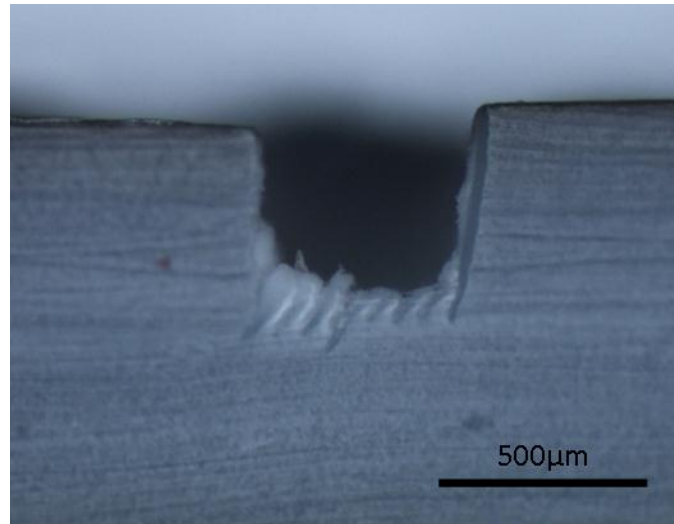


Figure 3-11: Femtosecond laser ablated channel cross-section showing the rough nature of the bottom of a channel created using laser ablation in PTFE. A series of 8 parallel lines were ablated in close proximity to each other to create this channel.

When testing design two using chloroform and water, it was found that segmented flow, rather than parallel flow, was achieved as shown in Figure 3-12. This was not the behaviour that was initially expected and as such was the focal point of following experiments. It was later established that this expectation was due to a lack of understanding of how fluids interact, using immiscible liquids for this exchanger design will not allow it to perform as detailed in the exchanger design two concept.

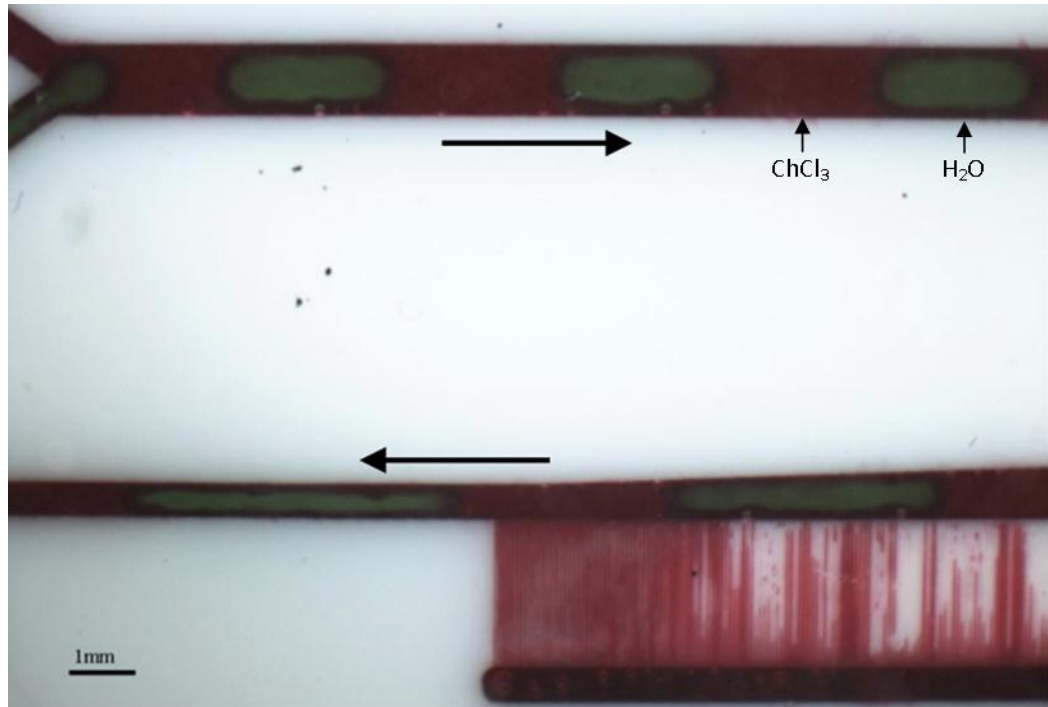


Figure 3-12: Segmented flow pattern set up by exchanger design two. Chloroform (red) and water (green) are introduced through inlets one and two. Chloroform is extracted via the separator array whilst the water is not extracted. Arrows indicate the direction of flow.

3.5 Exchanger Chip Two

3.5.1 Experimental

The objective of this chip was to determine whether or not the segmented flow achieved with design two, was a result of the Y-junction geometry used to bring the two phases together. To achieve this, two channels were brought together using two parallel channels separated by only $100\mu\text{m}$. It was hoped that this would reduce any possible turbulence that may result from the two streams coming together. The separator channel array was made up of 400 channels. The number of channels was increased in attempt to increase the amount of extraction.

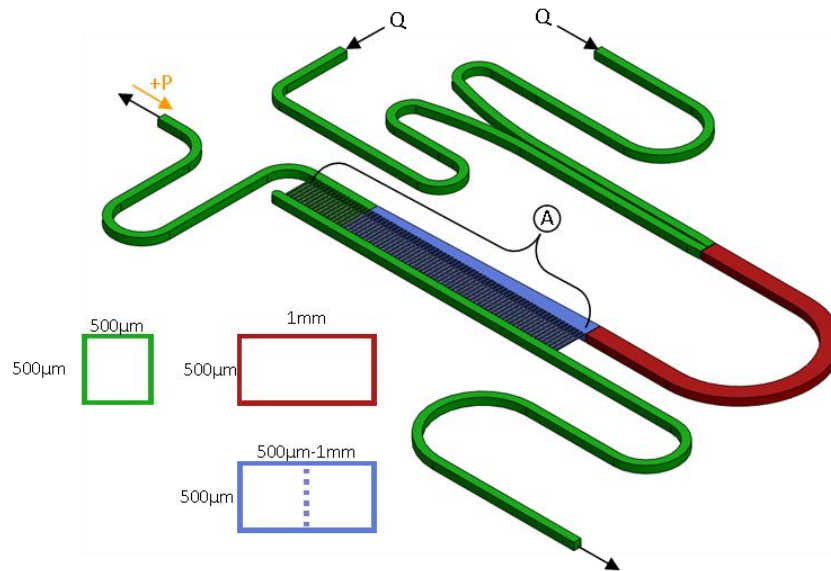


Figure 3-13: Channel cross-sectional dimensions of exchanger chip two. Inlets and Outlets (green), two phase flow region (red) and transition region (blue) all created through milling. Transition region narrows from 1mm – 500µm. Separator channel array (A) created via femtosecond laser ablation, dimensions as shown in Figure 3-3. Black arrows indicate the direction of flow. Flow through the inlets was supplied at a constant flow rate, Q , via a syringe pump. A pressure differential is created across the separator channels by applying pressure as indicated by an orange arrow. Main development: The two inlets are brought together in a straighter manner rather than the Y-junction formation used previously.

3.5.2 Results and Discussion

The purpose of chip two was to investigate whether the segmented flow achieved in design two of exchanger chip one was due to the Y-junction geometry. It was found, however, that segmented flow still occurred. This is due to the fundamental characteristics of how the fluids interact. Immiscible fluids such as chloroform and water are always liable to create some form of segmented flow or emulsion depending on the channel geometry at the initial interface boundary. Parallel flow of two immiscible liquids is only possible with identical contact angles.

During chip two testing, it was established that liquid-liquid phase exchange was possible with segmented flow as shown in Figure 3-14. When used with immiscible fluids the exchanger acts in much the same way as shown previously by Castell *et al.* [168].

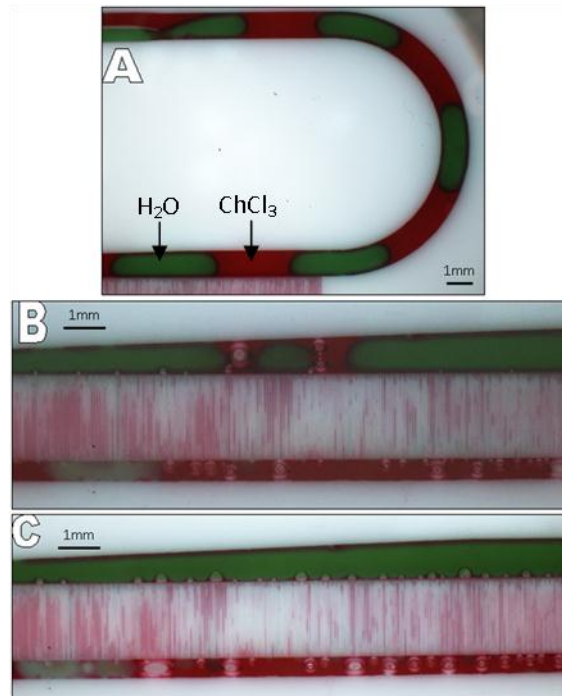


Figure 3-14: Exchanger design two working with segmented flow. A) Segmented flow pattern created. B) The chloroform (red) is extracted by the phase separator. C) The exchange is complete, leaving just water (green) in the main flow channel.

To confirm that the segmented flow pattern was a result of the characteristics of the liquids, chloroform was used as both the primary and secondary phases. Two phases of chloroform, which have identical contact angles and are miscible, present a significant contrast to water and chloroform, which are immiscible liquids with significantly different contact angles. To visually differentiate the two phases, Sudan red dye was added to the secondary chloroform phase.

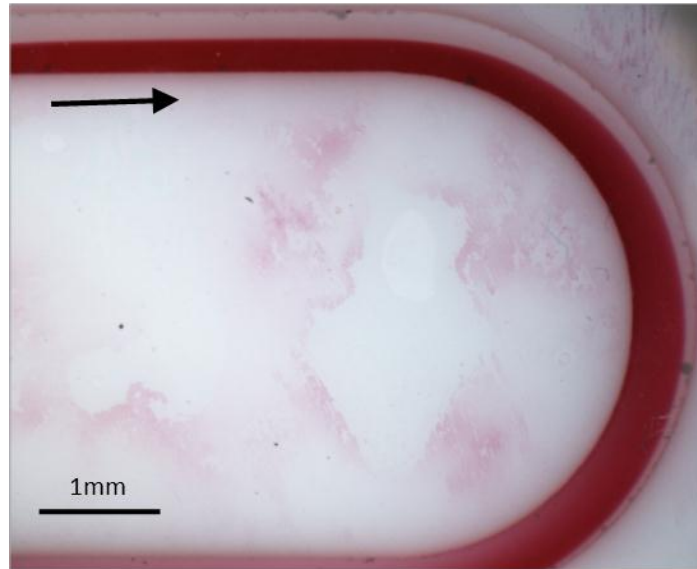


Figure 3-15: Parallel flow achieved using two streams of chloroform. It can be seen that there is crossover of the two streams at the bend leaving the secondary phase (red) in the wrong position. Arrow indicates the direction of flow.

Figure 3-15 shows that parallel flow was achieved with two streams of chloroform presenting the possibility that the exchanger will work as initially intended. It was also found, however, that crossover of the two streams occurred at the bend in the channel. This behaviour is a result of Dean flow [182] and is a problem that must be eliminated for the exchanger to work as it places the secondary phase, rather than the primary phase, in the position to be extracted. There is also an element of mixing that occurs due to nature of this crossover, for these reasons the bend should be eliminated from the exchanger design. Alternatively the Dean flow could be reduced or eliminated by increasing the radius of the curve or by reducing the flow rate [157], however as this curve was deemed to offer no particular benefit it was decided that removing it would be the most appropriate solution.

3.6 Exchanger Chip Three

3.6.1 Experimental

Exchanger chip three eliminates the bend in the channel prior to exchange. The two phases are brought together immediately prior to exchange. Both phases were chloroform, with phase one containing Sudan red to distinguish it from phase two.

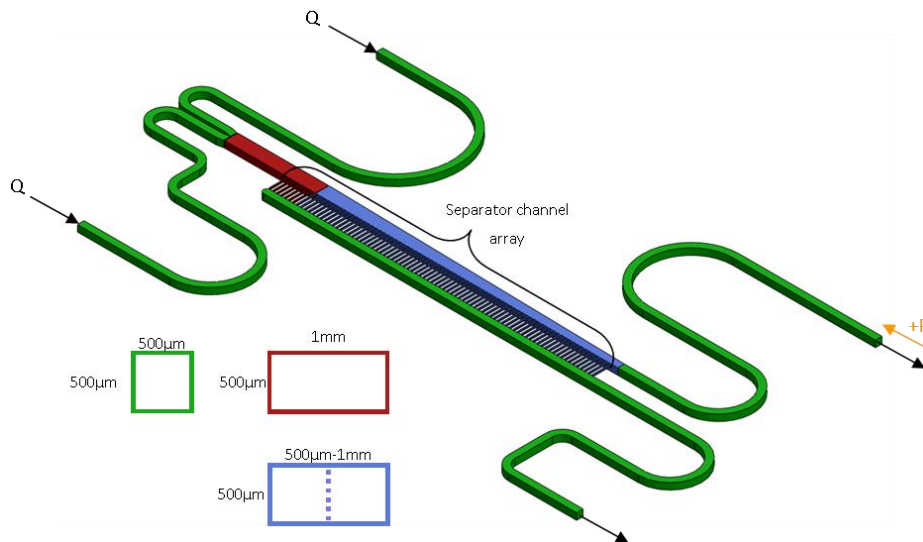


Figure 3-16: Channel cross-sectional dimensions of exchanger chip three. Inlets and Outlets (green), two phase flow region (red) and transition region (blue) all created through milling. Transition region narrows from 1mm – 500µm. Separator channel array created via femtosecond laser ablation, dimensions as shown in Figure 3-3. Black arrows indicate the direction of flow with flow supplied to the inlets at a constant rate, Q . A pressure differential is created across the separator channels by applying pressure as indicated by an orange arrow. Main development: Bend prior to the exchanger removed.

3.6.2 Results and Discussion

By bringing the phases together in line with the exchanger any problems created by Dean flow were eliminated. Having eliminated the crossover problem, it was now possible to deliver the phases to the exchanger in a

parallel flow formation, and thus demonstrate the possibility of miscible exchange. This is shown in Figure 3-17. The possibility of using this phase exchanger with both parallel and segmented flow patterns could potentially provide an advantage over other microfluidic exchangers as it would provide greater versatility in terms of the chemicals that can be exchanged [183].

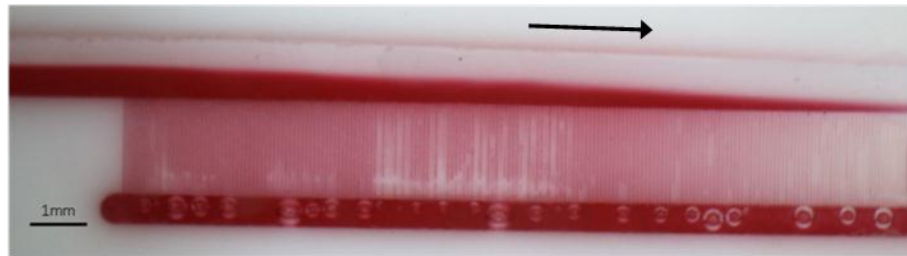


Figure 3-17: Parallel flow exchange. The primary phase (red) is exchanged for the secondary phase (clear). Both phases are chloroform. Direction of flow is indicated by the arrow.

Having established that purely liquid-liquid phase exchange is possible, the next necessary step was to introduce solid particles into the stream to confirm that particles would be transferred from phase to phase. To this end, 120 μ m porous silica spheres were added to the chloroform within the syringe to be pumped into the microfluidic chip. However, this did not provide a controlled, periodic supply and frequently caused blockages at the inlet. As a result, it was decided that spheres should be made and cured on chip.

3.7 Sphere Production

In order to create spheres on-chip they need to be capable of being created and cured quickly. It was decided that the spheres should be created using a polymer that cures under ultraviolet light. Using UV curing is more

controllable than many other curing techniques, such as heating, as it can more easily be localised to a certain region of the chip and also UV light can be supplied to the chip, almost instantly. UV curing also required no adaptations to the manifold so it could be tested immediately. Initially, a polyethylene glycol dimethacrylate (PEG) and Vazo 56 photo-initiator based mixture was used. However, this was found to cure too slowly. As an alternative, trimethylolpropane triacrylate (hereafter known as TMPTA) mixed with 2-hydroxy-2-methylpropiophenone photo-initiator, in a ratio of 10:1 was used. This was found to cure within seconds when exposed to a 365nm UV LED (LED Engin LZ1-00U600, 5W, 365nm). TMPTA can henceforth, be considered to include the photo-initiator, unless otherwise stated.

3.7.1 Sphere Production Chip One

3.7.1.1 Experimental

Liquid segments were created at a T-junction on-chip. The channel then expands causing these segments to become spherical droplets. These droplets then travel through a meandering channel allowing for prolonged exposure to the UV light source. The chip was produced with the exchanger architecture, but the separator channels were not ablated for initial testing of the sphere production.

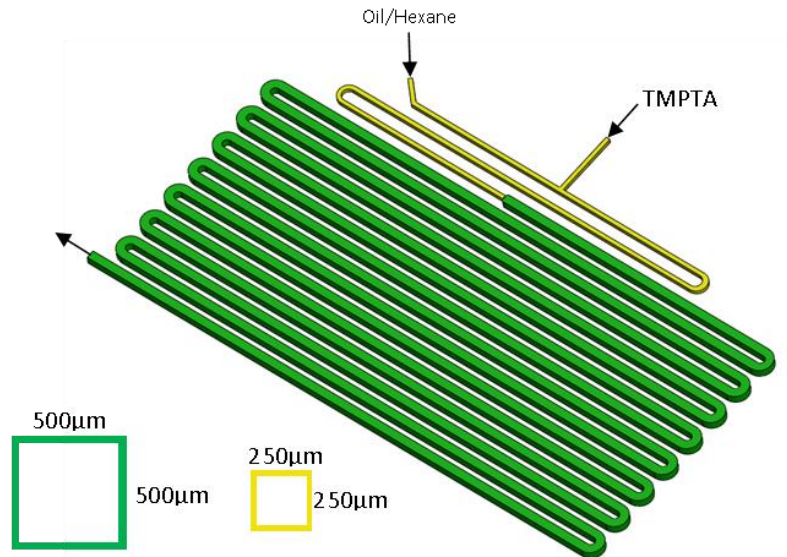


Figure 3-18: Sphere production chip one dimensions. Segments of TMPTA are created in a hexane/oil (1:4) carrier phase using a T-junction (yellow) and turned into spheres via a channel expansion to a meandering region (green) where UV curing occurs.

A mixture of hexane and mineral oil (1:4 ratio) was introduced via inlet one and TMPTA through inlet two. The hexane:oil mixture was pumped at a flow rate of 5ml/hr and the TMPTA at 1ml/hr.

The UV LED was powered using a Farnell 5V DC power supply and held against the surface of the glass cover plate during exposure.

3.7.1.2 Results and Discussion

This chip design successfully created TMPTA droplets in the mineral oil and hexane carrier fluid. However, when they were exposed to UV curing, the spheres stuck to each other creating a 'chain' of spheres as shown in Figure 3-19.



Figure 3-19: Photomicrograph of sphere production chip one showing a chain of cured TMPTA spheres stuck together causing a blockage in the channel.

This is likely as a result of the expansion region causing the spheres to become closer together, as shown in Figure 3-20, and, therefore, any slight slow-down in velocity, could cause the spheres to collide. To overcome this, the next stage of development removed the expansion region.

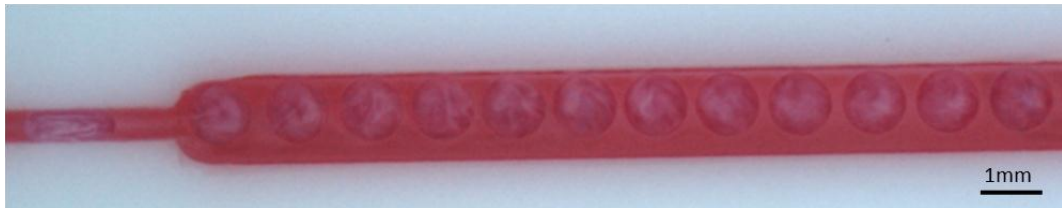


Figure 3-20: Photomicrograph of the expansion region used in sphere production chip one. The expansion region causes a reduction in the sphere spacing. Flow is from left to right.

3.7.2 Sphere Production Chip Two

3.7.2.1 Experimental

An adaptation was made to the T-junction to facilitate the production of spheres without the need of the expansion region. A narrowing of the channel at the junction, allows smaller droplets to be created at a manageable speed; i.e. a speed at which spheres could be observed and recorded in motion. The narrowing works as it increases the shear stress on the edge of the droplet, as it emerges from the junction. Due to this increased shear, the volume required to force a droplet to break off from the junction is lower. This narrowing is shown in the inset of Figure 3-21. The

channel from inlet two was also shallower than the main channel; this also aided with the formation of smaller controllable spheres.

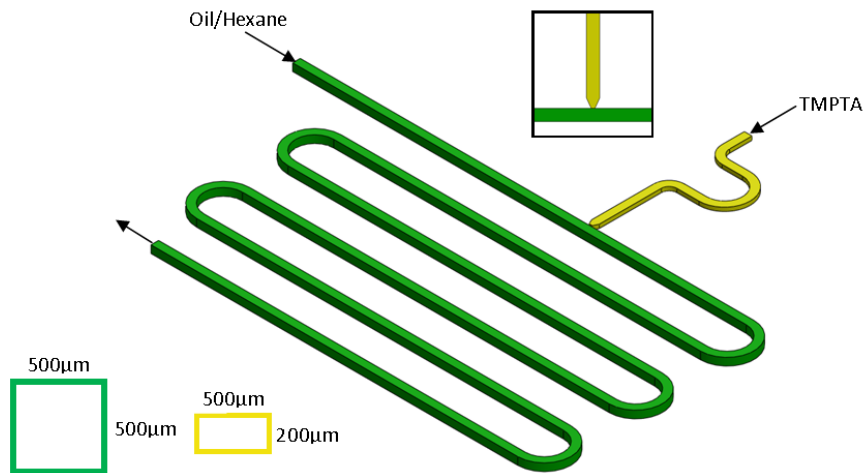


Figure 3-21: Cross-sectional dimensions of sphere production chip two. A shallower TMPTA inlet channel (yellow) meets the main flow channel (green) at a T-junction. The TMPTA channel narrows to 140µm wide at the junction in order to create spherical droplets within the Oil/Hexane carrier phase. The main channel meanders to create a UV curing region. Black arrows indicate flow. Inset: The T-junction showing the narrowing of the channel at the junction.

A flow of hexane and oil (1:4 mixture) through inlet one was set at 4.3ml/hr, and the flow of TMPTA through inlet two was set at 0.2ml/hr. The UV LED was held against the manifold glass cover plate, pointing downwards, during exposure.

3.7.2.2 Results and Discussion

Spheres created by this design were suitably sized and well spaced. However, after approximately 30 seconds of UV exposure, curing was evident in the TMPTA in the TMPTA inlet channel. This led to a blockage in this inlet channel. This was most likely a result of the dispersion that occurs as light travels through the glass used in the chip manifold. To overcome

this, it may be necessary to increase the distance between the sphere production and curing regions. In the short time prior to the inlet becoming blocked, there were some spheres produced, these spheres were cured and collected within a vessel at the outlet. The spheres are shown in Figure 3-22. These spheres appear to be highly monodisperse suggesting the T-junction is a suitable sphere producing technique.

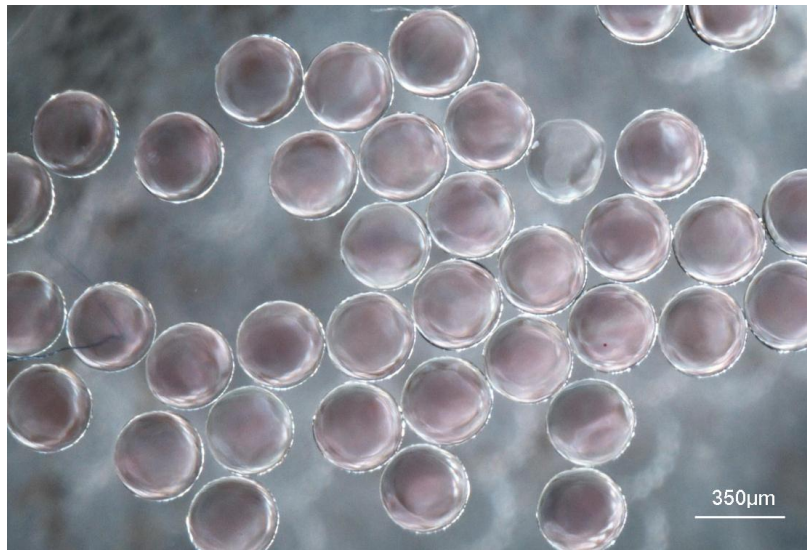


Figure 3-22: Photomicrograph of TMPTA spheres produced on exchanger chip five. Spheres were imaged after being collected in an outlet vessel and cleaned in acetone.

3.7.3 UV dispersion test

In order to determine the extent to which the UV light disperses through the glass a brief experiment was performed.

3.7.3.1 Experimental

A shallow reservoir was cut into a poly ethyl ketone (PEEK) disc and filled with TMPTA before a thin FEP film and a glass cover plate were placed on top of this, as shown in Figure 3-23.

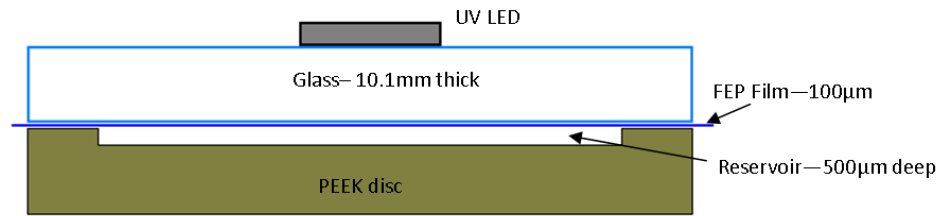


Figure 3-23: Illustration of the setup used to test the UV dispersion through the glass cover plate. A reservoir in a PEEK disc was filled with TMPTA which was cured by a UV LED placed in contact with the glass. By measuring the size of the cured region it was possible to determine the UV dispersion.

With the UV LED placed in the centre, in contact with the glass, it was switched on for 10s and the region that had cured was measured. This experiment was repeated three times.

3.7.3.2 Results and Discussion

The diameter of the cured region ranged from 28-29.4mm. The cured region can be seen in Figure 3-24.



Figure 3-24: Result of the UV dispersion test. The TMPTA was cured by the UV LED held against the glass using the setup shown in [Error! Reference source not found.](#) By measuring the size of the cured TMPTA the extent of the dispersion could be determined.

This curing region is far too big to be practical on 50mm diameter microfluidic chip. As such, the top of the glass was masked off with electrical

tape, save for a small rectangular hole measuring 2.3mm x 1.8mm. After 10s of UV exposure, the cured region was rectangular (with slightly rounded corners) with the dimensions 9.9mm x 8.2mm. By applying trigonometry, using the difference in the size of the cured rectangular region, and the size of the masked rectangle, it is possible to get an approximate idea of the extent of dispersion. It was found that the UV light dispersed at approximately 34° from the vertical.

Using this information, it was possible to design an LED housing that would restrict the size of the UV light profile, and therefore the size of the curing region. It was decided that, based on available tools, a 3mm diameter hole would be suitable as this would provide a circular curing region of roughly 17mm diameter. Having produced the housing, it was found that the curing region was approximately 15mm. This slight discrepancy is most likely due to the LED being raised a few mm above the glass by the housing.



Figure 3-25: LED housing viewed from both the bottom (right) and the top (left). The LED and wiring is placed in the grooves (shown on the left). The housing is then placed against the glass with the bottom of the housing (shown on the right) placed into contact with the glass.

3.7.4 Sphere Production Chip Three

3.7.4.1 Experimental

Based on the results of the UV dispersion test, the curing region was moved farther away from the sphere creation. To maximise the curing time in the area under UV exposure, the channel was milled in a spiral formation as this maximised the channel length to chip area ratio.

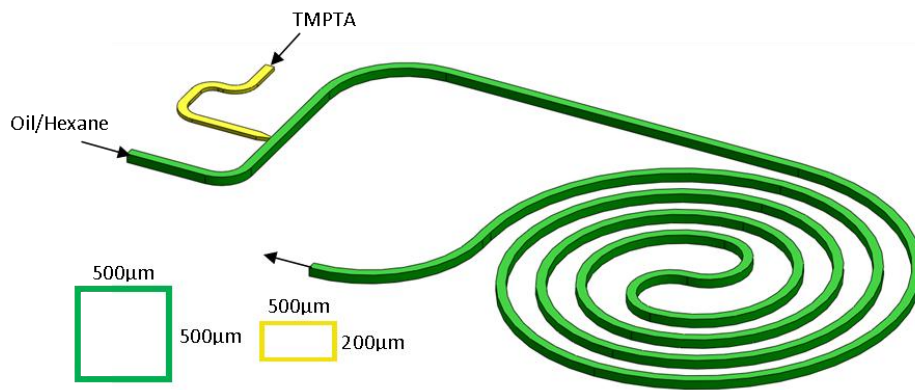


Figure 3-26: Cross-sectional dimensions of sphere production chip two. A shallower TMPTA inlet channel (yellow) meets the main flow channel (green) at a T-junction. The TMPTA channel narrows to $140\mu\text{m}$ wide at the junction in order to create spherical droplets within the Oil/Hexane carrier phase. The UV curing region is a spiral to maximise curing time spent under the UV light. Black arrows indicate direction of flow.

The flow rates used were 0.15ml/hr for the TMPTA and 6ml/hr for the hexane/mineral oil mixture.

3.7.4.2 Results and Discussion

Tests carried out on this chip confirmed that the distance between the curing and production regions was large enough to prevent inlet curing. However, blockages did occur every time curing was attempted. On this occasion blockages occurred in the curing spiral as shown in Figure 3-27.



Figure 3-27: Photomicrograph of a TMPTA blockage in the curing spiral on sphere production chip three. Droplets have come into contact during curing and are therefore stuck together.

This blockage appears to be a series of spheres that have stuck together as they cured. Droplets could be created in a consistent manner with this exchanger, as can be seen in Figure 3-28, but when curing was initiated blockages occurred on a consistent basis. This suggests that there was some slow-down of the spheres, causing them to become progressively closer together.



Figure 3-28: TMPTA droplets, in a mineral oil/hexane carrier solution, created on sphere production chip three travelling through the curing region. Droplets appear to have been made in a relatively consistent manner with little variation in their spacing prior to UV curing. Once curing was initiated blockages occurred on a regular basis.

This slow-down could be due to some manufacturing error, or dirt in the channels, or it could be caused by some inherent property of the curing process. To investigate this, additional spiral based chips were produced and compared with the meander used in chip two (Figure 3-21). From this it appeared that there was a higher likelihood of slowdown in the spiral, than in a series of meandering straight channels. Evidence of this apparent slow-down could be seen when droplets combined together to form larger droplets as highlighted in Figure 3-29. The slow-down shown in Figure 3-29 suggests that dirt, manufacturing errors or leakage are factors as there is some slow-down even before curing is initiated.

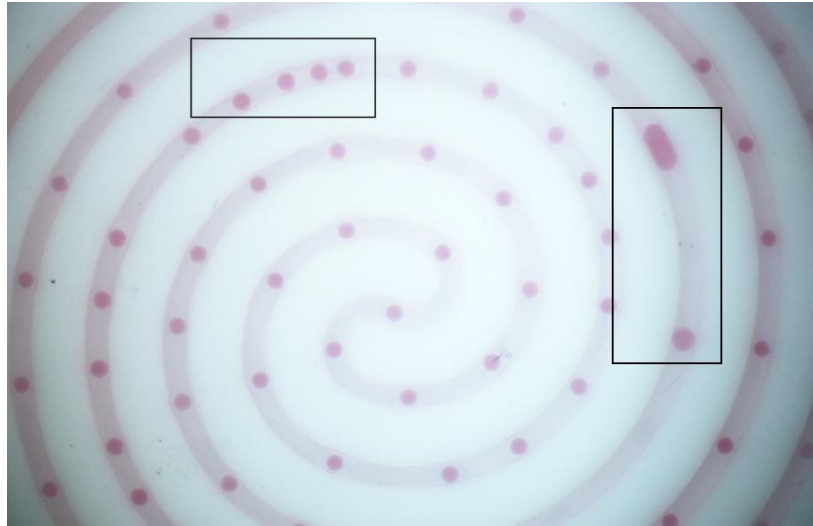


Figure 3-29: Spiral curing region with evidence of droplet slowdown. Highlighted: Droplets getting closer together; also droplets that have combined into a larger segment.

The increased probability of slow-down in spiralled channels, when compared to meandering channels, is possibly due to the limitations of the milling process. It was observed that machining 'frills' were more prevalent with curved channels than in straight channels. Machining 'frills' are thin strands of PTFE left around the top of the channels after the milling process. These 'frills' can be seen in Figure 3-30.

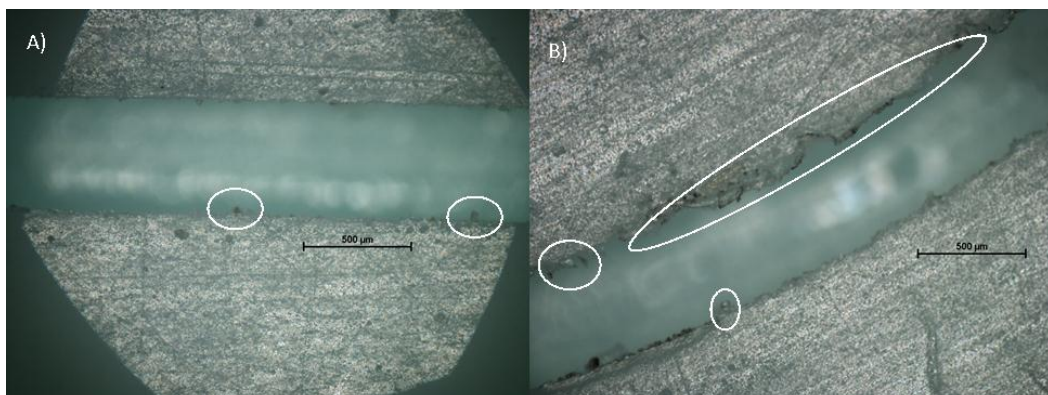


Figure 3-30: Photomicrographs of the surface of a PTFE chip at the edges of microfluidic channels. Highlights the machining 'frills' that occur when using micro milling to produce the chips. The frills (highlighted by white ovals) are much less prevalent in straight channels (A) than in curved channels (B). The curved channel shows numerous and large

frills along the channel edge whilst the straight channel has minor frills and there are fewer of them. In both images the scale bar represents 500 μm .

After polishing these frills can be removed by hand using tweezers but this is a laborious process that is not 100% effective and can also damage the channel walls.

3.7.5 Sphere Production Chip Four

3.7.5.1 Experimental

The spiral region was removed and replaced with a meandering channel in an attempt to reduce the number of blockages that occurred as a result of droplets combining. Additionally, a flow focusing junction was trialled for sphere production to determine whether it was possible to achieve greater control of sphere spacing and size.

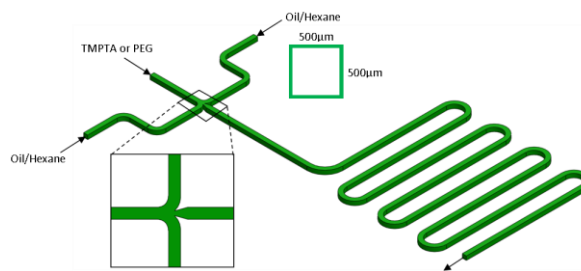


Figure 3-31: Cross sectional dimensions of sphere production chip four. All channels are 500x500 μm (green) apart from at the flow focusing junction which narrows to 200 μm wide (see inset). Arrows indicate direction of flow.

3.7.5.2 Results and Discussion

The flow-focusing junction was found to offer improved controllability and stability in terms of sphere production. Stability in this context, refers to consistency of sphere separation and size. By adjusting the flow rate of TMPTA through the central inlet, the size of the droplets could be altered

whilst the hexane/oil flow rate could be adjusted to control sphere spacing. Suitable flow rates were found to be 5ml/hr (hexane/oil) and 0.7ml/hr (TMPTA).



Figure 3-32: Image of the flow focusing junction creating droplets of TMPTA (white) in hexane/oil solution (red). Flow is from left to right.

The other change on this chip was the return to a series of straight channels as opposed to a spiral in the curing region. Despite this, a blockage still occurred once curing was initiated. To try to explain this it was postulated that the droplets may be sinking within the channels and then sticking to the PTFE as they cure. Evidence that this could be the problem was found by curing a drop of TMPTA on the surface of the chip (not in a channel) and finding that in the curing process the TMPTA did adhere slightly to surface.

To overcome this TMPTA adhesion problem an alternative UV curing liquid was obtained. Polyethylene glycol (PEG) was used instead. When cured with the same 10:1 ratio of 2-hydroxy-2-methylpropiophenone photo initiator as used with TMPTA, the PEG was found not to adhere with the PTFE during curing. Using PEG in sphere production chip four, was found to be more effective. The spheres could be created in a consistent and controllable manner, as shown in Figure 3-33, and were found to not stick together into chains as had occurred with the TMPTA. This led to spheres being created

and cured on chip, some of which can be seen in Figure 3-34. Forty five of these spheres were measured using the NIS elements software and were found to be reasonably monodisperse, having a mean diameter of $398.25\mu\text{m}$ with a coefficient of variation of approximately 3%. Some of the spheres were excluded from measurement as the droplets created during the initial set up stages of sphere production, were highly polydisperse until the pressure within the microfluidic system stabilised. A problem did arise at the outlet with spheres occasionally getting stuck at the outlet at the point where the spheres are required to make a 90 degree turn to drop down through the hole in the chip and manifold. This would occasionally lead to spheres coming together and lodging themselves across the width of the channel. This problem was later overcome by a colleague on a different project, by using an outlet that came out of the side of the manifold rather than turning 90 degrees.

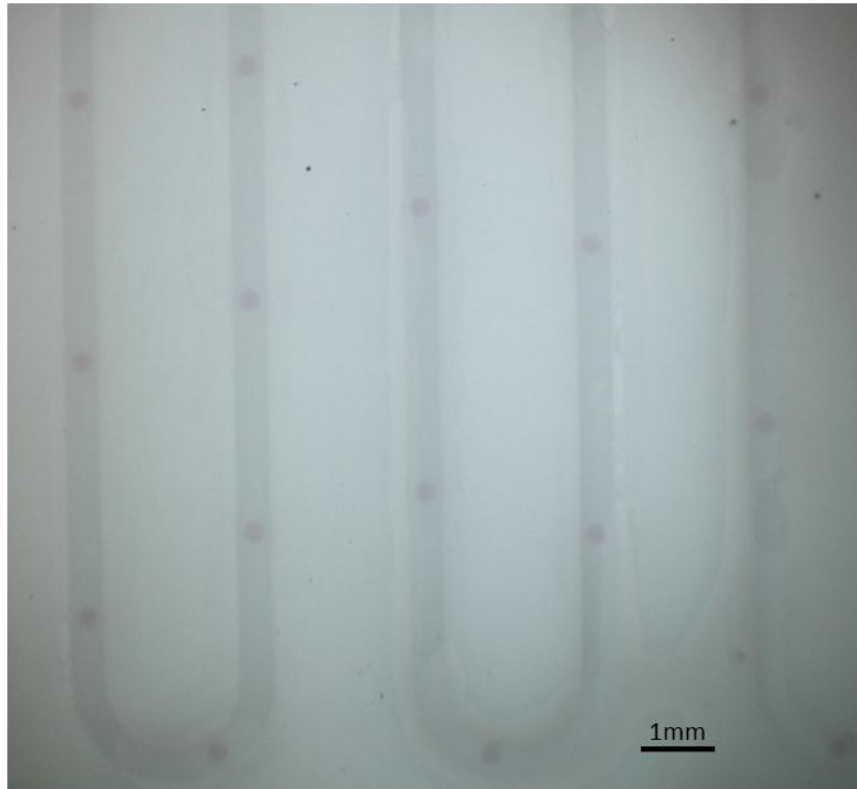


Figure 3-33: Photomicrograph of PEG spheres passing through the UV curing region of sphere production chip four. Highlighting the consistent and wide spacing between droplets, which helps to prevent the droplets sticking together during sphere curing. PEG inlet flow rate: 0.6ml/hr. Hex/Oil flow rate: 10ml/hr.

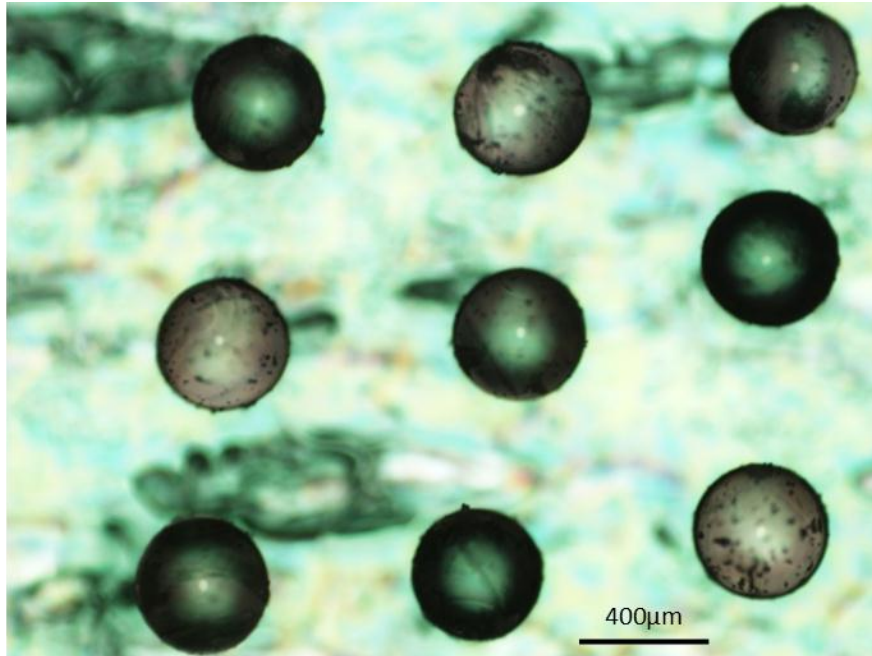


Figure 3-34: Photomicrograph of 9 sample PEG spheres that were created and cured on chip. 45 spheres were measured and found to have a mean sphere diameter of $398.25\mu\text{m}$ with a coefficient of variation of approximately 3%.

Spheres have been produced and cured on chip using ultraviolet curing of both TMPTA and PEG. It was found that PEG spheres were less prone to channel blockages than TMPTA, particularly when used in a meandering channel with a flow focusing junction to create the droplets. Spheres were produced with a coefficient of variation of approximately 3% this is close to the levels of monodispersity that has typically been achieved previously using microfluidic devices [184].

3.8 Sphere Exchange

Once a number of spheres had been created they were introduced to the medium exchanger as a proof-of-concept. The exchanger was found to

successfully transfer the sphere from one phase to the other as shown in Figure 3-35.

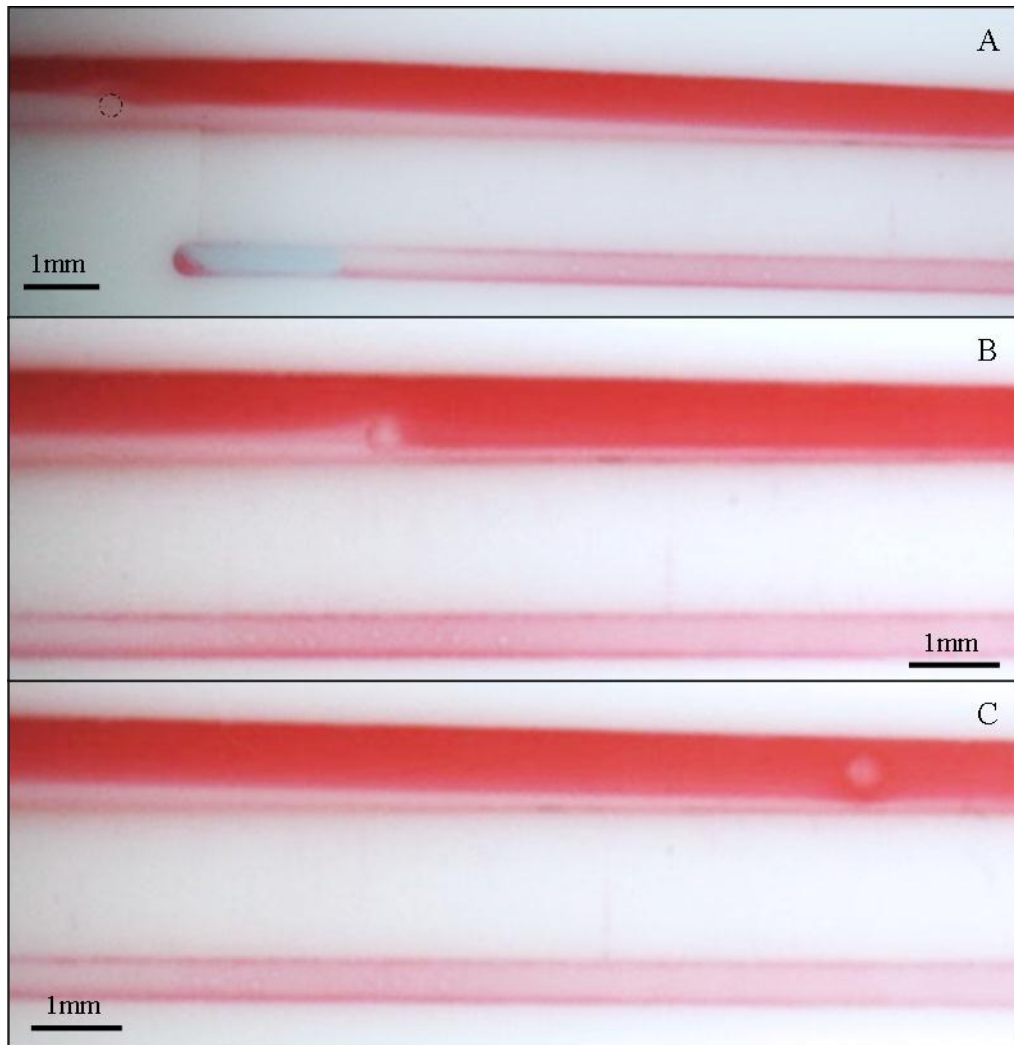


Figure 3-35: A series of video frames captured using a microscope showing sphere exchange. A) The sphere about to enter the exchanger carried in phase one (clear liquid) travelling left to right. Sphere highlighted by dashed line. B) Mid exchange: The sphere is still in phase one but some extraction has occurred. C) Enough of phase one has been extracted causing the sphere to cross into phase two (red liquid). The exchange is complete.

Whilst this brief test did confirm that a sphere could be exchanged using this design it was apparent that flow through the main channel outlet was very slow when a pressure high enough to achieve full exchange was used (approximately 7kPa). This is a major problem with this system as it means

the throughput of the device is almost nil. This problem must be overcome for the device to be viable.

The spheres were also used to test the exchanger when used with immiscible liquids. Phase one was chloroform and phase two was water dyed with blue Silver Spoon food colouring. The tests showed that phase one could be extracted and it seemed to show the sphere being transferred into the secondary phase. This is shown in Figure 3-36.

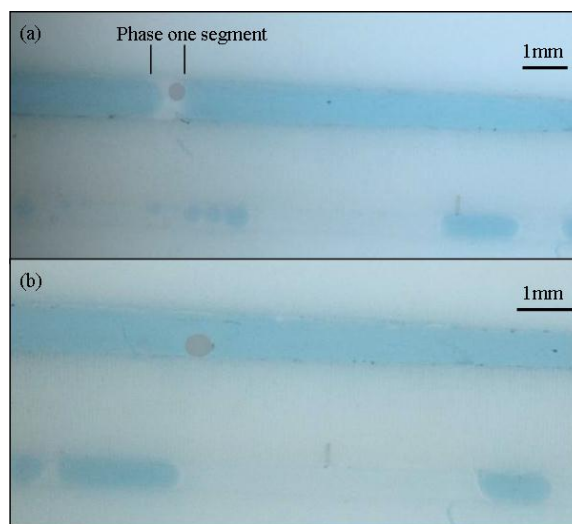


Figure 3-36: Exchange using immiscible fluids. a) The sphere is being carried by phase one (clear, chloroform) b) Phase one has been extracted; the sphere appears to have been transferred to phase two (blue, water). The image has been adjusted to highlight the position of the sphere.

Although at first glance the sphere appeared to have been transferred into the secondary phase, as shown by image b) of Figure 3-36, this was not the case. Instead it remained where it was when the primary phase was extracted rather than being collected into the flow of the secondary phase. The current hypothesis to explain this, is that there is a thin film of phase one still surrounding the sphere that causes the secondary phase to flow over the sphere rather than picking up the sphere and moving it. The

primary phase essentially creates a 'bunker' that protects the sphere from the secondary phase. This is illustrated in Figure 3-37.

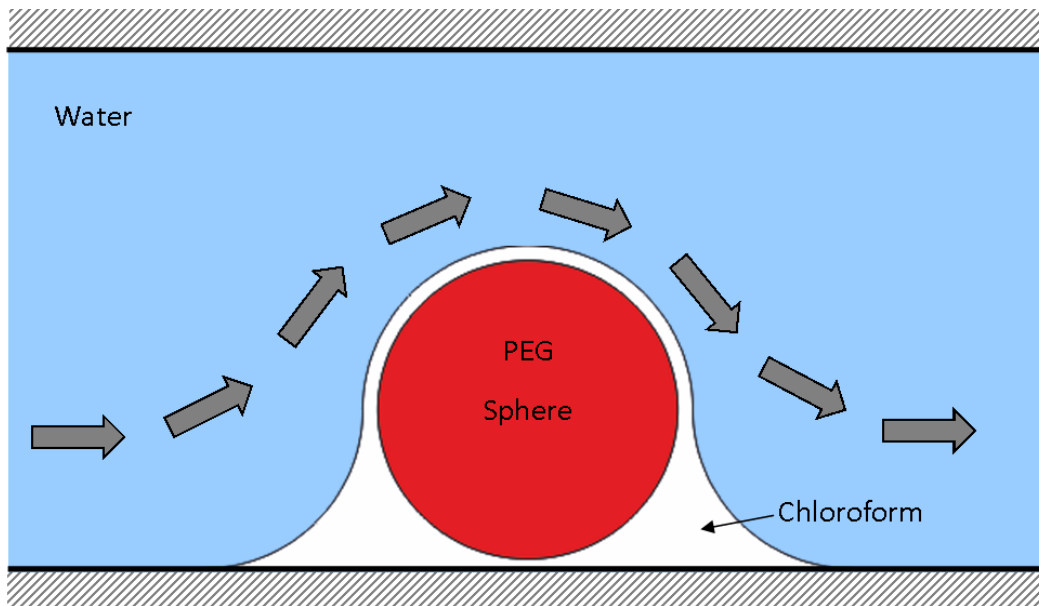


Figure 3-37: Illustration of the 'bunker' surrounding the sphere during an immiscible exchange. The sphere is shown in red, phase one in white and phase two in blue. The arrows indicate the flow of phase two up and around the sphere. This is a side-on view of the channel.

Evidence for this theory can be seen in Figure 3-38 where the chloroform phase appears to preferentially wet the surface of the PEG sphere. Even when the majority of the chloroform has evaporated away a thin film of chloroform is still evident on the surface of the sphere. This suggests that the surface of the sphere is more readily wetted by the chloroform than the water thus maintaining a barrier between the sphere and the water. More information about wetting characteristics can be found in section 1.5.

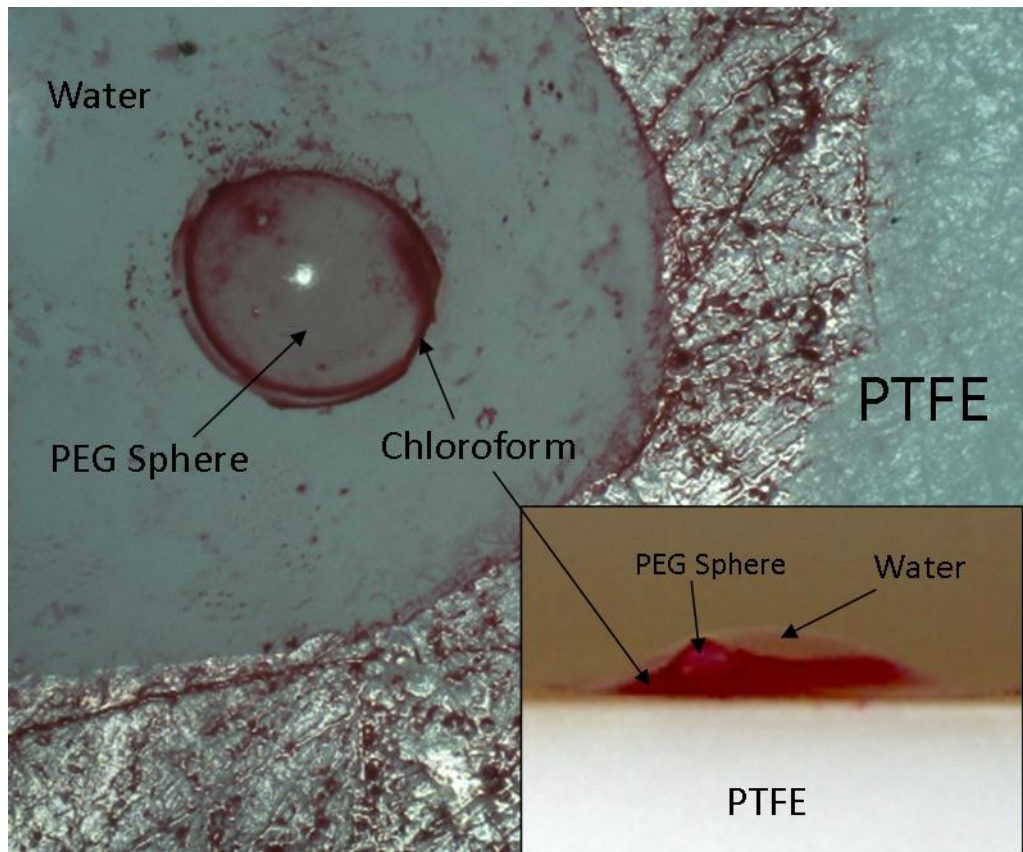


Figure 3-38: Evidence to support the bunker theory to explain the lack of movement of PEG spheres when performing an immiscible exchange. A PEG sphere is placed on a PTFE chip before water (clear) and chloroform (red) droplets are dropped on the sphere. The surface of the sphere is preferentially wetted by the chloroform, as can be seen by the red ring around the sphere. This can also be seen in the side profile shot (inset) where the sphere is contained within the chloroform rather than the water.

3.9 Conclusion

This chapter has introduced the concept of the microfluidic phase separator and adapted it to facilitate phase exchange. By creating ultraviolet curable spheres it has been possible to demonstrate the transfer of spheres between two phases. However, a problem with the throughput of the device was identified. Due to the increased pressure applied to outlet one, the flow rate out of this outlet dropped significantly. This is a problem that needs to be

overcome to make the medium exchanger viable and will be the initial focus of the next chapter.

3.10 Appendix - Device Fabrication

Microfluidic chips were designed using SolidWorks before being exported to CircuitCAM 5.0 (LPKF, Germany) as .DXF files. This software allows milling procedures to be assigned to cut the appropriate regions of the chip. These procedures are then exported to BoardMaster (LPKF, Germany) where tools are assigned to the milling procedures. The BoardMaster software controls the micromachining tool. Whilst the BoardMaster software controls the machine head movement in the X and Y planes the Z plane is controlled by manual adjustment to the desired depth. To ensure a good surface finish within the channels, and to minimise the stress placed on the tool, multiple machine passes were used; typically only increasing the depth by a quarter of the tool diameter for each pass. Milling was carried out with a milling tool spin speed of 30,000rpm. Inlet and outlet holes could be drilled in any of 12 positions; the holes were centred 3.25mm from the edge of the PTFE chip. These 12 positions lined up with holes in a prefabricated metal manifold. The chips were polished before and after milling to obtain a smooth and flat surface. Polishing was performed by hand by rubbing the PTFE chip over a series of polishing papers of increasing fineness with a cotton polish as the final stage (240-2500 grade SiC grinding paper for metallography, BUEHLER). The same production technique was used for the manufacture of all PTFE chips. Flat 2" diameter PTFE discs were used with channels machined into the surface of the PTFE.

The separator channels were created using 768nm femtosecond laser ablation. Short pulse femtosecond laser ablation was used as it has numerous advantages. Firstly the high precision machining that is possible with laser ablation allows for narrower channel widths than are generally possible with tradition milling techniques. Additionally the low operating temperature and minimal thermal penetration of femtosecond laser ablation greatly reduces the potential for melting to occur around the sight of the ablation [185]. The ablation path was created as a series of lines in the Advanced Profiling software that reached across the gap between the main channel and the secondary outlet channel plus an additional 50 μ m either side as a fabrication tolerance to ensure all channels reached all the way across the divide. This array of lines was fabricated with a single sweep of the femtosecond laser using the parameters detailed in Table 3-1.

Table 3-1: Laser ablation parameters used to ablate 30 μ m wide channels in PTFE

Parameter	Value
Power at point of ablation	0.38W
Machine Speed	50 mm/min
Machine Steps	2000 /mm
Max. Rep Rate	200 Hz
Loops	1
Lead in	0.05mm

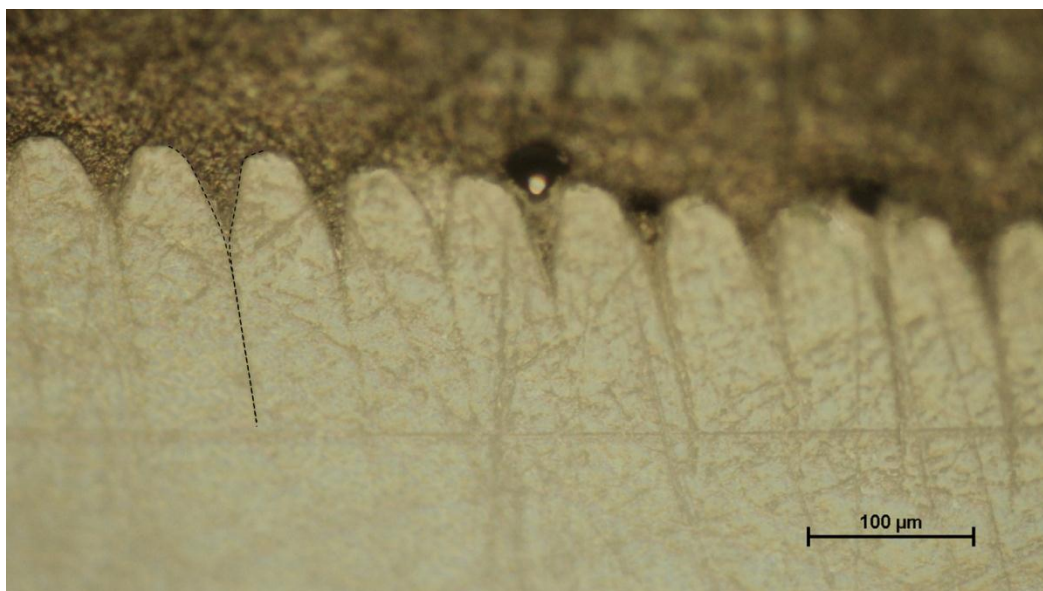


Figure 3-39: Profile of the separator channels created using femtosecond laser ablation. Channels were set in epoxy resin and polished down to gain a profile without significant damage occurring. One separator channel has been highlighted with a dashed line.

The chips were placed within a metal manifold beneath a 100 μ m thick layer of Teflon[®] PFA film and a glass window. Finger tight connectors were used to attach Teflon tubing (ID 0.5mm, OD 1.58mm) to the underside of the manifold, providing access to the chip inlets or outlets. 12 screws were then used to apply a compressive force across the glass window to ensure the fluidic channels were sealed.

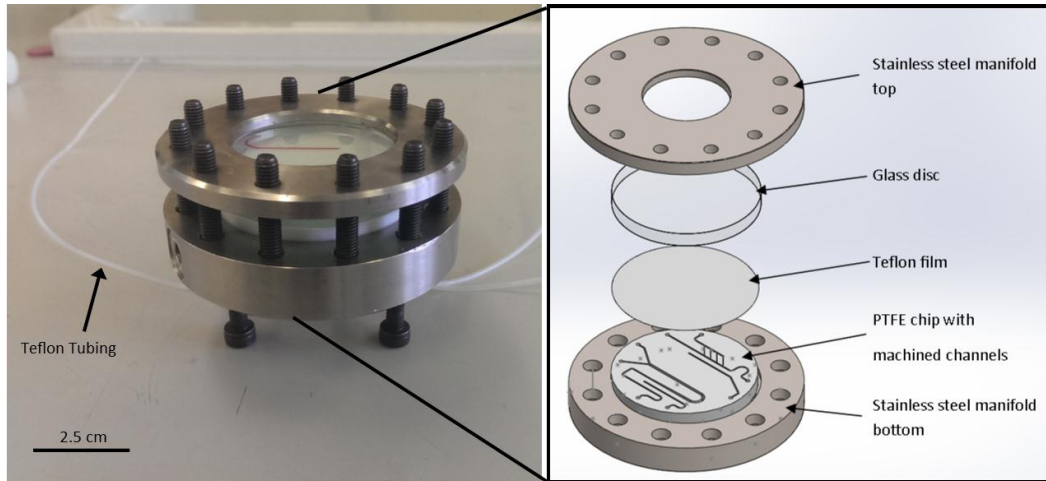


Figure 3-40: Image of the manifold used to create sealed PTFE devices with a diagram of the parts of the manifold exploded from the image. Two stainless steel plates are placed either side of a glass cover plate, Teflon film and a PTFE chip. Bolts are used to compress the film and glass against the PTFE creating a seal. Finger tight fittings are connected to the underside of the manifold to allow Teflon tubing to connect to inlet and outlet holes that are drilled through the PTFE chip.

4 Phase Exchanger Development

In the previous chapter, experiments indicated that the phase exchanger concept could work but it was clear that there were problems with the design. Chief among these problems was the issue of throughput at the pressures necessary for a complete exchange. This chapter details the work carried out to overcome this problem and also to develop the phase exchanger.

Development of the exchanger was driven by the concept of fluidic resistance. The flow of fluids through a tube or channel is analogous to that of current along a wire, and as such, there is an equivalent to Ohm's law. In electronics, Ohm's law states that voltage is equal to current multiplied by resistance. Similarly in fluidics, the pressure differential along the channel, ΔP , is equal to the volumetric flow rate, Q , multiplied by the fluidic resistance, R .

$$\Delta P = QR \quad (4-1)$$

When considering continuous laminar flow of incompressible liquids the Hagen-Poiseuille equation can be adapted to give [186]:

$$\Delta P = \frac{32U_{avg}\mu L}{D_h^2} \quad (4-2)$$

where, L is the channel length. Given that:

$$Q = U_{avg}A \quad (4-3)$$

with A being the channel cross-sectional area, it is then possible find an equation for fluidic resistance, namely:

$$R = \frac{32\mu L}{D_h^2 A} \quad (4-4)$$

The hydraulic diameter, D_h , is defined as:

$$D_h = \frac{4A}{p} \quad (4-5)$$

where p is the wetting perimeter of the channel. By considering these equations, many possible avenues of improvement can be established.

4.1 Development Simulations

In order to understand the pressure problem, and also to get a clearer view of how the exchanger works, it was decided that performing simulations using COMSOL Multiphysics® would be beneficial. Two physics types were used in every model; ‘Laminar Flow’ to simulate the flow and ‘Transport of Diluted Species’ to simulate the exchange. The ‘Laminar Flow’ physics module uses the Navier-Stokes equations for conservation of momentum and the continuity equation for conservation of mass whilst the ‘Transport of Diluted Species’ module uses the convection-diffusion equations. Due to their limitations these simulations would not serve as perfectly predictive simulations; i.e. a result of a 75% exchange would not necessarily match up exactly with the real world under the same flow conditions. This is because not all elements of the real world were possible to simulate using these two physics engines. For example, it is not possible to add the contact angle relationship between the liquid and the material that the chip is made from. However, by keeping the majority of the parameters the same between simulations, it is possible to create simulations that have merit as comparative tools. This means that alterations to elements such as the channel geometries, or flow rates, could be examined in comparison to other

simulations, to get an indication as to how these changes would impact the exchanger behaviour.

4.1.1 Model Parameters

Some parameters of the models remained consistent throughout all the simulations. These parameters are detailed here. As the models are not directly predictive it was deemed unnecessary to use many different liquids as may be used in the real world. Instead water was used, as the properties of water are most readily available. The in-built water material was used with some adjustments. The density and viscosity were set as 998 kg.m^{-3} and $1 \times 10^{-3} \text{ Pa.s}$ respectively [187] with the temperature set to 293K. The boundary conditions and parameters for the 'Laminar Flow' physics tree are shown in Table 4-1.

Table 4-1: Parameters and boundary conditions used with the 'Laminar flow' physics tree.

Feature	Boundary Condition / Parameters
Walls	No slip
Inlets	Laminar inflow
Outlets	Pressure, no viscous stress
Initial Values	Velocity field = 0 m/s Pressure = 0 Pa

Table 4-2 shows the boundary conditions and parameters for the 'Transport of Diluted Species' physics. The initial value was set to $1 \times 10^{-20} \text{ mol.m}^{-3}$ instead of 0 mol/m^3 as it was found to speed the computation time whilst having a negligible impact on the results.

Table 4-2: Parameters and boundary conditions used with the ‘Transport of diluted species’ physics tree.

Feature	Boundary Conditions / Parameters
Convection and diffusion	Velocity field: From Laminar Flow study Diffusion coefficient = $2.023 \times 10^{-9} \text{ m}^2/\text{s}$ [188]
No Flux	Apply to all species
Initial Values	$1 \times 10^{-20} \text{ mol}/\text{m}^3$
Concentration	Inlet 1 = $0 \text{ mol}/\text{m}^3$ Inlet 2 = $1 \text{ mol}/\text{m}^3$
Outflow	Outlets 1 and 2

The mesh parameters were also kept consistent throughout the simulations and had the following parameters.

Table 4-3: Mesh parameters for exchanger COMSOL simulations.

Max. element size	1.35×10^{-4}
Min. element size	2.9×10^{-5}
Max. element growth rate	1.23
Curvature factor	0.7
Resolution of narrow regions	0.6

The simulations were solved in two steps, first the ‘Laminar Flow’ physics was simulated and then the results of this step were used to simulate the ‘Transport of Diluted Species’ physics. The simulations were solved using a direct PARDISO solver.

4.1.2 The Pressure Problem

The first simulations were concerned with investigating the pressure vs. throughput problem.

4.1.2.1 Model Parameters

A 3D model was created as shown in Figure 4-1. The separator channels had a triangular cross-section and were $30 \mu\text{m}$ wide at the top, narrowing to a

point $130\mu\text{m}$ below. Triangular channels were chosen as a close approximation to the actual shape of the separator channels as it drastically reduced the computational time. They were $500\mu\text{m}$ long and separated by $60\mu\text{m}$. The number of separator channels in the initial experiments was 110 channels. This number was chosen as it offered a reasonably large number of channels without increasing the computing time to the point where it would be prohibitive for the number of simulations that were to be carried out.

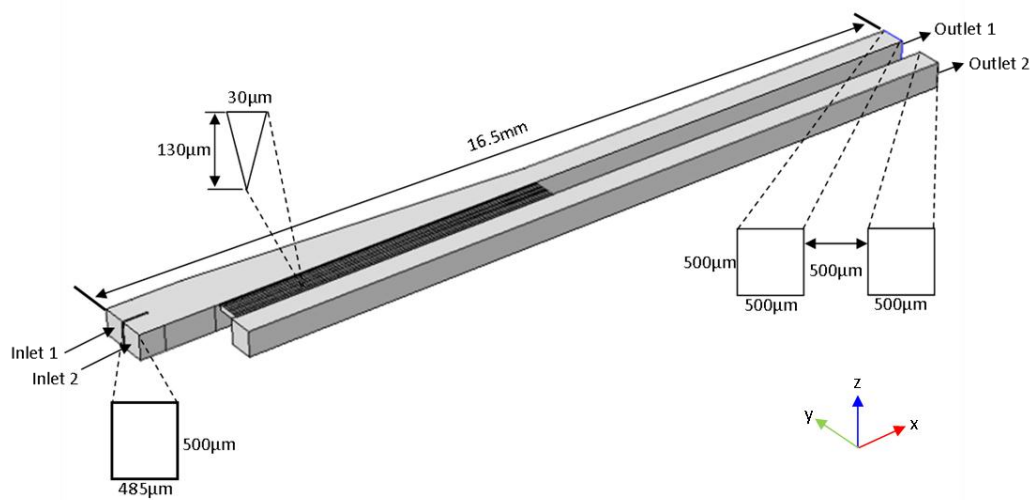


Figure 4-1: 3D model used in Pressure vs. Throughput simulations. The inlets are slightly narrower than $500\mu\text{m}$ to allow for a $30\mu\text{m}$ wide gap that is $500\mu\text{m}$ long, which is used to separate the two inlets. Inlet, outlet and separator channel cross-sections are exploded from the diagram.

The average flow rate was set as $U_{\text{avg}} = 0.03 \text{ m/s}$ for both inlets. This flow rate was chosen, as below this rate, even reasonably low outlet one pressures ($<1\text{kPa}$) could overwhelm the flow, pushing it back the wrong way. Additionally, 0.03m/s corresponds to approximately 27ml/hr , which is not outside of the realms of possibilities for real word applications. With a $Re \approx 15$, this flow rate is well within the laminar flow regime. The pressure

applied to outlet one was increased in steps of 0.2kPa starting at 0kPa. The results of the simulations were analysed by taking a surface average of the velocity and concentration at outlet one. This gave a number for the concentration of between 0 and 1. When multiplied by 100 this gave an exchange percentage with 0 being a 0% exchange and 1 being a 100% exchange.

4.1.2.2 Results and Discussion

A graphical illustration of the results of these simulations is shown in Figure 4-2. It clearly shows a partial exchange is taking place with the majority of phase one being extracted through the separator channels.

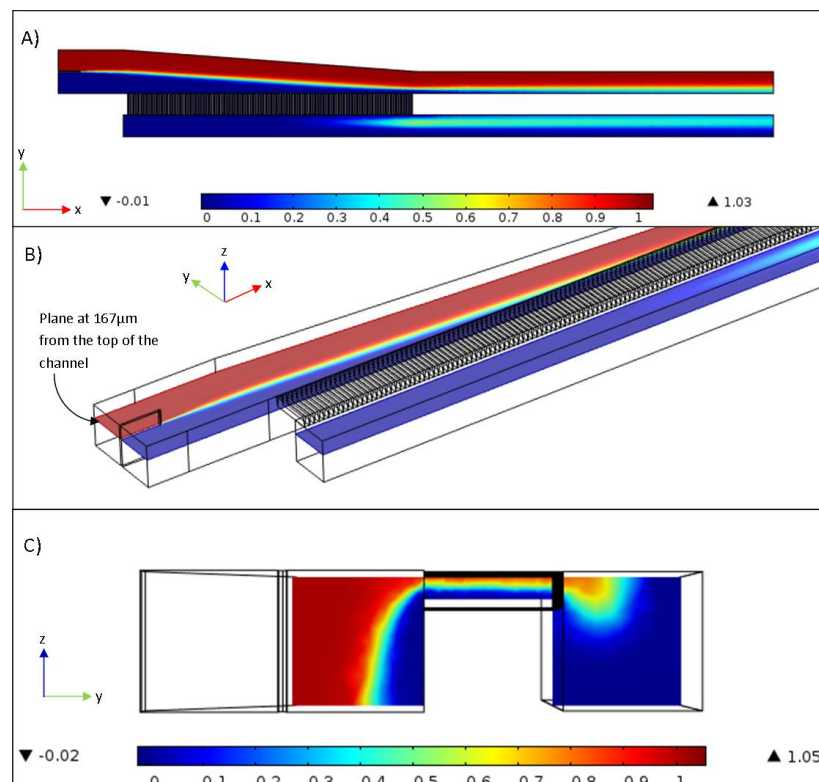


Figure 4-2: A) Rainbow plot of medium exchanger simulation showing high concentration in red and low concentration in blue. High concentration represents phase two whilst low concentration represents phase one. The plot is on an x-y plane positioned at 167 μ m from the top of the channel. The result is one plane of the simulation results for a pressure of

4 Phase Exchanger Development

0.6kPa applied to outlet one, which resulted in an average exchange of 73%. B) Illustration of the position of the x-y plane shown in image A in terms of its depth within the channel. C) Concentration plot on the yz-plane to show that the concentration is not uniform in the z-dimension. Phase two is extracted more readily near the top. This plane was taken through the last separator channel.

A statistical analysis using the values obtained from the surface averages highlights the pressure problem very clearly. It is clear that as the exchange improves the outlet one flow rate decreases. It appears that to achieve a 100% exchange the throughput of the device would be 0 m/s.

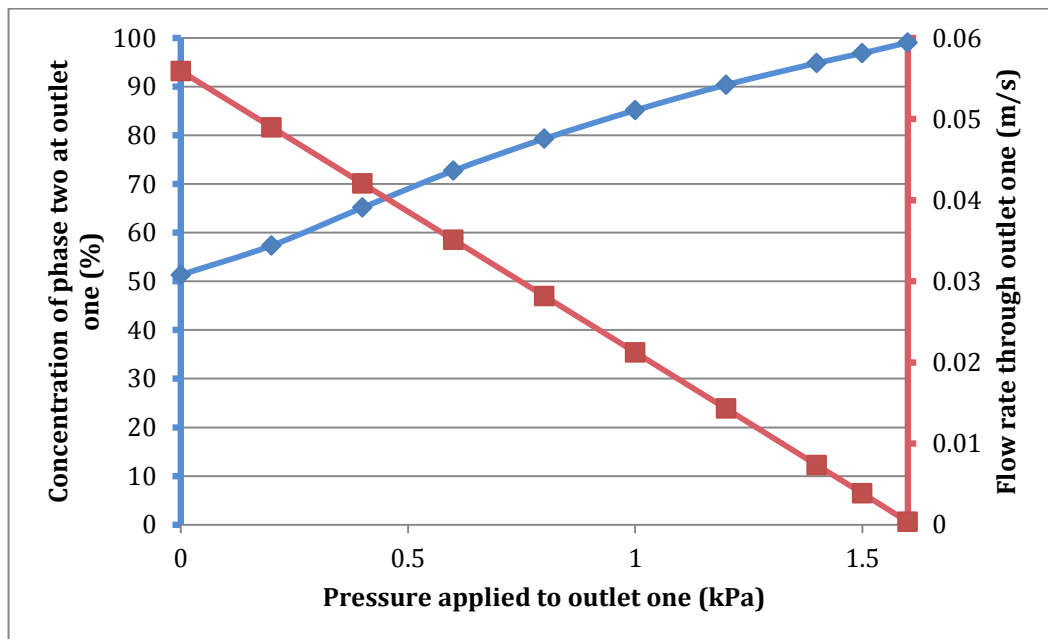


Figure 4-3: Phase two concentration versus average flow rate through Outlet One. As the level of exchange (blue) increases the flow rate (red) decreases. Both parameters are plotted against the pressure that was applied to outlet one.

As the flow rate is the problem here, the obvious first place to look for a solution is to alter the flow rates. As such, simulations were run over the same pressure range but with mismatched flow rates. The overall flow rate

of the inlets (0.06m/s) was maintained but the ratio of inlet one to inlet two flow was altered.

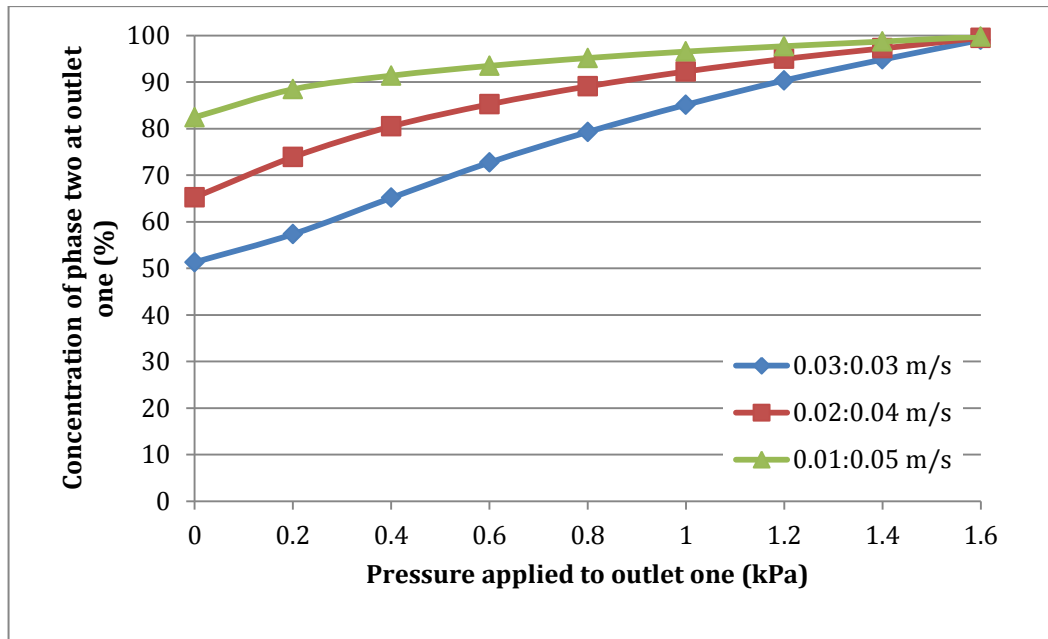


Figure 4-4: Concentration of phase two at outlet one for three different flow ratios against the pressure applied to outlet one. The overall speed remains consistent for all set-ups but the ratio of inlet one flow rate to inlet two flow rate varies. The flow rate out of outlet one remains as it is in **Figure 4-3**.

Figure 4-4 shows that altering the flow rate ratio does impact the level of exchange allowing a more complete exchange to be achieved at lower pressures, therefore reducing the impact on throughput. It was noted that the point at which the concentration difference was greatest, was at 0kPa. For this reason, flow rate differentials without an applied pressure were investigated.

4.1.3 Flow Rate Differential

4.1.3.1 Model

The same model as was used to investigate the pressure problem, was also used here, however, no pressure was applied to either outlet. The flow rate was set at 0.01 m/s for inlet one, whilst it was varied from 0.01 m/s up to 0.2 m/s for inlet two.

4.1.3.2 Results and Discussion

At first glance, the results in Figure 4-5 appear to show that differential flow rates provided a solution to the problem, as the concentration of phase two increases along with the device throughput, suggesting that reasonably high levels of exchange are possible. However, this does not take the initial input percentages, of the two phases, into account.

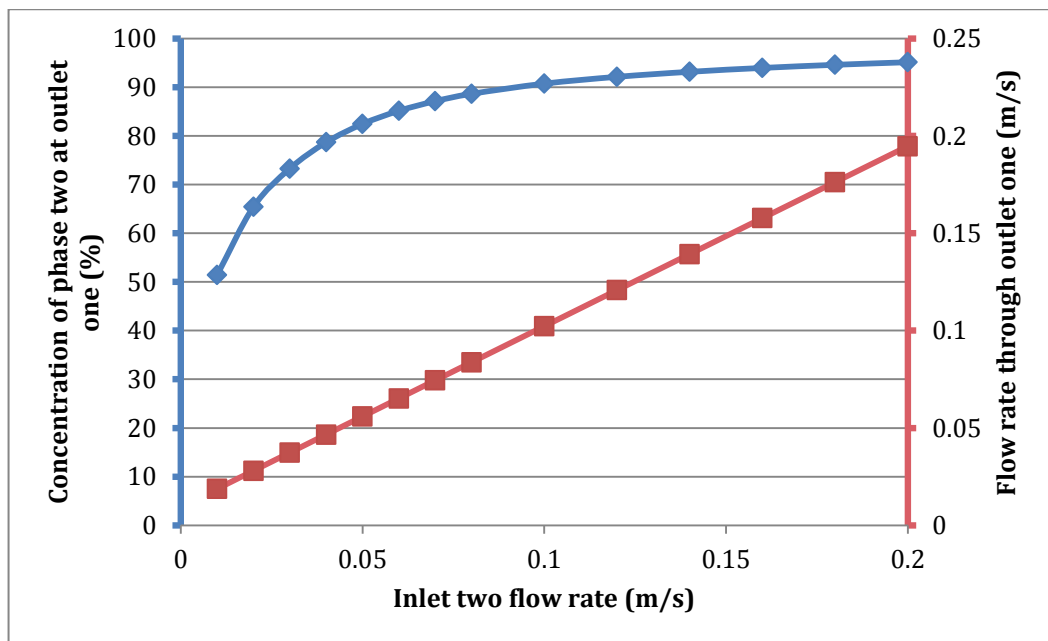


Figure 4-5: Differential flow-rate exchange, showing that the concentration of phase two (blue) does not cause a decrease in outlet one flow rate (blue), as it did with the pressure driven system.

When the inlet two flow rate is significantly higher than the inlet one flow rate, the output concentration of phase two will also be higher, irrespective of any impact the exchanger architecture may have. To demonstrate this, simulations were run without the separator channels, or the secondary outlet, to determine how much of the ‘exchange’ was down to the exchanger. One such result is shown in Figure 4-6.

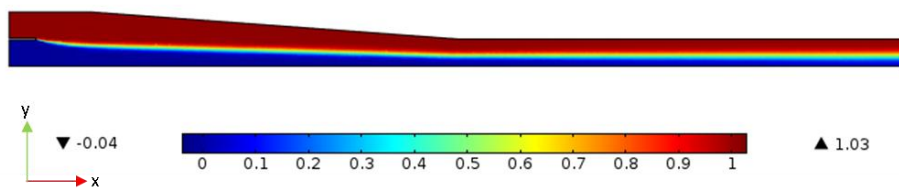


Figure 4-6: Rainbow concentration plot on the medium exchanger without separator channels. Plot is on an x-y plane taken at 250µm from the top of the channel. Plot shows low concentration in blue (phase one) and high concentration in red (phase two).

The data presented in Table 4-4 shows that the exchanger architecture is providing only a slight benefit, and after an initial increase, this slight benefit diminishes as the flow rate increases. The fact that the difference initially increases with flow rate, suggests that the mismatched flows do encourage the liquid to pass through the separator channels. However, to make the exchanger worthwhile, this difference needs to be significantly improved.

Table 4-4: Comparison of simulations with and without the exchanger showing the concentration of phase two at outlet one.

Inlet One Flow Rate (m/s)	Inlet Two Flow Rate (m/s)	Concentration w/ exchanger (%)	Concentration w/out exchanger (%)	Difference due to exchanger (%)
0.01	0.02	65.432	63.518	+1.914
0.01	0.08	88.633	85.353	+3.28
0.01	0.14	93.154	90.612	+2.542
0.01	0.2	95.123	92.905	+2.218

4.1.4 Shallower Exchanger

By analysing the simulation results a possible way to improve the device was found. It was noted that the position of the separator channels at the top of the 'chip' meant that liquid was extracted from the top of the main flow channel leading to phase two liquid near the top being extracted before all of phase one had been extracted. This is illustrated in Figure 4-7.

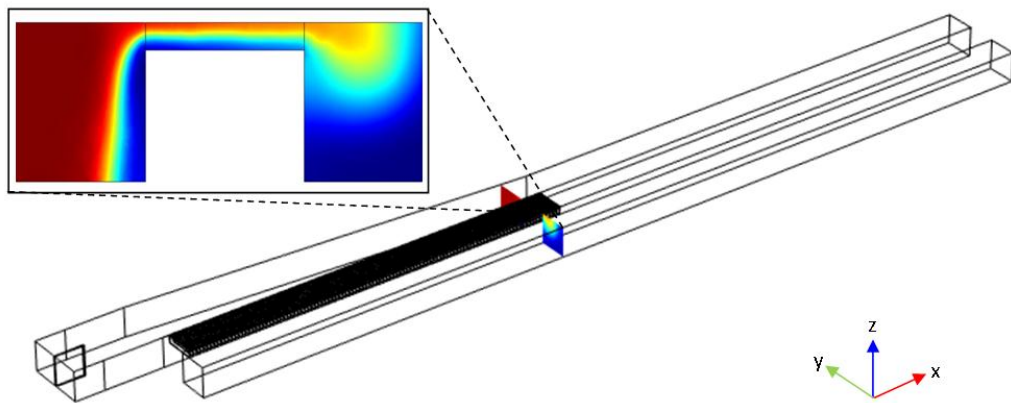


Figure 4-7: Mismatched flow rates cross-section (0.01:0.08 m/s) demonstrating the problem with the separator channels being positioned at the top of the channels. Phase two (red) is crossing into the outlet two channel before phase two (blue) has been completely extracted.

To overcome this extraction problem, simulations were carried out with channel depths more similar to the depth of the separator channels.

4.1.4.1 Model

A channel depth of $150\mu\text{m}$ was chosen as it is very similar to the $130\mu\text{m}$ depth of the separator channels, but it was decided that it would not be appropriate to have the exact same depth, as the extra depth gives more manufacturing tolerance. This is to account for slight machining errors plus variation in the power during femtosecond laser ablation. Also, the extra

depth to the main flow channel reduced the chance of the laser ablation significantly damaging the channel floor as it is farther from the laser focal position. The mesh was adjusted slightly to account for the decreased size; the minimum element size was lowered to 2.8×10^{-5} . All other parameters remained as they were in previous models.

4.1.4.2 Results and Discussion

The results shown in Figure 4-8 show very clearly, that a shallower exchanger offers significantly improved exchange levels.

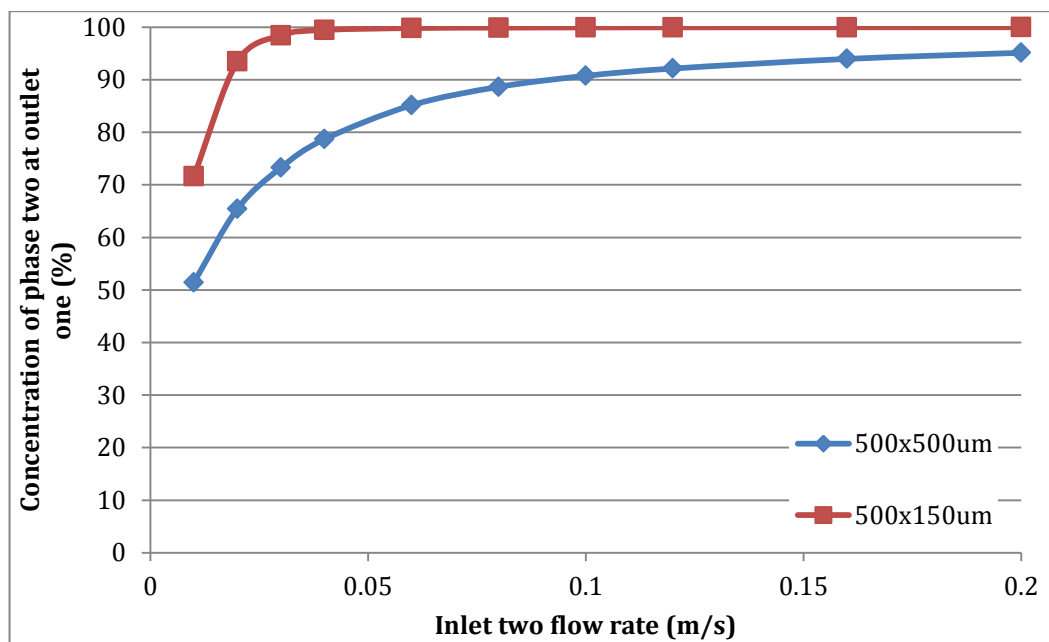


Figure 4-8: Concentration of phase two at outlet one for both 500 μ m square cross-section channels and shallower 150 μ m channels, demonstrating a clear improvement when using shallower channels.

It can also be seen in Table 4-5 that the difference that is attributable to the exchanger architecture, is also significant in this case. Again, there are diminishing returns, in terms of improving exchange, as the secondary flow rate is increased. This is to be expected as the overall exchange is

approaching 100%, therefore, there is less room for improvement. These results suggest that using differential flow rates is a viable technique to achieve high quality exchanges without an applied pressure.

Table 4-5: Comparison of simulations with and without the exchanger showing the concentration of phase two at outlet one.

Inlet one flow rate (m/s)	Inlet Two flow rate (m/s)	Concentration w/ exchanger (%)	Concentration w/out exchanger (%)	Difference due to exchanger (%)
0.01	0.02	93.468	64.92	+28.548
0.01	0.03	98.442	72.632	+25.81
0.01	0.04	99.46	77.565	+21.898

4.1.5 Separator Channel Length

The fluidic resistance equation has a length parameter suggesting that reducing the separator channel lengths should reduce said resistance, and as such, encourage the fluid to travel down the separator channels more easily.

4.1.5.1 Model

The shallow exchanger model was used with the only alteration being that L_{sep} was varied between 100 μ m and 1 mm, in steps of 100 μ m. Each test was performed with an inlet flow ratio of 0.01 to 0.02 m/s for inlets one and two respectively.

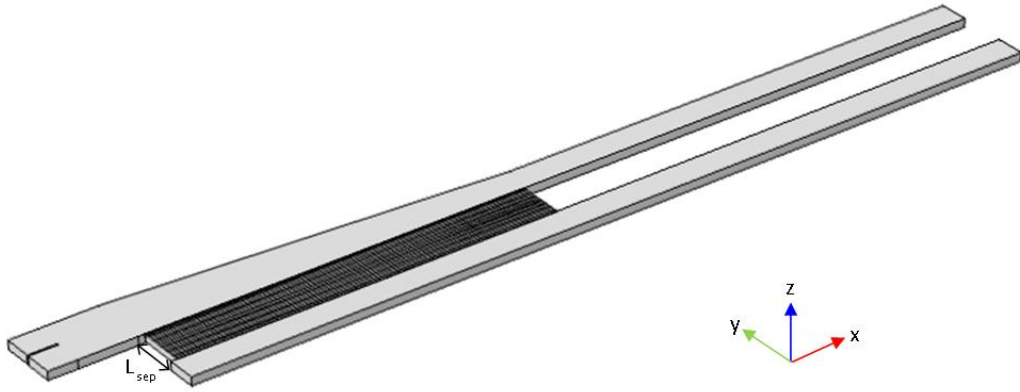


Figure 4-9: Model used to investigate the impact of channel length on the exchanger performance. L_{sep} refers to the length of the separator channels. L_{sep} was varied from $100\mu\text{m}$ up to 1mm in steps of $100\mu\text{m}$. Channel depth is set at $150\mu\text{m}$ whilst the inlet channels were $485\mu\text{m}$ wide and the outlet channels were $500\mu\text{m}$ wide.

4.1.5.2 Results and Discussion

It is clear in Figure 4-10 that shorter separator channels provide a better exchange; this is consistent with the previous published work [168]. However, other elements are also important and must be considered. Chief amongst these is the structural integrity of the channel walls. As these channels are not secured at the top when they are fabricated they are quite fragile, making them too short would make them even more fragile. For this reason $400\mu\text{m}$ was settled on as a suitable length as it provided good exchange without significantly weakening the channel structure.

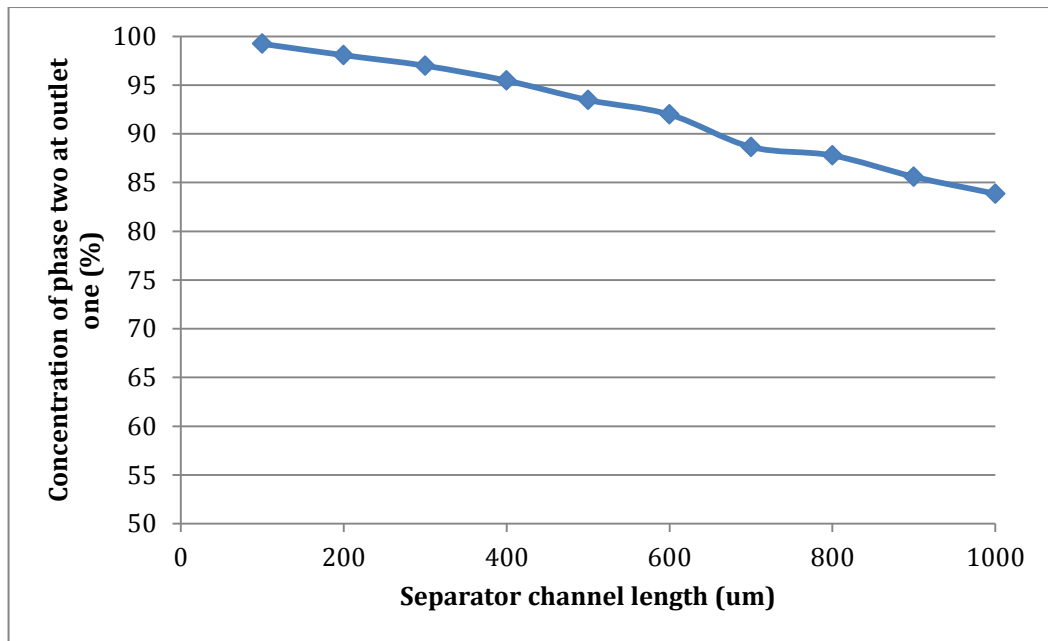


Figure 4-10: Impact of separator channel length on exchange, showing that shorter separator channels provide a more complete exchange.

4.1.6 Number of Separator Channels

In an electronic circuit, a number of equal resistors in parallel will give a lower overall resistance than an individual resistor. If the analogy of an electronic circuit to fluidic channels is valid, it should, therefore follow, that increasing the number of separator channels will lower the overall fluidic resistance of the separator channel array, and thus improve the level of exchange.

4.1.6.1 Model

For this model the shallower channel model was used again, as in the separator channel length simulations. The overall length of the device was increased to 21.5mm, to allow room for more channels. The flow rate ratio used for these simulations was 0.01m/s through both inlets one and two. This was chosen as it gave a concentration result with sufficient room for

variation; i.e. the result was not too near 100%. The angled wall region of the model was shortened, or extended, to match the length of the array of separator channels. The number of channels was varied from 0 to 300 in steps of 50 channels, with additional simulations at 1, 10 and 25 channels. In line with the decision taken in the previous section, the separator channel length was 400 μ m.

4.1.6.2 Results and Discussion

The results of these simulations, shown in Figure 4-11, suggest that the number of channels does have an impact, but it is not hugely influential above 50 channels. This is demonstrated by the fact that the full range of the results between 50 and 300 is only slightly over 8%. However, the objective of these simulations is to achieve the best exchange possible, and therefore, 200 channels was chosen as this gave the optimal result. It is also worth noting that 200 channels will not take up too much space on a microfluidic chip, as the array will only be 12mm long (with 30 μ m separator channel widths). These results also show that below 50 channels the impact is significant as the exchange drops from 72% at 50 channels to 51% at 1 channel. This is almost equivalent to no exchange at all as 50% is no exchange given that the two phases enter the device at equal concentration.

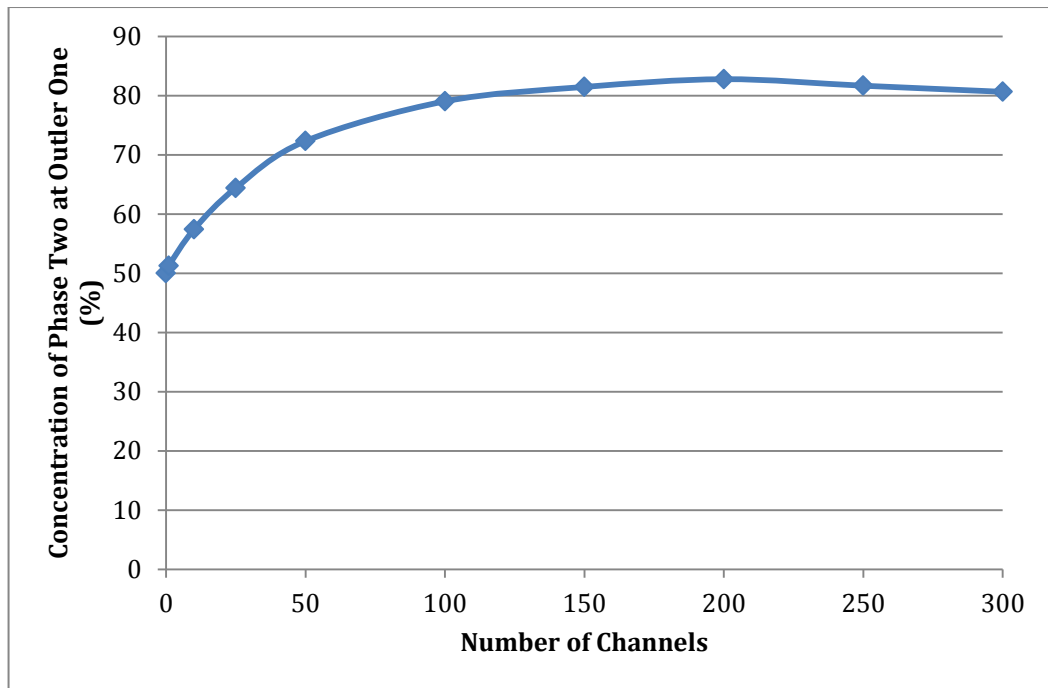


Figure 4-11: Impact of the number of channels on the concentration of phase two at outlet one showing that whilst the number of channels does have an impact it is only particularly significant below 50 separator channels with a range above this point of only approximately 8%. Below 50 channels the impact is significant. The optimum number of channels appears to be 200.

The slight decline in performance that is evident after 200 channels is likely a result of the average width of the channel on the outlet one side of the separator channels increasing. This increased width reduces the fluidic resistance of the channel therefore making the fluid less likely to go through the separator channels. It appears that beyond 200 channels the decrease in fluidic resistance causes a more significant performance reduction than the addition of extra channels causes an improvement in performance.

4.1.7 Exchanger Architecture

Simulations were also carried out to investigate a number of different adjustments to the shape of the exchanger to search for ways to further improve the level of exchange.

4.1.7.1 Model

The shallow exchanger model from section 4.1.4 was used as the base model for these simulations. The flow ratio used was 0.01m/s to 0.02m/s at inlets one and two respectively. The adjustments for each simulation are detailed in the results and discussion section.

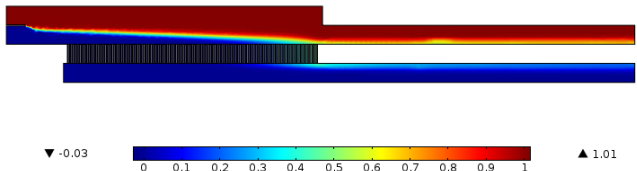
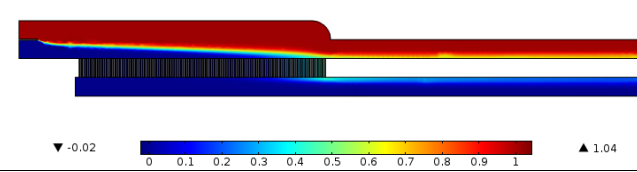
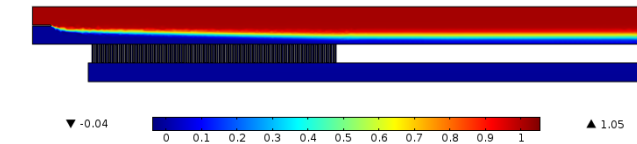
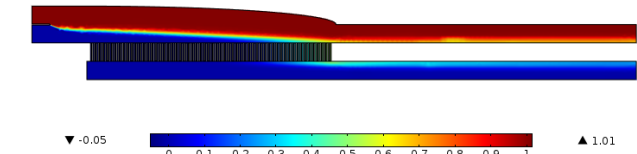
4.1.7.2 Results and Discussion

The results of the various simulations are shown in Table 4-6 along with images to give an idea of the changes to the exchanger shape. The models are:

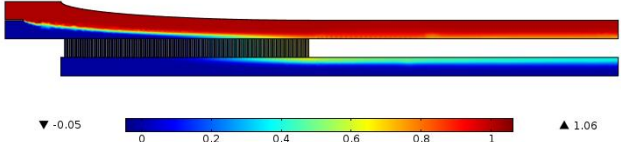
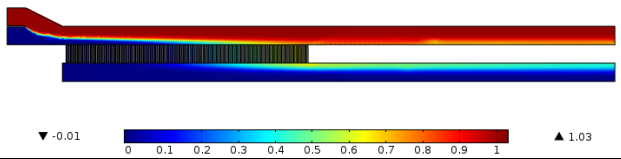
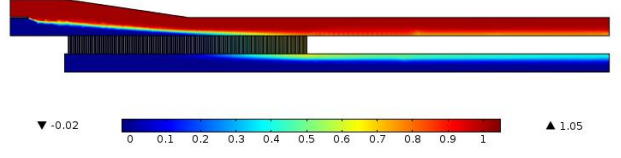
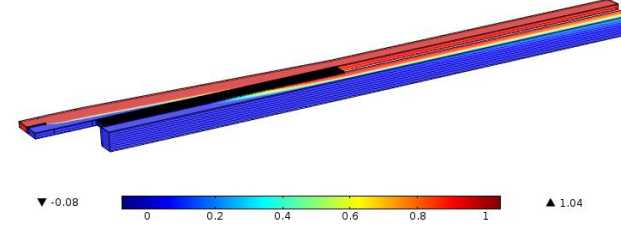
- a) Square channel: the narrowing region is replaced with a straight channel that narrows at 90° after the separator channels.
- b) Curved square channel: similar to the square channel simulation but the narrowing is slightly softened by using a curve. This is to remove the region where no flow was present. This was found in the corner of the square channel and could potentially act as a 'trap' for exchanged spheres.
- c) Wide: no narrowing occurs when the two phases are brought together.
- d) Positive ellipse: the narrowing region has an elliptical shape rather than the straight edge used previously

- e) Negative ellipse: the ellipse used in the narrowing region curves the other way.
- f) Pre-narrowed: the narrowing region occurs before the phases reach the separator channels.
- g) Shortened narrowing region: the narrowing occurs at a steeper angle and is completed in half the distance of the original model.
- h) Deeper outlet: the channel on the outlet two side of the separator channels is deeper. It is a 500 μ m square cross-section channel.

Table 4-6: Models used to investigate changing the exchanger architecture to improve the level of exchange. See above for a description of each model. The images show concentration plots, on an x-y plane taken at 50 μ m from the top of the outlet one channel, showing the concentration of phase two with 0 (blue) indicating phase one and 1 (red) indicating phase two.

	Model	Concentration of phase two (%)
a)		92.3%
b)		92.4%
c)		79.2%
d)		92.9%

4 Phase Exchanger Development

e)		93.5%
f)		93.1%
g)		93.8%
h)		99.3%

The results in Table 4-6 show that for the majority of the models tested, the impact is insignificant. The results for the concentration of phase two at outlet one are only marginally better, or worse, except for the wider channel model (c), which offers significantly worse exchange, and the deeper outlet model (h), which provides improved exchange. This deeper outlet model was further examined by varying the flow rate through inlet one from 0.01 m/s up to 0.1 m/s. This allowed for a more complete comparison with the original shallower exchanger. The results of this comparison are shown in Figure 4-12 showing that the deeper outlet exchanger can provide significant improvements for inlet two flow rates of 0.04 m/s and under.

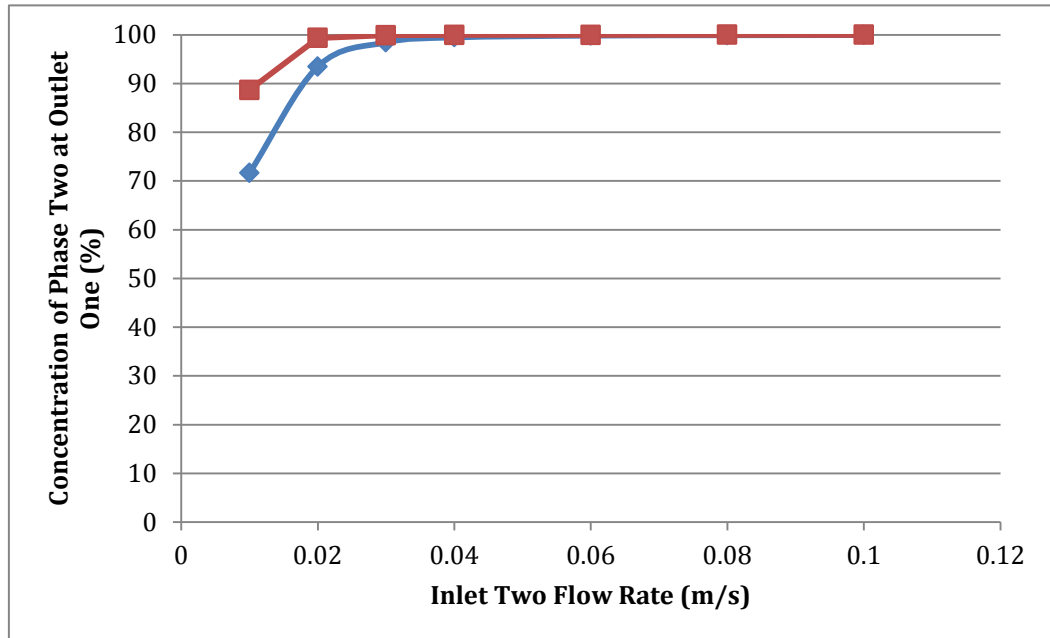


Figure 4-12: Comparison of the shallow exchanger (blue) and the deeper outlet exchanger (red) showing that the deeper outlet exchanger offers greater levels of exchange at lower flow rate differentials.

This improvement can be explained by considering the pressure drop along a channel and the fluidic resistance as given by equations 4-2 and 4-4 respectively. It is clear from the fluidic resistance equation that the channel resistance is proportional to the cross-sectional area of the channel. Therefore, by making the outlet two channel larger, the channel resistance is reduced, therefore, encouraging the liquid to go through the separator channels. To confirm this hypothesis, the pressure within the models was measured. A line was placed through the centres of the channels on either side of the separator channels and pressure data collected along this line, as shown in Figure 4-13. This data is presented in Figure 4-14.

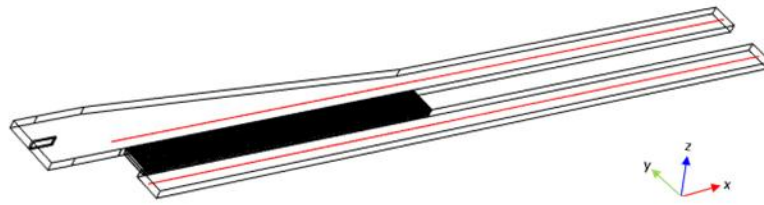


Figure 4-13: Diagram showing the lines along which pressure data was collected. Pressure data was recorded along the red lines, which were positioned in the centre of the channels in the z-direction and 250 μ m away from the separator channels in the y-direction. This was done for both the shallow exchanger and the deeper outlet exchanger at flow ratios of 0.01 m/s to 0.02 m/s.

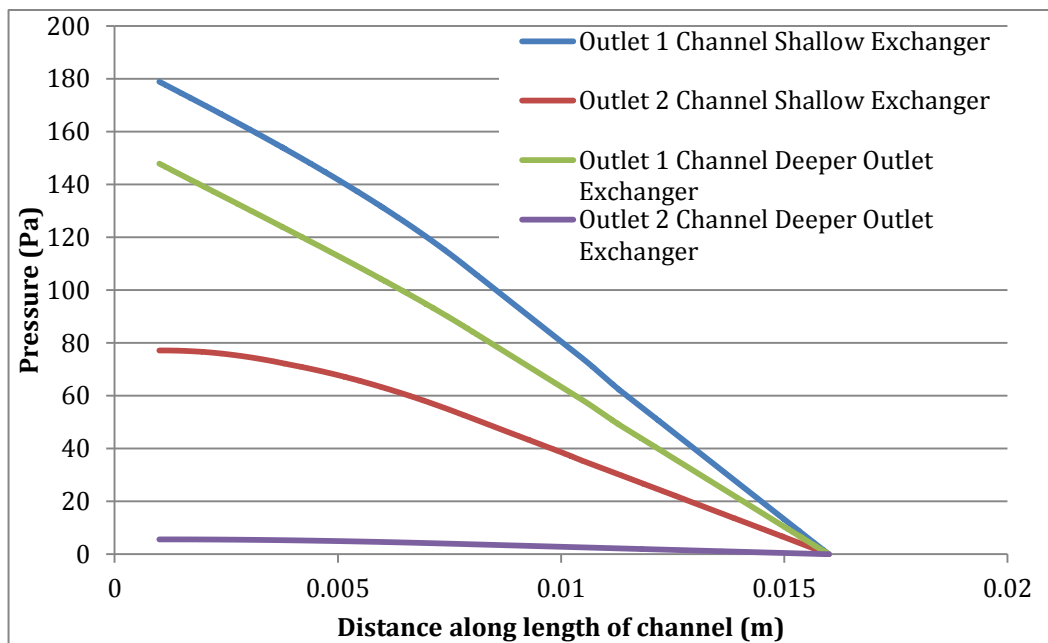


Figure 4-14: Pressure along the channels on both sides of the separator channels for the shallow exchanger and the deeper outlet exchanger showing the pressure drop between the two channels is greater with the deeper outlet exchanger than with the shallow exchanger.

The results in Figure 4-14 show that there is a much greater pressure drop between the two channels for the deeper outlet exchanger. This is consistent with the reasoning for the improved performance of the deeper outlet exchanger when compared with the shallow exchanger. It also explains the

poor result of the wide channel simulation (c) as the fluidic resistance will be less on the outlet one side of the separator channels.

The results of the deeper outlet exchanger simulations were further examined to try to understand how spheres passing the separator channels may behave. The work by Yamada and Seki examined spheres passing a series of perpendicular channels and found that the ratio of volumetric flow rates through a main channel and branch channels (equivalent of the separator channels used here) can be used to predict the size of spheres that will pass by an array of perpendicular branch channels without travelling down them [132]. They demonstrated that a sphere will not travel down a side channel unless the centre of the sphere is within a streamline that is going down said side channel. The ratio of flow rates is proportional to the partial area of the parabolic flow that will be directed through the main channel and the branch channels and thus determines which streamlines will continue onwards and which will travel down the side channels. As such it should be possible to find the distance (w_2) from the junction interface at which the crossover between streamlines proceeding onwards and going down the side channels occurs. This is illustrated in Figure 4-15.

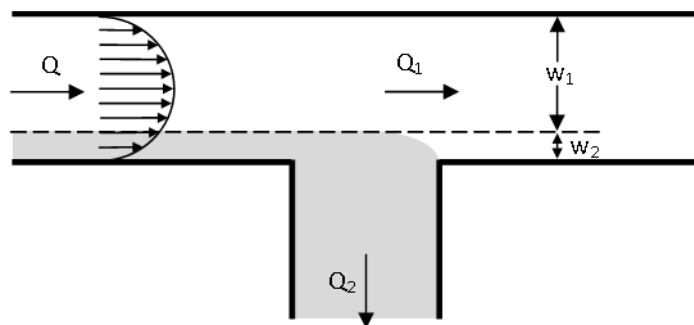


Figure 4-15: Illustration of the relationship between the flow rate ratios and minimum sphere size. Fluid entering at a volumetric flow rate, Q , will split at a ratio of $Q_1:Q_2$ between

the main channel and a perpendicular branch channel. This ratio can be used to determine the width of channel in which flow will travel down the branch channel (w_2) and the main channel (w_1)

The width of the channel that contains flow that will go down the branch channel, w_2 , allows the minimum sphere size to be calculated as, if the centre point of a sphere is farther from the wall than w_2 , then the sphere should proceed past the branch channel. Therefore as long as the sphere radius is larger than w_2 the spheres should stay in the main channel. This can be seen in Figure 4-16.

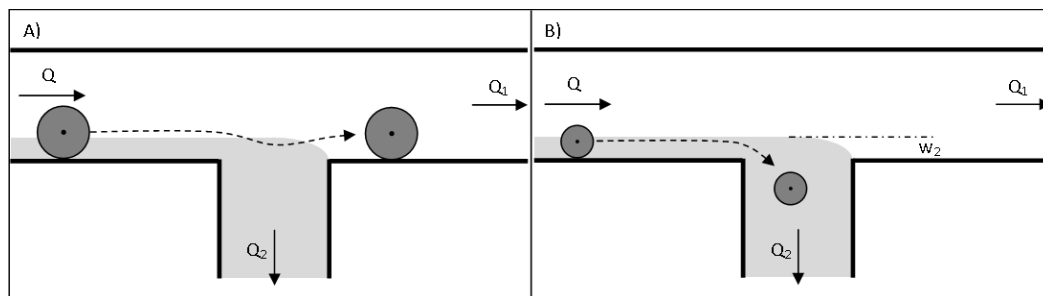


Figure 4-16: Spheres passing a perpendicular separator channel. Grey region indicates streamlines that will follow the separator channel. A) Sphere radius $> w_2$. The centre point of the sphere is outside the separator channel streamline so it passes by. B) Sphere radius $< w_2$. The centre point of the sphere is within the separator channel streamline so it goes down the perpendicular channel. In both cases, the separator channel is wider than the sphere diameter.

The flow rate ratios within the simulations were investigated through the use of parameterised surfaces to determine the speed of flow through and past a number of the separator channels. Surfaces were placed across the entire width immediately after a separator channel and also as a complete section of said separator channel (see Figure 4-17). This was done after the first channel and then at every 10 channels from 10 – 110 (the last channel

in the separator array). The average flow speed through these surfaces was then recorded.

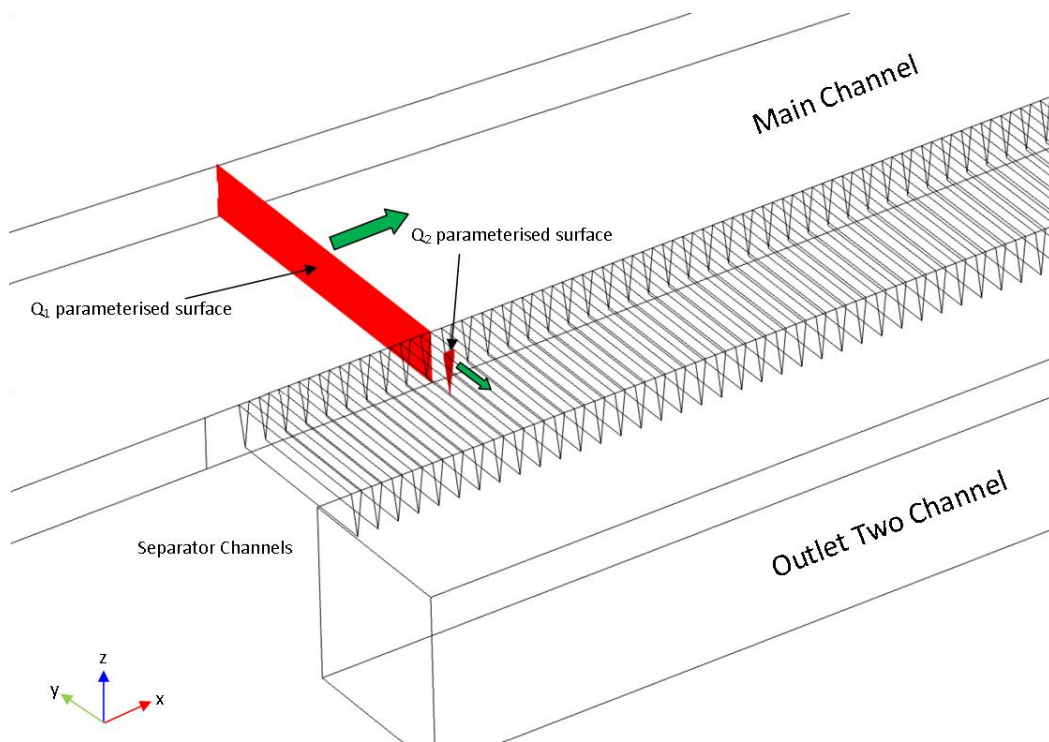


Figure 4-17: Positions of the parameterised surfaces that were used to investigate flow rate past and through the separator channels. In this case the 10th separator channel is being investigated. Surfaces are shown in red. The Q_1 surface is placed immediately after the channel and covers the complete cross section of the main channel; the average flow speed in the x-direction was taken. The Q_2 surface is placed within the 10th separator channel to create a full cross section of a single channel; the average flow speed in the y-direction is taken. These results are then used to determine the flow rate ratio between the main channel and the separator channel and therefore the minimum sphere size that can be expected to travel past the separator channel. Green arrows indicate the direction of flow.

The flow speed was converted to the volumetric flow rate and then the ratio of flows through the main and separator channels was determined. This could then be used to determine the minimum sphere diameter that can be expected to pass the separator array rather than go through it. The results of this analysis for the deeper outlet exchanger are shown in Figure 4-18. In

this case the inlet flow rate ratio was 1:3 (inlet one:inlet two) however it was found that the result remained the same for all flow rate ratios. This is consistent with the findings of Yamada and Seki as they report that the flow rate ratio between the investigated channels is proportional to the ratio of the channels hydrodynamic resistance, which is not dependent on flow rate [132]. The results of this simulation suggest that spheres with a diameter greater than $8.3\mu\text{m}$ should exit through outlet one after the exchange has occurred. This is an approximation as it does not take into account that the separator channels do not have a uniform width from top to bottom or that they do not reach the bottom of the channel. Spheres near the top of the main channel that are larger than $8.3\mu\text{m}$ may be encouraged to go down the separator channels as the separator channel is widest at the top, whereas at the bottom of the main channel there is no separator channels to go down so smaller spheres may travel past. Despite this the results should give a good indication of the sphere sizes that may be viable.

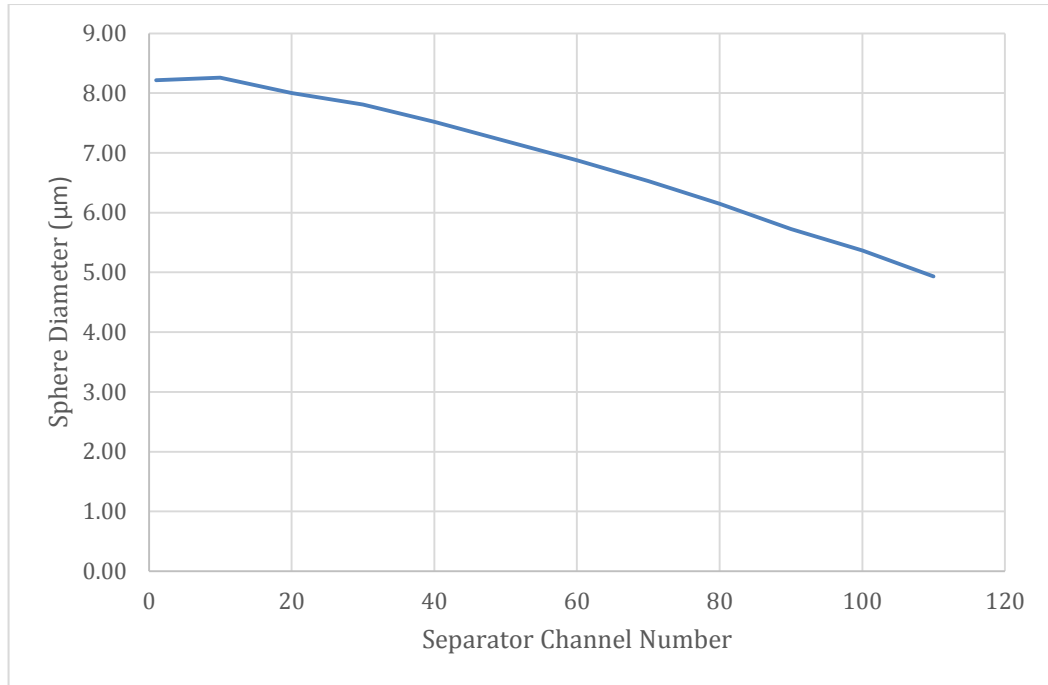


Figure 4-18: Minimum sphere diameter that will pass by a given separator channel based on the ratio of flow past and through said separator channel. Result shown is for the simulation of the deeper outlet exchanger run with a 1:3 inlet one to inlet two flow rate ratio.

The minimum sphere diameter that can be used with the medium exchanger is dependent on the geometries of the channels and it was found that there appeared to be an inverse relationship between the minimum size that can be used and the exchange performance of the device. This can be seen in Table 4-7.

Table 4-7: Comparison of exchanger performance in terms of level of exchange and minimum sphere size that can be used with the device. Data appears to show that there is an inverse relationship between the quality of exchange and the minimum sphere size that can be used.

Device	Exchange at 1:1 Inlet flow ratio (%)	Minimum sphere diameter (μm)
500 μm Square Channel (section 4.1.3)	51.4	2
Shallow Exchanger (Section 4.1.4)	71.6	5.9
Deeper Outlet Exchanger (Section 4.1.6)	88.7	8.3

It is important to note from Table 4-7 that the minimum sphere size for the shallower exchanger and deeper outlet exchanger are different. The separator channels and main flow channel have the same geometry in these two models meaning that the geometry of the outlet two channel is also important in determining the minimum sphere size. This makes the prediction of minimum sphere diameter a more complex problem than the device reported by Yamada *et al.* [134].

4.3 Testing the Exchanger

Having performed a number of simulations to develop a greater understanding of the exchanger, it was necessary to test the exchanger in the real world to confirm the validity of the simulations. In order to do this a method of quantitative analysis is needed.

4.3.1 Quantitative analysis using a spectrometer

By using a dye in one of the phases, it should be possible to analyse the percentage of the two phases by shining a light through the liquid and

analysing the spectral data. In this case, blue dye is used in one of the phases, and a red light emitting diode (LED) is used to shine a light through the liquid coming out of the exchanger. By measuring the absorption of the light it should be possible to quantify the amount of the blue phase passing by the spectrometer, and therefore, the quality of the exchange.

4.3.1.1 Method

For these tests it was decided that mineral oil (Sigma, Light Oil, bioreagent) would be used for both phases as it is a safe and readily available chemical. Although exchanging mineral oil for mineral oil is an unnecessary exchange here, it can be used as a way to analyse the exchanger without having to consider the interaction of the chemicals in the two phases. Additionally, the inclusion of an ingredient into one of the phases could make it a beneficial exchange for some applications. The mineral oil should behave in a similar manner to any two miscible liquids with similar contact angles. Clear mineral oil was used as phase one, whilst phase two was made up of Oil Blue N (Sigma, dye content 96%) and mineral oil (0.084g of Oil Blue N per 100ml of mineral oil). After mixing, the mineral oil was passed through a coffee filter (Sainsbury's, size 4) to remove any dye powder that had not been dissolved; this was to prevent blockages occurring in the separator channels. A spectrometer manifold was created to hold the spectrometer scope and the microfluidic tube in close proximity. This manifold is shown in Figure 4-19.

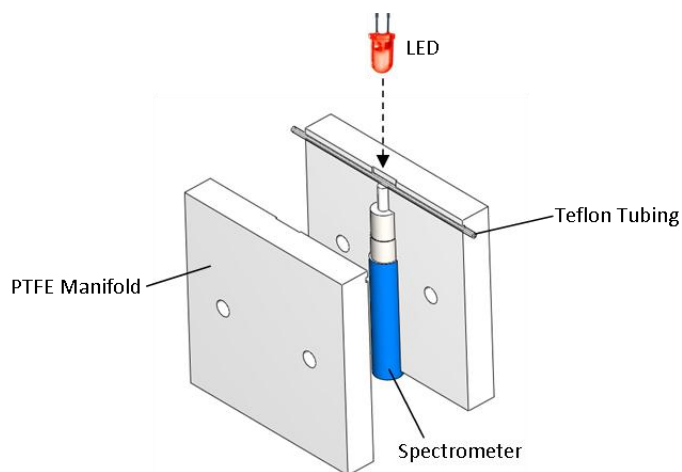


Figure 4-19: Spectrometer manifold. Bolts are placed through the holes in the manifold, and fixed in position using nuts, to bring the two sides together thus holding the spectrometer and tubing in place. An LED shine light into the manifold and through the tubing, as indicated by a dashed arrow.

This manifold was then placed in a rig that held a red LED at a fixed distance from the manifold. The LED was connected to a $150\ \Omega$ resistor and a 5V DC power supply. Initial tests were carried out using a Y-junction to mix the two phases prior to the spectral analysis; the ratio of the two phases was controlled via the flow rates of the two branches of the Y-junction. These flow rates were controlled using two syringe pumps (World precision instrument, AL-1000). The spectral data was analysed using an Ocean Optics spectrometer (Maya 2000Pro). Strip chart analysis was performed; this records the intensity over time at one specific wavelength (662.11nm). This wavelength was selected from a list of possible strip chart analysis wavelengths as specified by the SpectraSuite software. This wavelength was chosen as it was the wavelength closest to the peak wavelength emitted from the LED.

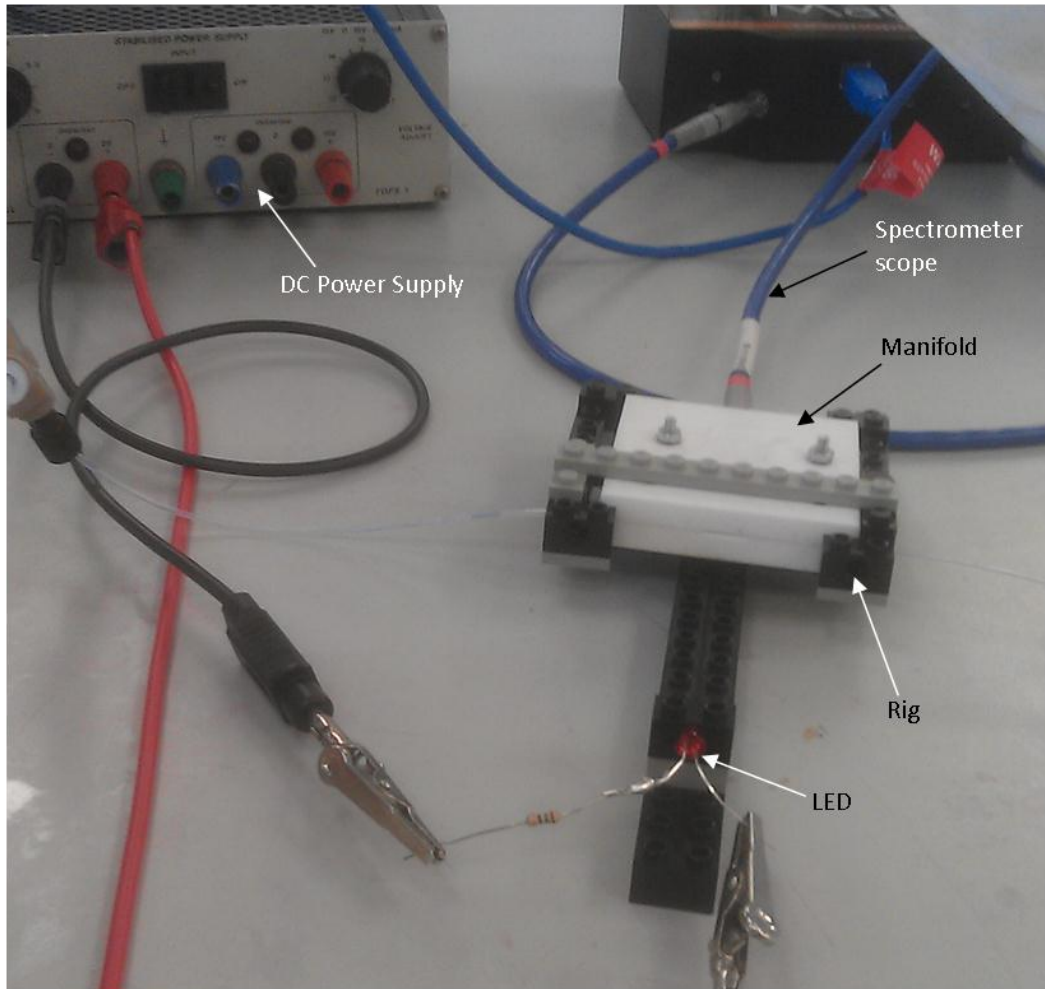


Figure 4-20: Initial spectrometer measurement system. Fluid is carried through the manifold via Teflon® tubing (I.D 500 μ m). The manifold and rig ensure that the tubing, spectrometer scope and light source are always in the same position relative to each other. A red LED powered by a 5V DC power supply is positioned such that the light emitted from it will pass through the fluid and tubing before being analysed by the spectrometer.

4.3.1.2 Results and Discussion

Initial tests were carried out to evaluate the spectral analysis concept. The results of these tests are shown in Figure 4-21. It is clear from this strip chart that there are distinct levels of intensity that correlate to the different concentrations of phase two. Each step of 10%, from 0% to 100% and back, is identifiable and distinct from the previous step. The brief drop at around

the 2500s mark is a result of an obstruction passing in between the light and the scope. The intensity is a count of photons the spectrometer has detected within the integration time. The integration time is analogous to the shutter speed in a camera, as it refers to the time over which the sensor absorbs light.

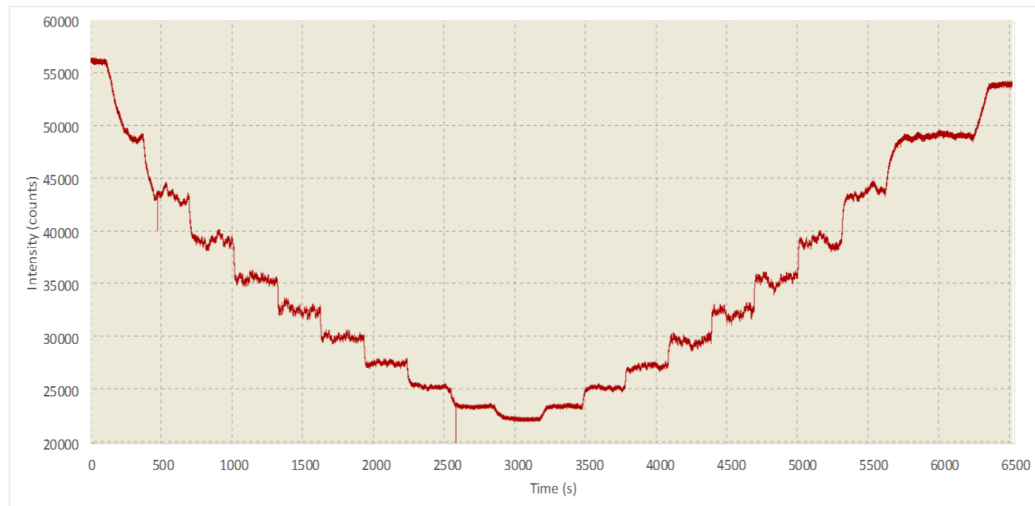


Figure 4-21: Strip chart at 662.11nm recording the intensity of the light that was transmitted through the liquid. The phases were mixed in steps from 0% phase two up to 100% phase two and then back to 0% in steps of 10%. The ratios were held at each step for 5 minutes each step of concentration can be clearly defined in this strip chart. There is dip slightly after 2500s, this was caused by an obstruction passing between the light source and the spectrometer.

This result shows that spectral analysis is a viable technique. However, there appears to be some variation in the intensity at each step, particularly when the ratio of the two phases are more even. The cause of this variation could be due to a number of reasons. The first possible cause of the interference investigated, was environmental light interference. This was done by operating the system with a 50% concentration (both phases at

0.05 ml/min) for 10 minutes in regular laboratory conditions, and then a further 10 minutes in complete darkness apart from the LED.

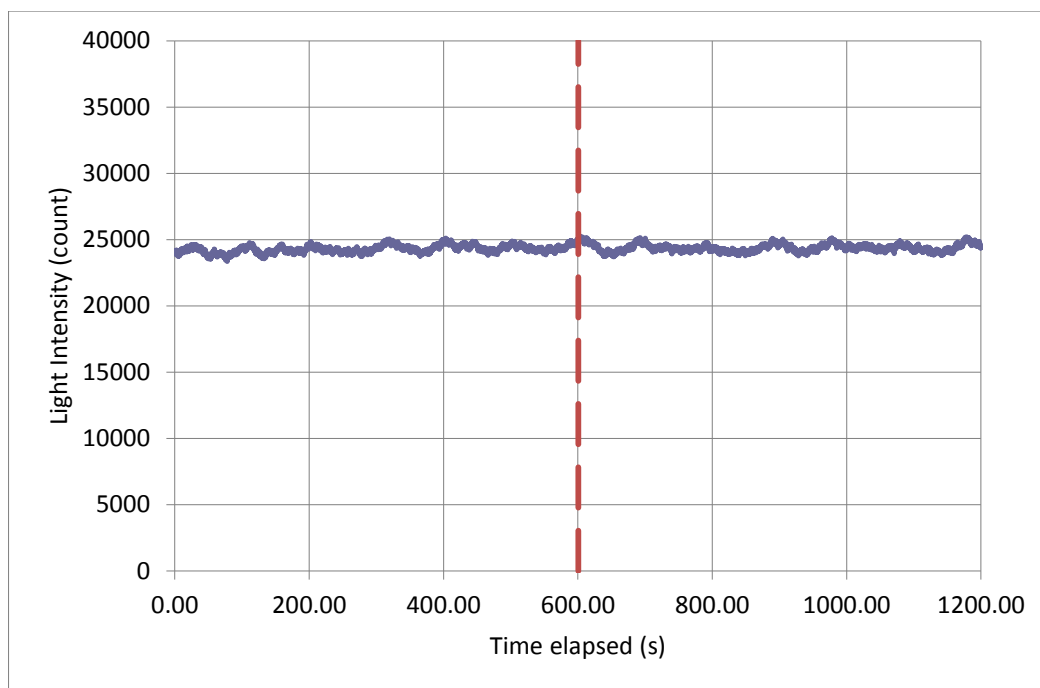


Figure 4-22: Measured light intensity during the light interference test. The dashed line indicates the point at which the environmental light was switched off. Data to the right of the dashed light was collected in darkness apart from the LED.

The data in Figure 4-22 suggests that background light has little impact on the results obtained with the spectrometer. Further evidence of this can be found by analysing the data collected before and after the environmental light was switched off. By performing a two tailed, two sample T-test on these two sets of data it was shown that the difference between the two was insignificant ($p < 0.001$). The conclusion can, therefore, be drawn that the variation found in Figure 4-21 is not a result of interference from the light in the laboratory.

Further tests were carried out to investigate whether the LED itself was the cause of the variation. To this end, the Teflon tubing was removed and the

light from the LED was measured for 10 minutes without passing through anything. The standard deviation of the LED measurement equates to approximately 0.8% suggesting that some of the variation is due to the LED and or power supply. The variation cannot be entirely due to the LED though as the variation seems to increase when the concentration level is around 50%. This suggests that some of the variation is due to the mixing of the liquids. It could be possible that the two phases are not completely mixed by the time of measurement and that some parallel flow of the phases is occurring. If the two phases are flowing side-by-side, in parallel, it could explain some variation as a result. The flow pattern, twisting slightly and absorbing more or less of the LED light output will alter the measured intensity depending exactly on how it has twisted as it passes the spectrometer. This is a problem that is unlikely to transfer to the use of the full exchanger as the phases will have travelled farther, and also will have traversed obstacles such as the 90° turn at the outlet, which will likely induce a greater amount of mixing of the two phases. A final test was carried out without the LED light source to ensure that there is no inherent variation in the spectrometer itself. Running the spectrometer with no light source pointed at it yielded a very slight variation with a standard deviation of 0.3%. A way to reduce this interference, and also the other causes of variation, is to introduce an element of averaging. Using the software it is possible to average a number of scans into one data point, therefore reducing the interference.

4.3.2 Spectrometer Calibration

Once it was established that a spectrometer could be used to determine the concentration of phase two it was necessary to run calibration experiments to quantify what intensity equates to what concentration of phase two.

4.3.2.1 Method

Pre-mixed concentrations were created in steps of 10% from 0-100% using syringes to mix up 10ml of oil to the desired concentration. Prior to mixing the extinction coefficient of the dyed mineral oil was measured using a spectrophotometer (6405 UV/Vis, Jenway). The mixtures were mixed on a Maxi-mix platform (Type 65800) for one and a half hours at a speed of 600. The mixtures were then pumped through Teflon tubing and past the measurement system and data recorded for 2 minutes. Using the Ocean Optics SpectraSuite software certain parameters were set for this and all future experiments. The number of scans to average was set to 15 and the boxcar width was set to 7. The boxcar width is another type of averaging. While the 'scans to average' setting determines how many spectral acquisitions will be collected before an average is taken, the boxcar width sets the area on the sensor over which an average will be taken. Increasing these numbers can result in a smoother plot. Before calibration, and all future experiments, clear mineral oil was passed through the system and the integration time was adjusted to set the 100% phase two point at 60000 counts. Adjusting the integration time prior to taking measurements compensates for any slight variation in the power of the light emitted from the LED, from experiment to experiment. The calibration test was

performed three times and an average taken. A housing was added around the LED to prevent any unwanted obstruction entering the path between the LED and the spectrometer scope. For this, and all future exchanger tests, phase one was the blue mineral oil, and phase two was clear mineral oil, unless otherwise stated. The blue mineral oil was mixed as in previous sections.

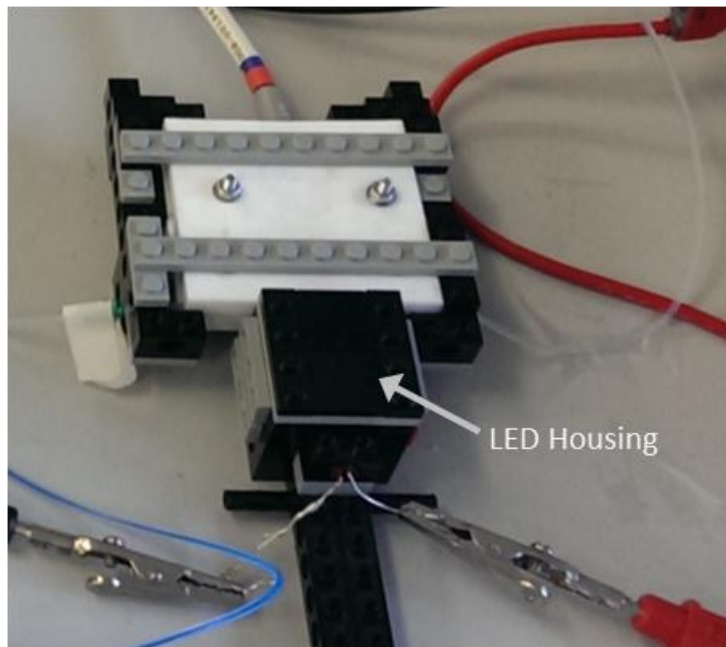


Figure 4-23: Spectrometer rig with LED housing. Setup is similar to that shown in Figure 4-20 but an LED housing has been added whilst the LED has been moved closer to the point of measurement. The housing was used to prevent any unwanted obstructions coming between the light source and the spectrometer scope.

4.3.2.2 Results and Discussion

The concentration, C_{one} , of phase one exiting the medium exchanger (as a percentage) can be calculated using the Beer-Lambert law, which can be stated as [189]:

$$A_l = \epsilon C_{one} l \quad (4-6)$$

Where A_l is the light absorption by the medium, l is the path length and ϵ is the extinction coefficient. The extinction coefficient is a constant for a given substance that defines how strongly it absorbs light. It was measured to be $15.75\text{mol}^{-1}\text{m}^{-1}$ and the path length was the tubing diameter, 0.5mm. Using this information it was possible to determine the concentration of phase two from the intensity of light that has travelled through the tubing and the oil. In order to convert the measured intensity into absorption the following equations must be used:

$$A_l = -\log T \quad (4-7)$$

where A_l is the light absorption and T is the light transmittance, given by Beer's law which, in turn states:

$$T = \frac{I}{I_0} \quad (4-8)$$

where I is the intensity of light recorded by the scope and I_0 is the intensity of light when no absorption occurs [190]. This should provide a linear relationship between absorption and concentration. In reality, linearity tends to be lost at high absorption levels [191]. However, it was found that the data used in these experiments was within this linear range. The measured intensity of light passing through the oil for each pre-mixed concentration of phase one was converted to a concentration using equation 6-6, the results of this can be seen in Figure 4-24. A trend line was added with a 0 intercept and has an R^2 value which is very close to one, indicating that the trend line is a fair representation of the data. If this technique for determining concentration is accurate the gradient of the curve should be one, as the x and y quantities should be equal, the graph equation shows that this is the case (to three decimal places).

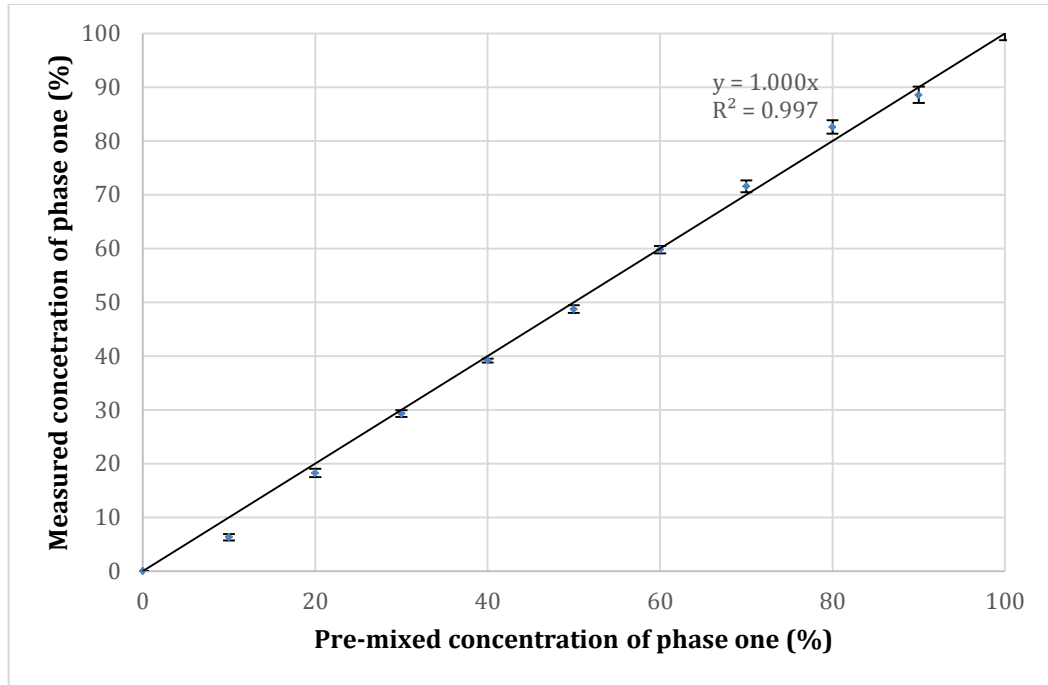


Figure 4-24: Confirmation that this technique is valid. Pre-mixed concentrations of phase one are measured and plotted against the specified levels. The gradient of 1 suggests the technique is accurate. Data is taken from the average of the three calibration tests. Error bars represent 95% confidence level. Linear trend line added.

The concentration percentage of phase two, c_{two} , can be calculated by simply subtracting the concentration of phase one from one hundred:

$$c_{two} = 100 - \frac{A_I}{\varepsilon l} \quad (4-9)$$

4.3.3 500 μ m Square Cross-section Exchanger

4.3.3.1 Method

The first exchanger that was tested with the spectrometer had a channel cross-section of 500 μ m square; the same as in the 'Pressure Problem' simulations. Due to a malfunction with the Cardiff University femtosecond laser, an alternative laser had to be used to ablate the separator channels. A SPIRIT 1040nm femtosecond laser was used at Laser Micromachining

Limited. This laser was operated at 0.4W average power at 20 kHz. To ablate 200 30 μ m wide, 100 μ m deep channels the laser was operated using the following parameters:

Table 4-8: Laser ablation parameters used to create 30 μ m channels with a SPIRIT 1040nm femtosecond laser.

Parameter Type	Value
No. of Loops	150
Machining Speed	50 mm/s
Power Usage	100%
Wobble	Yes, 10 μ m, 197Hz

The No. of loops refers to the number of times that the laser focal point ablated the same path. The remaining channels were milled using the same techniques detailed previously in section 3.10. The two phases were as used in the previous section with phase one as the dyed mineral oil, and phase two as the clear mineral oil. The phases were supplied to the exchanger by two syringe pumps used to power two glass syringes (20ml syringes). The flow rate for phase one was maintained at 1.8ml/hr, which equates to 2 mm/s. The flow rate of phase two was varied as a ratio of the phase one flow rate, up to a 10:1 ratio. The DC power supply was set at 4.5V. The experiment was carried out three times and an intensity reading was taken. The average of the three results was applied to equation 4-9 to determine the concentration of phase two. The integration time for the three experiments was 36.9ms, 37ms and 37.3ms ensuring 100% phase two equalled 60000 counts. To ensure consistency the tubing length was maintained between experiments and the spectrometer was kept at the same distance from the exchanger outlet. As with the calibration test the

data was collected for 2 minutes at each flow rate. Data collection was started once the data appeared to be levelling out; this was to remove the transition time from the data sets.

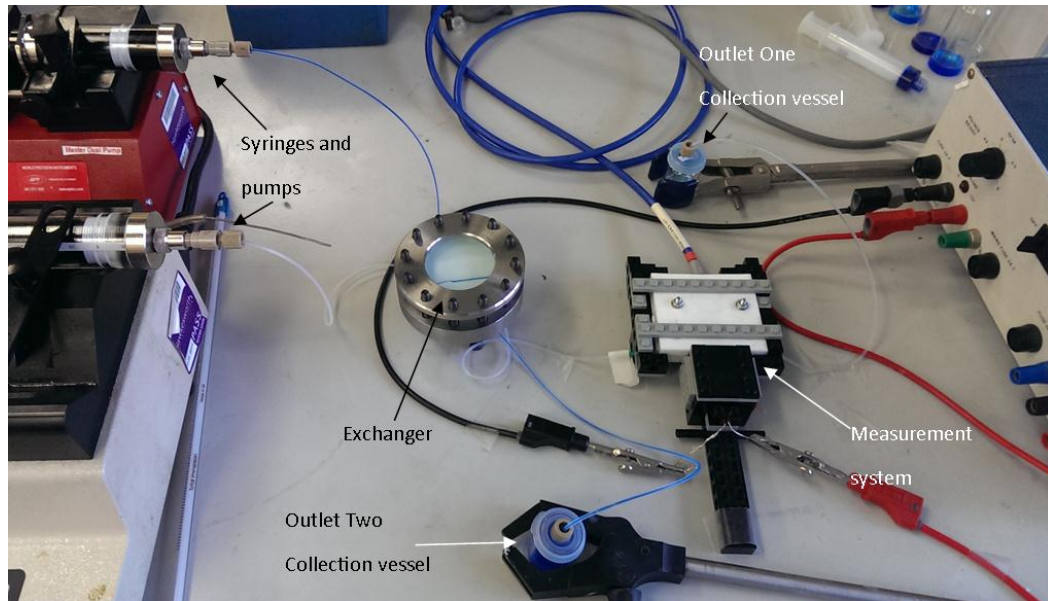


Figure 4-25: Experimental setup used to test the exchanger. Two phases are supplied to the exchanger via glass syringes driven by pumps. It is clear from this image that one phase is blue (the primary phase) and one is clear (the secondary phase). Phase one is extracted by the exchanger and exits via outlet two and is collected in the outlet two collection vessel. Non-extracted fluids exit through outlet one and pass through the spectrometer measurement system before being collected in the outlet one collection vessel.

4.3.3.2 Results and Discussion

The results shown in Figure 4-26 show that a reasonably high level of exchange can be achieved using this exchanger. The results also appear to be somewhat consistent with the simulation results shown in Figure 4-5 in that there are diminishing returns in the improvement to the exchange level that is gained from each increase in phase two flow rate. This is shown by the similarly flattening curve of the results for both this experiment and the simulations.

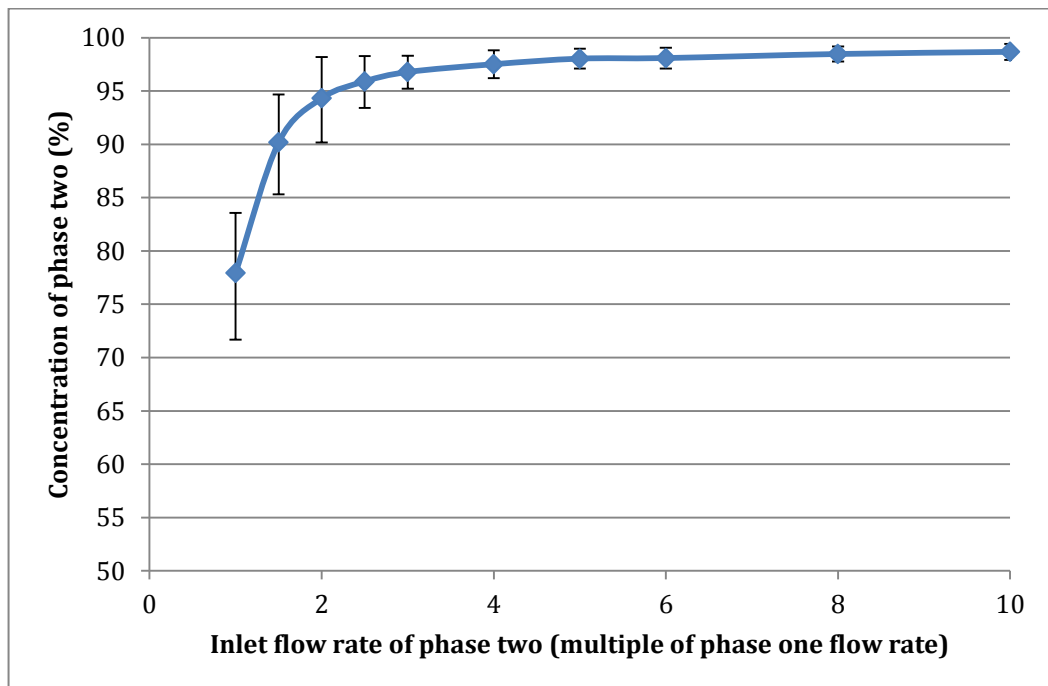


Figure 4-26: Experimental results showing the concentration of phase two as the phase two flow rate is increased by multiples of phase one (1.8ml/hr) (as measured by the spectrometer). Showing that the exchange improves as the phase two flow rate increases but there are diminishing returns in terms of the exchange performance gained as the flow rate increases. Error bars indicate the 95% confidence level.

The slightly better results obtained here are explained by the use of a different material and also the different lengths of the outlets. The scale of the error bars at the lower concentration values shows that the problem

during calibration tests of variation found when the concentration of phase two is closer to 50% is still an issue. However, the error bars are not so large as to discount the value of these results.

It is worth checking the value actually provided by the exchanger architecture in these results, by comparing the outlet concentration to the inlet concentration. If we take the inlet concentration as the ratio of the two flows it is possible to determine the improvement gained by using the exchanger. This is shown in Figure 4-27.

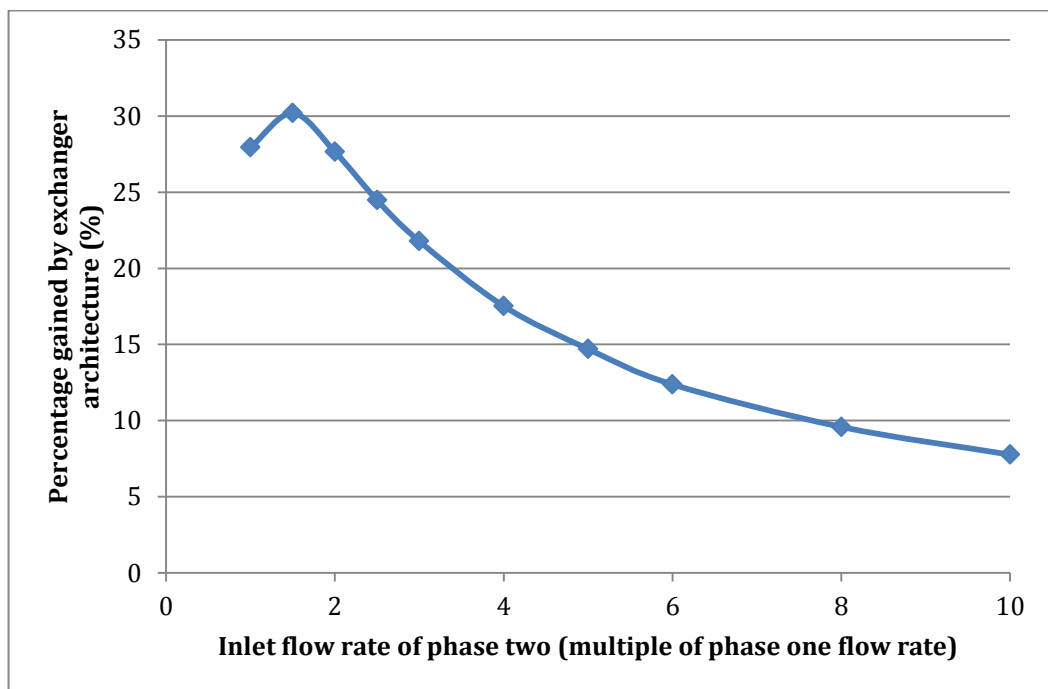


Figure 4-27: Performance gained by the exchanger architecture as phase two flow rate is increased. Performance gained determined by comparing the relative percentages of the two phases at the inlets to the percentages at outlet one. Significant exchange can be attributed to the exchanger architecture although diminishing returns are observed as the exchange approaches 100%. The initial increase suggests that mismatched flow is a factor in 'driving' the exchange.

It is clear from this graph that value in terms of performance gained diminishes as the ratio between flow rates increases. This is a result of the

exchanger approaching its maximum possible performance level. It is also worth noting that the performance gain from the exchanger initially increases, which provides more evidence of the value of mismatched flow rates as a technique to 'drive' the exchange. This initial improvement is consistent with the simulation data shown in Table 4-4.

4.3.4 150 μ m x 500 μ m Cross-section Channels

The next experiments were performed on the shallower exchanger, as simulated in section 4.1.4.

4.3.4.1 Method

The chip manufacture process was the same as detailed in the previous section. Two flow rate profiles were used; firstly the experiment was run with phase one set to 1.8 ml/hr as in the previous experiment. However, this equates to an inlet speed of 6.67 mm/s. This is over three times faster than the speed used with the 500 μ m square cross-section device therefore the experiment was also carried out with a phase one flow rate of 0.54 ml/hr, which was equal flow speed used previously, 2 mm/s. In both cases, the phase two flow-rate was increased in multiples of the phase one flow-rate up to 10x. For the faster flow measurements the integration times were 36.85 ms, 37.35 ms and 37.2 ms.

4 Phase Exchanger Development

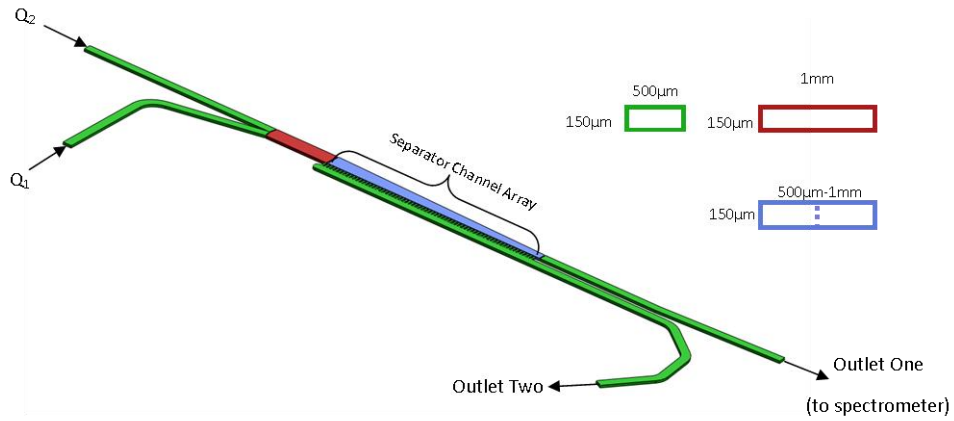


Figure 4-28: Channel cross-sectional dimensions of shallow channel exchanger. Inlets and Outlets (green), two phase flow region (red) and transition region (blue) all created through milling. Transition region narrows from 1mm – 500µm. Separator channel array created via femtosecond laser ablation, the separator channels had a triangular profile and were 30µm wide and 100µm deep. Black arrows indicate the direction of flow. Phase one was supplied through inlet one at a constant flow rate, Q_1 , whilst the phase two flow rate, Q_2 , was varied in multiples of Q_1 . Both phases delivered via syringe pumps.

4.3.4.2 Results and Discussion

Figure 4-29 shows the results of the experiment performed with a faster flow speed. It shows that an almost complete exchange can be achieved (99.8% at a 10:1 ratio) with this exchanger. The error bars for these results are quite large. This could be evidence for the theory of the cause of the variation that was postulated during the calibration tests. That the variation is partly due to parallel flow profile ‘wobbling’ as it passes the spectrometer. At these higher flow speeds there is less opportunity for diffusive mixing of the two phases after it has passed the exchanger, meaning that the two phases are more likely to remain as two streams running in parallel, as opposed to one mixed stream. If the divide between these two streams was not perpendicular to the scope, it could potentially let more or less light

through, than would be absorbed by the actual concentration level passing the sensor.

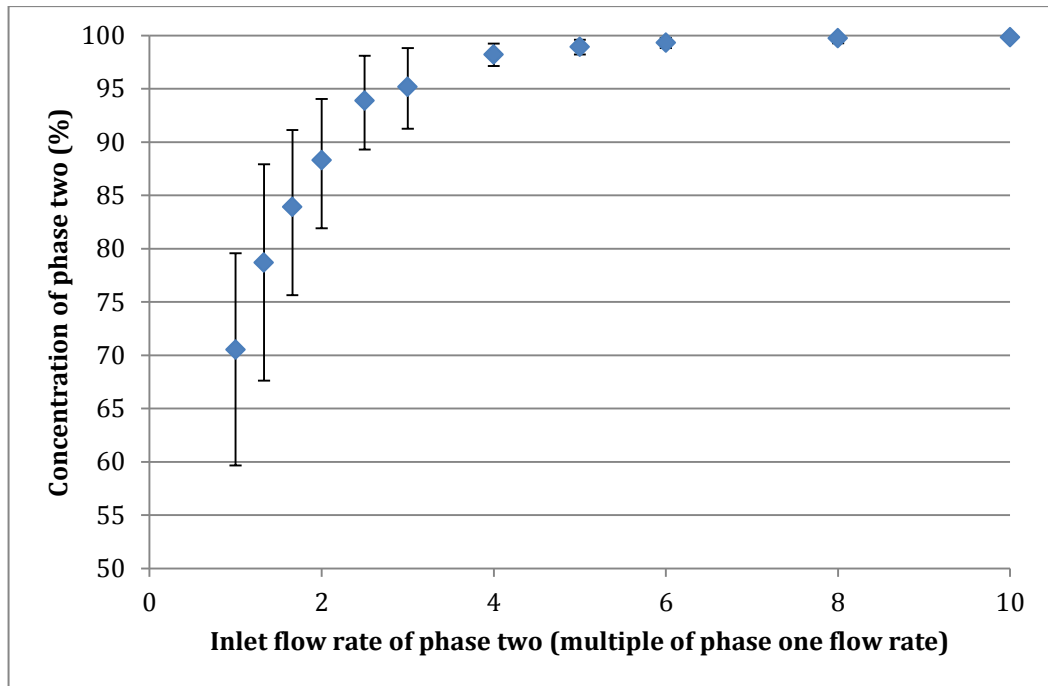


Figure 4-29: Experimental result of 150 μ m deep channels with inlet one flow rate of 1.8 ml/hr. Almost complete exchange (99.8%) can be achieved at a 10:1 inlet flow rate ratio (inlet two:inlet one), which is a slight improvement on the maximum level achieved using the 500 μ m square cross section channel (98.6%). Error bars indicate 95% confidence level.

Figure 4-30 shows that the slower flow rate provides significantly better exchange at lower flow mismatch ratios, than the faster flow rate. This means there is a balance that needs to be struck between throughput and quality of exchange. The relative quality of the exchanges is clearer in Figure 4-31.

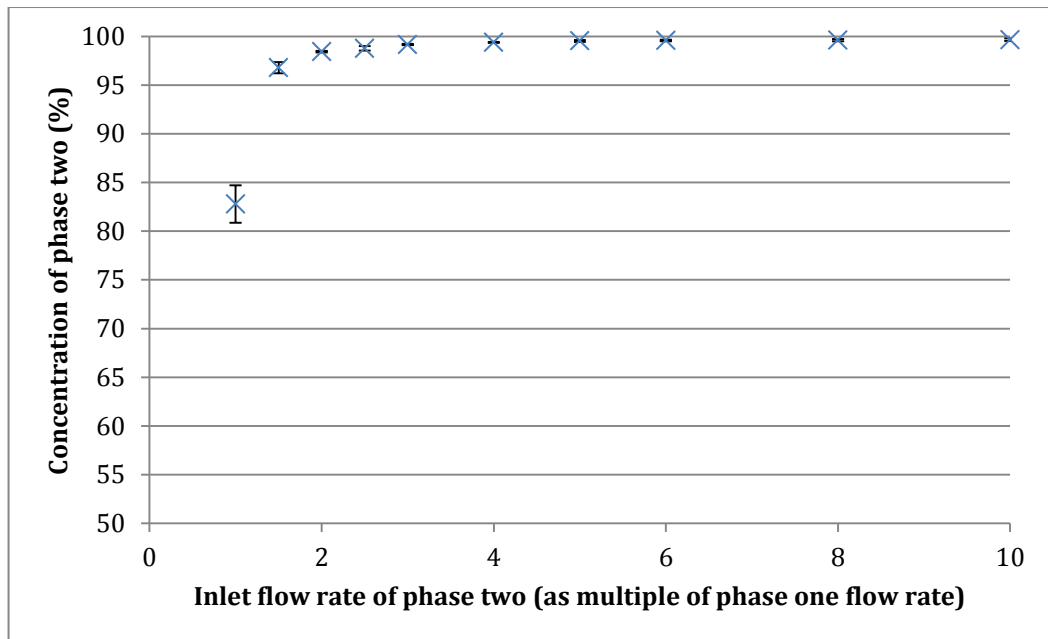


Figure 4-30: Concentration of phase two measured experimentally plotted against inlet flow rate ratio using the shallower exchanger with 150 μ m deep channels. An inlet one flow rate of 0.54 ml/hr was used. These results show significantly improved exchange at lower flow rate mismatch ratios than when the shallower exchanger was operated with an inlet one flow rate of 1.8ml/hr. Error bars indicate 95% confidence level.

Figure 4-31 illustrates the improved results achieved with the shallower exchanger. Even though the shallow exchanger with the faster flow regime, offers worse exchange at lower flow ratios, it is still capable of a greater maximum exchange level (99.8%) than the 500 μ m square channel device (98.6%). This improved performance with a shallower exchanger is consistent with the simulation results gained previously.

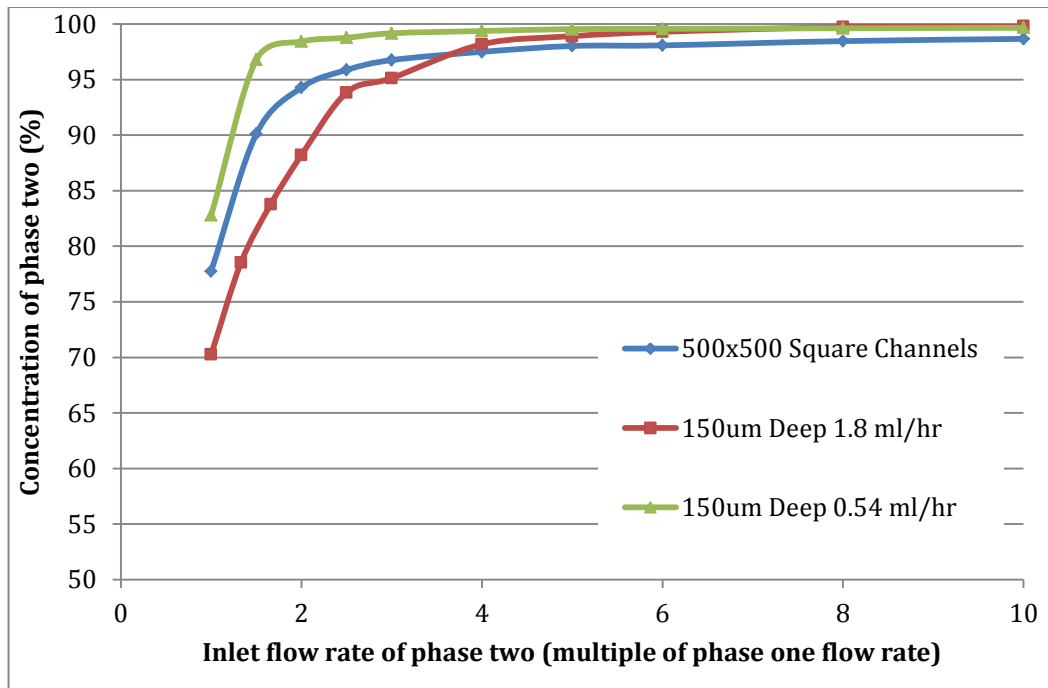


Figure 4-31: Comparative plot of the experimental results of all three experiments; the 500 μm square cross-section channels and the fast and slow shallower exchanger tests. This highlights the improved performance of the shallower exchanger relative to the 500 μm square cross-section exchanger. Although the faster flow rate test of the shallower exchanger initially offers slightly reduced performance, the maximum achievable exchange is still greater. Error bars left off for clarity.

4.3.5 Deeper Outlet

Having established that the shallower exchanger provides a more complete exchange, much as it did in simulations, the next step was to test the deeper outlet exchanger that was simulated in section 4.1.7.

4.3.5.1 Method

The chip was manufactured using previously described techniques with inlet channel cross-sections of 150 μm x 500 μm as in the previous section. The only difference between this exchanger and the shallower exchanger

created in the previous section was that the outlet two channel had 500 μm square cross-section.

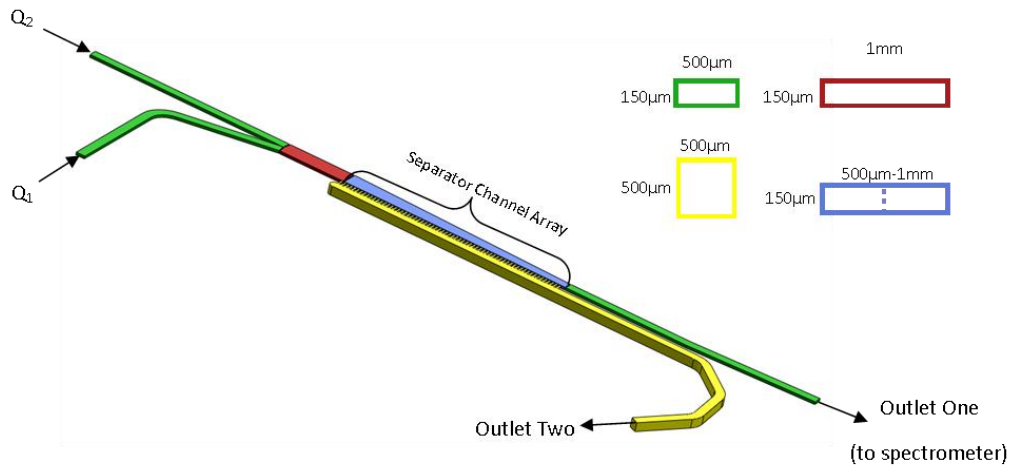


Figure 4-32: Channel cross-sectional dimensions of deeper outlet exchanger. Inlets and outlet one (green), outlet two (yellow) two phase flow region (red) and transition region (blue) all created through milling. Transition region narrows from 1mm - 500 μm . Separator channel array created via femtosecond laser ablation, the separator channels had a triangular profile and were 30 μm wide and 100 μm deep. Black arrows indicate the direction of flow. Phase one was supplied through inlet one at a constant flow rate, Q_1 , whilst the phase two flow rate, Q_2 , was varied in multiples of Q_1 . Both phases delivered via syringe pumps.

The inlet one flow rate was held at 0.54 ml/hr whilst the inlet two flow rate was increased in multiples of the inlet one flow rate as the experiment progressed. The integration times used for these experiments were 38ms, 38ms and 36.9ms.

4.3.5.2 Results and Discussion

The results shown in Figure 4-33 suggest that a high level of exchange can be achieved at a low flow mismatch ratio. However, it should be noted that these results do not appear to be significantly better than the results

obtained using just the shallow exchanger. This is illustrated in Figure 4-34, which shows only a marginal performance improvement from the deeper outlet exchanger.

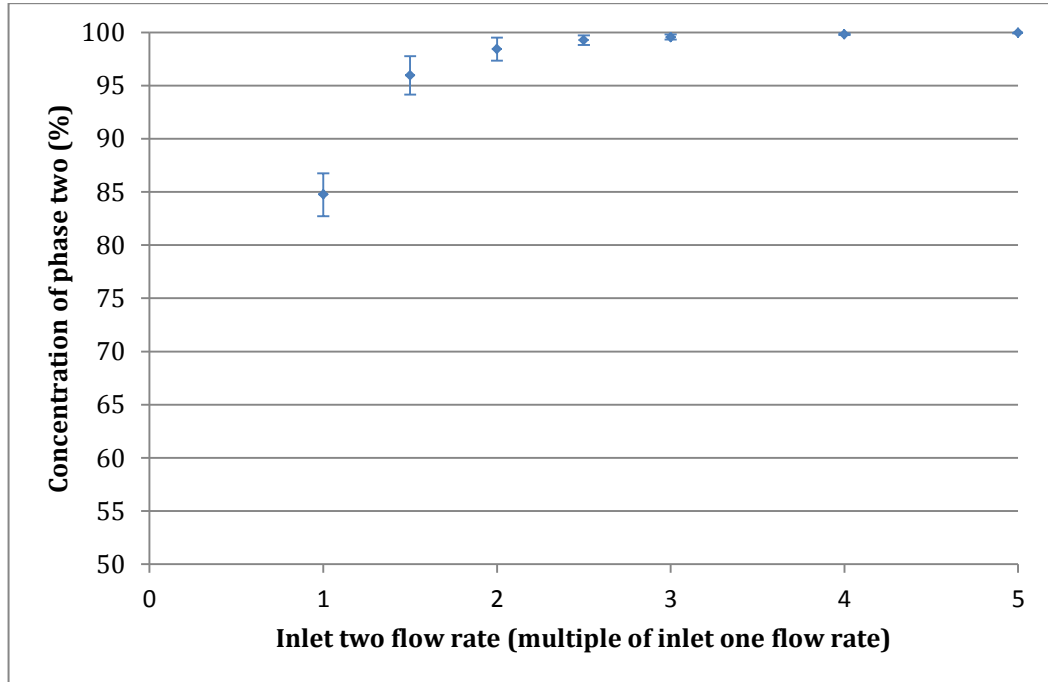


Figure 4-33: Experimental results obtained using the exchanger with the deeper secondary outlet. Plotting the measured concentration of phase two against the inlet flow rate ratio. A 100% exchange is achieved at a flow rate ratio of 5:1 (inlet two:inlet one)

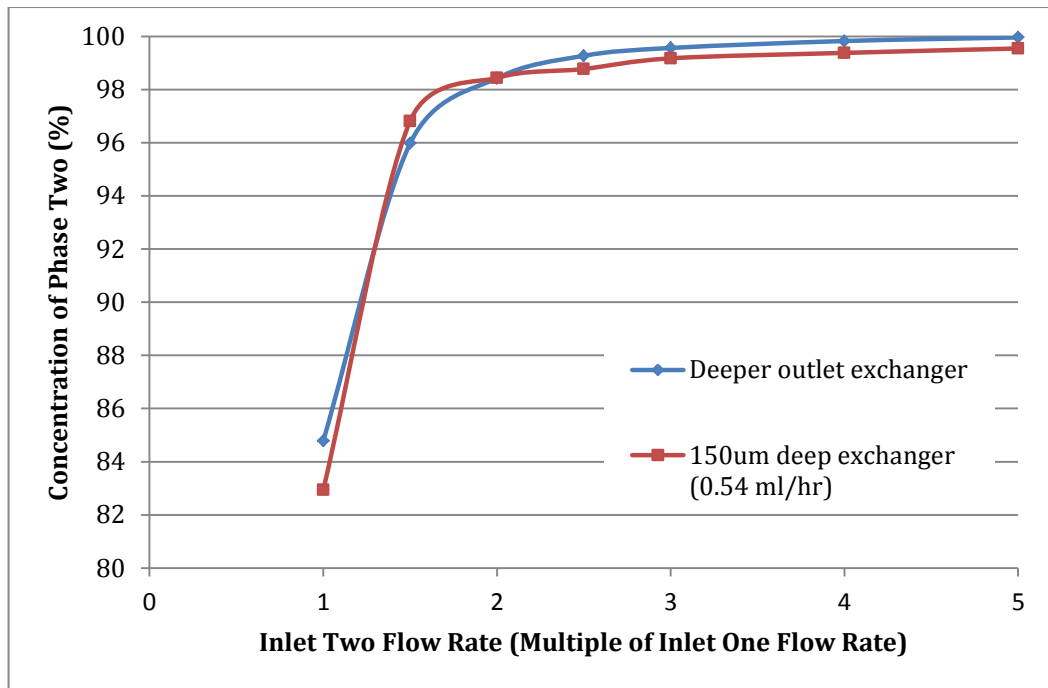


Figure 4-34: Comparison of the results of the deeper outlet exchanger and the 150 μ m deep exchanger. The two results are relatively similar with only a slight performance improvement achieved with the deeper outlet exchanger.

An additional test to investigate the usable flow rates with this exchanger presented some data to dispute the conclusion that the deeper outlet exchanger is no better than the shallower exchanger. In this experiment the ratio of the inlet one and inlet two flow rates was maintained at 1:1 as the flow rates was increased from 0.54 ml/hr to 5.4 ml/hr (an average flow speed of 2 mm/s up to 20 mm/s). The results obtained in this experiment, shown in Figure 4-35, represented a minimum exchange of 99.98%. This is significantly better than the results obtained in the previous tests of the deeper outlet exchanger. There was no obvious reason to explain this improved performance. One possible reason for the improvement could be a slight blockage of the tubing from outlet one which would increase the fluidic resistance differential between outlets one and two, encouraging a

greater exchange. It was also noted that the room temperature, as recorded with a glass mercury thermometer, was 2°C lower than the average room temperature during the initial testing of the deeper outlet exchanger. Temperature being the cause, would be counter intuitive as a temperature increase should lower the viscosity of the liquid and therefore, from equation 4-4, also lower the fluidic resistance across the separator channels. Despite this it was decided that it would be worthwhile investigating the impact temperature has on the level of exchange that is achieved.

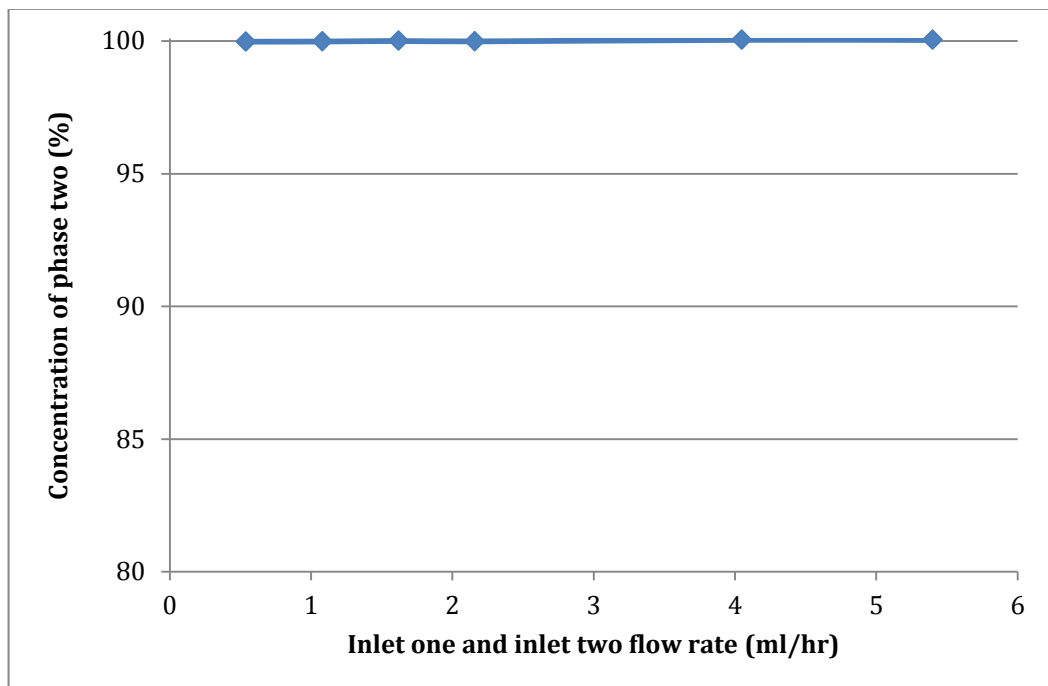


Figure 4-35: Measured concentration of phase two plotted against inlet flow rate. Complete exchange achieved with a 1:1 inlet flow ratio at various flow rates. A minimum exchange of 99.98% was achieved, which is in contrast to the results shown in Figure 4-33 suggesting greater performance may be possible with the deeper outlet exchanger than previously thought.

4.3.6 Impact of Temperature on Exchange

4.3.6.1 Method

In order to investigate the impact of temperature on the level of exchange it was necessary to be able to control the environmental temperature around the exchanger device. This was achieved by placing the entire device, chip and manifold, into an ice water bath. This ice bath was placed on a hot plate (IKA RCT basic) and heated at 60°C and the temperature recorded over time using a digital thermometer (RS 615-8212). By recording the temperature and time it is then possible to match up the data gathered from the spectrometer with the temperature. The temperature of the water bath was recorded every 3 minutes. The experiment was performed twice; on both occasions the flow rate at inlet one was held at 1.8 ml/hr. In experiment one, the inlet two flow rate was 2.7 ml/hr whilst in experiment two, the flow rate was 1.8 ml/hr. For both experiments the deeper outlet exchanger was used.

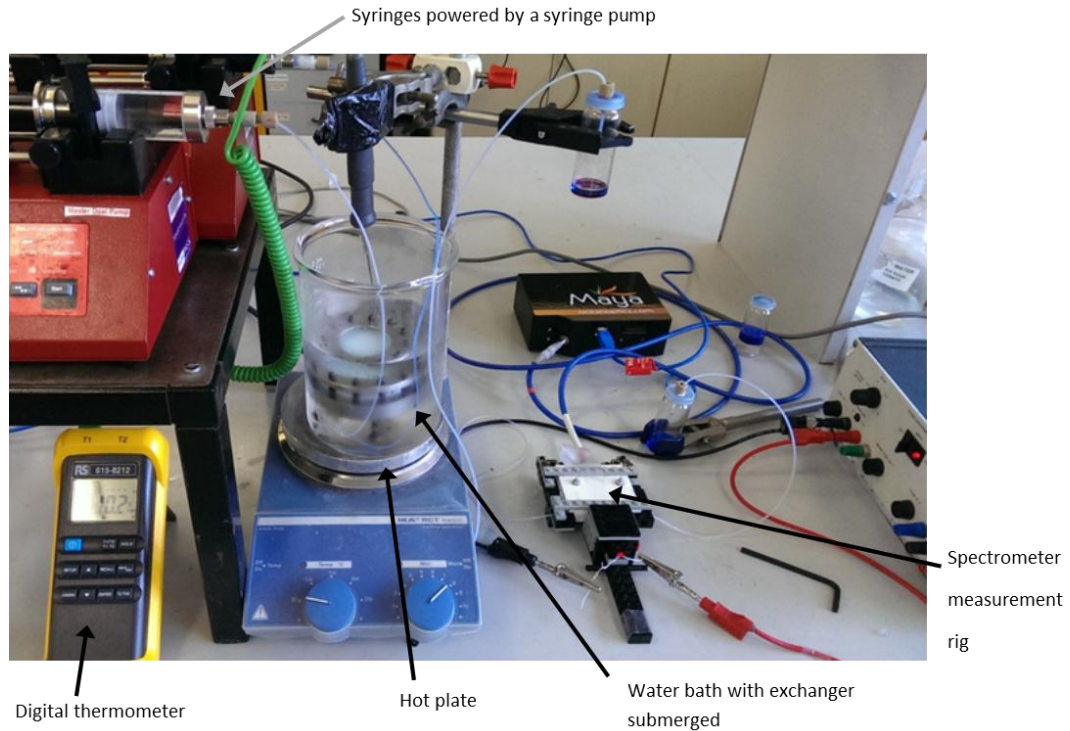


Figure 4-36: Experimental setup to investigate the impact of temperature on the level of exchange. The exchanger is kept in an ice bath, which is gradually heated using a hot plate whilst the temperature and level of exchange are recorded. The temperature was measured every 3 minutes whilst the level of exchange was monitored continuously.

4.3.6.2 Results and Discussion

As can be seen in Figure 4-37, the temperature does appear to have an impact on the level of exchange that is achieved. The concentration data has been time shifted by 630s to account for the delay created by the time between exchange and measurement, plus the time taken for the manifold to cool to the environmental temperature. In this experiment an approximately 30°C temperature increase causes a less than 3% rise in the concentration of phase two. The initial concentration level for this experiment was over 96.5%. It is, therefore, possible that the only slight increase, is a result of the

diminishing returns that occurs at high levels, in the same way that there were diminishing returns with mismatched flow rates.

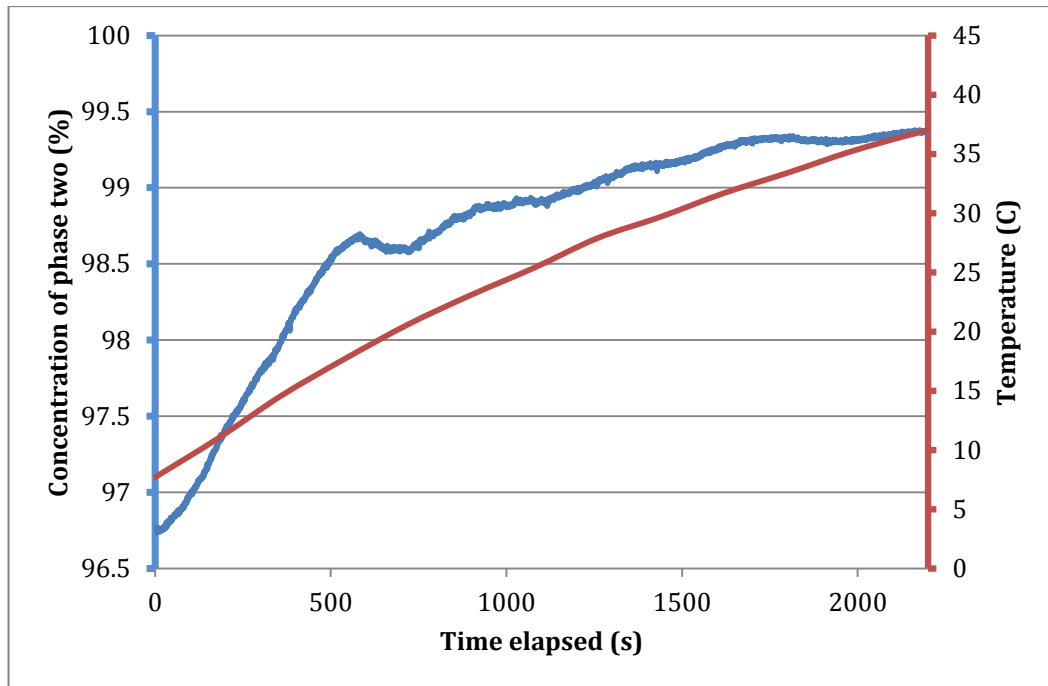


Figure 4-37: Results of investigation of the impact of temperature on the level of exchange. Inlet one flow rate 1.8 ml/hr, inlet two flow rate 2.7 ml/hr. Indicates that temperature does have an impact on the level of exchange. Due to diminishing returns as the exchange approaches 100% there is only a ~3% increase in performance over a 30°C temperature increase.

By operating the device with both inlet flow rates equal (a 1:1 flow ratio), the initial concentration level is reduced. This allows for a much greater concentration increase. Over a rise of 35°C an approximately 13% increase in concentration was observed. This can be seen in Figure 4-38. The concentration data is time shifted 900s for the same reasons as in the first experiment; a longer shift was required this time due to the reduced flow rate.

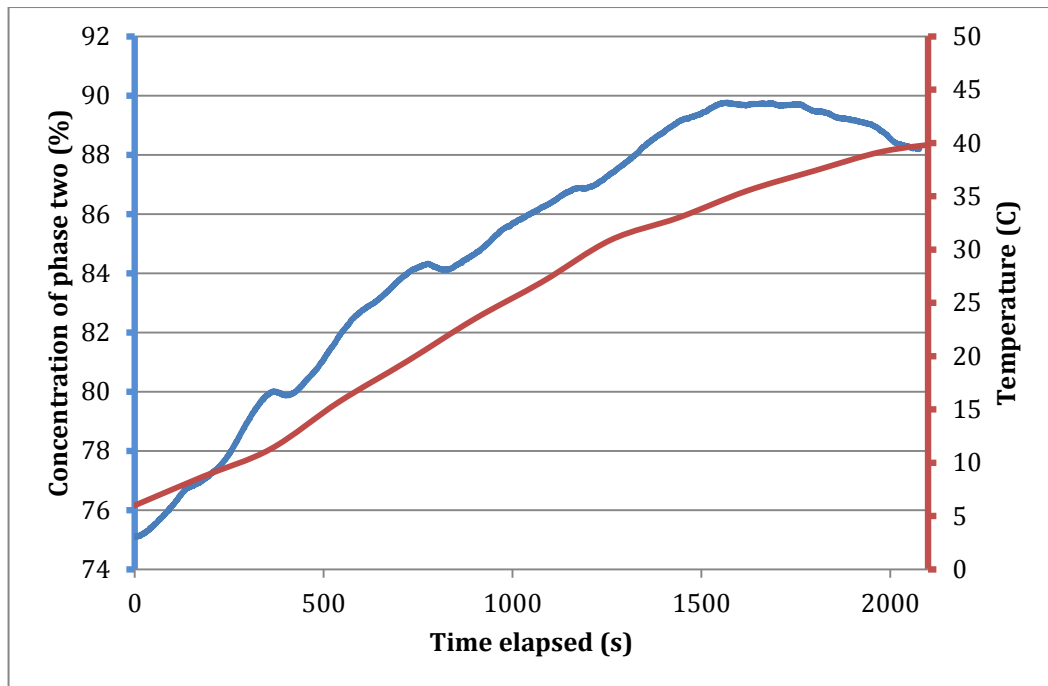


Figure 4-38: Investigation of impact of temperature on the level of exchange. Flow rate ratio of 1:1 (both inlets at 1.8 ml/hr). A more significant increase is achieved than was found previously in Figure 4-37. An improvement in exchange level of approximately 13% is achieved over an increase in temperature of 35°C. This supports the theory that the small increase found previously was a result of the diminishing returns achieved when exchange is close to 100%.

These experiments suggest that an increase in temperature will provide a greater level of exchange; this is as one would expect given the fluidic resistance equation (4-4). These results appear to show that temperature was not the reason behind the increased performance shown in Figure 4-35. The impact of temperature on the level of medium exchange is likely due to the change in viscosity that occurs in liquids as the temperature varies plus the thermal expansion, or contraction, of the device and the liquid. Generally materials expand as the temperature increases so this should have some impact on the fluidic resistance as it relies on the geometry of the channels.

The linear thermal expansion can be calculated using the following equation [192]:

$$\Delta L = \alpha \Delta T L_0 \quad (4-10)$$

where ΔL is the change in length, α is the thermal expansion coefficient, ΔT is the temperature change and L_0 is the original length. Similarly, the areal expansion can be found by the following:

$$\Delta A = 2\alpha \Delta T A_0 \quad (4-11)$$

Where ΔA is the change in area and A_0 is the original area. Using these equations, in combination with the fluidic resistance equation, it was possible to calculate the theoretical impact temperature change has on the fluidic resistance of the separator channels; this is shown in Figure 4-39. The thermal expansion coefficient for PTFE is $135 \times 10^{-6} \text{ K}^{-1}$ [193].

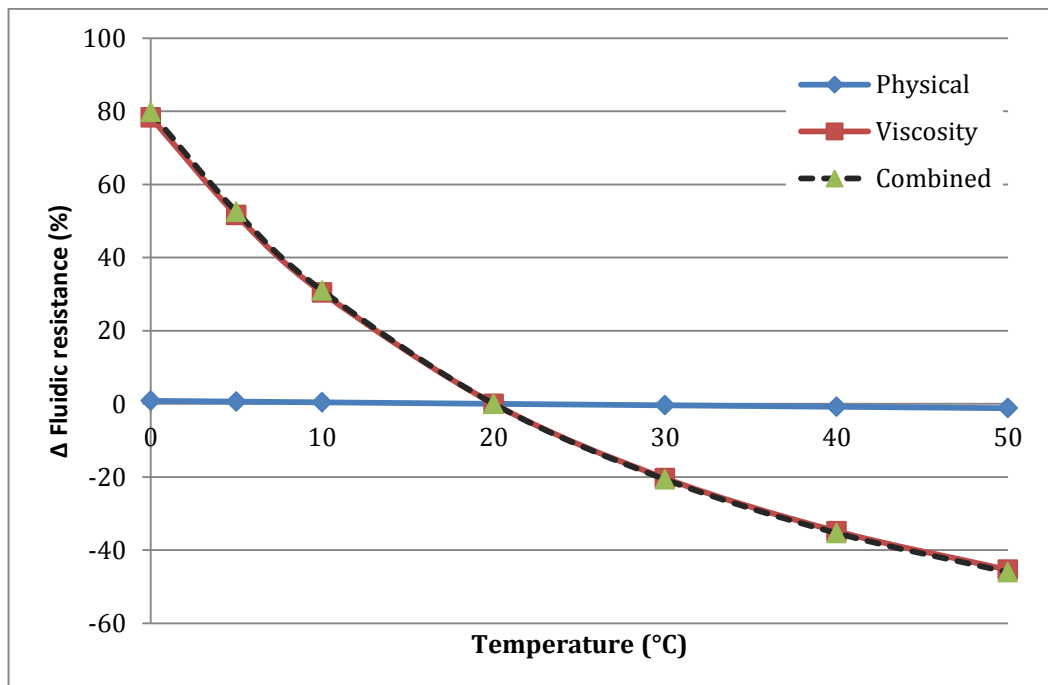


Figure 4-39: Impact of temperature on the fluidic resistance of the separator channels based on theoretical calculations showing the change in fluidic resistance as a percentage of the fluidic resistance at normal operating conditions (20°C). The changes attributable to

both physical expansion and due to changes in viscosity are plotted along with a combination of the two. Viscosity appears to have a significantly bigger impact.

The theoretical drop in fluidic resistance that is shown as temperature increases supports the experimental findings of improved exchanger performance at warmer temperatures. It is clear that there is an impact from both physical expansion and viscosity changes. However, it is also clear that the impact of viscosity is significantly greater than the change in fluidic resistance that is attributable to physical expansion (or contraction). The non-linear nature of viscosity change in fluids means that the temperature has less impact at higher temperatures; this is also shown in the experimental results where the performance appears to be levelling out after approximately 40°C.

4.3.7 Outlet Channel Length

The fluidic resistance equation (4-4) is dependent on a number of variables. The channel dimensions were tested in sections 4.3.4 and 4.3.5 and viscosity was tested in section 4.3.6. This leaves just the channel length to be considered. Whilst the length of the separator channels has been investigated through simulations, the length of the outlet channels has not been. The temperature impact study required a much longer length of tubing from outlet one than in previous tests, due to the distance between the water bath and the spectrometer measurement system. This provided an opportunity to quickly investigate the impact of outlet length on the level of exchange.

4.3.7.1 Method

The water bath and hot plate from the temperature experiments were removed and the excess tubing was fed through the spectrometer measurement system. Whilst recording the spectral data, a length of 0.65m was removed from the end of the outlet tubing. The inlet flow rates were set at 0.54 ml/hr for both inlets.

4.3.7.2 Results and Discussion

The data represented in Figure 4-40 indicates that channel length does have an impact on the level of exchange. With the extra 0.65m of outlet one tubing length, the level of exchange is held at 100% with a 1:1 inlet flow ratio; this drops to ~86% concentration when the tubing is shortened by 0.65m.

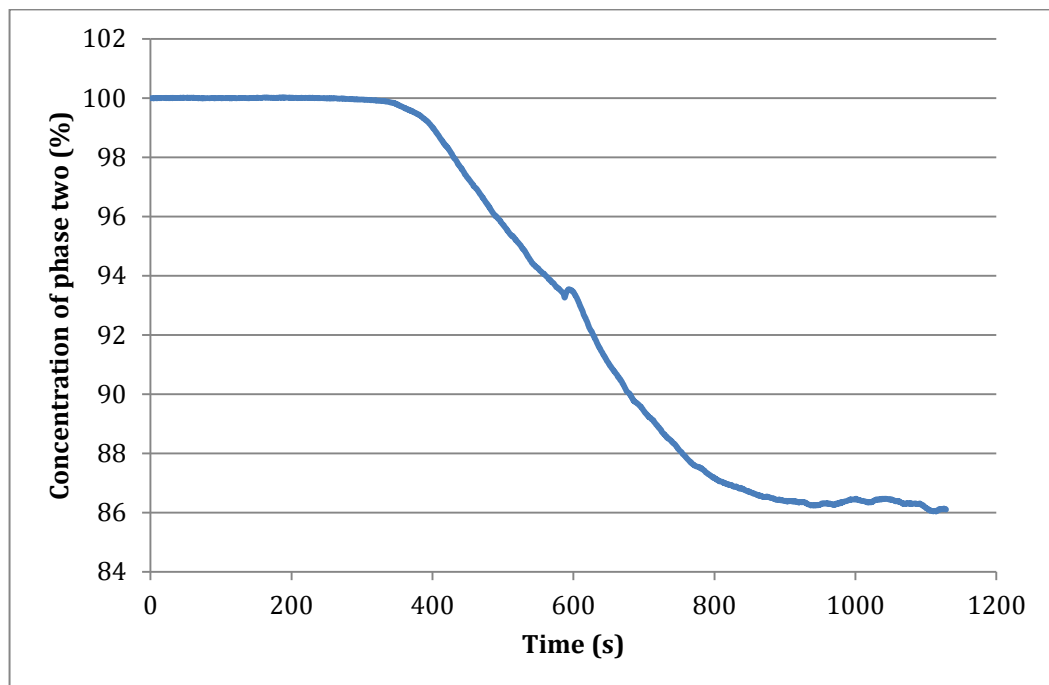


Figure 4-40: Concentration level recorded as a length of 0.65m was removed from the tubing connected to outlet one. The reduction in the length of the outlet one tubing reduces the fluidic resistance through this outlet leading to a reduction in the level of exchange achieved.

It is evident from Figure 4-40 that there is a long delay between the change occurring and the concentration settling at the final level, this was a consistent factor throughout the experiments using the spectrometer measure system. This delay is likely due to the parabolic nature of the flow at this scale; this means that the oil concentration changes quicker in the centre of the channel than it will at the edges, meaning the amount of light absorbed will change more slowly than the actual level of exchange will. This effect is known as Taylor dispersion [194, 195] and is illustrated in Figure 4-41.

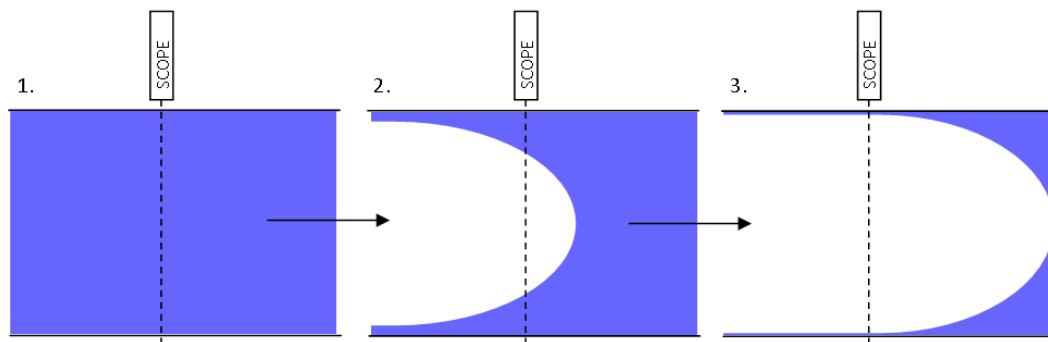


Figure 4-41: Illustration of the way parabolic flow could be the cause of the response delay. Flow is from left to right. The dashed line indicates the path of light received by the spectrometer scope. 1. Dyed oil fills the tubing, absorbing a significant amount of light from the LED. 2. Clear oil enters the measurement area but the flow profile means the clear oil replaces the dyed oil in the centre first, this reduces the amount of light absorbed. 3. More of the dyed oil has been replaced by clear oil further reducing the amount of light absorbed.

The illustration in Figure 4-41 is a simplification of the measurement response delay created by the parabolic flow but it demonstrates that oil at the edges of the channel will take longer to be replaced by oil of the new concentration level than oil at the centre. Hence, the slow decline in

measured concentration, despite the almost immediate response to the change that can be observed at the actual point of exchange.

4.3.8 Separator Channel Size

Whilst the geometry of the main flow channels has been investigated, the geometry of separator channels has not been experimentally investigated. Simulations were run to investigate the channel length in section 4.1.5 but the width and depth have not been considered up until now. Narrower channels may be needed to transfer smaller spheres to a secondary phases. Due to the limited access to the femtosecond laser at Laser Machining Limited, it was not possible to experimentally test both the length of the channels and the width/depth.

4.3.8.1 Method

The non-separator channels were manufactured using the same milling procedures used previously (section 3.10). Two chips were made, one using 20 μm separator channels, and one with 10 μm separator channels. The narrowing region of the exchanger chip was shortened to match the length of an array of 200 channels of these given widths. The distance between each ablation line was set at 43 μm , and 21 μm , for the 20 μm , and 10 μm arrays, respectively. These gaps were used to maintain the ratio of the separator channel width to the gap between each separator channel as was used for the 30 μm wide separator channel array. The separator channels were ablated using the same SPIRIT 1040nm femtosecond laser, as was used to ablate the 30 μm wide channels. It was operated at 20 kHz yielding a power output of 0.4W. The parameters used were:

Table 4-9: Laser ablation parameters employed to create 20 μ m wide channels.

Parameter Type	Value
No. of Loops	100
Machining Speed	10 mm/s
Power Usage	100%
Wobble	No

Table 4-10: Laser ablation parameters employed to create 10 μ m wide channels.

Parameter Type	Value
No. of Loops	100
Machining Speed	200 mm/s
Power Usage	60%
Wobble	No

Using these parameters, the 20 μ m and 10 μ m wide channels were 60 μ m and 30 μ m deep respectively. The inlet one flow rate was set at the 2mm/s speed used in the previous tests. The experimental setup, including tubing length, was as in the experiments prior to the temperature tests.

4.3.8.2 Results and Discussion

The results shown in Figure 4-42 show that a complete exchange is possible with the narrower 20 μ m wide channels.

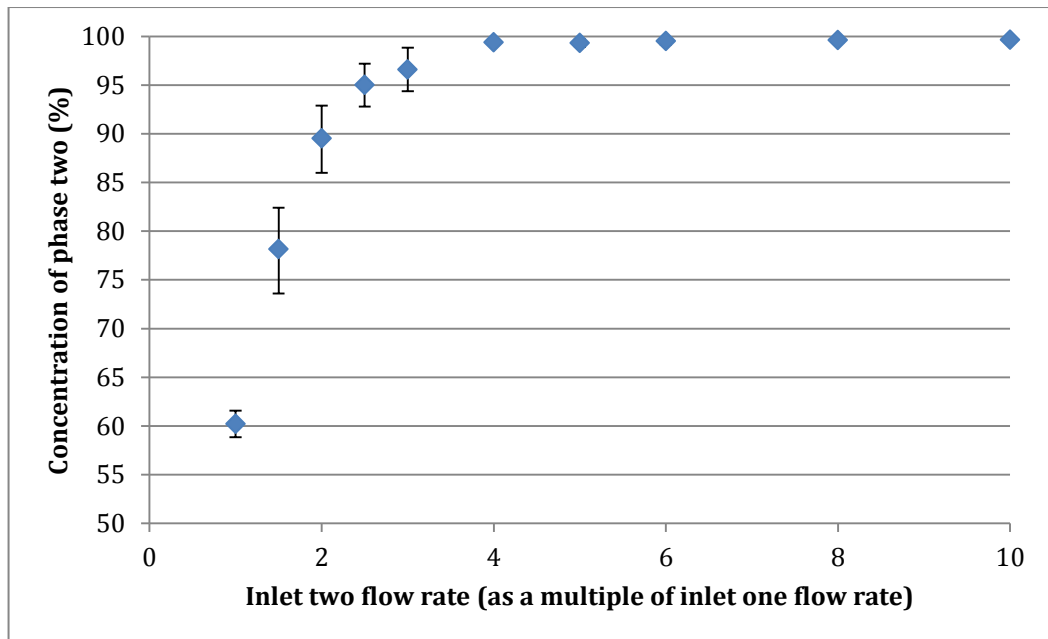


Figure 4-42: Measured concentration levels plotted against inlet flow rate ratio using exchanger with 20 μm wide separator channels. Inlet and outlet channel depths were 150 μm . Almost complete exchange was achieved at and above 4:1 flow rate ratios (inlet two:inlet one).

To get a clearer understanding of the impact of the narrower channels, it is necessary to compare these results to those achieved with 30 μm channels. Using the slower flow results in section 4.3.4, this is possible as the flow-rate and main channel geometries are equal (excluding the narrowing region).

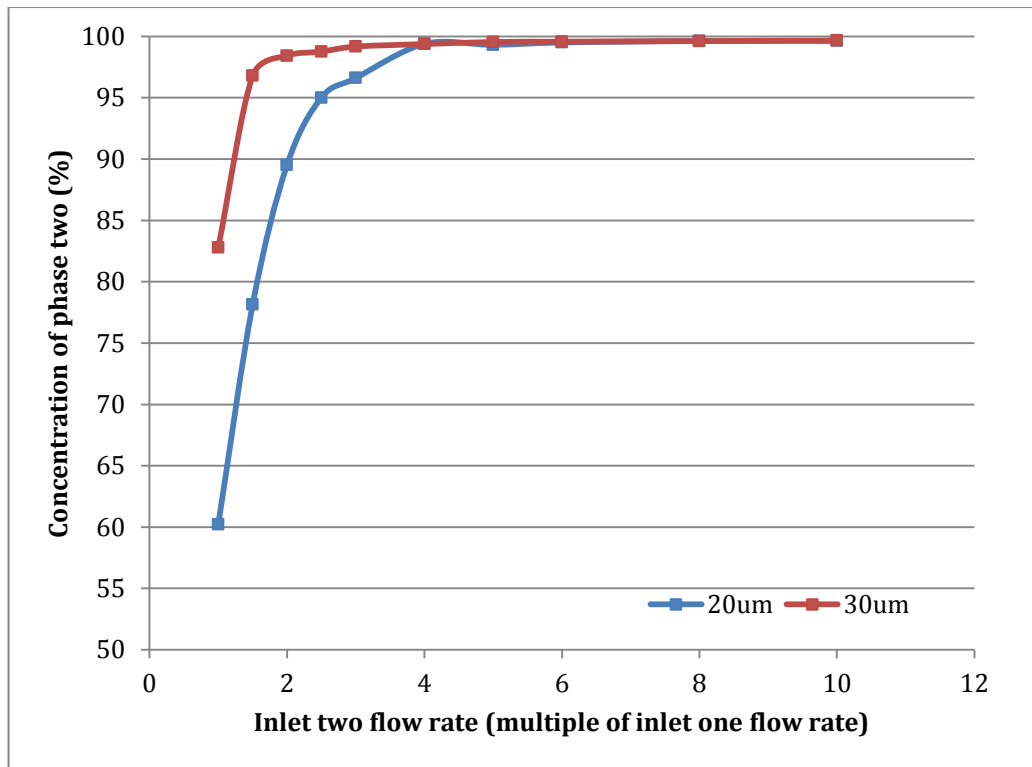


Figure 4-43: Comparison of results for the 20 μ m and 30 μ m wide separator channels. Both with inlet one flow rates of 0.54 ml/hr. Shows that the maximum achievable exchange is still approximately the same but the level of exchange possible at lower flow rate mismatches is greater with wider separator channels.

This comparison, shown in Figure 4-43, indicates that the 30 μ m wide channels offer much greater performance at lower flow mismatches, but both are able to achieve near full exchange. This reduced performance is as one would expect, as the smaller separator channels increase the fluidic resistance, and therefore, the primary phase requires more ‘encouragement’ to go down the separator channels.

Tests with the 10 μ m wide separator channels yielded no exchange even at a 10:1 inlet flow ratio. This shows that there is a limit to the size of separator channels with these conditions, it may be possible to achieve an exchange using 10 μ m wide channels if the exchanger design parameters are adjusted

based on the results of previous experiments (i.e. deeper outlet channel, longer outlet channel etc.) or when using fluids that wet the surface of PTFE more readily than mineral oil.

4.4 Overview

These simulations and experiments have shown that there are many design parameters to consider when designing the phases exchanger. These include the:

- Main flow channel depth – If this depth is close to the depth of the separator channel then the exchange is greater.
- Separator channel cross-section – Smaller channels provide lesser exchanges.
- Separator channel length – Shorter channels offer higher levels of exchange.
- Outlet channel depth – If the outlet two channel is deeper than the main flow channel (the outlet one channel) then higher levels of exchange can be achieved.
- Outlet channel lengths – Longer tubing attached to outlet one promotes more complete exchanges.
- Flow rate mismatch – The ratio of flow through inlets one and two is the foundation of the operation of this medium exchanger. Greater flow through inlet two drives an improvement in the level of exchange.
- Number of separator channels – There appears to be a peak exchange level at 200 channels.

- Operational temperature – The exchanger performs better in warmer environments.

These findings can be used to optimise an exchanger for a specific application, two possible applications are covered in the following sections although due to limited access to the femtosecond laser the exchanger could not be fully optimised for these applications.

4.5 Buffer Region

Having established how the exchanger works it was then necessary to test some possible uses of the exchanger. The first possible application for the exchanger was found from another project being carried out by a colleague, in our shared laboratory. The concept of that project was to encapsulate stem cells within microfluidic alginate droplets. To achieve this, an alginate and calcium carbonate solution was used to create droplets in mineral oil infused with glacial acetic acid. The acidic oil would initiate curing in the calcium carbonate, thereby, solidifying, or gelling, the droplets. A problem with the design was that the acid would gradually diffuse up the inlets causing an eventual blockage of the inlet channels. By using the exchanger it should be possible to create a buffer region between the creation of the spheres and the curing of the spheres.

4.5.1 Method

To create a buffer region, the spheres were formed in mineral oil without any acid added. The mineral oil, dyed with Oil Blue N, of previous experiments, was used. A flow-focusing device was used to create the droplets. The droplet was then transferred into the acid-infused mineral oil,

via the medium exchanger, allowing the spheres to cure. The alginate solution was created by adding 0.075g of calcium carbonate (CaCO_3) to 10ml of deionised water. This was then sonicated (Kerry) for 1 hour before 0.2g of alginic acid sodium salt (Sigma) was added. A magnetic stirrer and hot plate (IKA RCT basic) was then used to stir the solution for 30 minutes whilst it was heated to 45°C . Red food colouring (Silver spoon, cakecraft) was added to the solution to make it more visible. The acidic oil was made by adding $500\mu\text{l}$ of glacial acetic acid (Sigma) to 100ml of mineral oil. The mineral oil inlet flow rates were set to 0.6 ml/hr each. The alginate solution inlet flow rate was 0.07 ml/hr and the acid-infused oil flow rate was set to 4.8 ml/hr. The spectrometer measurement system was used as previously (section 0) with an integration time of 37.1ms.

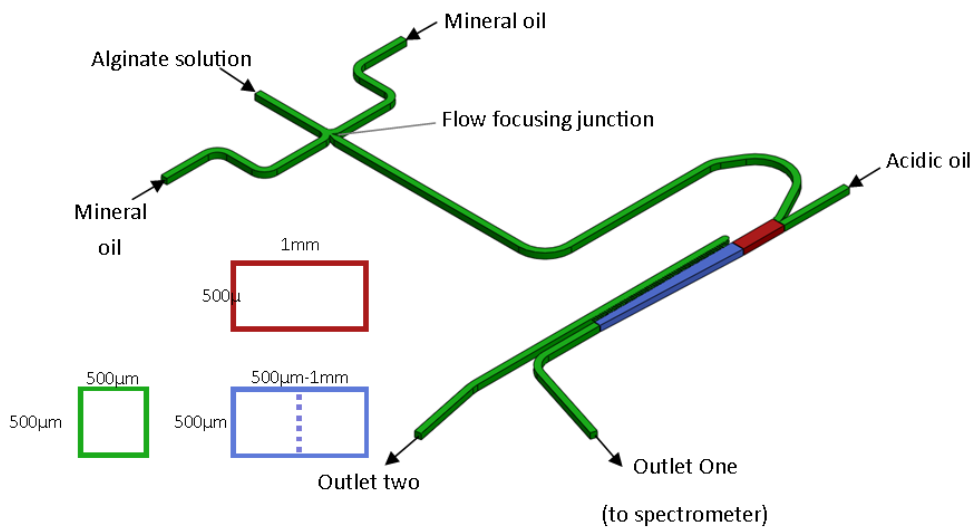


Figure 4-44: Channel cross-sectional dimensions of deeper outlet exchanger. Inlets and outlets (green), two phase flow region (red) and transition region (blue) all created through milling. There is a narrowing of the channel width to $200\mu\text{m}$ at the flow focusing junction. Transition region narrows from $1\text{mm} - 500\mu\text{m}$. Separator channel array created via femtosecond laser ablation, each channel had a triangular profile and was $30\mu\text{m}$ wide and $100\mu\text{m}$ deep. Black arrows indicate the direction of flow. Droplets are made in mineral oil at

the flow focusing junction, the exchanger is then used to transfer the droplets into a mineral oil containing acetic acid, which initiates droplet curing.

4.5.2 Results and Discussion

Figure 4-45 shows the droplets of alginate solution transferring between the two phases suggesting that this technique could be used effectively, although a full exchange is not achieved.



Figure 4-45: Photomicrograph of an alginate sphere (red) being transferred from mineral oil without glacial acetic acid (blue) to mineral oil containing the acid (clear). Flow is from left to right.

That the exchange is not complete is further evidenced by the data shown in Figure 4-46, which shows that a reasonably consistent exchange level of approximately 90% can be maintained whilst transferring the spheres between phases.

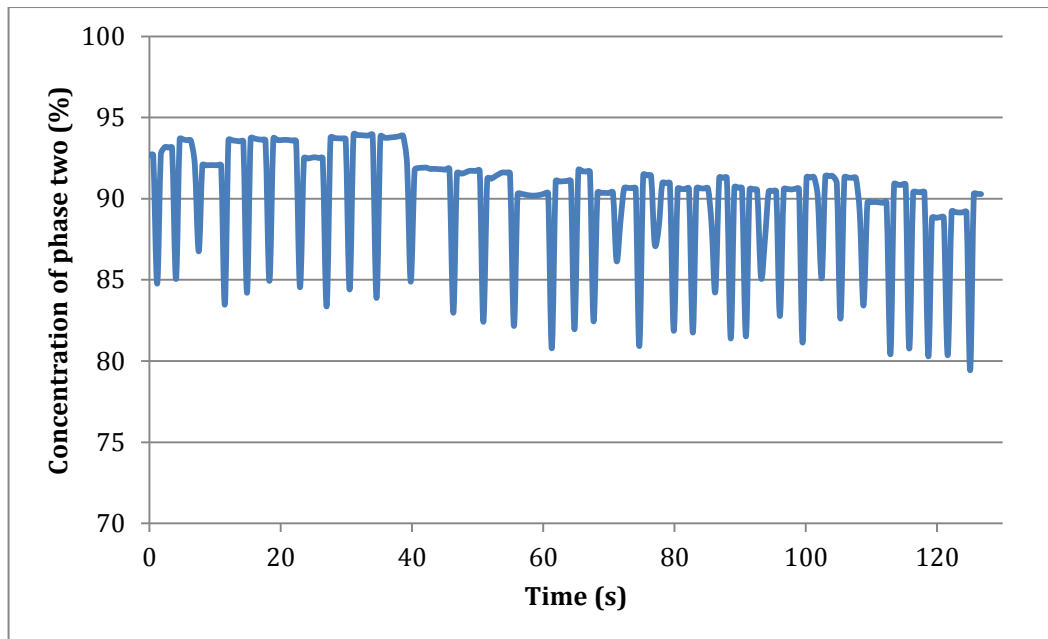


Figure 4-46: Concentration of phase two recorded over time gathered during the buffer region test showing a reasonably consistent exchange of approximately 90%. Each dip in concentration correlates to a sphere passing the spectrometer.

Figure 4-46 shows cured spheres indicating that the acid in phase two can effectively cure the spheres after an exchange has occurred.

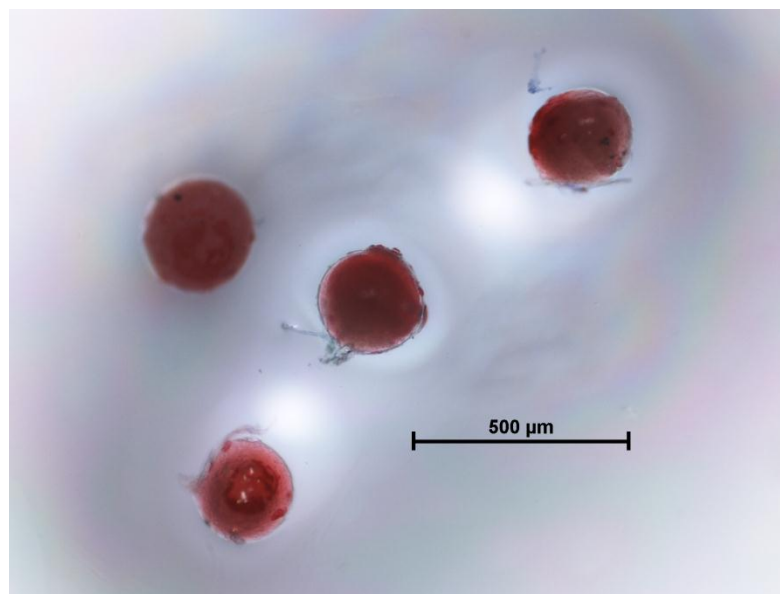


Figure 4-47: Cured alginate spheres created on chip in acid free mineral oil before being transferred into mineral oil containing glacial acetic acid by the medium exchanger. The

acid initiated curing of the spheres. Some debris has adhered to the spheres during the handling process whilst imaging.

There was an occasional problem with sphere blockages at the outlet, this is a problem that was also encountered in the sphere production experiments detailed in section 3.7. This is not a problem with the exchanger itself, but with the overall manifold. Additionally, as mentioned previously, this problem has been overcome by a colleague, using an in line outlet. There were no instances of the inlets becoming blocked, suggesting that using the exchanger to create a buffer region, is an effective technique.

4.6 Sphere Cleaning

Another possible use is cleaning spheres by the removal of surfactants from sphere suspensions. This is usually achieved using a centrifuge, separately from any microfluidic process. Therefore, being able to perform a cleaning process on-chip, would be advantageous.

4.6.1 Method

A deionised water based solution was created using 10ml of DI water with 3.5% tween 20 (w/w) and 1% cochineal red food colouring (w/w). Approximately 105-125 μ m diameter polystyrene spheres were added to this solution at a concentration of $\sim 1 \times 10^6$ spheres per ml. This solution was phase one. Phase two was purely deionised water. The deeper outlet exchanger was used with an inlet one flow rate of 10 ml/hr and an inlet two flow rate of 40 ml/hr.

4.6.2 Results and Discussion

A purely optical examination of the output from the two outlets suggests that exchange of these two phases is viable, as shown in Figure 4-48 and Figure 4-49.

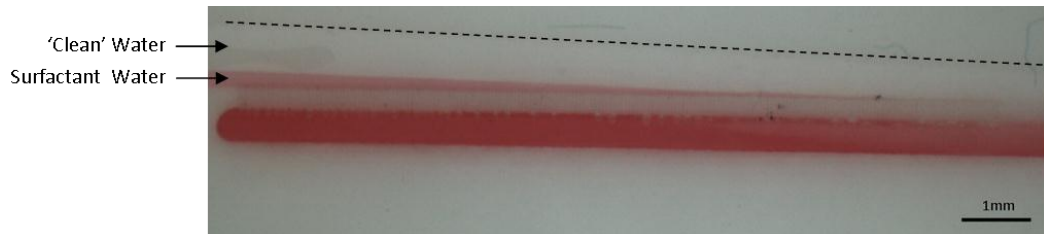


Figure 4-48: Photomicrograph of an exchange. Deionised water containing surfactant and red dye is exchanged for deionised water that is surfactant free. Water containing surfactant is extracted through the separator channels whilst surfactant free water replaces it. Flow from left to right as indicated by the arrows highlighting the surfactant water and the surfactant free ‘clean’ water. A dashed line was added to indicate the channel boundary.

Little evidence was gathered of the spheres crossing between the two phases and there were very few spheres collected in the collection vessels. There did not appear to be to any blockages occurring at the exchanger. The problem appeared to be due to a difficulty in getting the spheres to be carried onto the chip itself. This, once again, appeared to be a problem with the manifold or tubing rather than the exchanger as many other works [79, 122, 149] have successfully introduced spheres onto chips without any problems. Although this experiment did not prove that spheres could be cleaned using the exchanger, there was some evidence that it could be possible with an improved manifold design. Supporting evidence as to why blockages may have occurred can be found in the work by Sharp and Adrian, which investigated particle blockages in microtubes [196]. They reported that blockages caused by spheres ‘jamming’ together and arching across the

channel were more likely when the sphere width was 0.3-0.4 times the tubing diameter. In this experiment the spheres are approximately 0.23-0.25 the sphere diameter, which is just outside of this range. However, the reported blockages were found at very low volume concentrations of spheres (less than 1%). The reported concentration is significantly lower than the volume concentration used in this sphere cleaning experiment (approximately 80%) and it has been stated by Sharp and Adrian that blockages by arching can also occur for smaller spheres at higher concentrations. It was also found that blunt inlets were more liable to blockages. The combination of relatively large spheres, high volume concentration and blunt inlets makes it highly likely that a blockage occurred in or before the tubing prior to entering the exchanger chip. Due to time constraints it was not possible to perform this experiment again but further attempts to clean spheres should be performed with smaller spheres and a lower volume concentration.

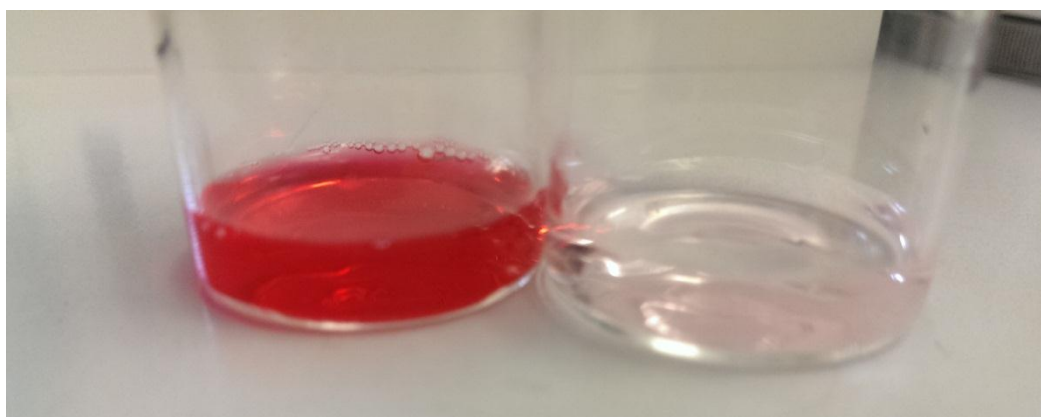


Figure 4-49: Fluid collected from outlets one (right) and two (left) after the exchange of deionised water containing surfactant and red dye for surfactant free deionised water. The water collected from outlet one was almost completely clear suggesting a high level of exchange was achieved.

4.7 Future Work

Future development of the phase exchanger should be focused on optimising the various design parameters for a specific use. Once the geometries have been optimised for a specific application it should be possible to achieve higher throughputs. Additionally, the experiments have shown there is a requirement for a new manifold design. It is likely that the phase exchanger would benefit from a manifold design that allowed for inlets and outlets that come in, or out, of the side of the manifold. This would prevent the problems that seem to be associated with the perpendicular inlets and outlets, which appear to increase the chances of blockages occurring. Creating a new manifold should also allow spheres to be introduced more readily allowing the exchanger to be tested with a greater number of applications.

Exploring other potential uses and examining what liquids can be exchanged could also potentially be a worthwhile avenue of investigation.

4.8 Conclusion

This chapter has greatly expanded the understanding of how the exchanger works. Through simulation and experimentation the problem whereby pressure on the outlet one channel would cause the throughput to drop significantly has been overcome via the use of inlet flow rate mismatches. This technique of increasing the flow through inlet two such that it is greater than through inlet one has been demonstrated as a way to drive the exchange. Further investigation has shown that there are many ways to

improve the level of exchange that is achieved, a summary of these adaptations can be found in section 4.4.

Based on the results of the simulations and experiments in this chapter it is possible to form an approximately 'ideal' exchanger. If the 'ideal' exchanger is defined as the exchanger that provides the most complete exchange at a low flow rate mismatch then the 'ideal' exchanger would have separator channels approximately as deep as the main flow channel with a significantly deeper outlet two channel. The device would have 200 separator channels and they would be as short as possible (whilst maintaining mechanical strength). Higher levels of exchange can also be achieved by using long outlet one tubing and operating the device in a warm environment. Wider separator channels can also be used to achieve greater exchange. It should be noted that all the previously mentioned conditions for an 'ideal' exchanger must also be weighed against the sphere size being used in the device as it was shown in section 4.1.6 that the minimum sphere size that is exchangeable increases with the devices that offer improved performance based on their geometry. As such, when considering very small spheres, it may be necessary to employ a somewhat less than ideal exchanger with a greater flow rate mismatch to achieve a complete exchange without losing spheres through outlet two.

Most previous medium exchangers have used active transport to 'push' or 'pull' the spheres from one phase to the other [50, 64, 65] meaning that this exchanger has an advantage due to its simplicity. The only similar passive exchanger is the exchanger created by Yamada *et al* which was able to achieve 99% exchange at similar inlet flow rates as used in these

experiments (1.8 ml/hr), however the smaller channels used by Yamada *et al.* mean that this relates to a faster flow velocity (~ 0.48 m/s) [134]. Although both exchangers seem to employ hydrodynamic filtration, and rely on the principle of fluidic resistance, the design considerations are quite different. In the Yamada exchanger, the side channels (equivalent of the separator channels) have the same cross-section as the main flow-channels, meaning efforts have to be made to discourage the liquid from passing down these channels by significantly increasing their length. Conversely, in the exchanger presented here, the liquid has to be encouraged to travel down the separator channels. The ease at which the liquid travels down the side channels in the Yamada exchanger means that high flow rates down the side-channels are achieved with ease. This is detrimental, as it will cause a greater number of spheres to travel down these channels due to the Zweifach-Fung effect. This suggests that the exchanger presented here, could be capable of working with greater throughput.

The medium exchanger presented here, has not been shown to improve the manufacture of silica spheres, as the throughput is too low to be used on an industrial manufacturing scale. Additionally, the medium exchange required in the manufacture of silica spheres requires acetone to be the secondary phase. The low contact angle of acetone would, most likely, present a problem, as it would travel down the separator channels more readily than the water present in the primary phase. This would mean that medium exchange would not be possible. It has, however, been shown to have alternative uses. The exchange of a surfactant-water solution for water that is surfactant free suggests that with some adaptation this device should be

capable of cleaning spheres. Additionally it has been demonstrated that the exchanger can be used to create a buffer region between droplet creation and curing to prevent inlet channel blockages.

5 Inertial Sorting of Microspheres

The original objective of this project was to find ways to improve the manufacture of silica spheres for use in chromatographic columns. One area of improvement that was identified was improving the monodispersity of the spheres. When the spheres are manufactured there is a bell curve distribution to the sphere diameters. Therefore, an element of size-based sorting is required. Currently, sorting is based on the mass of individual spheres, which is an accurate technique, but can cause some sorting errors if there is a variation in the densities of the spheres. As such, this chapter is focused on the development of a density-independent sorting technique.

5.1 Why does size matter?

In chromatography columns, maximising surface area is a key driving factor, as increased surface area leads to increased absorption of the target chemical. As such, greater monodispersity is desirable as this allows greater packing of the spheres, with less wasted space in the column, and therefore, more spheres per given volume. Sphere size is also important for many other industrial applications. Larger spheres will typically flow in liquid more easily, whilst powders in the range of 2-5 μm will aerosolise more easily, and could therefore become lodged in lungs, this highlights that accurate sizing is a safety issue as well as a practical one. Size sorting is also important to assess the effectiveness of size reduction techniques, such as crushing or emulsification, or sphere growth techniques like crystallization

and granulation. Some more industrial examples where sphere size is important are [197]:

- cocoa powder manufacture – affects colour and flavour
- glass spheres in road paint – impacts reflectivity
- cement particles – affects hydration rate and strength
- size of active ingredients in pharmaceuticals –dissolution/absorption rates.

5.2 Current Size Analysis Techniques

Currently, some common industrial techniques for size analysis include [197]:

- Laser diffraction – Exploits the fact that light scatters differently off differently sized spheres.
- Dynamic light scattering technique – Measures the light scattering effects that arise from the Brownian motion of particles in a suspension.
- Image analysis – Direct optical measurement of the spheres.
- Acoustic spectroscopy – Measures the attenuation caused by the acoustic waves scattering off the spheres. Amount of attenuation is related to sphere size.
- Gravitational – Sedimentation is used to separate spheres based on their size, shape or density. Currently ThermoFisher Scientific use a gravity based technique.

Whilst these techniques are well established and can offer impressive accuracy, the equipment necessary to perform these measurements is often bulky and expensive.

Microfluidics can be used to sort spheres on a significantly smaller scale, drastically reducing the cost and space required. Various microfluidic sorting techniques were reviewed in chapter 2. Due to their simplicity and effectiveness it was decided that the use of inertial lift force based techniques would be the focus of this chapter.

5.3 Tuneable Inertial Sorting

As previously discussed in chapter 2, the parabolic nature of flow within a microfluidic channel causes an inertial lift force to be induced across a sphere that is carried by said flow. This force is a result of the mismatch of the flow speeds on either side of the sphere. A more in depth description of this phenomenon can be found in section 2.2.4. Inertial sorting techniques have proven to be capable of being undertaken with reasonably high precision and throughput, whilst using very simple devices.

When designing an inertial sorting device, there are a number of parameters that must be considered. Firstly, it has been established that the following expression can be used to indicate whether inertial sorting is viable [147, 152, 198]:

$$\frac{a}{D_h} > 0.07 \quad (5-1)$$

as, the inertial force is weak below this value and will therefore require high flow rates or very long channels. Where a is the particle diameter and D_h is the hydraulic diameter. It is also important to have a high aspect ratio

(ideally aspect ratio ≥ 2) as this ensures that there are only two equilibrium positions. These equilibrium positions are at the centre of the sidewalls in the z -plane. This occurs as a result of the wall-induced forces that act on a sphere as it approaches the channel wall. These wall induced forces are minimised at the centre of the longest wall as it is the point at which the cumulative forces of the walls is weakest due to the distance from the shorter walls [199]. In rectangular channels the hydraulic diameter can be approximated as the characteristic length, which is the narrowest dimension. In high aspect-ratio channels the characteristic length is the channel width.

In order to determine how long the channel should be, it is necessary to understand the lateral migration velocity of the spheres. This can be found by considering the inertial lift force, F_z , exerted on the sphere[147]:

$$F_z = \frac{\rho U_m^2 a^4}{D_h^2} f_c(Re_c, w) \quad (5-2)$$

where f_c is the lift coefficient (as a function of channel width, w , and channel Reynolds number, Re_c), U_m is the maximum flow velocity and ρ is the fluid density. If it is assumed that the inertial lift force balances with the stokes drag force, F_s , then it is possible to find the migration velocity, U_p , as:

$$F_z = F_s \quad (5-3)$$

$$\frac{\rho U_m^2 a^4}{D_h^2} f_c(Re_c, w) = 3\pi\mu a U_p$$

$$U_p = \frac{\rho U_m^2 a^3}{3\pi\mu D_h^2} f_c(Re_c, w) \quad (5-4)$$

where μ is the dynamic viscosity of the fluid. As both the lateral migration velocity and the maximum flow velocity are known quantities, it is then

possible to determine how long the channel needs to be for full migration to occur. The equilibrium position is between 0.1 and 0.2 times the width of the channel, from the channel wall, therefore, the maximum migration distance, L_p , can be considered to be $0.4w$ [149]. Additionally, the lift coefficient can be approximated as 0.5 assuming $Re < 100$. Hence the minimum channel length, L , is:

$$L = \frac{U_m L_p}{U_p} = \frac{2.4w^3 \pi \mu}{U_m a^3 \rho} \quad (5-5)$$

From these equations the required channel dimensions were calculated for 1.9 μm , 3 μm , 5 μm , 8 μm and 12 μm silica spheres if the channel length is set to 40mm and the spheres are assumed to be neutrally buoyant with U_m set at 0.25m/s. These sphere sizes were the average batch sizes of silica spheres supplied by ThermoFisher Scientific for sorting. The channel cross sections are shown in Table 5-1.

Table 5-1: Calculated channel dimensions for a given sphere size. Channel width is rounded down to the nearest micrometre. Channel height is determined by doubling the channel width.

Sphere Diameter	Channel Width	Channel Height
1.9 μm	$\leq 26\mu\text{m}$	$\geq 52\mu\text{m}$
3 μm	$\leq 41\mu\text{m}$	$\geq 82\mu\text{m}$
5 μm	$\leq 69\mu\text{m}$	$\geq 138\mu\text{m}$
8 μm	$\leq 110\mu\text{m}$	$\geq 220\mu\text{m}$
12 μm	$\leq 166\mu\text{m}$	$\geq 332\mu\text{m}$

There is one significant drawback with previous inertial sorting techniques. That is, that they have very little ‘tuning’ capacity, and, therefore, must be designed for a specific particle size. Some tuning can be achieved by altering the flow rate. For example based on equation 5-5, a 40 μm wide, 40mm long,

channel with an aspect ratio of 2 should be capable of focusing $8\mu\text{m}$ (and above) polystyrene spheres in water at a flow speed of 0.024 m/s , whilst at a flow rate of 0.45 m/s it should be capable of sorting spheres as small as $3\mu\text{m}$. This increased flow rate would result in a pressure increase by a factor greater than 18 when focusing $3\mu\text{m}$ spheres. Additionally, the $8\mu\text{m}$ spheres would be relatively large in comparison to the channel width, meaning that particle interactions could cause spheres to exit through the wrong outlet more readily. The problem with this increased pressure is illustrated in Figure 5-1. Using equation 5-5 along with the Hagen-Poiseuille equation (4-2) it is possible to calculate the pressure within a channel at the flow rate necessary to focus spheres in a 40mm long channel. This is shown for two channel widths, $130\mu\text{m}$ and $200\mu\text{m}$. It is clear that, for spheres smaller than $6\mu\text{m}$ in the $200\mu\text{m}$ wide channel the necessary flow speeds will exceed the 300kPa bond strength of plasma bonded PDMS [200]. This is not the case for the $130\mu\text{m}$ wide device.

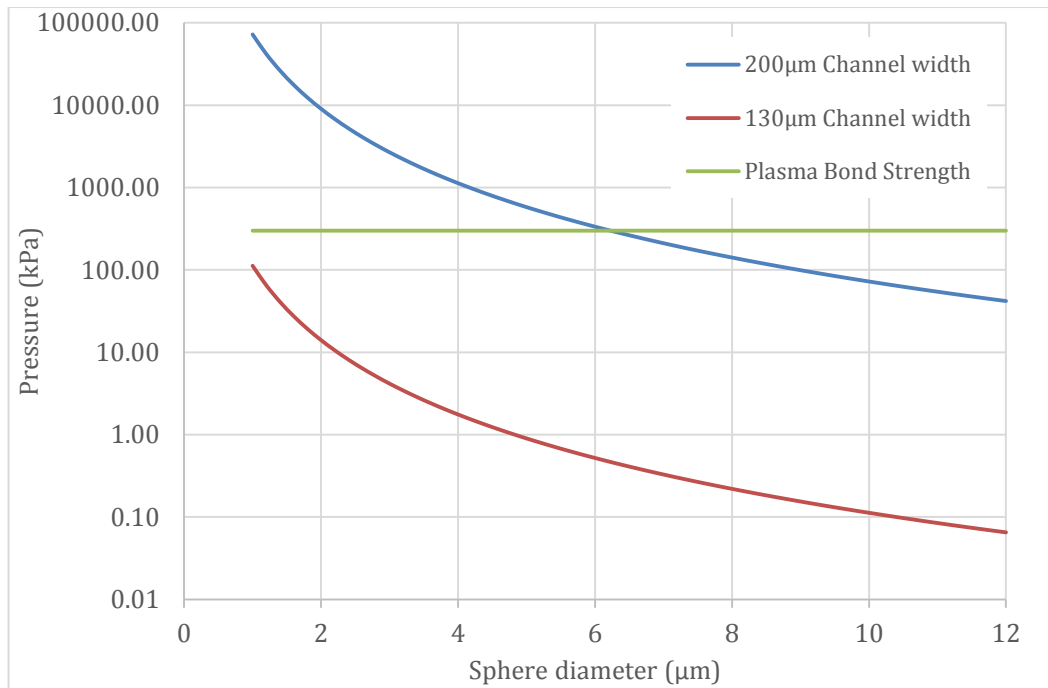


Figure 5-1: Plot of the pressure within a channel when the flow rate is pushed high enough to focus a sphere within a 40mm long channel. Shows plots for both 130μm and 200μm wide channels along with a line representing the bond strength of a PDMS device created using plasma bonding (300kPa) [200]. Shows that a 200μm wide, 40mm long channel would be unable to focus spheres below 6μm without damaging the device whereas a narrower device could sort spheres down to 1μm without damaging the device. The pressure is plotted on a logarithmic scale.

Deformation of the device would allow the channel geometry to be changed to a more appropriate size for the desired sphere size therefore removing the problem of either experiencing very high pressure or increased chance of blockages. As such, it would be highly advantageous if a device could be created, the size-sorting functionality of which, could be dynamically tuned to specific sphere sizes.

Typically, inertial sorting devices have been made by bonding a layer of cured polydimethylsiloxane (PDMS) to a sheet of glass. By instead bonding two layers of PDMS it should be possible to create a flexible device that can

be manipulated to alter the channel geometry and, therefore, the size of spheres that are focused. Clearly, if the device can be deformed such that the channel width is able to transition through the intervals shown in Table 5-1 it should be possible to ‘tune’ which spheres are focused, and which are not.

5.4 Device Design

By positioning outlets correctly it should be possible to remove the focused spheres through two side outlets whilst taking the majority of the unfocused spheres through a central outlet. If the side outlets are each one quarter of the width of the channel, it should mean that focused and unfocused spheres can exit through these channels, whilst the central outlet will have exclusively unfocused spheres travelling through it. The outlets are illustrated in Figure 5-2.

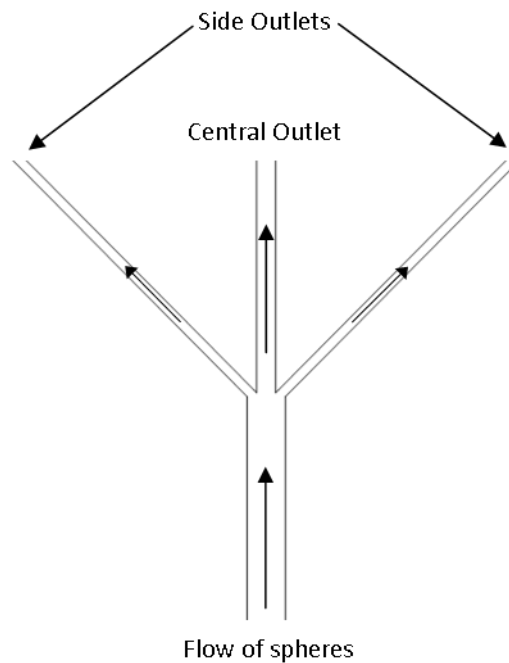


Figure 5-2: Outlets for an inertial tuning device. The side outlets are quarter of the width of the channel whilst the central outlet is half the width. Focused and unfocused spheres will

leave through the side outlets, whereas only unfocused spheres should exit through the central outlet.

Using the information in Table 5-1 it was determined that the channel width should be 80 μ m as this should focus two out of five sphere sizes and would require only a small narrowing to include smaller spheres. When operating at a suitable flow rate, the 8 μ m and 12 μ m spheres should exit exclusively through the side outlets. Therefore, by collecting spheres from the central outlet, the smaller spheres will have been selectively filtered over the larger spheres. The side outlets would have a mixture of all sphere sizes. A channel length of 40mm was chosen as this should allow 8 μ m and 12 μ m spheres to focus at a flow rate of 0.1m/s without any compression. The properties of the carrier liquid were set as $\mu=1\times 10^{-3}$ Pa.s and $\rho=2000$ kg/m³. This viscosity estimate was used as this is the viscosity of water and the carrier solution was water based. The density was set at this value to ensure neutral buoyancy of spheres.

To improve the performance of the device a widening of the channel was included after focusing had occurred to increase the distance between the focused stream and the centre of the channel. This has been used previously, in several other sorters [156, 159].

5.5 Deformation Modelling

In order to investigate the feasibility of a tuneable microfluidic device it was decided that COMSOL Multiphysics simulations should be performed to determine how a straight channel would be affected when a flexible PDMS device is subjected to some form of deformation. Models were created to

simulate stretching the device in parallel to the channel and also perpendicular to the channel. Additionally, perpendicular compression was simulated.

5.5.1 Parallel Stretching

If the device is stretched along the length of the channel it should be expected that the cross-section of the channel would be decreased much like the width of a rubber band is reduced when it is stretched. This was examined in this section using COMSOL Multiphysics.

5.5.1.1 Model Parameters

A previously created mould determined the model geometry. The mould was created using SU-8 spun on to a silicon wafer. For details of the mould production see section 5.10. This defined the dimensions of the inertial sorting region of the channel as $80\mu\text{m}$ wide and $140\mu\text{m}$ deep.

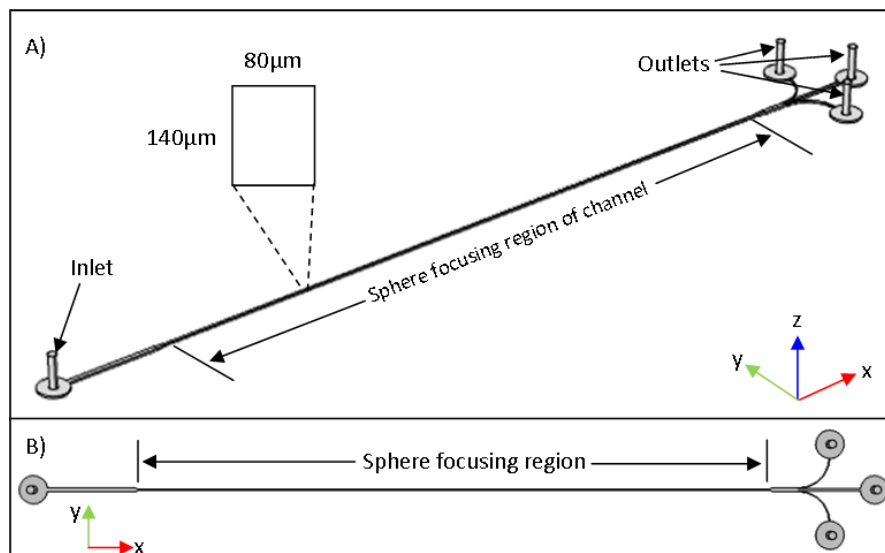


Figure 5-3: Illustration of the channels modelled in COMSOL Multiphysics simulations to investigate the impact of device deformation. A) 3D illustration of the channels that were simulated, in the simulation these channels were represented by a void in a block of PDMS. The void was in the shape shown here. Measurements of the extent of deformation were

taken along the length of the sphere focusing region. This region was 40mm long and had cross sectional dimensions as shown (80x140 μ m). B) The same illustration of the channels but viewed from above (on the xy-plane).

The channel in this model was represented as a void within a block of PDMS. The block was 57.5mm long, 10mm wide and 4mm deep. The block and the channel void within were then cut in half, parallel to the longest dimension of the channel, to allow a symmetry plane to be used to reduce simulation time. The material properties of the block are defined in Table 8.2. The Young's modulus is a measure of the material stiffness whilst the Poission's ratio indicates the extent of transverse contraction that will occur when a material is stretch (or expansion if it is compressed).

Table 5-2: PDMS Material Properties used in COMSOL model to investigate the impact on channel dimensions when the device is deformed [201]. For PDMS mixed at a 10:1 elast to curing agent ratio.

Property	Value
Young's Modulus	7.5x10 ⁵ Pa
Poisson's Ratio	0.499
Density	920 kg/m ³

The Poission's ratio was stated as 0.5 for PDMS but this causes a singularity in the simulation so it was defined as 0.499. This approximation has been used previously for simulations [202]. The position of the channel was located centrally within the block, but simulations were run that showed that the position of the channel in the z-plane had negligible impact on the channel dimensions after stretching. The same was also true when the depth of the PDMS block was varied.

The model used the 'Solid Mechanics' physics module and the material was defined as a linear elastic material. The solid mechanics module solves for the displacement field and computes the total strain tensor from the displacement gradient. Stresses are then found from the strain using Hooke's law for continuous media. A prescribed displacement was applied to the ends of the PDMS block such that the device was stretched from 0-8mm in intervals of 1mm. This displacement was applied in a manner that represented the block being held between two plates. This is shown in Figure 5-4. The prescribed displacement was applied equally in each direction along the x-plane. The cross-section through the middle of the block can also be seen in this figure.

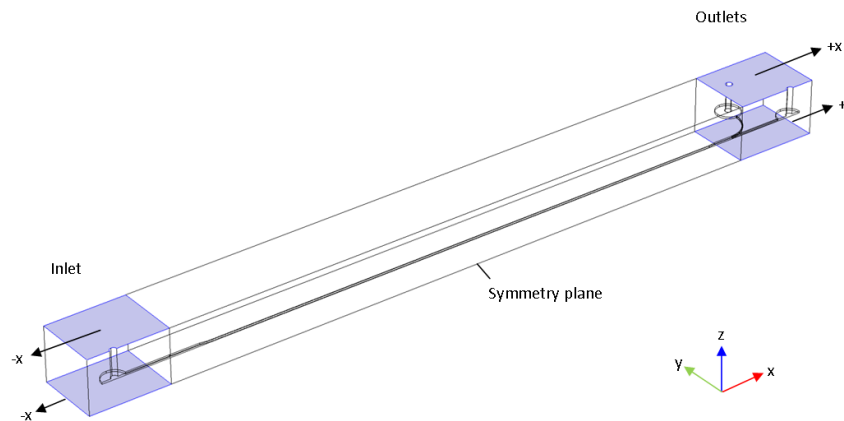


Figure 5-4: COMSOL model highlighting the faces that were given a prescribed displacement in blue. Prescribed displacements were used to simulate the device being stretched along the length of the channel, a prescribed displacement means the highlighted area is moved by a defined distance. At the inlet, the top and bottom of the device was given a prescribed displacement of $-x$ ($-4-0\text{mm}$), with the displacement in the y and z directions set to 0. Similarly, the outlets end of the device was given an equal but positive displacement of $+x$ ($0-4\text{mm}$), again with 0 displacements for y and z . These displacements at

each end of the device simulated the device being stretched in both directions in the x -dimension about the centre of the device.

The mesh was created using the pre-defined COMSOL extra-fine physics-controlled mesh setting. The default MUMPS direct solver was used.

Measurements of displacement of the channel were taken along the corner edges of the focusing region of the channel; i.e. where the side-walls meet the top and bottom of the channel. This is shown in Figure 5-5. Displacement data in the x , y and z planes was exported from COMSOL for analysis.

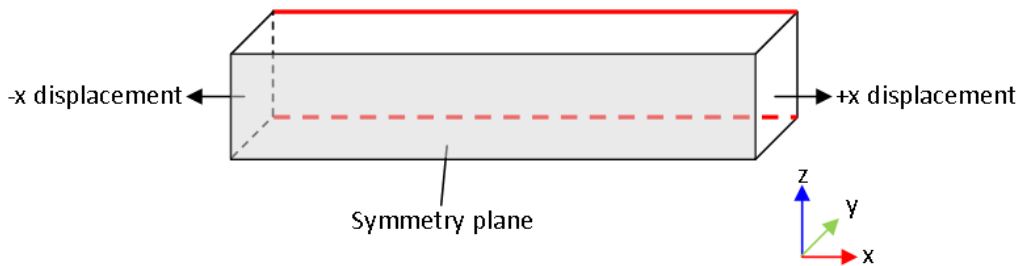


Figure 5-5: Illustration of where data was collected within the channel. Data was collected along the length of the channel at the edges that join the side wall to the top and bottom of the channel. These edges are highlighted in red. The amount of displacement in each of the three dimensions was recorded along these edges. The illustration shows half the channel as there is a symmetry plane (shaded); this was also the case in the COMSOL model.

5.5.1.2 Results and Discussion

The stretching of the device along the length of the channel can be seen in Figure 5-6. Although the primary purpose of these simulations was to examine the extent and nature of the stretching it is still useful to observe the extent of the stress that the device is being placed under as excessive stress could cause the device to be damaged. Previous work has determined that the tensile strength of PDMS mixed at a 10:1 elastomer-to-curing agent ratio is approximately $8 \times 10^6 \text{ N/m}^2$ [203], clearly the stress on the device

shown in Figure 5-6 is well below this value. This figure shows the surface stresses induced by the stretching. It is clear that the stress is greatest at the edge of the gripping point. In reality, there would also be a slight compression in the z-plane between the two plates. A simulation was carried out that included this compression but was found to have negligible impact on the critical channel dimensions. As such, this was not included in the remaining simulations, in order to reduce simulation time.

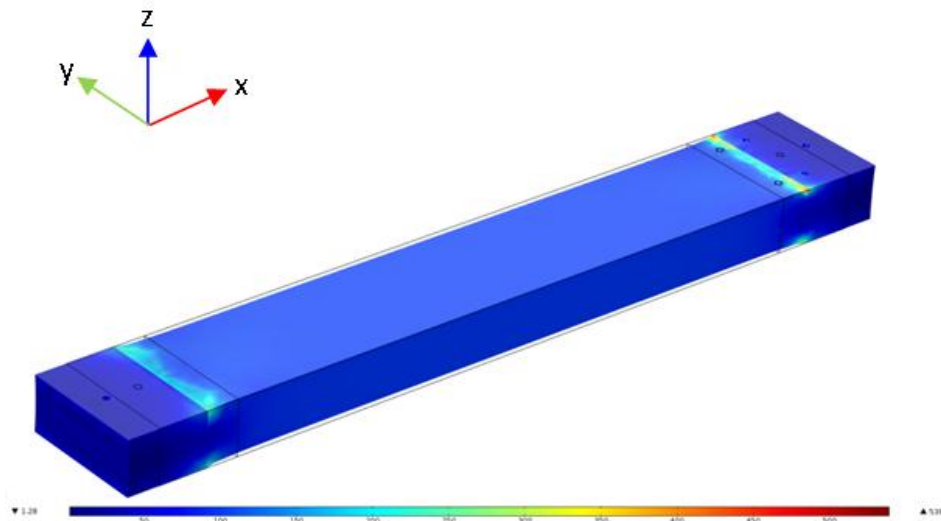


Figure 5-6: COMSOL result of stretched device showing von Mises stresses on the surface of the sphere focusing device. The colour represents the magnitude of the stress on the device surface. The scale is linear running from 0 (blue) to 550 N/m² (red). The result has been mirrored to show the entire device. The original dimensions are represented by a wireframe. The device has been stretched by 6mm.

Data taken from the channel edges demonstrated that the channel depth and width were both reduced by the stretching process. The impact on the width of the focusing region is shown in Figure 5-7, showing clearly that the stretching reduces the width. This reduction in the width should allow for smaller spheres to be focused by the inertial forces. It appears that the

channel walls are slightly distorted at both the start and at the end. This results in a shorter region of consistent channel width, which would affect the inertial lift force on the sphere. As this distortion increases the more the device is stretched, it suggests that the stretching distance may be limited. It is also observable that parallel stretching lengthens the focusing region of the channel. This could go some way to counteracting the effects of shortening due to distortion, as it will slightly increase the performance of the device, since it allows a greater distance over which the spheres can migrate to the focusing position. The increase in length is not equal to the displacement of the device. The increase ranges from 0.87mm (1mm displacement) to 6.97mm (8mm displacement).

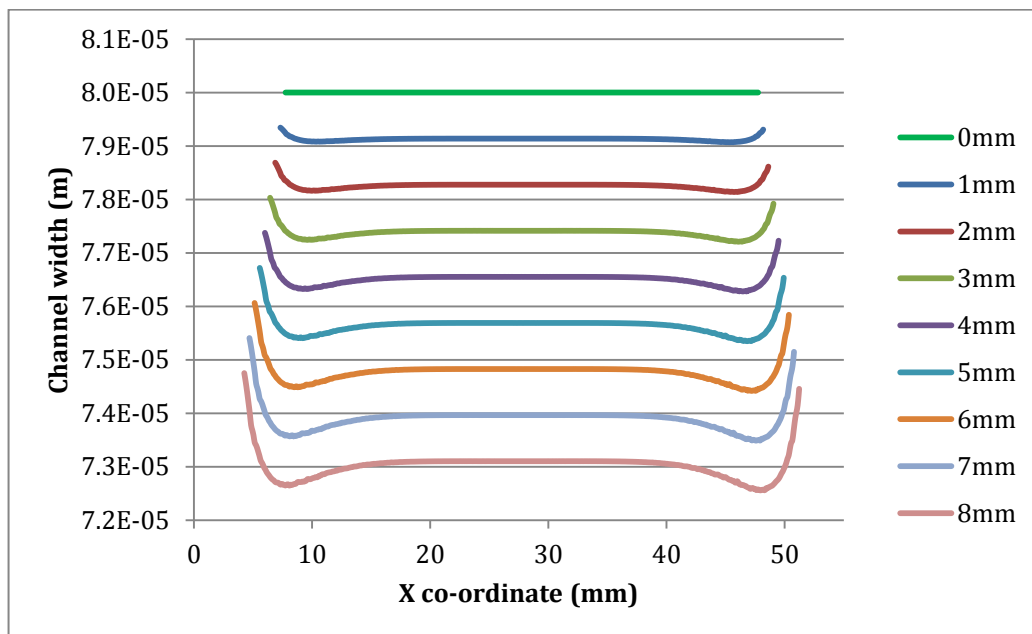


Figure 5-7: Simulation results showing channel width along the length of the channel as a result of the device being stretched along the length of the channel by a given prescribed displacement (see legend). The data is collected from the positions shown in Figure 5-5. Shows that stretching the device causes the channel to become narrower with some unwanted wall distortion at the ends of the channel.

To get a clearer idea of the wall distortion, the profile of the channel sidewalls was plotted for the 5mm stretch simulation. The data was plotted as a distance from the centre of the channel. This is shown in Figure 5-8 where it can be seen that on the scale of the entire channel width, this deformation is relatively small. However, the same can be said of the displacement created by the stretching itself.

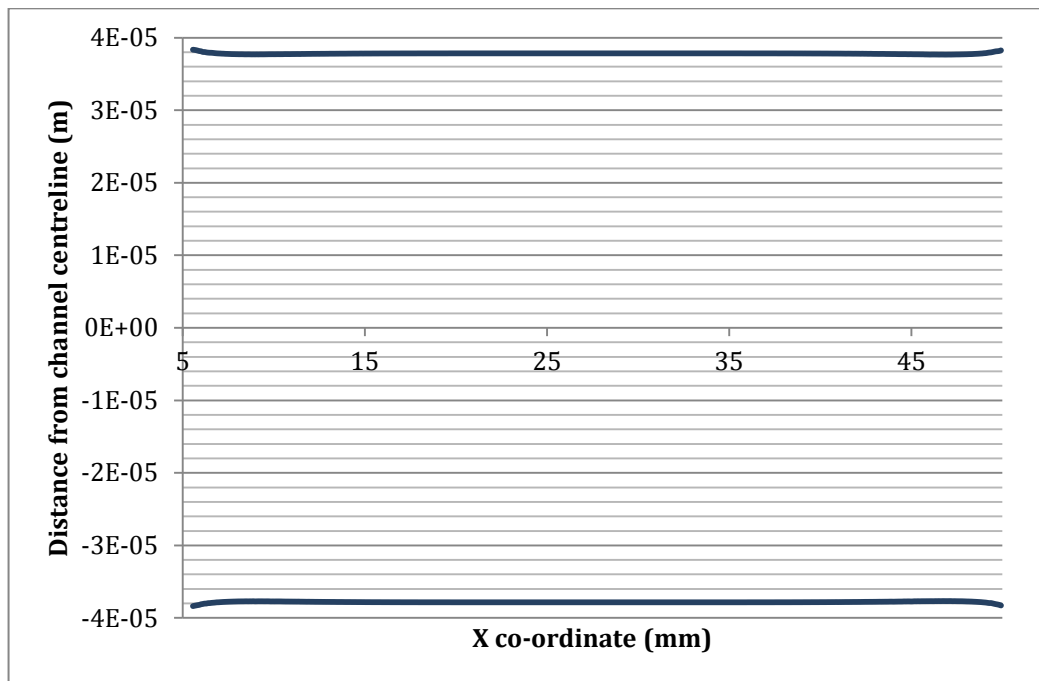


Figure 5-8: COMSOL simulation results showing the width profile of the channel along the length of the channel when the device is subjected to a 5mm stretch parallel to the focusing channel. Showing the unwanted distortion at the ends of the channel was relatively small.

The effect the stretching has on the height of the channel is shown in Figure 5-9. The channel depth displacement caused by the stretching is very similar to the effect of the stretching on the width of the channel. This is clear from the fact that the average aspect-ratio of the channel is maintained at 1.75 throughout the stretching process. This is illustrated in Figure 5-10, which shows the average cross-section of the channel when subjected to a given

parallel stretch. This figure also highlights that the impact of parallel stretching is not very significant as the channel dimensions are relatively similar throughout. This means that the device would most likely, only be capable of fine tuning, as the minimum sphere diameters that will be focused will vary from 5.6-6.9 μm .

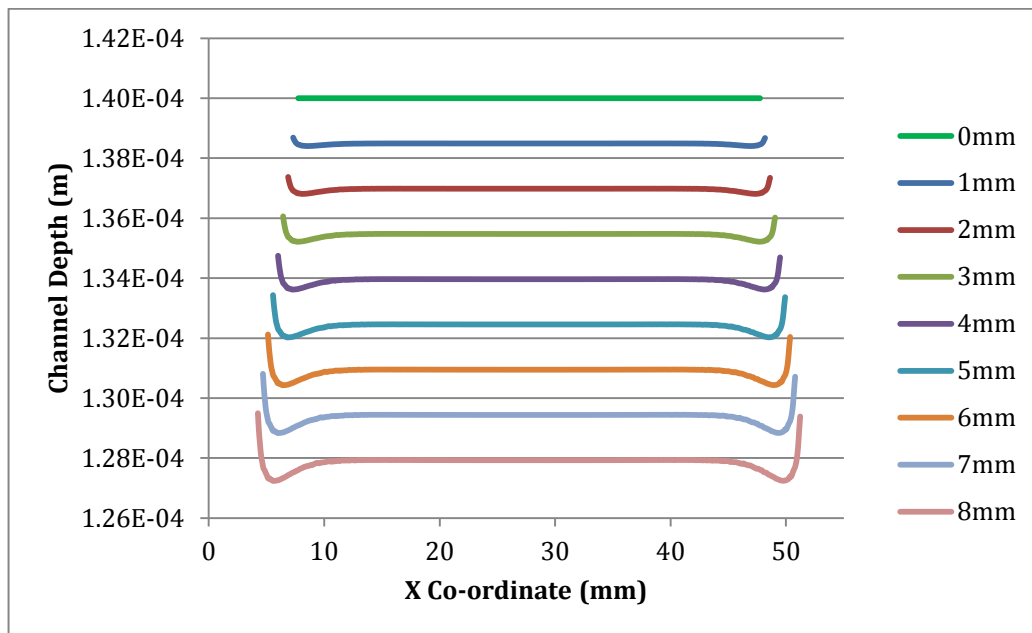


Figure 5-9: COMSOL simulation results depicting the channel depth along the length of the channel as a result of a parallel stretch of a given displacement (see legend). Parallel stretching of the device results in a reduction in channel depth. There appears to be some channel distortion at the start and end of the channel.



Figure 5-10: Scale illustrations of the average cross-section of the focusing region channel when subjected to a parallel stretch of a given length. The number within each box indicates the extent of the prescribed displacement length (mm). An average is taken of the width and depth data shown in Figure 5-7 and Figure 5-9. The channels have the following width x depth dimensions. 0mm: 80 x 140 μm . 1mm: 79.13 x 138.48 μm . 2mm: 78.26 x 136.96 μm .

3mm: 77.38 x 135.45 μm . 4mm: 76.51 x 133.93 μm . 5mm: 75.64 x 132.41 μm . 6mm: 74.77 x 130.89 μm . 7mm: 73.90 x 129.37 μm . 8mm: 73.03 x 127.86 μm . Highlights that, whilst the channel does get smaller, the aspect ratio of the channel remains the same.

5.5.2 Perpendicular Stretching

An alternative to stretching the device along the length of the channel is to stretch the device across the channel. This should lead to a widening of the channel, which in turn should impact the focusing behaviour of the device.

5.5.2.1 Model Parameters

The model used for parallel stretching was adapted to allow the device to be stretched perpendicular to focusing channel. This was achieved by adding more PDMS to the block, an additional 15mm was added either side of the channel. A region was created for metal plates to grip and apply the displacement, this region was 30mm x 10mm. These adaptations can be seen in Figure 5-11.

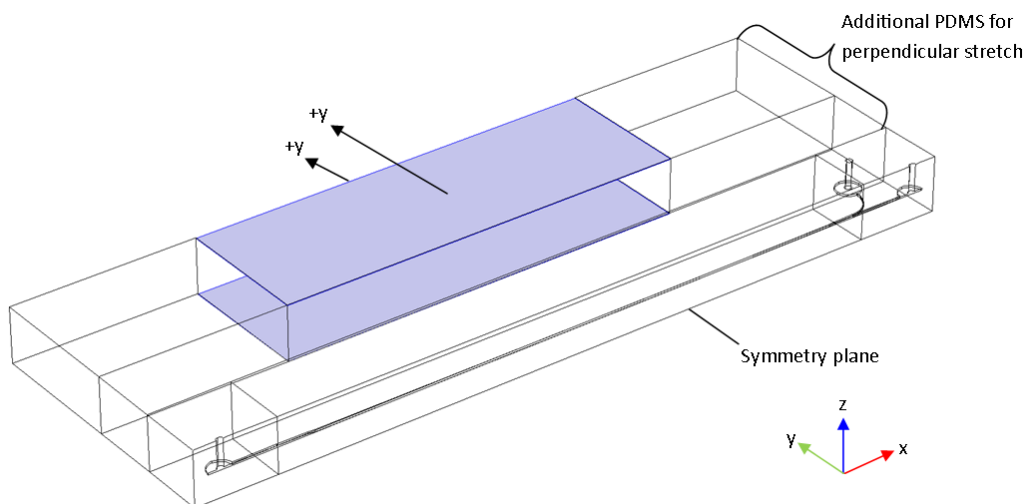


Figure 5-11: Adaptations to the COMSOL model to facilitate perpendicular stretching. An additional 15mm is added to the PDMS block (in the y-direction) that was used previously in the parallel stretching section. The 'grip' positions, where the prescribed displacement is applied, are highlighted in blue. Prescribed displacements were defined on the top and

bottom surface of the device. The displacements were both defined as $+y$ (0-3mm) in the y -dimension and 0 in the x - and z -dimensions. As previously, half of the device was simulated with the use of a symmetry plane.

In order to simulate a stretch of 0-6mm, a prescribed displacement of 0-3mm was applied to the 'grip' positions along the y -plane. It was necessary to increase the density of the mesh due to the variation in the displacement that results from the way the software approximates the result within each element of the mesh. The predefined 'extremely fine physics controlled mesh' was used. The variation can be seen in Figure 5-12. It is clear that whilst there is still some variation with this mesh setting it has been reduced from the variation found using the 'extra fine' mesh.

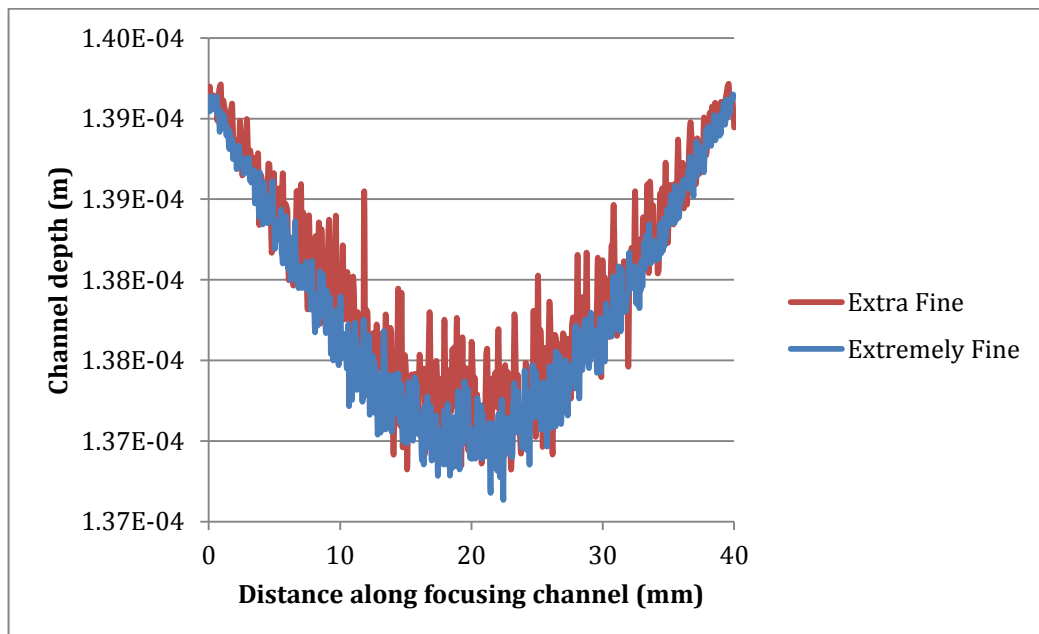


Figure 5-12: Simulation results showing the channel depth along the length of the focusing channel. Two results are shown, each with different mesh densities to highlight the reduction in variation that is achieved with a finer mesh. Both meshes are created using the COMSOL predefined 'physics controlled' mesh setting. In both cases the device was stretched by 1mm.

All other model parameters were maintained from the parallel stretching model.

5.5.2.2 Results and Discussion

Perpendicular stretching results in a significant distortion in the shape of the device. As can be seen in Figure 5-13, stretching the device along the y-plane results in shortening along the x-plane. This reduction in length could lead to the spheres not being focused, as their may no longer be sufficient time for the focusing to occur. It is also worth noting that the von Mises stresses are significantly higher with this type of stretching. This could potentially lead to the device being damaged.

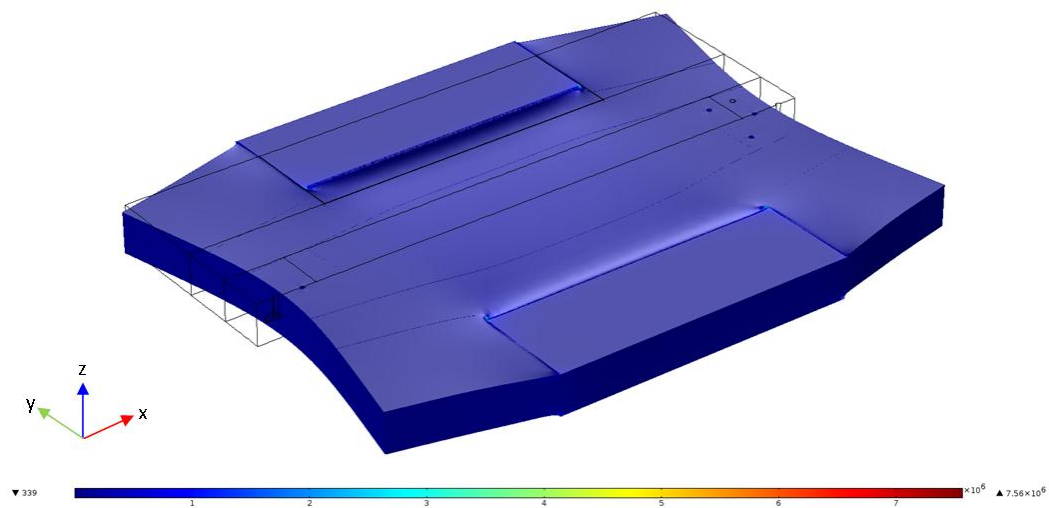


Figure 5-13: Distortion of the dynamic sphere-focusing device, as a result of a 4mm perpendicular stretch. Colour represents the magnitude of the von Mises stress on the device surface using a linear scale from 0 (blue) to 7560 N/m² (red). This is well below the tensile strength of PDMS mixed at a ratio of 10:1 elastomer-to-curing agent.

Stretching the device perpendicular to the channel causes significant widening of the channel. This can be seen in Figure 5-14. This figure also illustrates the aforementioned shortening of the channel. Unlike parallel

stretching, this type of stretching could be used to prevent spheres from focusing. Whilst the parallel stretching allowed selection by bringing larger spheres into focus, this device would allow for selective tuning by taking smaller spheres out of focus. A possible problem with this device is that the edge is curved along the length of the focusing region. This means that the inertial force of the sphere would not be consistent, which could mean that there may be focusing when it is not expected, or vice versa. The curved nature of the channel walls is illustrated in Figure 5-15, which plots the position of the sidewalls in relation to the centre line of the channel.

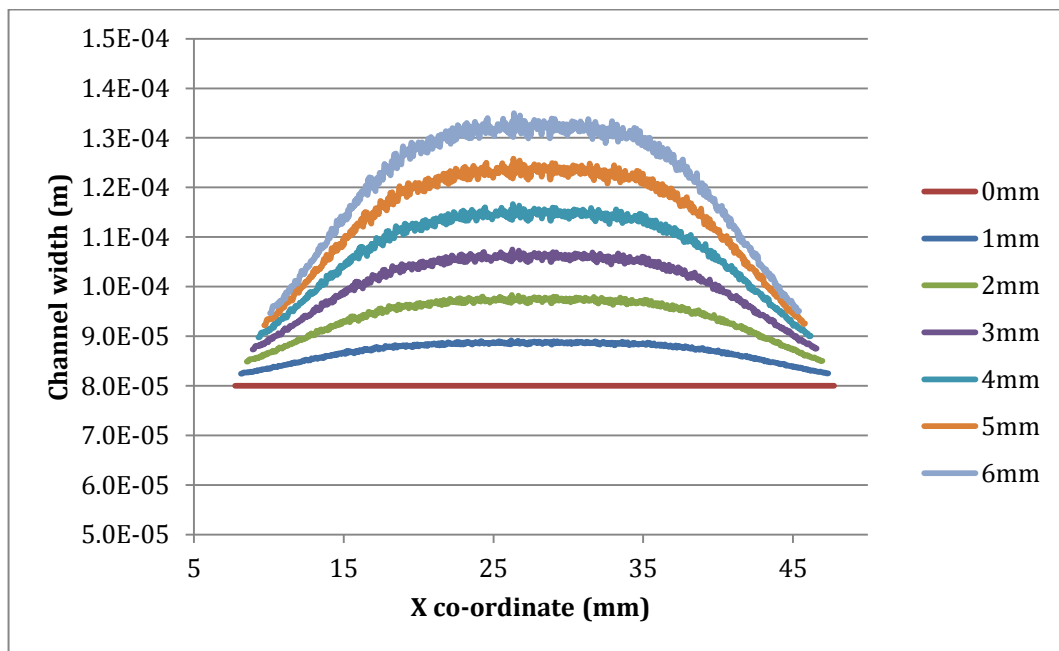


Figure 5-14: Simulation results depicting the channel width along the length of the channel as the device is stretched by a given distance (see legend) perpendicular to the channel. The perpendicular stretching causes the channel to get wider. This stretching also causes the channel wall to be curved with a peak channel width at the midpoint of the channel length.

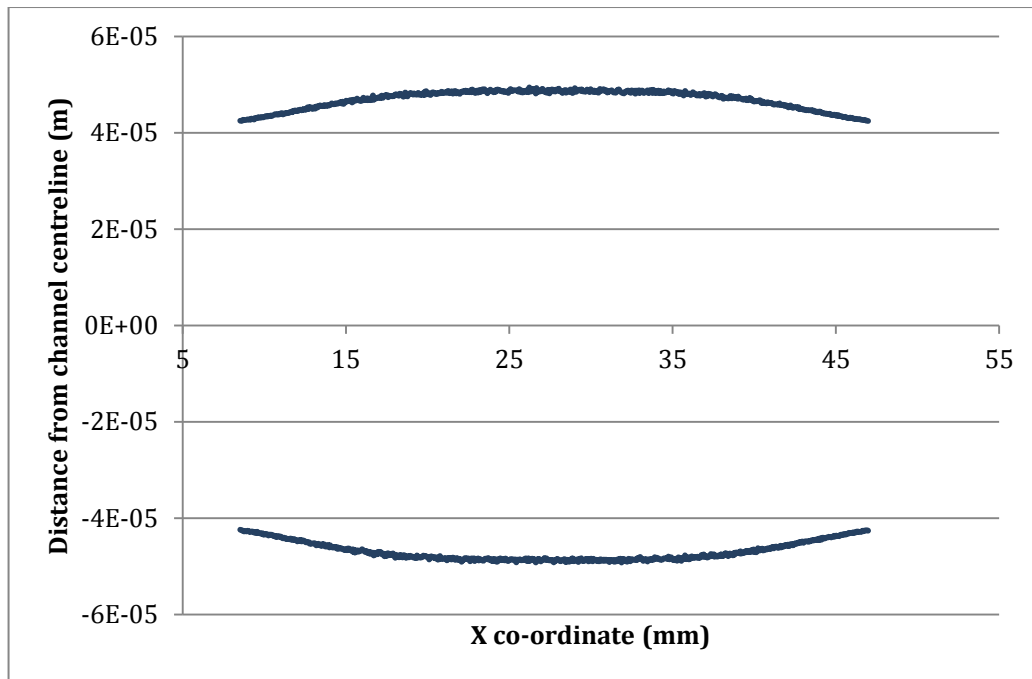


Figure 5-15: Simulation results of the channel sidewall profiles along the length of the channel. Shows the bowing of the channel walls causing the channel to be widest at the halfway point along the channel length. The device has been stretched by 2mm.

The effect that this perpendicular stretching has on the channel depth is shown in Figure 5-16. The depth is significantly reduced by the stretching process, which means that the aspect ratio of the channels will be changed. To an extent, this could enhance the ‘de-focusing’ tuning of the perpendicular stretching, but this could also create problems, as it could lead to additional equilibrium positions being created at the top and bottom of the channel. This would be problematic, as focused spheres would exit through the outlet that is intended to collect non-focused spheres. The changing cross-section of the channel, when distorted by a perpendicular stretch, is illustrated in Figure 5-17. These average channel dimensions would relate to a shift in the minimum diameter that can be focused from $6.9\mu\text{m}$ up to $12\mu\text{m}$.

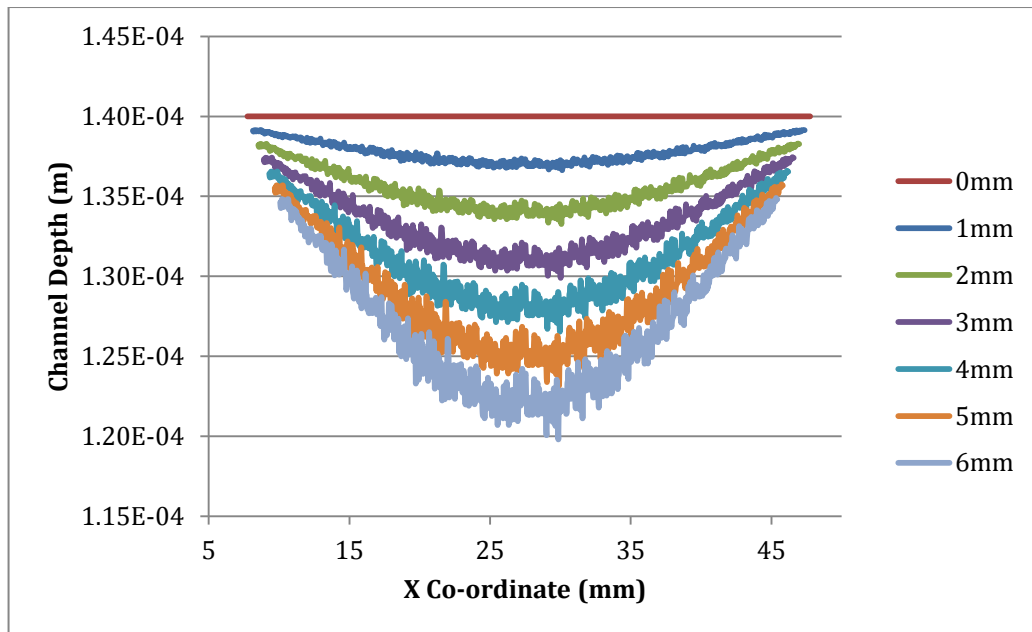


Figure 5-16: Simulation results of the channel depth along the length of the channel when the device is subjected to a given perpendicular stretch (see legend). The channel depth is reduced as the device is stretched. The nature of the distortion is curved with a depth minima at the midpoint of the channels length.

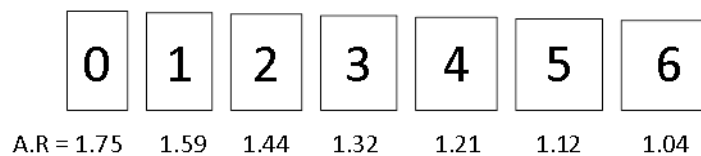


Figure 5-17: Scale illustrations of the average cross-section of the focusing region of the channel when subjected to a perpendicular stretch of a given length as denoted by the number shown within the boxes (mm). Length and width calculated by taking averages from the data shown in Figure 5-14 and Figure 5-16. Shows that perpendicular stretching causes an increase in channel width and a reduction in channel depth leading to a significant change in the channel aspect ratio. The aspect ratios of the channels are given directly below each cross-section. The channels have the following width x depth dimensions. 0mm: 80 x 140 μ m. 1mm: 86.92 x 137.78 μ m. 2mm: 93.85 x 135.57 μ m. 3mm: 100.77 x 133.36 μ m. 4mm: 107.70 x 131.14 μ m. 5mm: 114.62 x 128.92 μ m. 6mm: 121.55 x 126.71 μ m.

5.5.3 Compression

Stretching is not the only way to distort a flexible device; another possible technique is to subject the device to some sort of compression. Compression perpendicular to the channel should cause a narrowing and hence alter the focusing behaviour.

5.5.3.1 Model Parameters

The parallel stretching model was adapted to feature a 30mm wide face that was located centrally along the length of the device (in the x-plane). This face covered the full depth of the device. The width was chosen as it matched the size of a milling vice that would be used experimentally to compress the device.

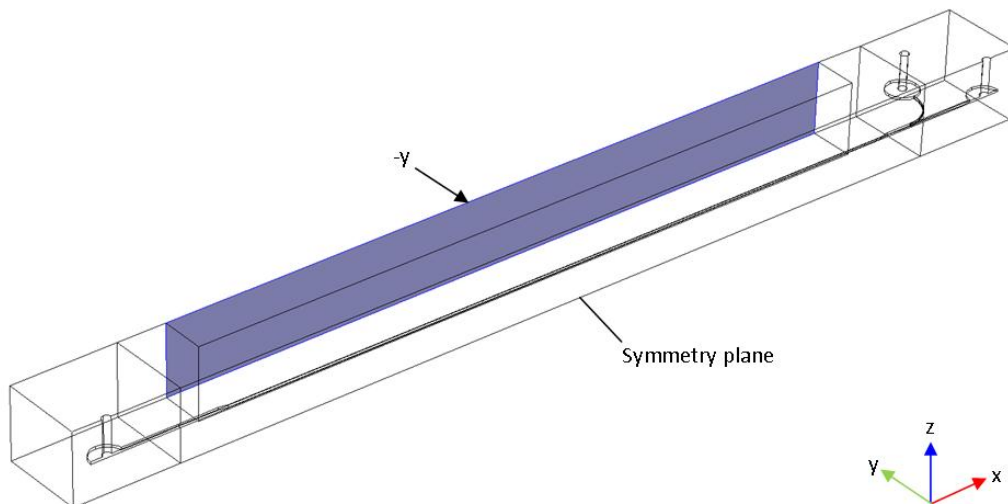


Figure 5-18: Model used to simulate compressive distortion. A prescribed displacement was applied to the side of the device (highlighted in blue). The length of the area to which the prescribed displacement was applied was determined by the width of the machining vice that was used to apply the compressive force in the experimental section. To simulate a compression of 0-2mm the prescribed displacement was defined as $-y$ (-1-0mm) in the y -dimensions whilst the x - and z - dimension displacements were set at 0. Only half of the device was simulated through the use of a symmetry plane.

The model is shown in Figure 5-18 with the compression face highlighted. This compression was applied via a prescribed displacement along the y-plane such that the device was compressed between 0 and 2mm in steps of 0.5mm.

5.5.3.2 Results and Discussion

The maximum stress induced on the surface of the device is significantly higher in compression than it was when stretching was applied. This stress, however, is still lower than the tensile strength of the PDMS so should not cause the PDMS to be damaged. However, it would most likely cause stress to be applied to the bond between the two layers of the PDMS as the top and bottom of the device are forced away from the centre as shown in Figure 5-19. This is potentially a problem as this stress does exceed the bond strength of plasma bonded PDMS [200]. The maximum stress is highly localised so may not cause significant damage but this should be monitored during the experimentation stage to ensure no problems occur between the PDMS layers.

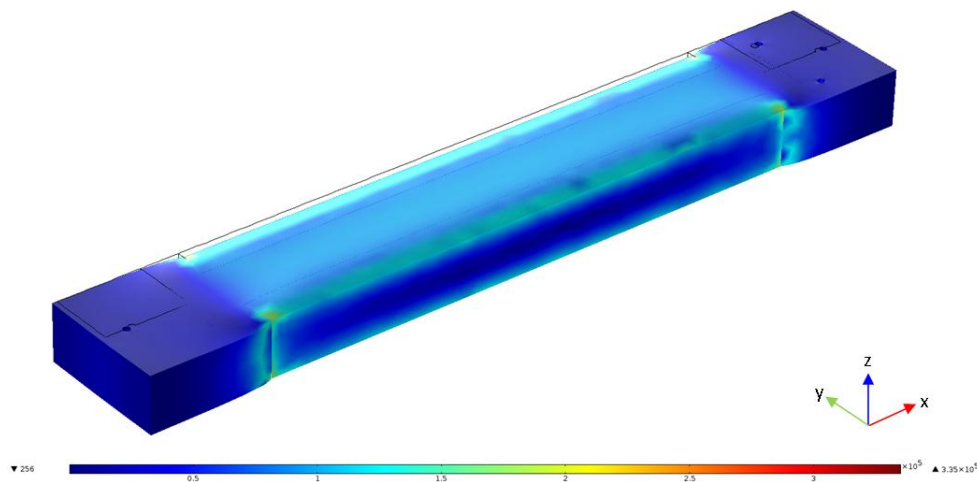


Figure 5-19: Simulation results showing von Mises stresses on the surface of the device when it is subjected to a 1mm compression perpendicular to the length of the channel.

5 Inertial Sorting of Microspheres

Magnitude of the stress is indicated by the colour on a linear scale from 0 (blue) to $3.35 \times 10^5 \text{ N/m}^2$ (red). Wireframe indicates the original device dimensions.

Importantly, the narrowing that is achievable with compression, appears to be much greater than that which is achieved using parallel stretching. This is shown clearly in Figure 5-20. The device width is reduced to less than half its original width with just 2mm of compression. The edge of the channel also appears to be relatively straight; although there is distortion at the edge this is likely due to the compression region only being 30mm wide whereas the channel is 40mm long. This reduction should equate to a drop in the minimum diameter of focused spheres from $6.9\mu\text{m}$ down to $2.7\mu\text{m}$. This is a similar change to that found using perpendicular stretching.

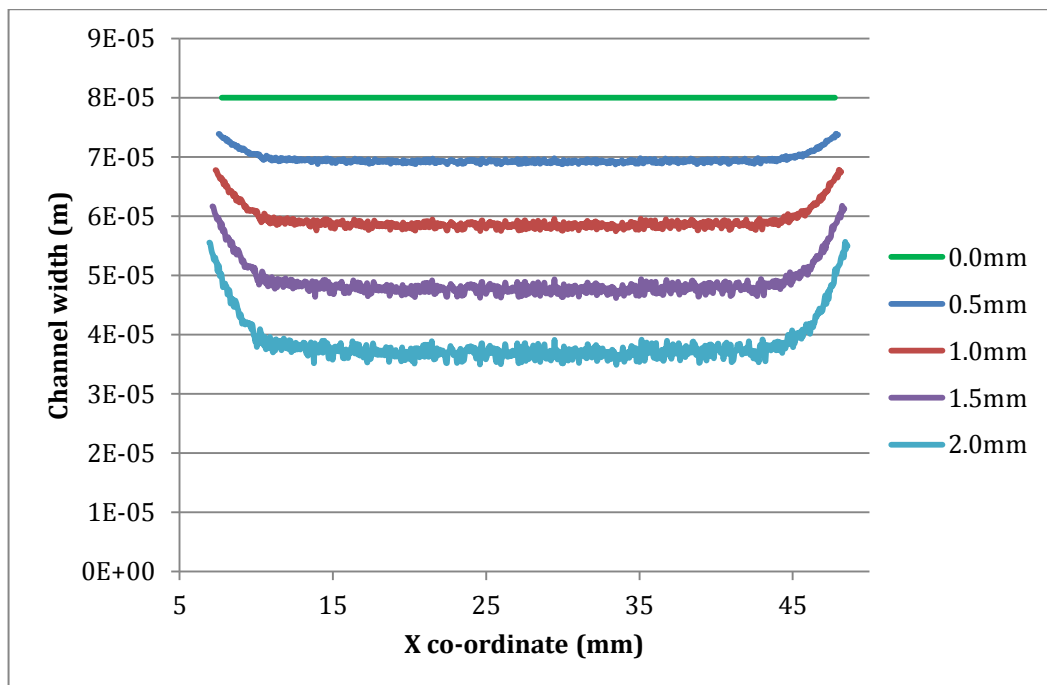


Figure 5-20: Simulation results of channel width along the length of the channel as the device is compressed by a given displacement (see legend). Shows that compression of the device causes a reduction in the width of the channel. The distortion at the ends of the channel is likely a result of the compression region being shorter than the channel length.

The perpendicular stretching device created a problem with the aspect ratio as the reduction in depth could potentially add additional equilibrium positions. It can be seen in Figure 5-21 that this is not a problem when the device is compressed. In fact, the aspect ratio increases as the device is compressed. The top and bottom walls appear to be curved but, unlike with perpendicular stretching, this should not be a problem as the focusing should occur along the straighter side-walls, rather than at the top and bottom.

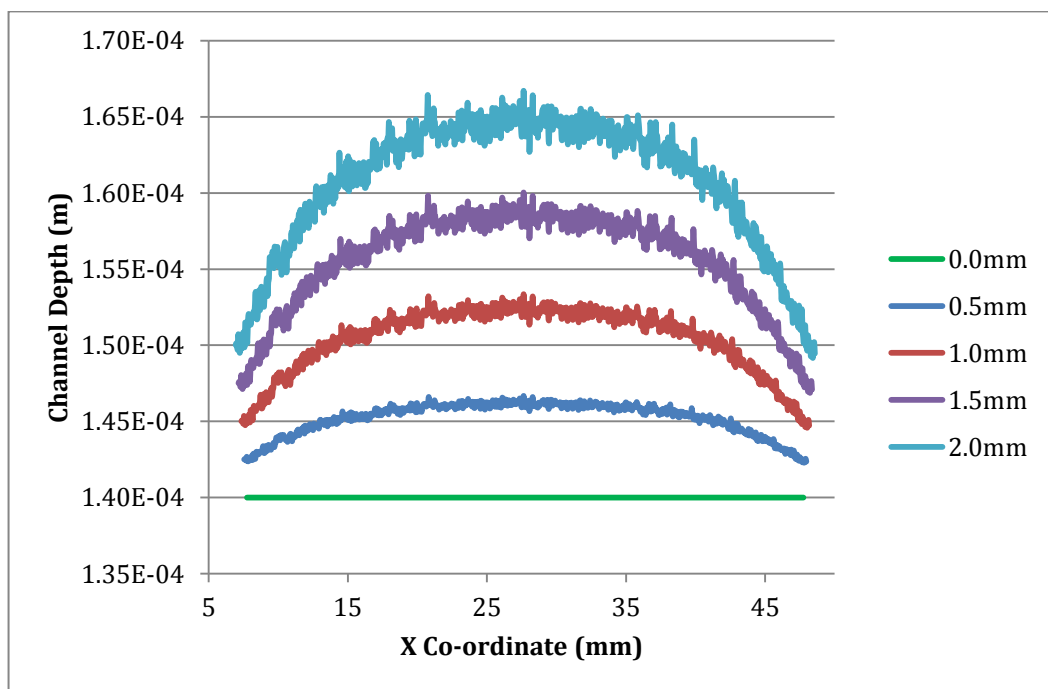


Figure 5-21: Results of compression simulations depicting the depth of the channel along its length as the device is compressed by a given displacement (see legend). Shows the channel depth increases as the device is compressed, this increase has a curved nature with a maxima at the channel midpoint (in terms of the channel length).

The average cross-sections of the channels are shown in Figure 5-22. This demonstrates the significant increase of the aspect ratio.

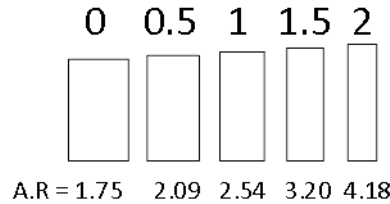


Figure 5-22: Scale illustration of the average cross-section of the focusing region channel when subjected to a given compressive displacement. The number above the channel cross-sections indicates the displacement (mm) whilst the number below shows the aspect ratio (A.R.). Channel width and depth calculated by taking averages from the data shown in Figure 5-20 and Figure 5-21. Highlights that compression of the device results in an increase in aspect ratio of the channel. The cross-sectional dimensions are: width x depth 0mm: 80 x 140 μ m, 0.5mm: 69.63 μ m x 145.22 μ m, 1mm: 59.26 μ m x 150.44, 1.5mm: 48.89 x 155.67 μ m, 2mm: 38.52 x 160.89 μ m.

These results suggest that compression is the most promising deformation technique to create a tuneable device, offering significant dimension change without any problematic change in the aspect ratio.

5.6 Modelling Sphere Focusing

Having established how the device can be deformed it was then deemed worthwhile to investigate how sphere focusing would be affected by the change in the channel dimensions.

5.6.1 Model Parameters

A two dimensional model was created using the ‘single phase, laminar flow’ and the ‘particle tracking’ physics modules in COMSOL Multiphysics. The 2D channel was 40mm long whilst the channel width was defined as the average width of the channel, found from the deformation simulations. The maximum inflow speed, U_m , was set to 0.1m/s but changing the channel width should lead to a change in the speed of flow through the channel. To

account for this, the inlet edge was fixed at $80\mu\text{m}$ wide with a short flow-rate control zone channel prior to the focusing channel. The flow-rate control zone allowed the inlet to expand or reduce to the width of the focusing channel, while maintaining the inlet flow rate edge parameter. This is shown in Figure 5-23.

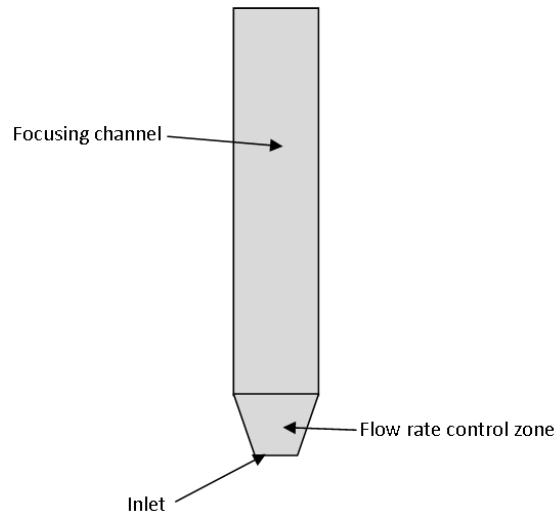


Figure 5-23: Illustration of the flow rate control zone used in the sphere focusing simulations. This was used at the channel inlet to account for the increase or decrease in flow rate that results from the expansion or reduction of the channel width. The flow rate parameter that is applied to the inlet edge remains constant whilst the flow through the focusing channel is altered by the channel width. This change in channel width is based on the results of section 5.5. The inlet shown here is for a channel subjected to a 6mm perpendicular stretch.

The model was simulated in two stages. The first stage used the laminar flow physics module with the boundary conditions set as shown in Table 5-3.

Table 5-3: Laminar flow boundary conditions used in sphere focusing simulations.

Boundary Condition	Parameters
Inlet	Velocity – $U_m/1.5$ [147]
Outlet	Pressure – 0kPa
Symmetry	Line representing the centre of the channel

Wall	Bounce
------	--------

A stationary solver was used to simulate the flow, in this case using the default PARDISO solver. Water was used as the fluid flowing through the channel.

The second stage was simulated using the particle tracing module for fluid flow physics. The walls were set to the bounce condition for all walls excluding the inlet and outlet to ensure spheres did not adhere to the side walls. The particle properties were specified such that they would be neutrally buoyant spheres with diameter a . Neutrally buoyant spheres were used as they can be carried in flow more readily and also are not subject to excessive gravitational or buoyancy forces. Two hundred of these particles were released with a uniform distribution from the inlet at a velocity set by the result of the laminar flow stage of the simulation. The outlet settings ensured that spheres would ‘freeze’ for analysis against the outlet, upon reaching it. Two forces were applied to the entire domain to simulate the forces that a sphere is subjected to when in flow. Firstly, a Stokes drag force was applied, again with the velocity set by the laminar flow result. Secondly, a custom force was applied to simulate the inertial lift force. This was applied by using the inertial lift force equation (5-2). This equation includes a lift coefficient term, f_c , which varies depending on position within the channel. To represent this in the model an approximate function had to be created. It has been stated by Di Carlo *et al.* that the lift coefficient is 0 at the channel centreline before rising with proximity to the channel wall until a maximum is reached [149]. The coefficient then decreases back to zero at a

distance 0.1-0.2 times the channel width from channel wall. The coefficient then becomes negative to indicate that the force is now acting away from the wall [149]. It has also been stated that, if $Re < 100$, the lift coefficient can be approximated as 0.5 [147, 159]. Given this information, a sine function was defined such that the waveform intersected zero at the channel centre, and at 0.15 times the channel width away from the wall. It was defined to have a magnitude such that its average was 0.5 (for $x \geq 0$). Using a sine function means that when $x < 0$ the sign of the function is switched to represent that the force is acting in the opposite direction, i.e. the force acts away from the channel centre in both directions until a sphere approaches the channel wall. This function is shown in Figure 5-24.

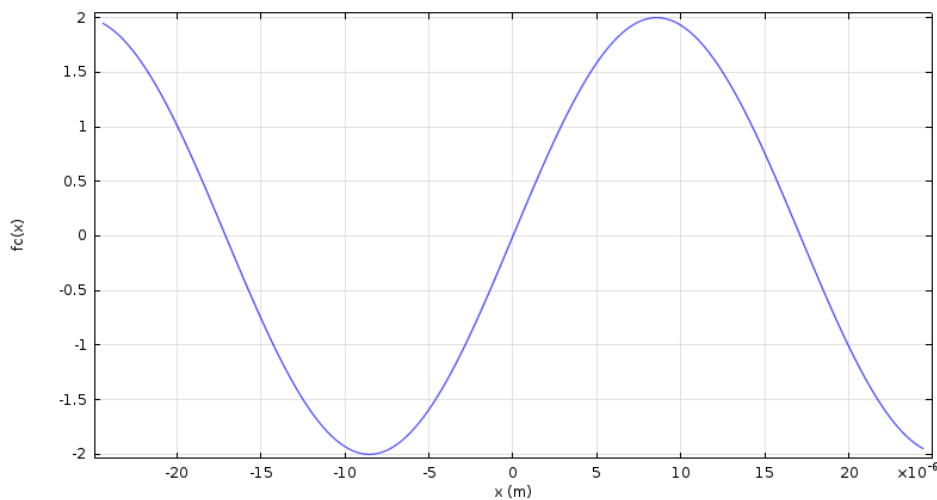


Figure 5-24: Lift coefficient as a function of the position, x , across the width of the channel. The horizontal axis is the distance from the centre of the channel in the x -direction. In this case the channel width is $48.86\mu\text{m}$ to simulate the device being compressed by 1.5mm . The lift coefficient is 0 at $x=0\text{m}$ (the centre of the channel) before rising to a maximum and dropping back to 0 at $0.15w$ from the channel wall. Beyond this it is negative as the force acts in a different direction. The average of the function from $x=0$ to the positive wall is 0.5, with the average equal to -0.5 for $x \leq 0$.

This function was used in the inertial lift equation where the velocity was represented by the flow velocity found in stage one of the simulation. This force was applied to the sphere throughout the channel. Unlike in the first stage, it was necessary to solve this stage using a time dependent solver. In this case, the default iterative GMRES solver was used to simulate over a time running from 0-5 seconds at 0.01 second intervals.

For both stages an extremely fine, free, triangular mesh was used. The predefined values were customised slightly to define the maximum element size, as a tenth of the channel width, and the minimum element size as a twentieth of the width.

The simulations carried out in this section used the channel geometries found in the deformation modelling. The channel width was defined as the average width found in the previous models, as simulating the curved sidewalls was not found to be possible due to the nature of the approximation of the lift coefficient. The channel depth was not defined, as the model is only two-dimensional; this means that any possible focus position at the top and bottom of the channel will not be represented. The channel length was also determined in the deformation simulations.

The particle diameters used were selected to match the diameters of the spheres that were available for experimentation. They were: 1.9 μm , 3 μm , 5 μm , 8 μm and 12 μm . In order to analyse their behaviour the particle position data was exported from COMSOL for analysis allowing the outlet distribution to be plotted,

5.6.2 Results and Discussion

To confirm the validity of the model it was tested against results in previously published works. Firstly the inertial focusing by *Zhou and Papautsky* was simulated [199]. By recreating the conditions used in this paper, it was possible to compare the results of the article and the model. As can be seen in Figure 5-25 the focusing appears to be relatively similar at three positions along the length of channel. In the simulation the sphere streams appear more clearly defined than in the experimental results, however this is likely due to the discrete nature of a simulation as opposed to a fluorescence intensity plot. Given this, the simulation and the published experiment appear to match up relatively well.

5 Inertial Sorting of Microspheres

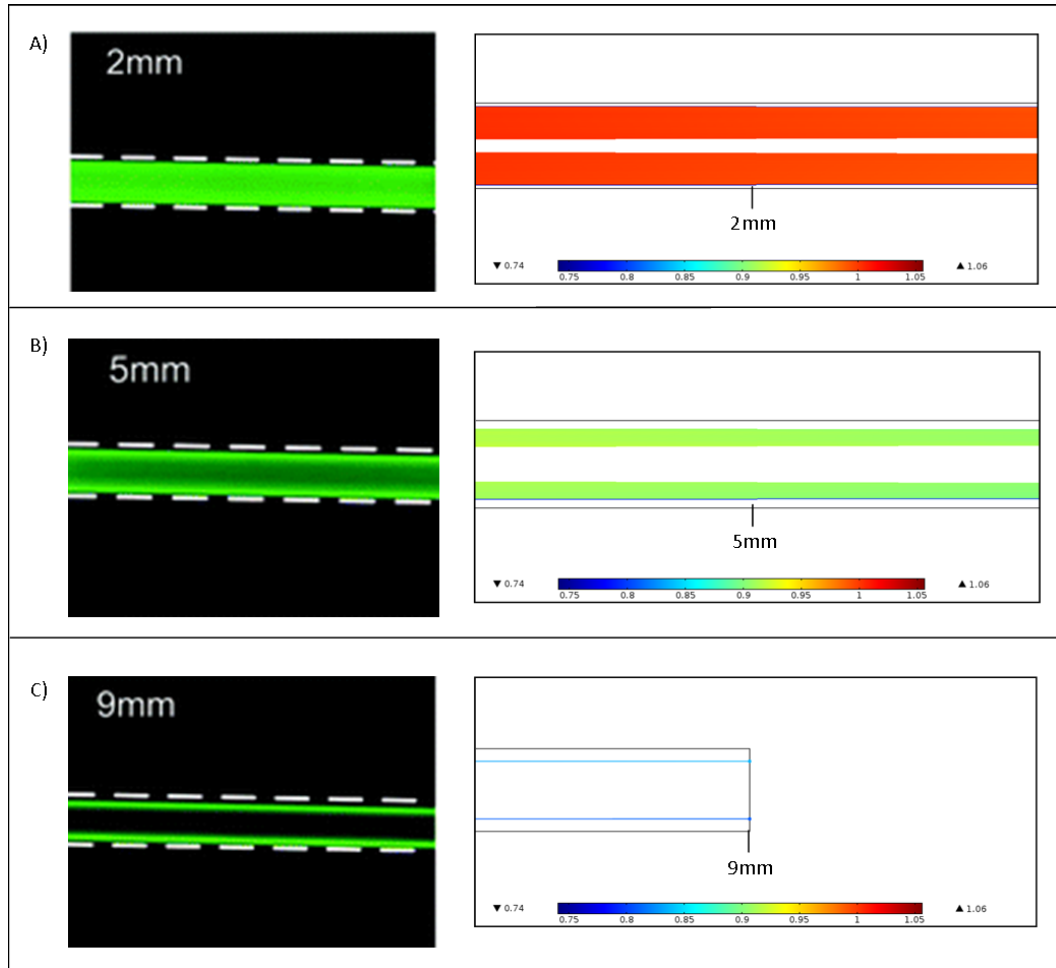


Figure 5-25: Comparison of model results (right) to experimental results (left) as reported by Zhou and Papautsky [199]. A) At 2mm along the channel little focusing has occurred with just the spheres right in the middle of the channel noticeably affected. B) 5mm along the channel some focusing has been achieved, two clearly distinct streams are emerging. C) 9mm along the channel, complete focusing has been achieved. The simulation results show the particle trajectories, the colour of these trajectories represent the speed of the particles when they passed that point. The colours represent a linear scale from 0.74 m/s (blue) up to 1.06 m/s (red). The particle diameter was $7.32\mu\text{m}$. The experimental spheres are tracked using fluorescent imaging.

The model was also tested against the work by *Bhagat* [159] where focusing was observed at a particle Reynolds number of 0.09 but not at 0.009. As can be seen in Figure 5-26 this is also the case when simulated using this model.

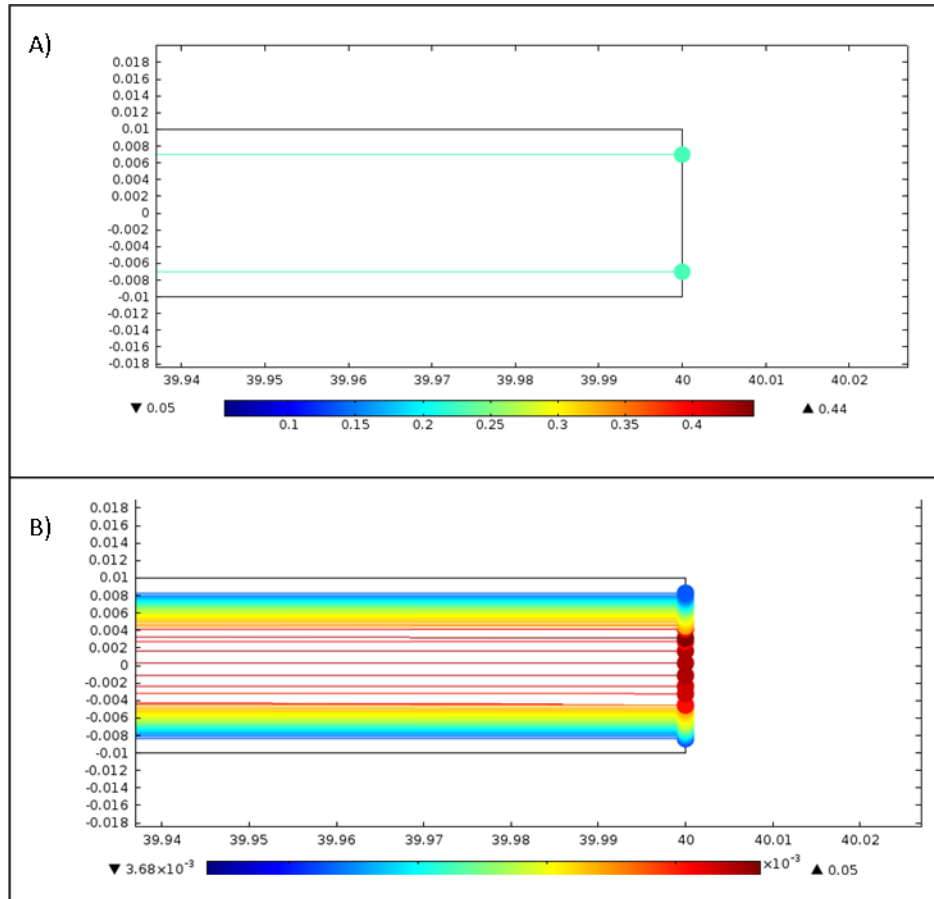


Figure 5-26: Simulation of experimental setup as reported by Bhagat showing the sphere positions at the outlet of the channel. A) Flow rate defined such that $Re_p=0.09$; much like in the referenced paper focusing is achieved as can be seen by the two distinct particle streams. Sphere speed indicated by colour on a linear scale from 0.05 m/s (blue) to 0.44 m/s (red). B) Flow rate defined to give $Re_p=0.009$; no significant focusing is achieved as can be seen by spheres being present across the full width of the channel. Sphere speed scale from 3.68×10^{-3} m/s (blue) to 0.05 m/s (red). These results are broadly in accordance with the reported experimental results from Bhagat. Particle diameter was $1.9\mu\text{m}$. Channel width was $20\mu\text{m}$. [159]

Having established that the model is capable of a reasonable approximation to observed behaviour, simulations were carried out to investigate how the spheres behaved in the deformable device. To save time and for easier analysis of the results the model was adapted such that only half of the

channel was simulated through the use of a symmetry boundary. The number of released spheres was reduced to 100 to reflect the fact that only half of the channel was simulated. The behaviour of the five sphere sizes in the undistorted device can be seen in Figure 5-27. It is clear from the distribution of the spheres at the channel outlet, that significant focusing is only present for spheres sized $8\mu\text{m}$ and $12\mu\text{m}$. This is as expected given the channel width dimensions that were calculated for Table 5-1.

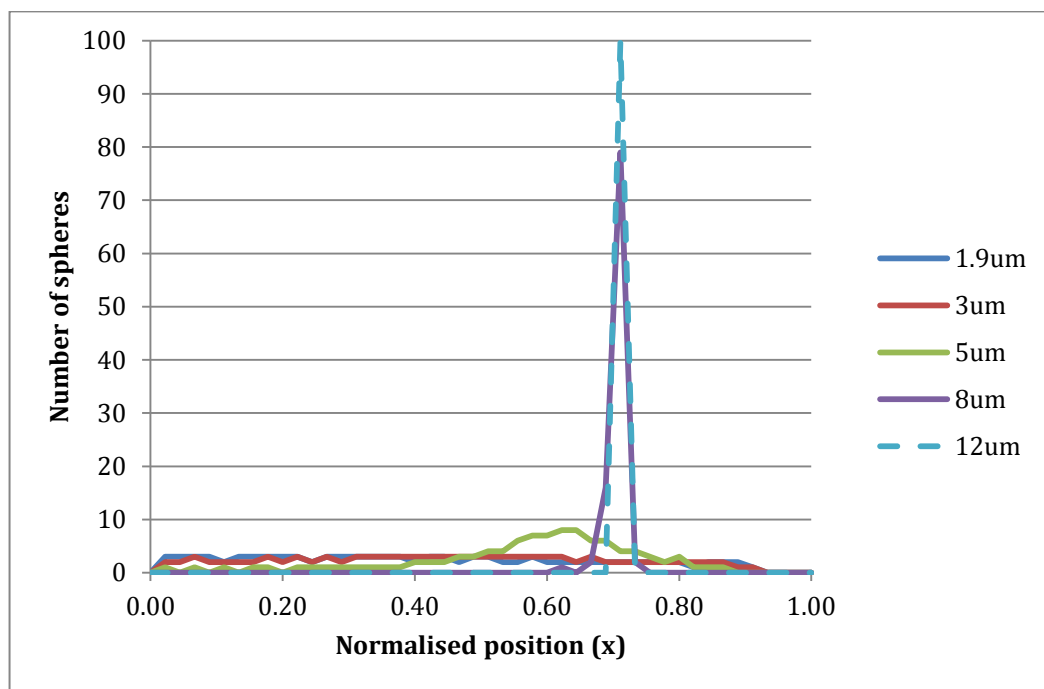


Figure 5-27: Sphere focusing simulation results depicting the normalised distribution of spheres measured at the channel outlet. Each line relates to the number of spheres at a given position for five different sphere sizes (see legend). One hundred spheres of each size were carried along a 40mm long, $80\mu\text{m}$ wide channel (only half of the channel width is simulated). Channel width is normalised and sphere data is broken up into 45 equal distribution bins.

By concentrating on the behaviour of the $8\mu\text{m}$ spheres, it is possible to illustrate how the perpendicular stretching device could work. Figure 5-28 shows that as the device is stretched across the channel, and the channel

becomes wider, the level of focusing decreases. This would allow for selection by exclusion, as when there is no stretching, the central outlet of the device would contain no $8\mu\text{m}$ spheres. However, as the device is stretched, the $8\mu\text{m}$ spheres would begin to exit through the central outlet too. This would mean that the minimum size of the sphere that can be focused, and therefore not be collected through the central outlet, can be increased by stretching the device.

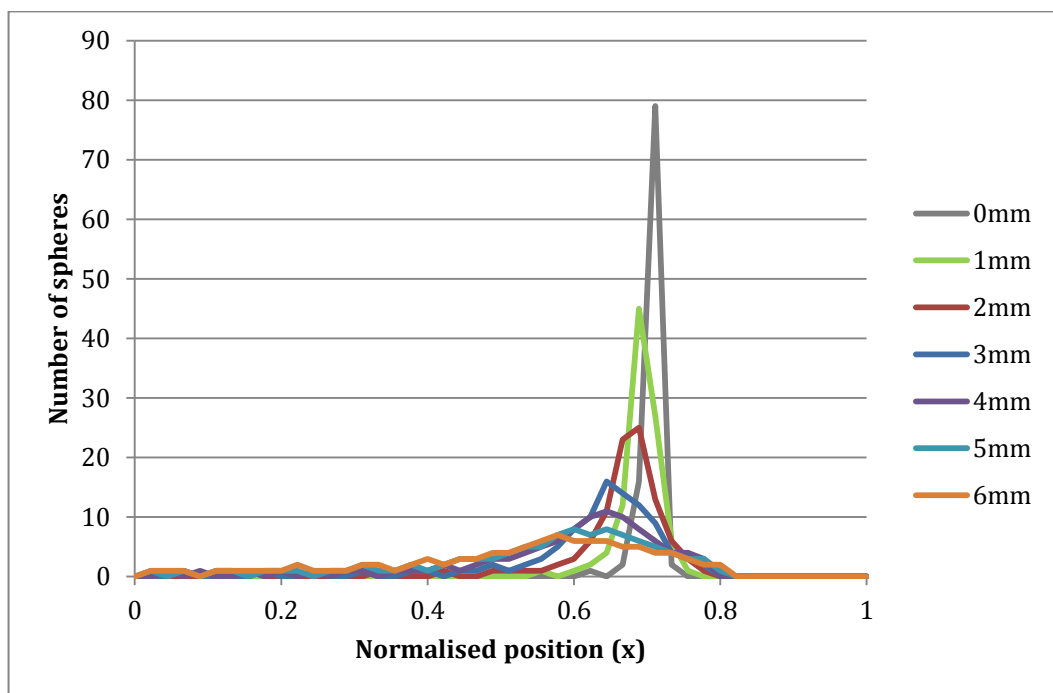


Figure 5-28: Simulated $8\mu\text{m}$ sphere distribution at the channel outlet as the device is stretched perpendicular to the channel by varying degrees (as given in graph legend). The channel width is normalised for each result with the data split into 45 equal bins. Results are for one half of the channel so the positions of one hundred spheres are shown here.

In order to understand the impact compression would have on the focusing behaviour, $3\mu\text{m}$ and $5\mu\text{m}$ spheres were used. As shown in Figure 5-27 these spheres remain unfocused when the device is not deformed. As the device is compressed, and the channel narrows, the $a/D_h > 0.07$ indicator is fulfilled

and the spheres begin to enter into focused streams. This is shown in Figure 5-29 and Figure 5-30, where it is clear that complete focusing has been achieved for $5\mu\text{m}$ spheres, when the device is compressed by 1.5mm and significant focusing of $3\mu\text{m}$ spheres has occurred at 2mm compression. This means there is substantial scope for tuning through compression. The uncompressed device is likely to have no $8\mu\text{m}$ or $12\mu\text{m}$ spheres travelling out of the central outlet meaning they have been filtered out. As the device is compressed, smaller sized spheres are added to this exclusion list. First, the $5\mu\text{m}$ spheres are filtered out, and then the $3\mu\text{m}$ spheres. Clearly this could be a very effective technique for sorting spheres. Indeed, if the spheres collected through the side outlets are collected it is easy to see how each size could be selected with this device. If we consider the five previously used sizes then at 2mm compression, all but the $1.9\mu\text{m}$ spheres would be focused, and, therefore, the spheres collected from the central outlet should all be $1.9\mu\text{m}$. If the spheres from the side outlets are passed through the device again with the compression reduced then the $3\mu\text{m}$ spheres become unfocused and can be collected through the central outlet. If this is repeated a number of times then each size can be removed excluding the $8\mu\text{m}$ and $12\mu\text{m}$ spheres (unless perpendicular stretching is also employed or the device is wider to begin with). It would however, most likely, not be completely accurate, as in the first stage, some of the $1.9\mu\text{m}$ spheres may enter the side outlets, meaning that they could potentially be collected with the $3\mu\text{m}$ spheres, or even larger spheres. This could potentially happen at every stage. A possible way to overcome this would be to focus the spheres in the middle of the channel before they enter the focusing region. This

would mean that the spheres that were not caused to migrate across the channel would be more likely to be collected through the central outlet. This could be achieved by having secondary inlet streams, either side of the main inlet. This would focus the flow stream out of the primary inlet to the middle of the channel (illustrated in Figure 5-31).

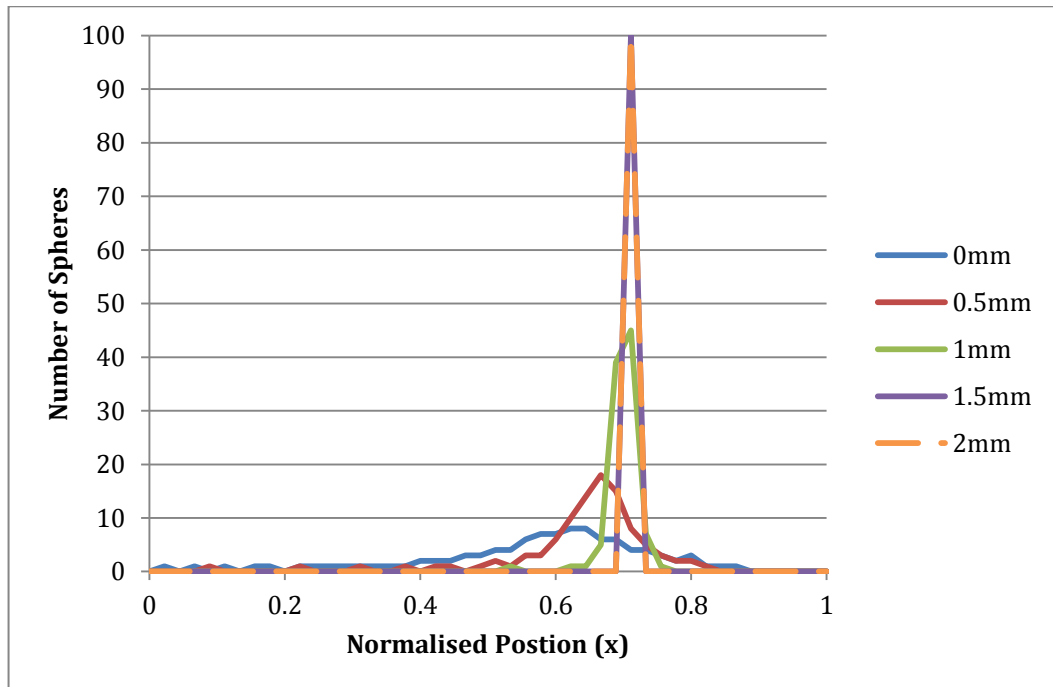


Figure 5-29: Simulated 5 μ m sphere distribution at the channel outlet as the device is compressed perpendicular to the channel by varying degrees (as given in graph legend). The channel width is normalised for each result with the outlet width split into 45 equal bins. A count of the number of spheres within each bin was taken. One hundred spheres were released for each simulation.

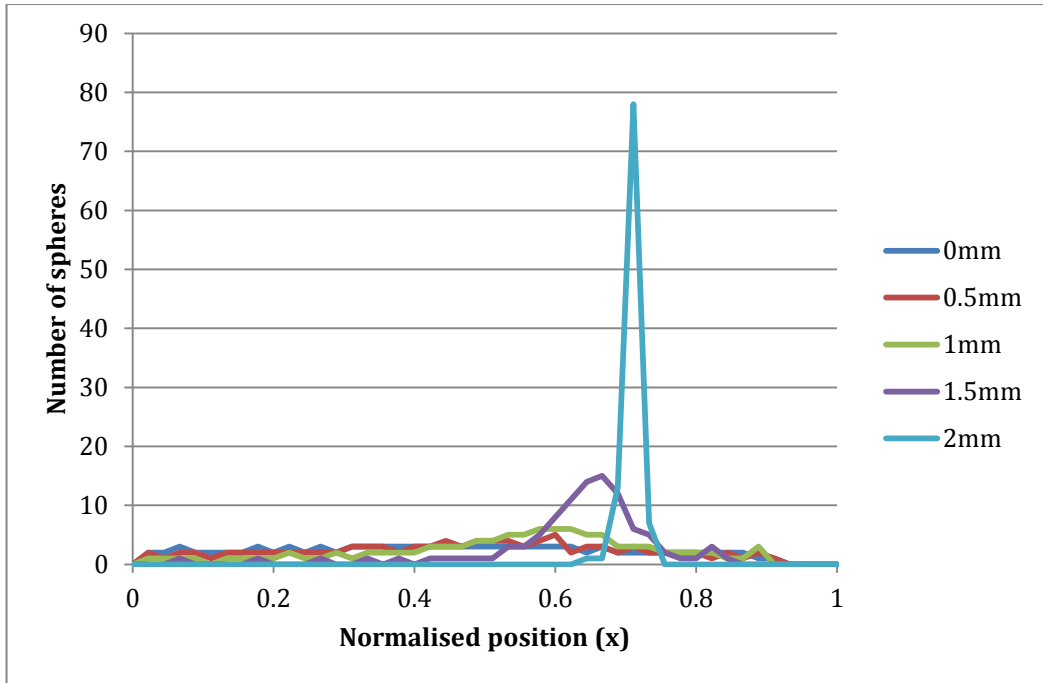


Figure 5-30: Simulated $3\mu\text{m}$ sphere distribution at the channel outlet as the device is compressed by varying degrees (as given in the legend). The channel width is normalised. The outlet was split into 45 equal bins and a sphere count was taken within each bin to determine sphere distribution. 100 spheres were released for each simulation.

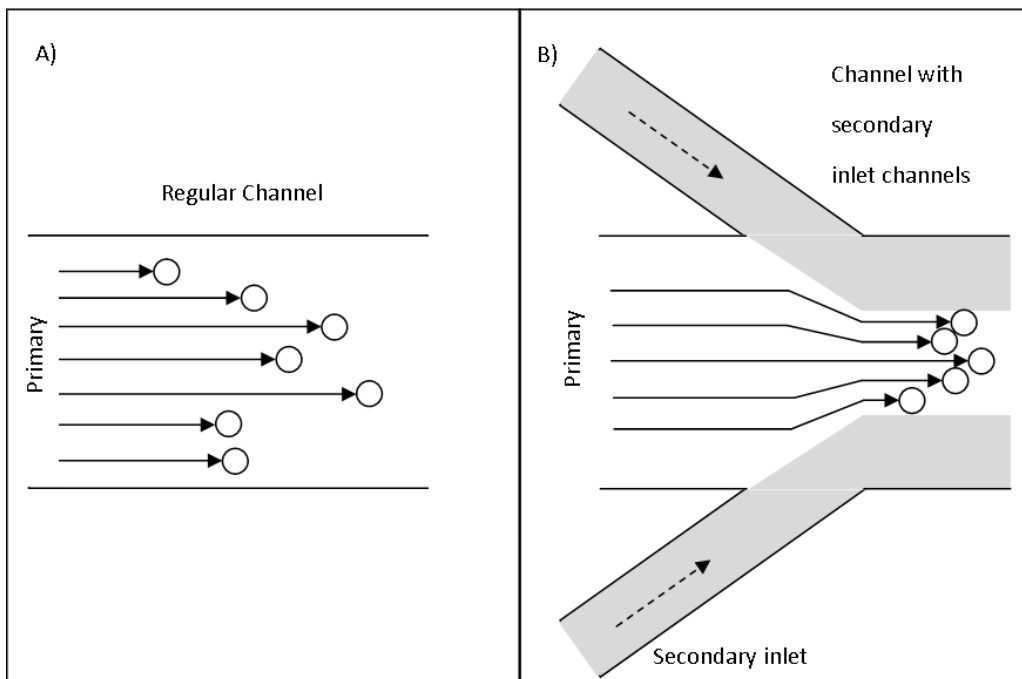


Figure 5-31: Illustration of the pre-focusing that could be achieved with secondary inlets.

A) Spheres are introduced to a regular straight channel, they can be distributed across the

width of the channel. B) Secondary inlets are used to introduce flows at the sides of the channel. This pushes the spheres into the centre of the channel prior to entering the focusing region thus reducing the chance of spheres that haven't been focused by inertial forces exiting through the side outlets. Solid black arrows indicate sphere paths, dashed arrows indicate flow.

The results of these simulations appear to suggest that compression is the most effective way to tune focusing via device deformation. As such, the compression technique will be the focus of any experimental work.

5.7 Device Testing

The simulations appear to show that deforming the device is a viable technique for tuning the focusing of microspheres, but it is necessary to test the device experimentally to confirm the validity of these simulations. The techniques used to fabricate the device are covered in the appendix at the end of this chapter.

5.7.1 Methods

The first stage of testing the device was to ensure that it could be deformed as expected. This was achieved by placing the device in a machining vice. The vice was positioned such that it compressed just the focusing region of the device. The width of the channel was measured using a measuring microscope (Nikon MM-800) connected to a digital measurement system (Metronics, Quadra-chek 200). The distance between each side of the vice was also measured to determine the extent of the compression. The experiment was performed three times to ensure that the device maintained its elasticity.

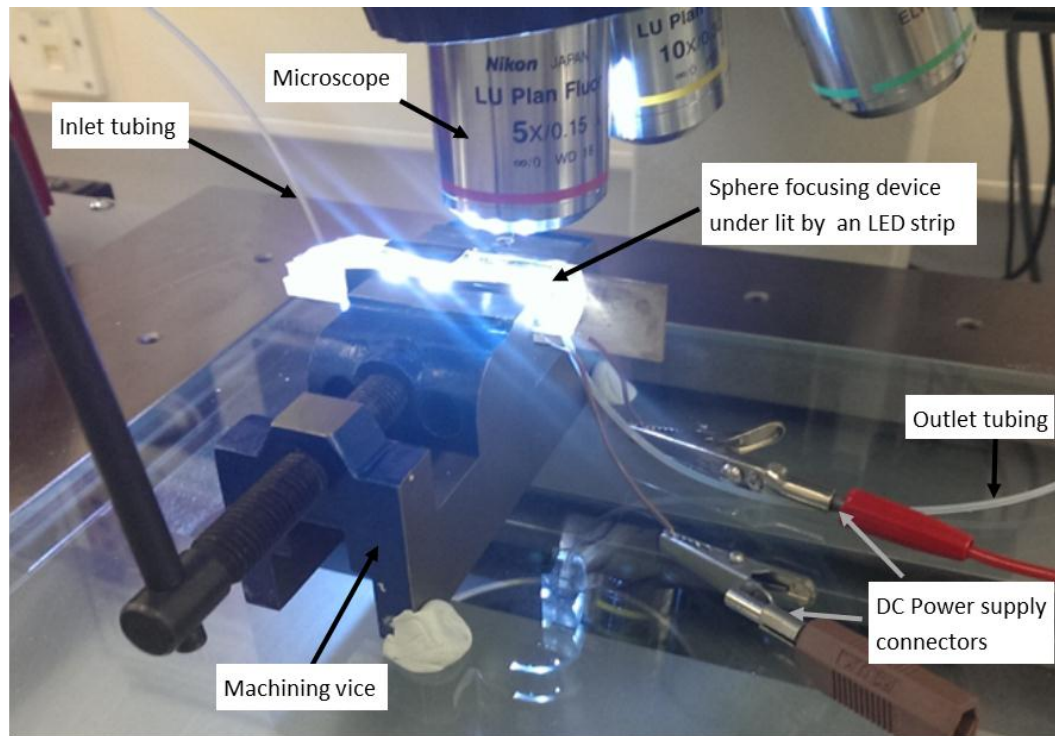


Figure 5-32: Sphere focusing device held in a machining vice. The machining vice applies a compressive force to the device inducing a reduction in the width of the focusing channel. The device is made from PDMS and is under lit by a strip of LEDs powered by a 12V DC power supply. A microscope is used observe the extent of the channel width reduction and determine sphere position.

To test whether focusing was occurring, silica spheres (ThermoFisher Scientific) were carried into the device in a solution of sodium metatungstate (ThermoFisher Scientific) and deionised water at a density of 2×10^6 spheres per ml. The solution was mixed at 55% sodium metatungstate and 45% deionised water, volume-to-volume, to achieve a density of 2000 kg/m^3 . This density was required, so that the spheres would be approximately neutrally buoyant as the sphere density is $1800\text{-}2200 \text{ kg/m}^3$. Neutral buoyancy was necessary to ensure that the spheres were carried from a syringe, placed in a syringe pump (AL-1000, WPI), into the focusing channel. The sodium metatungstate was found to solidify into a

white powder when it dried out so it was necessary to ensure the device was well flushed with deionised water after every use of the device.

The position of the spheres was determined using a high speed camera (Megaspeed MS40K) to observe the spheres as they passed through the channel. To supply sufficient light for the high speed camera, a strip of ultra-bright white LEDs (12V, 220mA, Maplin) were used to backlight the device by placing them into contact with the underside of the PDMS device. The LEDs were powered by a 12V DC power supply. The particle tracking tool in the Megaspeed AVI player software was used to determine sphere speed.

5.7.2 80 μ m Wide Channel Results and Discussion

Measurement of the channel width during compression is shown in Figure 5-33. It can be noted that, whilst the results of the experiment and the simulation do not match, the important features of device behaviour were still observed. The key features are the linear elastic nature of the material, as shown by the linear decrease in channel width, and also the extent of the channel width reduction that is possible. In both the simulation and the experiment, the channel width was reduced to approximately 40 μ m. However, the experiment was found to require twice the compression distance of the simulation. The difference between the two results may be a result of slight differences in the material properties between the simulation and the experiment. Additionally, the compressive force may not have been applied in a perfectly square manner. If the force was applied off-square it would cause the device to bow or contort slightly.

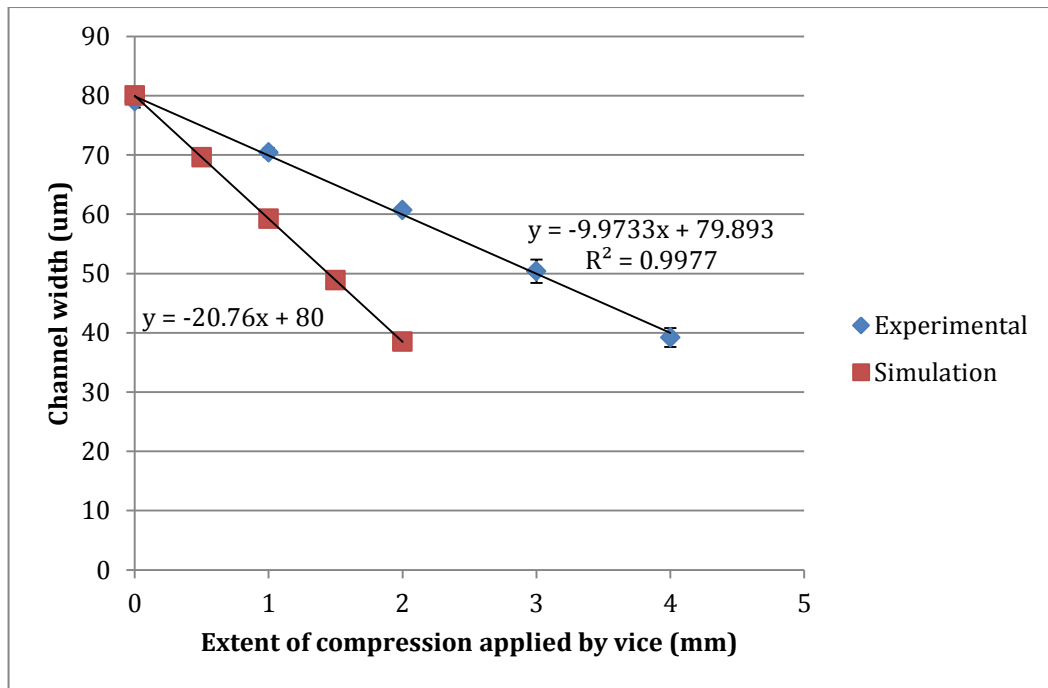


Figure 5-33: Focusing channel width as the distance between the two sides of the vice is reduced. The experimental results appear to show that the compression required experimentally is twice of that which was found through simulations.

The extent of the change in channel width is demonstrated in Figure 5-34. The side-by-side comparison clearly shows that the channel width has been dramatically reduced.

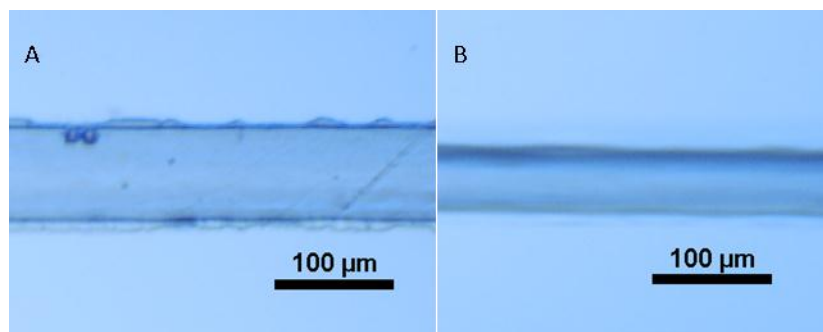


Figure 5-34: Comparison of channel width during compression of the sphere focusing device. A) Uncompressed device (80µm wide) and B) device subjected to 3mm compression (50µm wide).

12µm spheres were found to form two focused streams at a flow rate of 4.03 ml/hr without any compression. This is consistent with the simulations, but

the key to establishing the merit of compressing the channels, is to use spheres that are not focused when the device is uncompressed. To this end another test was carried out with $5\mu\text{m}$ spheres that would not be expected to focus without compression. However, it was not possible to observe the $5\mu\text{m}$ spheres, as the increased magnification required to view them meant there was insufficient light for it to be possible to view the spheres through the camera. As a result it was deemed necessary to produce a larger device so that the concept could be shown using $12\mu\text{m}$ spheres. The device needs to be wide enough to ensure that focusing of $12\mu\text{m}$ spheres did not occur when the device is not compressed. The manufacture of the larger channel device is covered in section 5.10.2.

5.7.3 Image Analysis

The sphere behaviour was analysed by recording the location of each sphere in a given frame of the high speed video. 20 frames were assessed at 25 frame intervals. The 25 frame interval between each sphere count was chosen as it gave sufficient time for spheres to traverse the entirety of the channel length under observation, thereby ensuring that spheres were not counted twice when collecting data. The images were enhanced by applying local equalization (50 height and weight) using Corel PHOTO-Paint X5, this helped highlight the sphere locations as demonstrated in Figure 5-35.

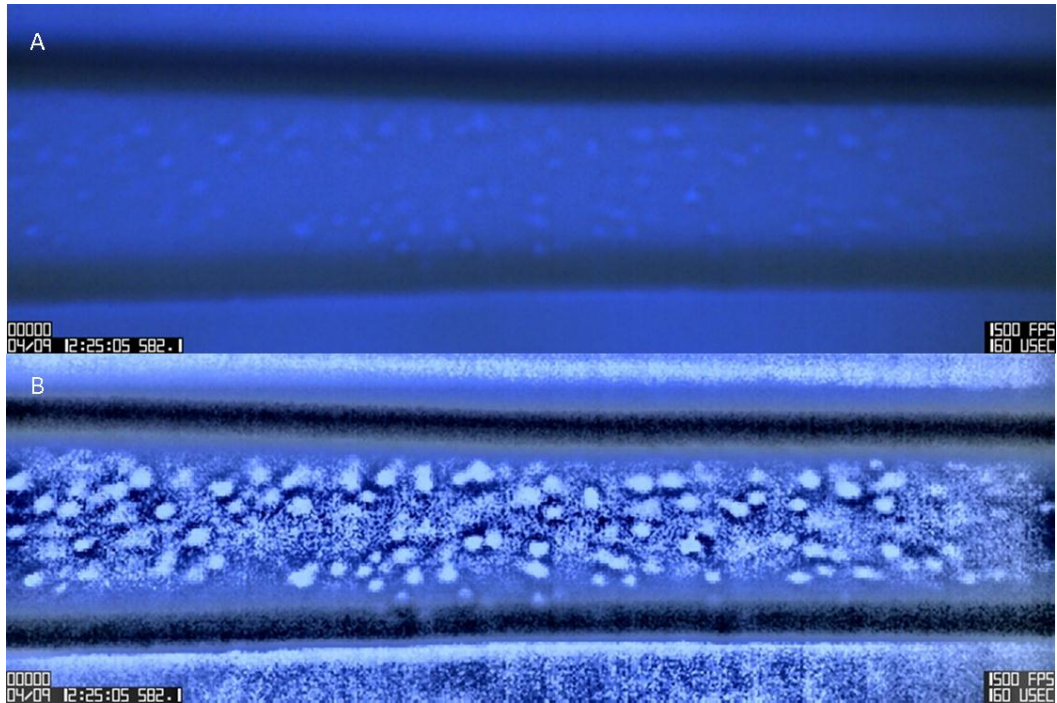


Figure 5-35: Single frame of the spheres observed flowing through the sphere focusing device with a channel width of $200\mu\text{m}$. Image taken using an MS40K high speed camera attached to an optical microscope. A) Raw unedited image. B) Local equalization applied to the image to highlight the sphere position.

Spheres were considered to be focused if the centre of the sphere was found to be within 0.25 times the channel width of the wall. Within this distance, spheres should enter the side outlets of the device rather than the central outlet, as long as there is no obstruction in the channel. Sphere position was assessed using Nikon NIS elements software 3.2 by positioning a line representing the division between ‘focused’ and ‘unfocused’ spheres and then counting the number of spheres on each side of these lines. This process is shown in Figure 5-36.

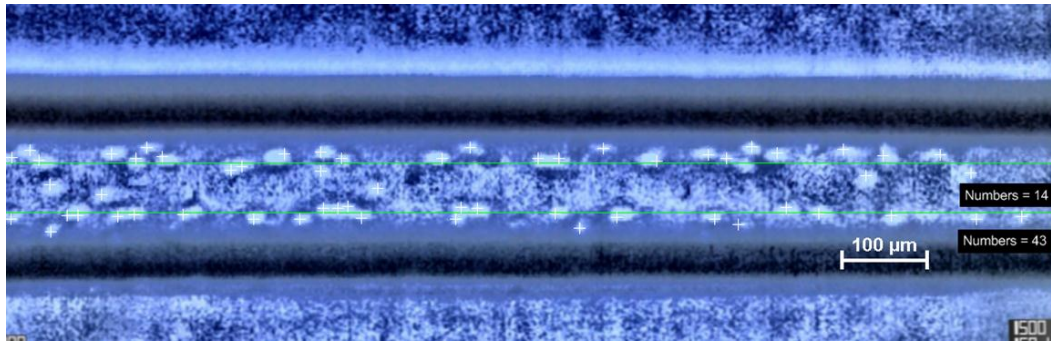


Figure 5-36: Single frame of video captured using a high frame rate camera attached to an optical microscope. Local equalisation has been applied to the image to highlight the sphere position. Sphere position analysis is performed using Nikon NIS elements 3.2 software. Two green lines indicate the division between the area of the channel where spheres are considered either ‘focused’ or ‘unfocused.’ The focused spheres, which are outside of these lines, are counted (in this case 43) and the unfocused spheres between the two lines (in this case 14) are also counted.

5.7.4 200 μ m Wide Channel Results and Discussion

By re-arranging equation 5-5 it was calculated that a channel width of 130 μ m should focus the spheres in a 40mm long channel with a maximum flow speed of 0.12 m/s. It was, therefore, imperative to ensure that the channel width could be compressed from 200 μ m to 130 μ m. It was shown to be possible to reduce the width of the channel sufficiently, which can be seen in Figure 5-37.

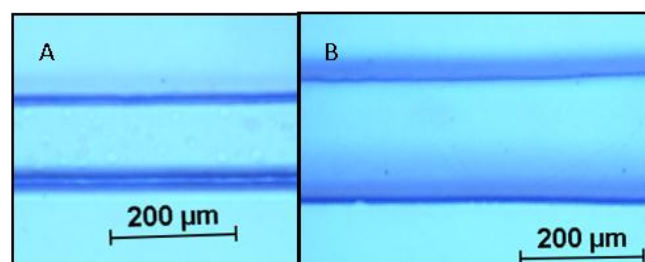


Figure 5-37: Photomicrograph to inspect the channel width of the larger channel sphere focusing device under differing levels of compression. A) Compressed to 130 μ m wide. B) Uncompressed, channel width 200 μ m.

Whilst examining the compression of the channel, it was noted that the channel width did not appear to be consistent over the entire depth of the channel. In order to gain a fuller understanding of this phenomenon the device was sectioned such that compression could be applied whilst viewing the cross-section of the channel. The two extremes of the observed channel compression are shown in Figure 5-38. This shows that there is some bowing of the channel walls as the compression is applied. Similar bowing was also observed in the COMSOL simulations. It was also noted at this stage that the channel depth was slightly less than initially thought, as it was measured at $350\mu\text{m}$ for a channel width of $200\mu\text{m}$. This is slightly less than the desired aspect ratio of 2. However, the channel depth increases as the channel width is reduced, such that the depth of the channel at $130\mu\text{m}$ wide is $374\mu\text{m}$, which is an aspect ratio in excess of 2.

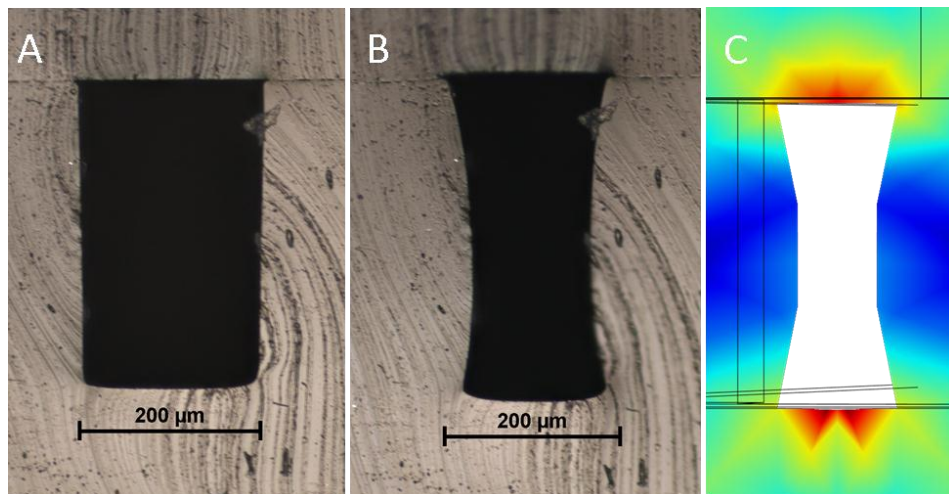


Figure 5-38: Channel cross-section of the larger sphere focusing device when A) Uncompressed and B) Compressed to $130\mu\text{m}$ wide. C) Cross section of channel when compressed in COMSOL Multiphysics simulation. The colours indicate the intensity of the von Mises stresses with red indicating relatively high stress and blue indicating lower stress.

Table 5-4: Channel cross-sectional dimensions as the larger sphere focusing device is compressed.

Channel Width	Channel Depth	Aspect Ratio
200 μm	350 μm	1.75
190 μm	352 μm	1.85
180 μm	354 μm	1.97
170 μm	357 μm	2.1
160 μm	361 μm	2.26
150 μm	366 μm	2.44
140 μm	370 μm	2.64
130 μm	374 μm	2.88

The focusing behaviour was then tested at a flow rate of 13.8 ml/hr at 10 μm channel width intervals, from 200 μm down to 130 μm wide. The results of these tests are shown in Figure 5-39. It appears that the level of focusing does improve as the channel width is reduced. The relationship appears to be linear. However, it is likely that the results would actually form a curve that flattens out at around 50%, as that is the level that corresponds to random sphere positioning. Evidence that this is the case can be seen in the results for 190 μm and 200 μm channel width, which were both 49.4% \pm 1.6%.

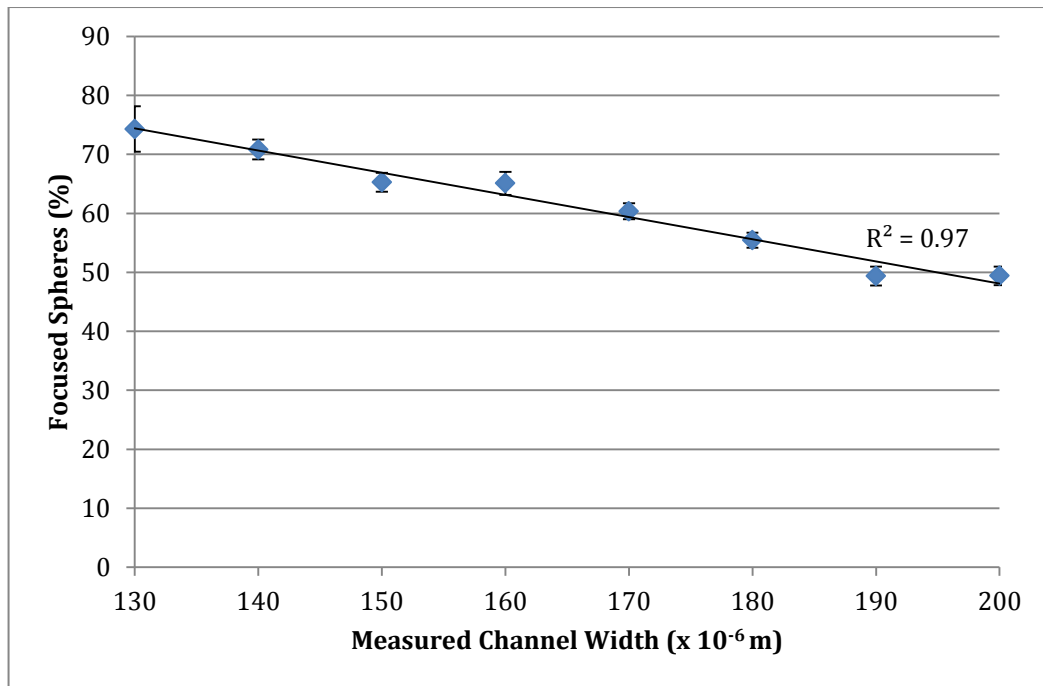


Figure 5-39: Percentage of spheres that are focused as the channel width is varied. Error bars represent 95% confidence level. The number of spheres counted, n , ranges from 45 to 104 for the data points shown. Inlet flow rate of 13.8 ml/hr.

The peak focusing level was 74.3% with a 95% confidence level of $\pm 3.9\%$ which is a relatively poor level of focusing when compared to some of the literature shown in section 2.2.4. But, this could possibly be improved by increasing the flow rate. The flow speed was selected so that 12 μm spheres would just about focus by the end of the channel, if it was 130 μm wide. However, the spheres are not all exactly 12 μm as can be seen in Figure 5-40. This polydispersity may cause some of the spheres to take longer to migrate across the channel to the equilibrium positions. The size distribution of the spheres was investigated using the auto measurement feature of NIS elements to measure the diameter of 518 spheres. The spheres were found to have a mean diameter of 13.18 μm with a standard deviation of 2.08. The diameter ranged from 4.31 μm up to 20.16 μm . This actually highlights the

real necessity for improved industrial size sorting, as this is a large distribution of sizes, despite these spheres being previously classified as 12 μm spheres by ThermoFisher scientific.

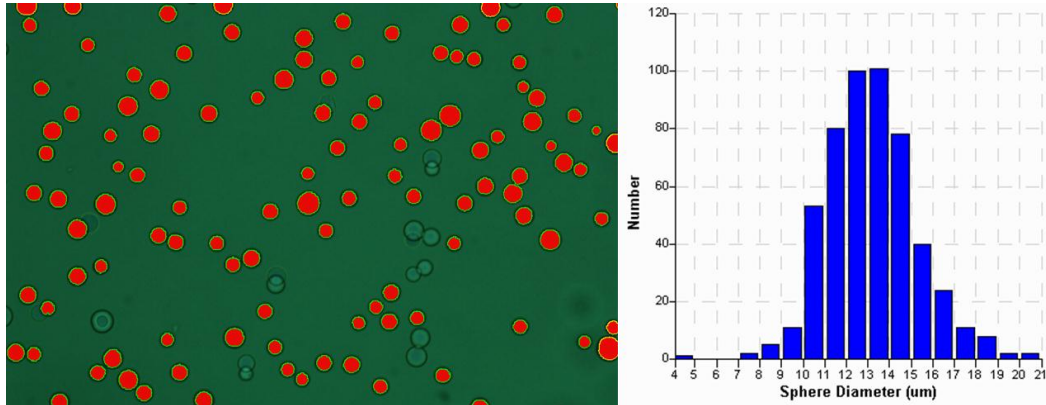


Figure 5-40: One of five photomicrographs (left) that were used to investigate sphere sizing alongside the size distribution of all the measured spheres (right). The spheres were measured using NIS elements auto measurement. Spheres that were auto detected and measured are shown in red. They are detected by using a defined threshold based on intensity and circularity.

In addition to this size distribution issue there was a problem with the carrier liquid viscosity. In the design stage the viscosity was estimated as being equal to water due to a lack of access to a viscometer. Access to a glass U-tube BS/U C viscometer was gained after the design and manufacture process and the sodium metatungstate and DI water solution was found to have a dynamic viscosity of 2.7×10^{-3} Pa.s. This higher viscosity meant that the focusing channel is not long enough for focusing to be achieved for many of the sphere sizes at the flow rate used here. By using the experimentally found viscosity and applying equation 5-5 to the sphere diameter data it was found that theoretically, only approximately 74% of the spheres would be expected to migrate to the equilibrium position given the channel length and

flow speed. This is within the range of the experimentally obtained result. The equation was adapted slightly to account for the line that determines focusing being 0.25 times the channel width from the wall as opposed to 0.1 times in the stated equation. The size distribution also explains why there appears to be some improvement in focusing at 180 μm channel width, despite it not fulfilling the $a/D_h > 0.07$ indicator for 12 μm spheres, as the larger spheres are big enough for some focusing to occur.

The theory that focusing could be improved by increasing the flow rate was investigated by raising the flow rate to 30 ml/hr. This flow rate should be fast enough for it to be possible to sort approximately 93% of the sphere sizes found in the previous measurement with a channel width of 130 μm based on the adapted equation 5-5. Based on the sphere sizes 100% exchange would not be possible with a channel width of 130 μm without raising the flow rate to levels that could damage the device. A comparison of the level of focusing when the channel is 200 μm wide, and 130 μm , is shown in Figure 5-41. There appears to be two focused streams when the channel is 130 μm wide, whereas, the spheres appear to be randomly positioned when the channel is 200 μm wide. This is a good indication that the device is behaving as expected.

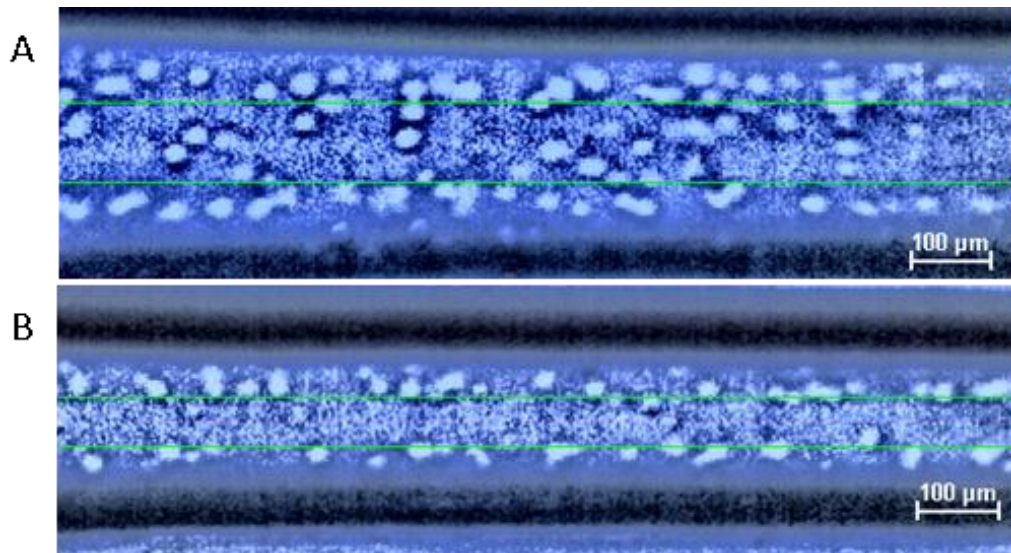


Figure 5-41: Single frames of video captured using a high speed camera attached to an optical microscope showing a comparison of focusing when the channel width is: A) 200 μm wide. The sphere position appears to be random. B) 130 μm wide. Spheres seem to be focused into two equilibrium streams. Flow rate is 30 ml/hr for both. Local equalisation has been applied to both images to highlight sphere positions.

By comparing the focusing behaviour of the device at the dimensional extremes of its operation, the impact of flow rate can be investigated. This comparison is shown in Table 5-5. The level of focusing has been improved for the narrow width, but not for the wider channel widths. This is an important result in confirming that the compression is a driving force in the tuning capacity of the device. Clearly, there is some tuning that can be achieved using flow-rate alone, as the improved tuning for 130 μm and 140 μm wide channels shows. However, the lack of significant improvement at 190 μm and 200 μm indicates that flow-rate is not the only driving factor. This is compelling evidence that the compression that exploits the critical a/D_h parameter is indeed a factor in tuning the sphere focusing. This finding was also backed up by simulations that recreated the experimental

circumstances using the model used in section 5.6. The model was adapted to provide a normally distributed range of sphere diameters such that they had a mean of $13.18\mu\text{m}$ and a standard deviation of $2.08\mu\text{m}$, as was found above from measuring the spheres used experimentally. Sphere focusing percentage in the simulations was determined in the same manner as was used experimentally. The improved performance of the simulation in comparison to experimental results may be a result of the curved nature of the walls found in the real world as opposed to the straight walls of the simulations. Additionally the simulations do not consider the depth of the channel. Despite these differences the simulations do appear to support the general trend of the results obtained.

Table 5-5: Comparison of the focusing performance achieved using the larger sphere focusing device at two different flow rates. Both experimental and simulation results are shown for comparison. Experimental focusing is shown with a 95% confidence level. Experimental data collected using the image analysis technique described in section 5.7.3.

Channel Width (μm)	Experimental		Simulation	
	Focusing at 13.8 ml/hr (%)	Focusing at 30 ml/hr (%)	Focusing at 13.8 ml/hr (%)	Focusing at 30 ml/hr (%)
200 μm	49.4% \pm 1.6%	51.4% \pm 2.1%	47.6%	49.6%
190 μm	49.4% \pm 1.6%	52.2% \pm 2.1%	47.2%	50.8%
140 μm	70.8% \pm 1.7%	83.5% \pm 2.2%	71.6%	96.4%
130 μm	74.3% \pm 3.9%	88% \pm 1.1%	82.8%	97.2%

The maximum experimental focusing rate of 88% is reasonably high and is comparable to previous sorting techniques that have been achieved using straight channel inertial sorting, which range from 69% - 97% [159, 161, 164]. This is not quite a like-for-like comparison, as the cited studies measured the spheres at the outlets, whereas these measurements were

taken in-flow. However, the laminar nature of flow in a straight microfluidic channel, means the position of the spheres at the end of the focusing channel, should predict which outlet the spheres will enter, as long as the pressure is not significantly different at the three outlets.

5.8 Future Work

There is ample scope for future work with this tuneable device. Primarily, the sorting capabilities of the device should be further examined by measuring spheres at the channel outlets to establish whether the device can be effectively used to reduce the size distribution of the spheres.

It would also be useful to determine how large the range of spheres that can be focused, actually is. This may require the use of alternative analysis techniques, such as the measurement of the fluorescence intensity of fluorescent spheres. The majority of inertial focusing work is analysed using fluorescent polystyrene spheres [153, 159, 161] and it is an approach that will be performed for a future publication. The initial project aim necessitated the use of silica, rather than polystyrene, spheres and, attempts to dye the spheres with fluorescent dye, proved to be unsuccessful. Although some dyeing occurred, the intensity was not sufficient that the sphere position could be determined. Polystyrene spheres would also allow the device to be used without the sodium metatungstate solution, and, therefore, reduce the likelihood of blockages occurring (as the sodium metatungstate dries to a powder).

The use of secondary inlets to initially focus spheres to the centre of the channel, would also be worth investigating, as it has the potential to ensure the majority of unfocused spheres exit through the central outlet.

It would also be worthwhile to develop a simple actuator to apply the compression. Without the need to under-light the device to view the spheres, it should be easier to ensure that the compression is applied along the channel plane and therefore prevent any bowing of the device. This would be improved by having plates above and below the device to hold it flat whilst compression is applied. A well designed actuator could also involve a level of computer control to target a sphere size-range using a specific level of compression.

Future work could also test the alternative deformation technique of stretching the device rather than compressing it.

5.9 Conclusion

Tuneable focusing of 12 μ m spheres via the compression of a deformable PDMS device has been demonstrated. An improvement of focusing from 51.4% \pm 2.1% up to 88% \pm 1.1% was achieved by applying a compressive force to reduce the channel width. Although sorting has not been demonstrated the ability to focus spheres is the key to achieving sorting and therefore a significant proportion of the development of a tuneable sorting device has been achieved. The ability to tune an inertial sorting device represents a significant advantage over alternative techniques. Previously, tuning in an inertial sorting device, was only achievable by varying the flow rate of the device. By introducing the ability to change to channel

dimensions, the range over which the device can be tuned is significantly expanded whilst still maintaining the flow-rate tuning capability demonstrated in previous published studies. To the best of the author's knowledge, this is the first time that device deformation has been used to tune an inertial focusing device.

The benefit of using compression as the deformation technique, as opposed to stretching techniques, was also demonstrated via COMSOL Multiphysics simulations. The advantage is primarily related to requirement to have high aspect ratio channels, in order to maintain just two equilibrium positions. Compression was shown to increase the aspect ratio of channels, whilst stretching was shown to maintain or reduce the channel aspect ratio.

5.10 Appendix - Device Fabrication

5.10.1 80 μ m Wide Channels

In order to test the tuneable focusing device it was first necessary to fabricate it using PDMS. To do this a mould needed to be created. The mould was made by spinning SU-8 2075 photoresist (Microchem) on to a 4" silicon wafer and exposing it to create the required pattern. The wafer was prepared within a clean room environment and was cleaned using acetone and deionised water prior to spinning. The wafer was dehydrated by placing it on a hotplate at 120°C for 30 minutes prior to the SU-8 being poured onto the wafer. It was poured onto the centre of the wafer such that approximately half of the wafer surface was covered. The SU-8 was spread using a spinner (SPS Spin 150) at 500 rpm for 30 seconds, at an acceleration rate of 100 rpm/s followed by a second spin at 1500 rpm for 60 seconds

with a 300 rpm/s acceleration, to achieve the desired depth of 160 μ m. Following the spin-coating, the wafer was placed onto a hot-plate that was then turned on and set to 65°C and left for 10 minutes. Starting at room temperature (approximately 22°C), and then ramping up to 65°C was found to give a flatter surface with fewer imperfections. This ramping was at the rate at which it took for the hot plate to heat up to 65°C from room temperature. After 10 minutes the temperature was set to 95°C allowing the temperature to ramp up over time and was then held there over the course of 35 minutes. SU-8 is a negative photoresist, which means that areas that are exposed to ultraviolet light become polymerised and remain after development. To expose the desired area a printed emulsion film photo-mask was used (JD Photo, 1 μ m resolution). The mask was placed in contact with the wafer and then a glass disc was placed on top to ensure a good contact was achieved. The wafer was then placed on a movable stage below a stationary ultraviolet LED (5mm, 20mW, 505nm, 15°, RS Components) whilst the stage moved to track the areas that were to be exposed at 1.5 mm/min. This is shown in Figure 5-42.

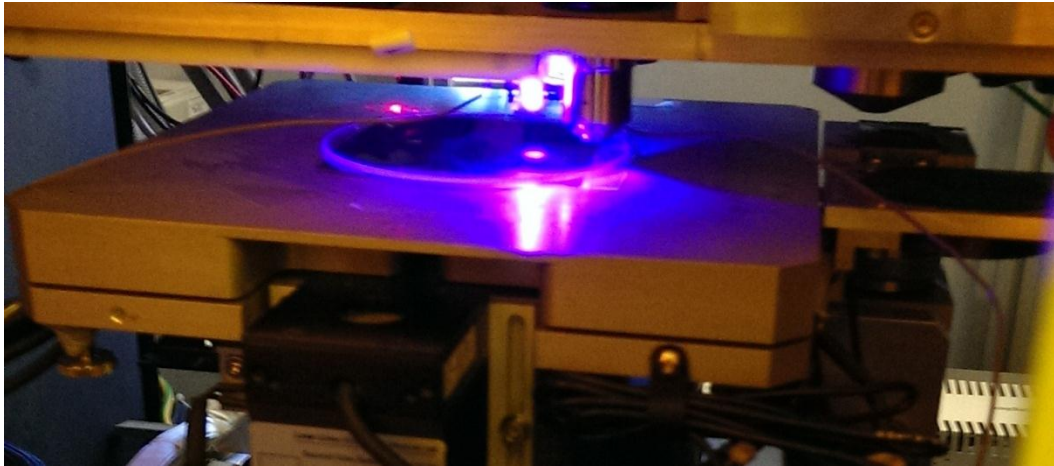


Figure 5-42: UV exposure setup. The wafer is exposed using a 405nm LED that is shone through an acetate photo-mask whilst the wafer is moved along the path of the channels at 1.5mm/min.

Following exposure the wafer was again transferred to the hot plate and baked for 8 minutes at 65°C and then at 95°C for 30 minutes. Finally, the wafer was developed in EC solvent for 20 minutes and then cleaned with isopropanol. The mould was measured using an interferometer (Veeco Wyko NT3300) and was found to be 80µm wide and 140µm deep. This was not quite the desired depth but the aspect ratio should be sufficient. This highlights another potential advantage of a tuneable device as it allows greater tolerance in the manufacturing process as errors can be accounted for through deformation.

Having created the mould the next stage was to create the PDMS device. The PDMS was made by mixing the elastomer and the curing agent (Dow Corning) at a 10:1 ratio. The PDMS was then degassed at 100mPa until there were no bubbles visible, before being poured over the wafer that has been placed in a foil-lined dish. This pressure was selected as below this pressure the PDMS tended to creep up the walls of the mixing vessel and spill over the

edge. PDMS was also poured into an empty dish with a flat bottom in order to create the secondary piece that would be bonded to the moulded PDMS.

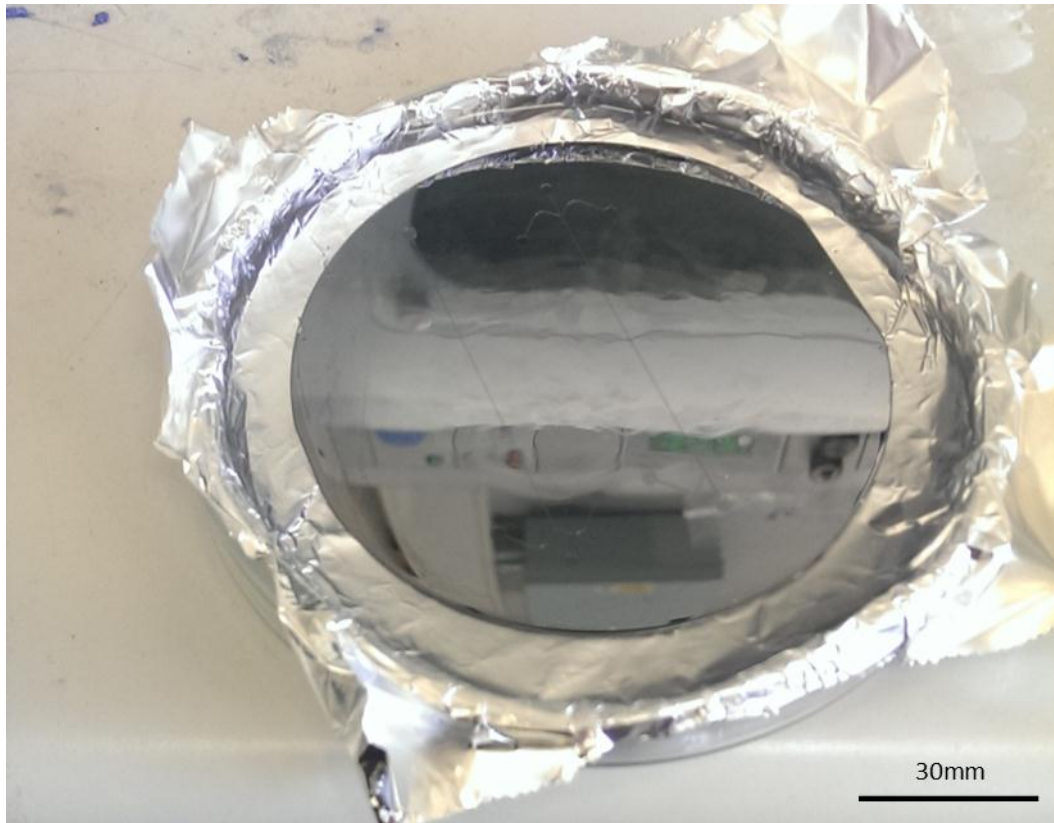


Figure 5-43: PDMS device fabrication. PDMS (10:1 elastomer to curing agent ratio) is poured onto a silicon wafer that has a negative mould of the channels made of SU-8 2075 on its surface. The wafer is placed in a foil lined glass dish so the PDMS can be removed from the mould after curing. The PDMS, wafer and dish are cured in an oven at 80°C for 3 hours.

The PDMS was placed into an oven at 80°C for 3 hours to cure it. The dishes were kept as level as possible to ensure that the PDMS was the same thickness for the entire device. After curing, the PDMS was removed from the mould in the clean room and a 1.2mm corer (Harris Uni-core) was used to make the inlet and outlet holes. The two layers of PDMS were then placed into a plasma etching machine (Plasma Technology) and exposed to air plasma at 150W for 30s. Immediately following the plasma exposure, the two sheets were brought into contact, causing an immediate and

irreversible bond. The final stage was to attach the tubing by pushing Teflon tubing into the cored holes (0.5mm I.D, 1.5mm O.D) and then applying a small amount of PDMS around the base of the tubing to ensure the joint remains sealed. The ends of the Teflon tubes were tapered using a grinding disc to reduce the chance of damaging the PDMS as they were pushed into the holes.

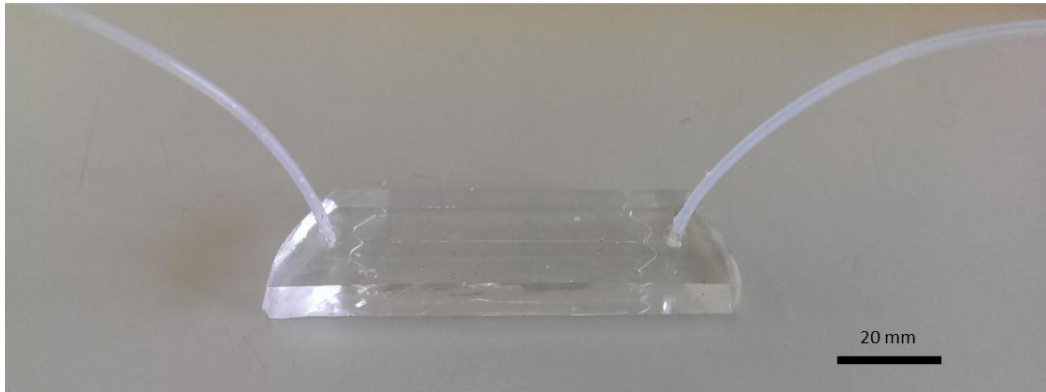


Figure 5-44: Complete PDMS device. Two layers of PDMS are bonded together to form a water tight seal around a microfluidic sphere focusing channel. Teflon tubing is inserted through holes at either end of the channel to create an inlet and an outlet. Additional PDMS is added around the base of the tubing to improve the seal around the hole into which the tubing is pushed. Fluid is supplied to the inlet by a syringe powered by a syringe pump at the end of the inlet tubing (not shown).

5.10.2 200 μ m Wide Channel

The process for making a larger device was very similar to the process used to make the 80 μ m device. To ensure the channel was sufficiently large that 12 μ m spheres would not be focused a channel cross-section of 200 μ m wide by 400 μ m deep was chosen. To achieve this, a mould was created by spinning two layers of SU-8 2075 onto a silicon wafer. As done previously, the SU-8 was spread using a spin speed of 500 rpm and an acceleration rate of 100 rpm/s for 30 seconds. This was followed by a spin at 1000 rpm for 60

seconds with an acceleration rate of 300 rpm/s to achieve the desired depth. Immediately after the spinning process the wafer was placed on a hot plate set to 65°C and left to bake for 15 minutes as the temperature ramped up followed by 45 minutes at a temperature of 95°C. After this baking period more SU-8 was applied to wafer on top of the previously baked SU-8. The spin process was then repeated followed by a secondary bake, again at 65°C and 95°C but this time for 7 and 30 minutes respectively. The wafer was exposed as before using a photomask, an ultraviolet (UV) LED and a moving stage. Due to the thicker layer of SU-8 a greater level of exposure was necessary. This was achieved by moving the stage more slowly than done previously, thereby extending the exposure time. The stage was moved at 1mm/min. Upon completion of the exposure, the wafer was baked for a third time. The baking time and temperature were the same as with the secondary bake. The wafer was developed for 45 minutes in EC solvent, which was refreshed every 15 minutes until only the desired channel remained.

The PDMS fabrication process remained identical to that used previously for the 80µm device.

6 Conclusion

This thesis has presented two novel devices, one to facilitate medium exchange and another device that allows for tuneable inertial sphere focusing to potentially enable size based sphere sorting.

The medium exchanger exploits the principals of fluidic resistance, along with the surface wetting characteristics, to continuously exchange two mediums. By employing mismatched flow rates, whereby the secondary medium is supplied at a higher flow rate, the primary medium can be extracted via an array of narrow perpendicular channels. The use of narrow channels allows droplets and spheres to be transferred from the first medium into the second medium whilst the exchange is occurring. Through simulations and experiments it has been demonstrated that the level of exchange is related to a number of factors associated with the device geometry along with the surrounding environment. It has been shown that the performance of the exchanger, as measured by the exchange percentage, can be improved by the following means:

- Milling the main flow channel such that it is approximately as deep as the separator channel array.
- Ensuring the outlet two channel is significantly deeper than the main flow channel and the separator channels.
- Increasing the number of channels up to 200 channels.
- Shortening the length of the separator channels, although this must be weighed against the diminished mechanical strength of shorter channels.

- Widening the separator channel width, however the size of the sphere to be exchanged must be considered when widening the channels to ensure that the spheres do not travel through the separator channels.
- Increasing the temperature of the primary fluid. This is due to the reduction in viscosity that occurs at higher temperatures. A slight increase in exchange can also be attributed to thermal expansion of the device itself.
- Increasing the length of the outlet one channel to increase the fluidic resistance of outlet one and therefore encourage more fluid to travel towards outlet two.

An application of the medium exchanger has been demonstrated that uses the exchanger to create a buffer region in the creation of alginate spheres. This buffer region reduces the chances of unwanted channel blockages occurring. The work presented here has expanded the knowledge of how the medium exchanger works but there is still significant scope for future work. The primary areas of focus for future work should be in optimisation of the device for a specific application to achieve the maximum possible exchange, throughput and sphere retention. Another area with potential scope for future work is making improvements to the surroundings of the device. The manifold used here was found to present some problems in terms of blockages occurring at the inlets and outlets of the microfluidic chips. As such it would be highly beneficial to redesign the manifold, or to investigate other manufacturing techniques that would not require a surrounding manifold such as PDMS manufacture or 3D printing.

The second device presented in this thesis is an inertial focusing device that uses the balance of inertial lift forces and wall effect induced forces to focus spheres into two distinct streams. The focusing of spheres can potentially facilitate sphere sorting as the inertial lift force is dependent on the sphere size. The advancement presented here is the use of device deformation to tune the focusing. Along with sphere size, inertial focusing is also dependent on channel geometries therefore, by deforming the device such that there is a reduction in the channel width, different sphere sizes can be focused. Simulations were used to determine the optimum technique for deforming PDMS device and it was found that compression was a more effective technique than stretching in terms of the extent of the channel geometry change that was achievable and also in terms of the aspect ratios achieved. Given this information a simple mechanical actuator was used to reduce the channel width of a straight channel within a PDMS device from 200 μm to 130 μm . This deformation was shown to improve the focusing of 12 μm silica spheres from 51.4% \pm 2.1% up to 88% \pm 1.1%. To the authors knowledge this is the first time that device deformation has been used to tune an inertial focusing device. This device could be further developed to show actual sorting of spheres by using well placed outlets to collect unfocused spheres independently of the focused spheres. Focusing could also potentially be improved by using additional inlets to focus all spheres to the centre of the channel prior to entering the inertial focusing channel. This would decrease the chances of spheres being randomly positioned such that they could be incorrectly classified as focused. There is also scope for improving the device deformation by developing an actuator specifically for the purpose of

compressing the PDMS device. This could achieve greater accuracy and repeatability when compressing the device to specific channel widths. Future work should also look to investigate the impact of the wall curvature that was observed along the length of the channel and also the pinching across the depth of the channel. It would be beneficial to understand to what extent, if any, this bending affects the inertial focusing.

7 References

1. Hohenesche, C.d.F.v., V. Ehwald, and K.K. Unger, *Development of standard operation procedures for the manufacture of n-octadecyl bonded silicas as packing material in certified reference columns for reversed-phase liquid chromatography*. *Journal of Chromatography A*, 2004. **1025**(2): p. 177-187.
2. Scientific, F. *Thermo Scientific™ 8000 Series Silica Particle Size Standards*. [cited 2014 28/04/14]; Available from: http://www.fishersci.com/ecommerce/servlet/fsproductdetail_10652_10718618_-1_0.
3. Pihl, J., M. Karlsson, and D.T. Chiu, *Microfluidic technologies in drug discovery*. *Drug Discovery Today*, 2005. **10**(20): p. 1377-1383.
4. Dittrich, P.S. and A. Manz, *Lab-on-a-chip: microfluidics in drug discovery*. *Nature Reviews Drug Discovery*, 2006. **5**(3): p. 210-218.
5. Tabeling, P., *Introduction to Microfluidics*. 2 ed. 2006, Oxford: Oxford University Press. p. 1-14.
6. Reynolds, O., *An experimental investigation of the circumstances which determine whether the motion of water shall be direct or sinuous, and of the law of resistance in parallel channels*. *Proceedings of the Royal Society of London*, 1883. **35**(224-226): p. 84-99.
7. Feynman, R.P., *There's plenty of room at the bottom*. *Engineering and Science*, 1960. **23**(5): p. 22-36.
8. Hartstein, A.M. and K.E. Petersen, *Micromechanical display logic and array*. 1980, Google Patents.
9. Frobenius, W.D., A.C. Sanderson, and H.C. Nathanson, *A Microminiature Solid-State Capacitive Blood Pressure Transducer with Improved Sensitivity*. *Biomedical Engineering, IEEE Transactions on*, 1973. **BME-20**(4): p. 312-314.
10. Terry, S.C., J.H. Jerman, and J.B. Angell, *A gas chromatographic air analyzer fabricated on a silicon wafer*. *Electron Devices, IEEE Transactions on*, 1979. **26**(12): p. 1880-1886.
11. Lovelock, J.E., *LOVELOCK VAPOR PHASE DETECTORS*. 1972, Google Patents.
12. Bollet, C., *Dispositif de mélange de deux liquides (Device for mixing two liquids)*. 1979.
13. Manz, A., et al., *Planar chips technology for miniaturization and integration of separation techniques into monitoring systems: Capillary electrophoresis on a chip*. *Journal of Chromatography A*, 1992. **593**(1-2): p. 253-258.
14. Harrison, D.J., et al., *Micromachining a miniaturized capillary electrophoresis-based chemical analysis system on a chip*. *SCIENCE-NEW YORK THEN WASHINGTON-*, 1993. **261**: p. 895-895.
15. Jacobson, S.C., et al., *Effects of Injection Schemes and Column Geometry on the Performance of Microchip Electrophoresis Devices*. *Analytical Chemistry*, 1994. **66**(7): p. 1107-1113.

16. Harrison, D.J., A. Manz, and P.G. Glavina. *Electroosmotic pumping within a chemical sensor system integrated on silicon*. in *Solid-State Sensors and Actuators, 1991. Digest of Technical Papers, TRANSDUCERS '91., 1991 International Conference on*. 1991.
17. Weigl, B.H. and P. Yager, *Tech. Sight*. Science, 1999. **283**(5400): p. 346-347.
18. Evans, J., D. Liepmann, and A.P. Pisano. *Planar laminar mixer*. in *Proceeding of the 10th IEEE international workshop on micro electro mechanical systems (MEMS'97), Nagoya, Japan*. 1997.
19. Wilding, P., M.A. Shoffner, and L.J. Kricka, *PCR in a silicon microstructure*. *Clinical Chemistry*, 1994. **40**(9): p. 1815-8.
20. Northrup, M.A., et al., *A Miniature Analytical Instrument for Nucleic Acids Based on Micromachined Silicon Reaction Chambers*. *Analytical Chemistry*, 1998. **70**(5): p. 918-922.
21. Smith, D.E. and S. Chu, *Response of flexible polymers to a sudden elongational flow*. *Science*, 1998. **281**(5381): p. 1335-1340.
22. Altendorf, E., et al., *Results Obtained using A Prototype Microfluidics-Based Hematology Analyzer*, in *Micro Total Analysis Systems '98*, D.J. Harrison and A. Berg, Editors. 1998, Springer Netherlands. p. 73-76.
23. Eijkel, J.C., et al., *Micromachined heated chemical reactor for pre-column derivatisation*. *Journal of Chromatography A*, 1998. **815**(2): p. 265-271.
24. Whitesides, G.M., *The origins and the future of microfluidics*. *Nature*, 2006. **442**: p. 368-373.
25. Comer, E. and M.G. Organ, *A microcapillary system for simultaneous, parallel microwave-assisted synthesis*. *Chemistry (Weinheim an der Bergstrasse, Germany)*, 2005. **11**(24): p. 7223-7227.
26. Jensen, K.F., *Microreaction engineering--is small better?* *Chemical Engineering Science*, 2001. **56**(2): p. 293-303.
27. Sia, S.K. and G.M. Whitesides, *Microfluidic devices fabricated in Poly(dimethylsiloxane) for biological studies*. *ELECTROPHORESIS*, 2003. **24**(21): p. 3563-3576.
28. Effenhauser, C.S., et al., *Integrated Capillary Electrophoresis on Flexible Silicone Microdevices: Analysis of DNA Restriction Fragments and Detection of Single DNA Molecules on Microchips*. *Analytical Chemistry*, 1997. **69**(17): p. 3451-3457.
29. Doyle, P.S., et al., *Self-Assembled Magnetic Matrices for DNA Separation Chips*. *Science*, 2002. **295**(5563): p. 2237.
30. Kim, U., et al., *Selection of mammalian cells based on their cell-cycle phase using dielectrophoresis*. *Proceedings of the National Academy of Sciences*, 2007. **104**(52): p. 20708-20712.
31. Nisisako, T., T. Torii, and T. Higuchi. *Formation of Droplets Using Branch Channels in a Microfluidic Circuit*. 2002. Citeseer.
32. Tice, J.D., et al., *Formation of droplets and mixing in multiphase microfluidics at low values of the Reynolds and the capillary numbers*. *Langmuir*, 2003. **19**(22): p. 9127-9133.
33. Garstecki, P., et al., *Formation of droplets and bubbles in a microfluidic T-junction—scaling and mechanism of break-up*. *Lab on a Chip*, 2006. **6**(3): p. 437-446.

34. Burns, M.A., et al., *An Integrated Nanoliter DNA Analysis Device*. Science, 1998. **282**(5388): p. 484-487.
35. Ong, S.-E., et al., *Fundamental principles and applications of microfluidic systems*. Frontiers in Bioscience, 2008. **13**: p. 2757-2773.
36. Tesař, V., *Pressure-driven microfluidics*. 2007: Artech House. p. 20-22.
37. Li, D., *Encyclopedia of microfluidics and nanofluidics*, ed. D. Li. Vol. 3. 2008. p. 2094.
38. Stokes, S.G.G., *On the Friction of Fluids in Motion, and the Equilibrium and Motion of Elastic Solids*. 1846.
39. Poiseuille, J.L.M., *Experimental investigations upon the flow of liquids in tubes of very small diameter*. Vol. 1. 1940.
40. Brown, R., *XXVII. A brief account of microscopical observations made in the months of June, July and August 1827, on the particles contained in the pollen of plants; and on the general existence of active molecules in organic and inorganic bodies*. The Philosophical Magazine, or Annals of Chemistry, Mathematics, Astronomy, Natural History and General Science, 1828. **4**(21): p. 161-173.
41. Albert Einstein, R.F., A D W Cooper, *Investigations on the Theory of Brownian Movement*, ed. R. Furth. 1956: Dover Publications.
42. Bakunin, O.G., *Turbulence and diffusion: scaling versus equations*. Vol. 101. 2008: Springer.
43. Tabeling, P., *Introduction to Microfluidics*. 2 ed. 2006, Oxford: Oxford University Press. p. 139-140.
44. Young, T., *An Essay on the Cohesion of Fluids*. Philosophical Transactions of the Royal Society of London, 1805. **95**(ArticleType: research-article / Full publication date: 1805 /): p. 65-87.
45. Gascoyne, P.R. and J. Vykoukal, *Particle separation by dielectrophoresis*. Electrophoresis, 2003. **23**: p. 1973-1983.
46. Voldman, J., *Electrical forces for microscale cell manipulation*. Annual Review of Biomedical Engineering, 2006. **8**(1): p. 425-454.
47. Prakash, M. and N. Gershenfeld, *Microfluidic Bubble Logic*. Science, 2007. **315**(5813): p. 832-835.
48. Fuerstman, M.J., P. Garstecki, and G.M. Whitesides, *Coding/Decoding and Reversibility of Droplet Trains in Microfluidic Networks*. Science, 2007. **315**(5813): p. 828-832.
49. Morton, K.J., et al., *Crossing microfluidic streamlines to lyse, label and wash cells*. Lab on a Chip, 2008. **8**(9): p. 1448-1453.
50. Tornay, R., T. Braschler, and P. Renaud, *Wide channel dielectrophoresis-based particle exchanger with electrophoretic diffusion compensation*. Lab on a Chip, 2009. **9**(5): p. 657-660.
51. Lenshof, A. and T. Laurell, *Continuous separation of cells and particles in microfluidic systems*. Chemical Society Reviews, 2010. **39**(3): p. 1203-1217.
52. Giddings, J.C., *A New Separation Concept Based on a Coupling of Concentration and Flow Nonuniformities*. Separation Science, 1966. **1**(1): p. 123-125.
53. Giddings, J.C., *A System Based on Split-Flow Lateral-Transport Thin (SPLITT) Separation Cells for Rapid and Continuous Particle*

- Fractionation*. Separation Science and Technology, 1985. **20**(9-10): p. 749-768.
54. Nilsson, A., et al., *Acoustic control of suspended particles in microfluidic chips*. Lab on a Chip, 2004. **4**(2): p. 131-135.
 55. Laurell, T., F. Petersson, and A. Nilsson, *Chip integrated strategies for acoustic separation and manipulation of cells and particles*. Chemical Society Reviews, 2007. **36**(3): p. 492-506.
 56. Yosioka, K. and Y. Kawasima, *Acoustic radiation pressure on a compressible sphere*. Acustica, 1955. **5**(3): p. 167-173.
 57. Liu, Y. and K.-M. Lim, *Particle separation in microfluidics using a switching ultrasonic field*. Lab on a Chip, 2011. **11**(18): p. 3167-3173.
 58. Johnson, D.A. and D.L. Feke, *Methodology for fractionating suspended particles using ultrasonic standing wave and divided flow fields*. Separations Technology, 1995. **5**(4): p. 251-258.
 59. Kumar, M., D.L. Feke, and J.M. Belovich, *Fractionation of cell mixtures using acoustic and laminar flow fields*. Biotechnology and Bioengineering, 2005. **89**(2): p. 129-137.
 60. Kapishnikov, S., V. Kantsler, and V. Steinberg, *Continuous particle size separation and size sorting using ultrasound in a microchannel*. Journal of Statistical Mechanics: Theory and Experiment, 2006. **2006**(01): p. P01012.
 61. Shi, J., et al., *Continuous particle separation in a microfluidic channel via standing surface acoustic waves (SSAW)*. Lab on a Chip, 2009. **9**(23): p. 3354-3359.
 62. Adams, J.D. and H.T. Soh, *Tunable acoustophoretic band-pass particle sorter*. Applied Physics Letters, 2010. **97**(6).
 63. Petersson, F., et al., *Free Flow Acoustophoresis: Microfluidic-Based Mode of Particle and Cell Separation*. Analytical Chemistry, 2007. **79**(14): p. 5117-5123.
 64. Hawkes, J.J., et al., *Continuous cell washing and mixing driven by an ultrasound standing wave within a microfluidic channel*. Lab on a Chip, 2004. **4**(5): p. 446-452.
 65. Petersson, F., et al., *Carrier Medium Exchange through Ultrasonic Particle Switching in Microfluidic Channels*. Analytical Chemistry, 2005. **77**(5): p. 1216-1221.
 66. Augustsson, P., et al., *Buffer medium exchange in continuous cell and particle streams using ultrasonic standing wave focusing*. Microchimica Acta, 2009. **164**(3): p. 269-277.
 67. Augustsson, P., et al., *Decomplexing biofluids using microchip based acoustophoresis*. Lab on a Chip, 2009. **9**(6): p. 810-818.
 68. Çetin, B. and D. Li, *Dielectrophoresis in microfluidics technology*. Electrophoresis, 2011. **32**(18): p. 2410-2427.
 69. Hughes, M.P., *Nanoelectromechanics in engineering and biology*. 2002: CRC press.
 70. Honegger, T., et al., *Determination of Clausius-Mossotti factors and surface capacitances for colloidal particles*. Applied Physics Letters, 2011. **98**(18): p. 181906-3.

71. Morgan, H. and T. Sun, *AC Electrokinetic Particle Manipulation in Microsystems*, in *Microfluidics Based Microsystems*, S. Kakaç, et al., Editors. 2010, Springer Netherlands. p. 481-506.
72. Cheng, I.F., et al., *A continuous high-throughput bioparticle sorter based on 3D traveling-wave dielectrophoresis*. *Lab on a Chip*, 2009. **9**(22): p. 3193-3201.
73. Barbulovic-Nad, I., et al., *DC-dielectrophoretic separation of microparticles using an oil droplet obstacle*. *Lab on a Chip*, 2006. **6**(2): p. 274-279.
74. Kang, K.H., et al., *Continuous separation of microparticles by size with Direct current-dielectrophoresis*. *Electrophoresis*, 2006. **27**(3): p. 694-702.
75. Zhu, J., T.R.J. Tzeng, and X. Xuan, *Continuous dielectrophoretic separation of particles in a spiral microchannel*. *Electrophoresis*, 2010. **31**(8): p. 1382-1388.
76. Lewpiriyawong, N., C. Yang, and Y.C. Lam, *Continuous sorting and separation of microparticles by size using AC dielectrophoresis in a PDMS microfluidic device with 3-D conducting PDMS composite electrodes*. *Electrophoresis*, 2010. **31**(15): p. 2622-2631.
77. Yunus, N.A.M., H. Nili, and N.G. Green, *Continuous separation of colloidal particles using dielectrophoresis*. *Electrophoresis*, 2013.
78. Li, M., et al., *Continuous manipulation and separation of particles using combined obstacle-and curvature-induced direct current dielectrophoresis*. *Electrophoresis*, 2013: p. 952-960.
79. Tornay, R., et al., *Dielectrophoresis-based particle exchanger for the manipulation and surface functionalization of particles*. *Lab on a Chip*, 2008. **8**(2): p. 267-273.
80. Seger, U., et al., *Cell immersion and cell dipping in microfluidic devices*. *Lab on a Chip*, 2004. **4**(2): p. 148-151.
81. Carr, C., et al., *Design, fabrication and demonstration of a magnetophoresis chamber with 25 output fractions*. *Journal of Magnetism and Magnetic Materials*, 2009. **321**(10): p. 1440-1445.
82. Pamme, N. and A. Manz, *On-chip free-flow magnetophoresis: continuous flow separation of magnetic particles and agglomerates*. *Analytical Chemistry*, 2004. **76**(24): p. 7250-7256.
83. Afshar, R., et al., *Magnetic particle dosing and size separation in a microfluidic channel*. *Sensors and Actuators B: Chemical*, 2011. **154**(1): p. 73-80.
84. Hatch, G.P. and R.E. Stelter, *Magnetic design considerations for devices and particles used for biological high-gradient magnetic separation (HGMS) systems*. *Journal of Magnetism and Magnetic Materials*, 2001. **225**(1): p. 262-276.
85. Fuh, C.B. and S.Y. Chen, *Magnetic split-flow thin fractionation of magnetically susceptible particles*. *Journal of Chromatography A*, 1999. **857**(1): p. 193-204.
86. Fuh, C.B., H.Y. Tsai, and J.Z. Lai, *Development of magnetic split-flow thin fractionation for continuous particle separation*. *Analytica Chimica Acta*, 2003. **497**(1): p. 115-122.

87. Adams, J.D., U. Kim, and H.T. Soh, *Multitarget magnetic activated cell sorter*. Proceedings of the National Academy of Sciences, 2008. **105**(47): p. 18165-18170.
88. Williams, P.S., M. Zborowski, and J.J. Chalmers, *Flow rate optimization for the quadrupole magnetic cell sorter*. Analytical Chemistry, 1999. **71**(17): p. 3799-3807.
89. Jing, Y., et al., *Blood progenitor cell separation from clinical leukapheresis product by magnetic nanoparticle binding and magnetophoresis*. Biotechnology and Bioengineering, 2007. **96**(6): p. 1139-1154.
90. Yue, P., et al., *On the motion of superparamagnetic particles in magnetic drug targeting*. Acta Mechanica, 2012. **223**(3): p. 505-527.
91. Ashkin, A., *Acceleration and trapping of particles by radiation pressure*. Physical review letters, 1970. **24**(4): p. 156-159.
92. Ashkin, A., et al., *Observation of a single-beam gradient force optical trap for dielectric particles*. Optics letters, 1986. **11**(5): p. 288-290.
93. Lin, S.-C.S. and T.J. Huang, *Surface acoustic wave (SAW) acoustophoresis: now and beyond*. Lab on a Chip, 2012. **12**(16): p. 2766-2770.
94. Dasgupta, R., S. Ahlawat, and P.K. Gupta, *Microfluidic sorting with a moving array of optical traps*. Applied Optics, 2012. **51**(19): p. 4377-4387.
95. Dholakia, K., et al., *Optical separation of cells on potential energy landscapes: Enhancement with dielectric tagging*. Selected Topics in Quantum Electronics, IEEE Journal of, 2007. **13**(6): p. 1646-1654.
96. Jonáš, A. and P. Zemánek, *Light at work: the use of optical forces for particle manipulation, sorting, and analysis*. Electrophoresis, 2008. **29**(24): p. 4813-4851.
97. Ladavac, K., K. Kasza, and D.G. Grier, *Sorting mesoscopic objects with periodic potential landscapes: optical fractionation*. Physical Review E, 2004. **70**(1): p. 010901.
98. Ma, B., et al., *Optical sorting of particles by dual-channel line optical tweezers*. Journal of Optics, 2012. **14**(10): p. 105702.
99. MacDonald, M.P., G.C. Spalding, and K. Dholakia, *Microfluidic sorting in an optical lattice*. Nature, 2003. **426**(6965): p. 421-424.
100. Milne, G., et al., *Fractionation of polydisperse colloid with acousto-optically generated potential energy landscapes*. Optics letters, 2007. **32**(9): p. 1144-1146.
101. Wang, X., et al., *Enhanced cell sorting and manipulation with combined optical tweezer and microfluidic chip technologies*. Lab on a Chip, 2011. **11**(21): p. 3656-3662.
102. Barat, D., et al., *Simultaneous high speed optical and impedance analysis of single particles with a microfluidic cytometer*. Lab on a Chip, 2012. **12**(1): p. 118-126.
103. Zmijan, R., et al. *Differentiation of micro spheres by narrow angle scattered light detection on low cost PMMA micro flow cytometer chip*. in *microTAS*. 2011. Seattle, Washington, USA.

104. Huh, D., et al., *Gravity-Driven Microfluidic Particle Sorting Device with Hydrodynamic Separation Amplification*. Analytical Chemistry, 2007. **79**(4): p. 1369-1376.
105. Cadle, R.D., *Particle size: theory and industrial applications*. 1965: Reinhold Pub. Corp.
106. Kwon, M.H., et al., *Size-sorting of micron-sized particles using two gravitational SPLITT fractionation (GSF) connected in a series (Tandem GSF)*. Bulletin of the Korean Chemical Society, 2011. **32**(2).
107. Lee, S., et al., *Effect of sample-loading on fractionation efficiency (FE) in a large scale splitter-less gravitational SPLITT fractionation (GSF)*. Bulletin of the Korean Chemical Society, 2011. **32**(12): p. 4291-4296.
108. Allen, T., *Particle Size Measurement*. Second ed. 1975, London: Chapman and Hall.
109. Kowalczyk, B., I. Lagzi, and B.A. Grzybowski, *Nanoseparations: strategies for size and/or shape-selective purification of nanoparticles*. Current Opinion in Colloid & Interface Science, 2011. **16**(2): p. 135-148.
110. Inglis, D.W., et al., *Critical particle size for fractionation by deterministic lateral displacement*. Lab on a Chip, 2006. **6**(5): p. 655-658.
111. Lubbersen, Y.S., M.A.I. Schutyser, and R.M. Boom, *Suspension separation with deterministic ratchets at moderate Reynolds numbers*. Chemical Engineering Science, 2012. **73**(0): p. 314-320.
112. Quek, R., D.V. Le, and K.H. Chiam, *Separation of deformable particles in deterministic lateral displacement devices*. Physical Review E, 2011. **83**(5): p. 056301.
113. Beech, J.P., P. Jonsson, and J.O. Tegenfeldt, *Tipping the balance of deterministic lateral displacement devices using dielectrophoresis*. Lab on a Chip, 2009. **9**(18): p. 2698-2706.
114. Inglis, D.W., M. Lord, and R.E. Nordon, *Scaling deterministic lateral displacement arrays for high throughput and dilution-free enrichment of leukocytes*. Journal of Micromechanics and Microengineering, 2011. **21**(5): p. 054024.
115. Morton, K.J., et al., *Hydrodynamic metamaterials: Microfabricated arrays to steer, refract, and focus streams of biomaterials*. Proceedings of the National Academy of Sciences, 2008. **105**(21): p. 7434-7438.
116. Cerbelli, S., *Separation of polydisperse particle mixtures by deterministic lateral displacement. The impact of particle diffusivity on separation efficiency*. Asia-Pacific Journal of Chemical Engineering, 2012. **7**: p. S356-S371.
117. Huang, L.R., et al., *Continuous Particle Separation Through Deterministic Lateral Displacement*. Science, 2004. **304**(5673): p. 987-990.
118. Nguyen, N.T. and S.T. Wereley, *Fundamentals and Applications of Microfluidics*. 2006: Artech House.
119. Huang, L.R., et al., *Role of Molecular Size in Ratchet Fractionation*. Physical review letters, 2002. **89**(17): p. 178301.

120. Bogunovic, L., et al., *Particle sorting by a structured microfluidic ratchet device with tunable selectivity: theory and experiment*. *Soft Matter*, 2012. **8**(14): p. 3900-3907.
121. Matthias, S. and F. Muller, *Asymmetric pores in a silicon membrane acting as massively parallel brownian ratchets*. *Nature*, 2003. **424**(6944): p. 53-57.
122. Choi, S. and J.-K. Park, *Continuous hydrophoretic separation and sizing of microparticles using slanted obstacles in a microchannel*. *Lab on a Chip*, 2007. **7**(7): p. 890-897.
123. Choi, S., et al., *Continuous blood cell separation by hydrophoretic filtration*. *Lab on a Chip*, 2007. **7**(11): p. 1532-1538.
124. Bakajin, O. and A. Noy, *Microfluidic sieve using intertwined, free-standing carbon nanotube mesh as active medium*. 2007, Google Patents.
125. Sethu, P., A. Sin, and M. Toner, *Microfluidic diffusive filter for apheresis (leukapheresis)*. *Lab on a Chip*, 2006. **6**(1): p. 83-89.
126. Crowley, T.A. and V. Pizziconi, *Isolation of plasma from whole blood using planar microfilters for lab-on-a-chip applications*. *Lab on a Chip*, 2005. **5**(9): p. 922-929.
127. Beech, J.P. and J.O. Tegenfeldt, *Tuneable separation in elastomeric microfluidics devices*. *Lab on a Chip*, 2008. **8**(5): p. 657-659.
128. Fung, Y.-C., *Stochastic flow in capillary blood vessels*. *Microvascular Research*, 1973. **5**(1): p. 34-48.
129. Svanes, K. and B.W. Zweifach, *Variations in small blood vessel hematocrits produced in hypothermic rats by micro-occlusion*. *Microvascular Research*, 1968. **1**(2): p. 210-220.
130. Doyeux, V., et al., *Spheres in the vicinity of a bifurcation: elucidating the Zweifach–Fung effect*. *Journal of Fluid Mechanics*, 2011. **674**: p. 359.
131. Yang, S., A. Undar, and J.D. Zahn, *A microfluidic device for continuous, real time blood plasma separation*. *Lab on a Chip*, 2006. **6**(7): p. 871-880.
132. Yamada, M. and M. Seki, *Hydrodynamic filtration for on-chip particle concentration and classification utilizing microfluidics*. *Lab on a Chip*, 2005. **5**(11): p. 1233-1239.
133. Yamada, M. and M. Seki, *Microfluidic Particle Sorter Employing Flow Splitting and Recombining*. *Analytical Chemistry*, 2006. **78**(4): p. 1357-1362.
134. Yamada, M., et al., *Millisecond treatment of cells using microfluidic devices via two-step carrier-medium exchange*. *Lab on a Chip*, 2008. **8**(5): p. 772-778.
135. Migita, S., et al., *Cell cycle and size sorting of mammalian cells using a microfluidic device*. *Analytical Methods*, 2010. **2**(6): p. 657-660.
136. Yamada, M., M. Nakashima, and M. Seki, *Pinched Flow Fractionation: Continuous Size Separation of Particles Utilizing a Laminar Flow Profile in a Pinched Microchannel*. *Analytical Chemistry*, 2004. **76**(18): p. 5465-5471.

137. Morijiri, T., et al., *Sedimentation pinched-flow fractionation for size- and density-based particle sorting in microchannels*. *Microfluidics and Nanofluidics*, 2011. **11**(1): p. 105-110.
138. Takagi, J., et al., *Continuous particle separation in a microchannel having asymmetrically arranged multiple branches*. *Lab on a Chip*, 2005. **5**(7): p. 778-784.
139. Zhang, X., et al., *Continuous flow separation of particles within an asymmetric microfluidic device*. *Lab on a Chip*, 2006. **6**(4): p. 561-566.
140. Sai, Y., et al., *Continuous separation of particles using a microfluidic device equipped with flow rate control valves*. *Journal of Chromatography A*, 2006. **1127**(1-2): p. 214-220.
141. Kawamata, T., et al., *Continuous and precise particle separation by electroosmotic flow control in microfluidic devices*. *Electrophoresis*, 2008. **29**(7): p. 1423-1430.
142. Lee, K.H., et al., *Enhancement by optical force of separation in pinched flow fractionation*. *Lab on a Chip*, 2011. **11**(2): p. 354-357.
143. Vig, A.L. and A. Kristensen, *Separation enhancement in pinched flow fractionation*. *Applied Physics Letters*, 2008. **93**(20): p. -.
144. Srivastav, A., T. Podgorski, and G. Couplier, *Efficiency of size-dependent particle separation by pinched flow fractionation*. *Microfluidics and Nanofluidics*, 2012. **13**(5): p. 697-701.
145. Matas, J.P., J.F. Morris, and E. Guazzelli, *Lateral forces on a sphere*. *Oil & gas science and technology*, 2004. **59**(1): p. 59-70.
146. Park, J.-S., S.-H. Song, and H.-I. Jung, *Continuous focusing of microparticles using inertial lift force and vorticity via multi-orifice microfluidic channels*. *Lab on a Chip*, 2009. **9**(7): p. 939-948.
147. Di Carlo, D., et al., *Continuous inertial focusing, ordering, and separation of particles in microchannels*. *Proceedings of the National Academy of Sciences*, 2007. **104**(48): p. 18892-18897.
148. Yang, W.C., *Handbook of Fluidization and Fluid-Particle Systems*. 2003: Taylor & Francis.
149. Di Carlo, D., et al., *Equilibrium Separation and Filtration of Particles Using Differential Inertial Focusing*. *Analytical Chemistry*, 2008. **80**(6): p. 2204-2211.
150. Yoon, D.H., et al., *Size-selective separation of micro beads by utilizing secondary flow in a curved rectangular microchannel*. *Lab on a Chip*, 2009. **9**(1): p. 87-90.
151. Di Carlo, D., *Inertial microfluidics*. *Lab on a Chip*, 2009. **9**(21): p. 3038-3046.
152. El Hasni, A., et al., *Focusing and Sorting of Particles in Spiral Microfluidic Channels*. *Procedia Engineering*, 2011. **25**(0): p. 1197-1200.
153. Martel, J.M. and M. Toner, *Inertial focusing dynamics in spiral microchannels*. *Physics of Fluids*, 2012. **24**(3): p. 032001.
154. Russom, A., et al., *Differential inertial focusing of particles in curved low-aspect-ratio microchannels*. *New Journal of Physics*, 2009. **11**(7): p. 075025.

155. Bhagat, A.A.S., et al., *Inertial microfluidics for sheath-less high-throughput flow cytometry*. Biomedical microdevices, 2010. **12**(2): p. 187-195.
156. Kuntaegowdanahalli, S.S., et al., *Inertial microfluidics for continuous particle separation in spiral microchannels*. Lab on a Chip, 2009. **9**(20): p. 2973-2980.
157. Bhagat, A.A.S., S.S. Kuntaegowdanahalli, and I. Papautsky, *Continuous particle separation in spiral microchannels using dean flows and differential migration*. Lab on a Chip, 2008. **8**(11): p. 1906-1914.
158. Wu, L., et al., *Separation of Leukocytes from Blood Using Spiral Channel with Trapezoid Cross-Section*. Analytical Chemistry, 2012. **84**(21): p. 9324-9331.
159. Bhagat, A., S. Kuntaegowdanahalli, and I. Papautsky, *Inertial microfluidics for continuous particle filtration and extraction*. Microfluidics and Nanofluidics, 2009. **7**(2): p. 217-226.
160. Nam, J., et al., *Continuous separation of microparticles in a microfluidic channel via the elasto-inertial effect of non-Newtonian fluid*. Lab on a Chip, 2012. **12**(7): p. 1347-1354.
161. Hansson, J., et al., *Inertial microfluidics in parallel channels for high-throughput applications*. Lab on a Chip, 2012. **12**(22): p. 4644-4650.
162. Lee, M.G., S. Choi, and J.-K. Park, *Inertial separation in a contraction-expansion array microchannel*. Journal of Chromatography A, 2011. **1218**(27): p. 4138-4143.
163. Parichehreh, V. and P. Sethu, *Inertial lift enhanced phase partitioning for continuous microfluidic surface energy based sorting of particles*. Lab on a Chip, 2012. **12**(7): p. 1296-1301.
164. Nieuwstadt, H.A., et al., *Microfluidic particle sorting utilizing inertial lift force*. Biomedical microdevices, 2011. **13**(1): p. 97-105.
165. Johnston, I.D., et al., *Dean flow focusing and separation of small microspheres within a narrow size range*. Microfluidics and Nanofluidics, 2014: p. 1-10.
166. Frising, et al., *The liquid/liquid sedimentation process: From droplet coalescence to technologically enhanced water/oil emulsion gravity separators : A review*. Vol. 27. 2006, Philadelphia, PA, ETATS-UNIS: Taylor & Francis. 23.
167. Kashid, M.N., Y.M. Harshe, and D.W. Agar, *Liquid-Liquid Slug Flow in a Capillary: An Alternative to Suspended Drop or Film Contactors*. Industrial & Engineering Chemistry Research, 2007. **46**(25): p. 8420-8430.
168. Castell, O.K., C.J. Allender, and D.A. Barrow, *Liquid-liquid phase separation: characterisation of a novel device capable of separating particle carrying multiphase flows*. Lab on a Chip, 2009. **9**(3): p. 388-396.
169. Colman, D.A. and M.T. Thew, *Correlation of separation results from light dispersion hydrocyclones* 1983: p. 233-240.
170. Schütz, S., G. Gorbach, and M. Piesche, *Modeling fluid behavior and droplet interactions during liquid-liquid separation in hydrocyclones*. Chemical Engineering Science, 2009. **64**(18): p. 3935-3952.

171. Scheiff, F., et al., *The separation of immiscible liquid slugs within plastic microchannels using a metallic hydrophilic sidestream*. Lab on a Chip, 2011. **11**(6): p. 1022-1029.
172. Kralj, J.G., H.R. Sahoo, and K.F. Jensen, *Integrated continuous microfluidic liquid-liquid extraction*. Lab on a Chip, 2007. **7**(2): p. 256-263.
173. Nord, L. and B. Karlberg, *Extraction based on the flow-injection principle : Part 5. Assessment with a Membrane Phase Separator for Different Organic Solvents*. Analytica Chimica Acta, 1980. **118**(2): p. 285-292.
174. Angelescu, D.E. and D. Siess. *Microfluidic phase separation*. in *Sensors, 2005 IEEE*. 2005.
175. Matsuoka, S., et al., *Phase separation of organic-aqueous droplet and segmented mixed phase flows by using a capillarity restricted surface modification*, in *microTAS Conference*. 2005: Boston, MA, USA. p. 1143-1145.
176. Ishiguro, K., et al., *Separation of Gas from Downward Gas-Liquid Two-Phase Flow Using a Y-Junction of Poor Wettability*. JSME International Journal Series B Fluids and Thermal Engineering, 2004. **47**(4): p. 795-803.
177. Xiao, H., et al., *Initial study of two-phase laminar flow extraction chip for sample preparation for gas chromatography*. Lab on a Chip, 2006. **6**(8): p. 1067-1072.
178. Kikutani, Y., et al. *Temperature dependent phase behaviour of N-cyclohexyl-2-pyrrolidone/water system in a microchannel and phase separation using viscosity difference*. in *MicroTAS*. 2007. Paris.
179. Tesfai, J.T., R.N. Perry, and E.L. Jablonski, *Water-in-oil emulsion separation within a milli-fluidic device*. Journal of Colloid and Interface Science, 2011. **354**(2): p. 895-899.
180. Anthemidis, A.N., et al., *On-line liquid-liquid extraction system using a new phase separator for flame atomic absorption spectrometric determination of ultra-trace cadmium in natural waters*. Talanta, 2004. **62**(3): p. 437-443.
181. Atencia, J. and D.J. Beebe, *Controlled microfluidic interfaces*. Nature, 2005. **437**(7059): p. 648-655.
182. Dean, W.R., *Fluid Motion in a Curved Channel*. Proceedings of the Royal Society, 1928. **121**: p. 402-420.
183. Kim, C., et al., *Rapid exchange of oil-phase in microencapsulation chip to enhance cell viability*. Lab on a Chip, 2009. **9**(9): p. 1294-1297.
184. Serra, C.A. and Z. Chang, *Microfluidic-Assisted Synthesis of Polymer Particles*. Chemical Engineering & Technology, 2008. **31**(8): p. 1099-1115.
185. Wang, Z.B., et al., *Femtosecond laser ablation of polytetrafluoroethylene (Teflon) in ambient air*. Journal of Applied Physics, 2003. **93**(10): p. 6375-6380.
186. Bird, R.B., W.E. Stewart, and E.N. Lightfoot, *Transport phenomena*. 2007: John Wiley & Sons.
187. Keslin, J., *Viscosity of Liquid Water in the Range—8 C to 150 C*. J. Phys. Chem. Ref. Data, 1978. **7**(3).

188. Holz, M., S.R. Heil, and A. Sacco, *Temperature-dependent self-diffusion coefficients of water and six selected molecular liquids for calibration in accurate 1H NMR PFG measurements*. Physical Chemistry Chemical Physics, 2000. **2**(20): p. 4740-4742.
189. Bonnett, R., *Chemical Aspects of Photodynamic Therapy*. 2000: Taylor & Francis.
190. Robinson, J.W., *Atomic Spectroscopy, Second Edition*. 1996: Taylor & Francis. p. 27.
191. David, G.L., *Analytical Chemistry*. 2001: University Press. p. 130.
192. Callister, W.D. and D.G. Rethwisch, *Materials Science and Engineering: An Introduction*. 2013: Wiley.
193. *Engineer's Handbook*. 22/10/14]; Available from: <http://www.engineershandbook.com/Tables/plasticthermalexp.htm>.
194. Probstein, R.F., *Physicochemical Hydrodynamics: An Introduction*. 2005: Wiley.
195. Taylor, G., *Dispersion of soluble matter in solvent flowing slowly through a tube*. Proceedings of the Royal Society of London. Series A. Mathematical and Physical Sciences, 1953. **219**(1137): p. 186-203.
196. Sharp, K. and R. Adrian, *On flow-blocking particle structures in microtubes*. Microfluidics and Nanofluidics, 2005. **1**(4): p. 376-380.
197. Scientific, H., *A Guidebook to Particle Size Analysis*. www.horiba.com.
198. Bhagat, A.A.S., S.S. Kuntaegowdanahalli, and I. Papautsky, *Enhanced particle filtration in straight microchannels using shear-modulated inertial migration*. Physics of Fluids, 2008. **20**: p. 101702.
199. Zhou, J. and I. Papautsky, *Fundamentals of inertial focusing in microchannels*. Lab on a Chip, 2013. **13**(6): p. 1121-1132.
200. Eddings, M.A., M.A. Johnson, and B.K. Gale, *Determining the optimal PDMS-PDMS bonding technique for microfluidic devices*. Journal of Micromechanics and Microengineering, 2008. **18**(6): p. 067001.
201. Armani, D., C. Liu, and N. Aluru. *Re-configurable fluid circuits by PDMS elastomer micromachining*. in *Micro Electro Mechanical Systems, 1999. MEMS '99. Twelfth IEEE International Conference on*. 1999.
202. Du, P., H. Lu, and X. Zhang. *Measuring the Young's Relaxation Modulus of PDMS Using Stress Relaxation Nanoindentation*. in *MRS Fall Meeting*. 2009.
203. Mata, A., A. Fleischman, and S. Roy, *Characterization of Polydimethylsiloxane (PDMS) Properties for Biomedical Micro/Nanosystems*. Biomedical Microdevices, 2005. **7**(4): p. 281-293.
204. Serafetinides, A.A., et al., *Ultra-short pulsed laser ablation of polymers*. Applied Surface Science, 2001. **180**(1-2): p. 42-56.
205. Hauer, M.R., *Laser ablation of polymers studied by time resolved methods*. 2004, Swiss Federal Institute of Technology Zurich.

8 APPENDIX A - Laser Machining Study

8.1 Experimental

A 768nm femtosecond laser (THALES) was used to mill short channels (1mm x 5mm) into PTFE at approximately 0.4W. The channel was ablated using a series of lines separated by 25 μ m. Once ablation was complete, loose debris was removed from the channel using a separate piece of PTFE. This was used to ensure that only loose debris was removed, rather than damaging the bottom of the channel. The channels were ablated in a grid meaning that three channels were ablated for each parameter to be tested. This channel grid was then coated in gold using a sputter coater (BALTEC SCD 005) at 50mA for 200 seconds. Gold sputtering was performed to improve the results obtained when using the interferometer (Veeco Wyko NT3300) to measure the channel dimensions. Measurements were taken using the Veeco 'Vision' software at three points at the bottom of the channel, followed by three sub-regions (350 μ m x 350 μ m) and also one larger sub-region (0.6mm x 2.5mm). A final measurement of the peak depth of the channel was taken.

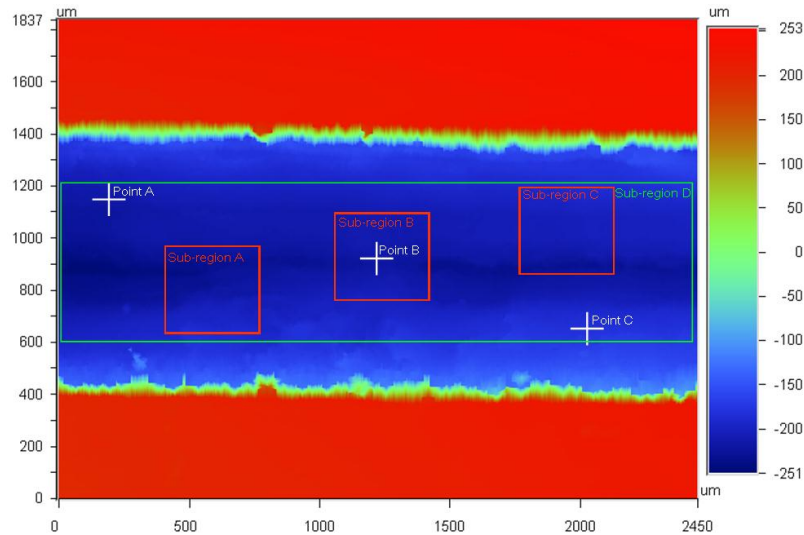


Figure 8-1: Interferometer depth plot of a channel created using femtosecond laser ablation showing the approximate measurement locations. Measurements were taken at points A, B and C (white) followed by sub-regions A, B and C (red) that were each approximately $350\mu\text{m} \times 350\mu\text{m}$. A final measurement was taken using a larger sub-region (green) that was $600\mu\text{m} \times 2.5\text{mm}$.

Measurements were taken as indicated in Figure 8-1. Point measurements give data along lines in the X and Y directions (the full length and height of the region examined) that intersect at the given point. Point measurements were used to measure the average roughness in the X-direction, $Ra(x)$, and also the Peak to valley difference in the X-plane, R_t , and Y-plane, d . The roughness in the Y-direction, $Ra(y)$, was taken by using a point measurement within each of sub-regions A, B and C. The three $350\mu\text{m} \times 350\mu\text{m}$ sub-regions were then examined and measurements were taken of average roughness (Ra), root-mean-squared roughness (R_q) and peak to valley difference (R_t). The same measurements were also taken for a larger $600\mu\text{m} \times 2.5\text{mm}$ sub-region. A final measurement of the peak depth was taken by noting the peak to valley difference of the whole region.

The Vision software's in built 'data restore' was used to smooth the data and also fill any gaps shown in the raw data, the benefit of this is clearly demonstrated in Figure 8-2. 'Tilt removal' was used to remove tilt from the 2D analysis plots. 'Tilt removal' was also used when taking data from the sub-regions.

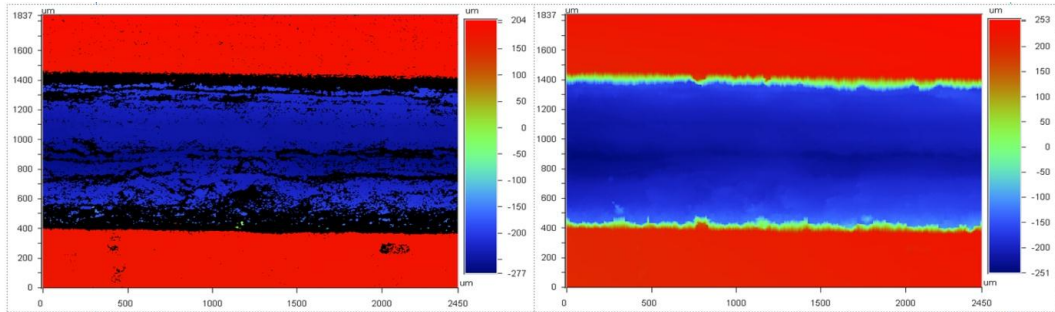


Figure 8-2: Depth plot created from an interferometer measurement demonstrating the benefit of data restore. Gaps in the raw data (left) are covered when data restore is used (right)

8.2 Results

8.2.1 Number of loops

A loop is determined, as one complete pass of the laser over the ablated region. Therefore, multiple loops means the same place is ablated more than once, but the z-plane focal position of the laser is not altered. The first obvious assumption to make would be that additional loops gives greater channel depth. This assumption can be tested by measuring the depth of the channels. The results of this are shown in Figure 8-3.

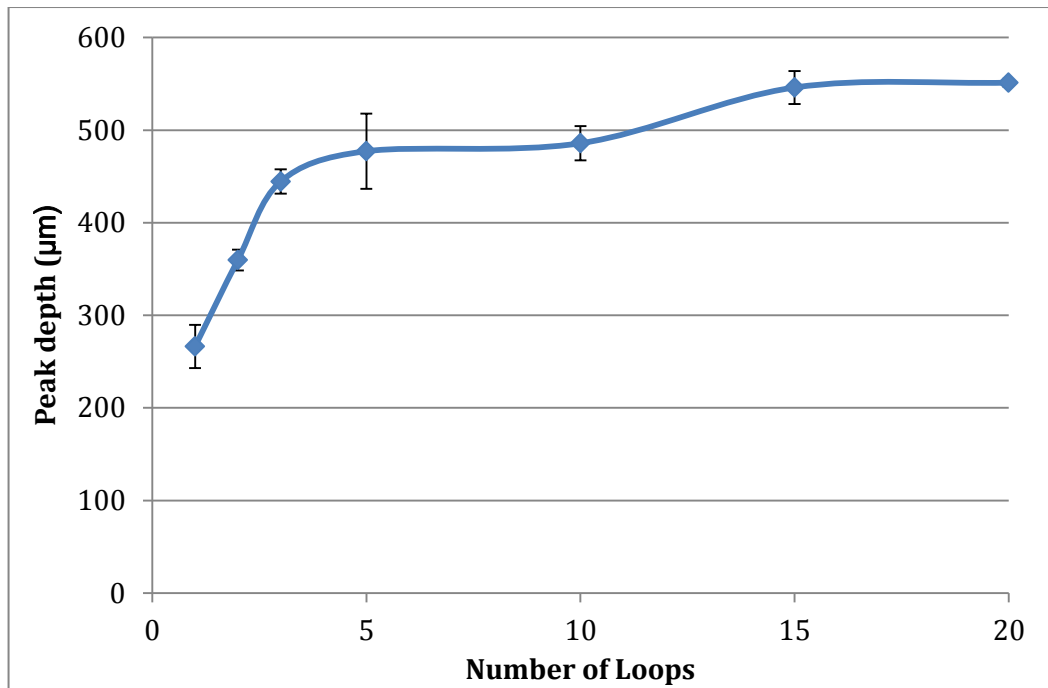


Figure 8-3: Impact of number of loops on the peak depth of the channels as measured using an interferometer. There is a significant gain in depth as loops is increased between 1 and 5 after which there is little performance gain in terms of depth. Error bars represent 95% confidence level.

As can be seen in Figure 8-3, initially extra loops do significantly increase the depth. After 5 loops, the depth gained by additional loops is only slight, suggesting that more than 5 loops offers little value when attempting to achieve greater depth. This is likely due to the channel depth going beyond the focal point of the laser, therefore, greatly reducing the power of the laser on the PTFE surface. The small step-up between 10 and 15 loops is likely due to a slight variation of the laser power.

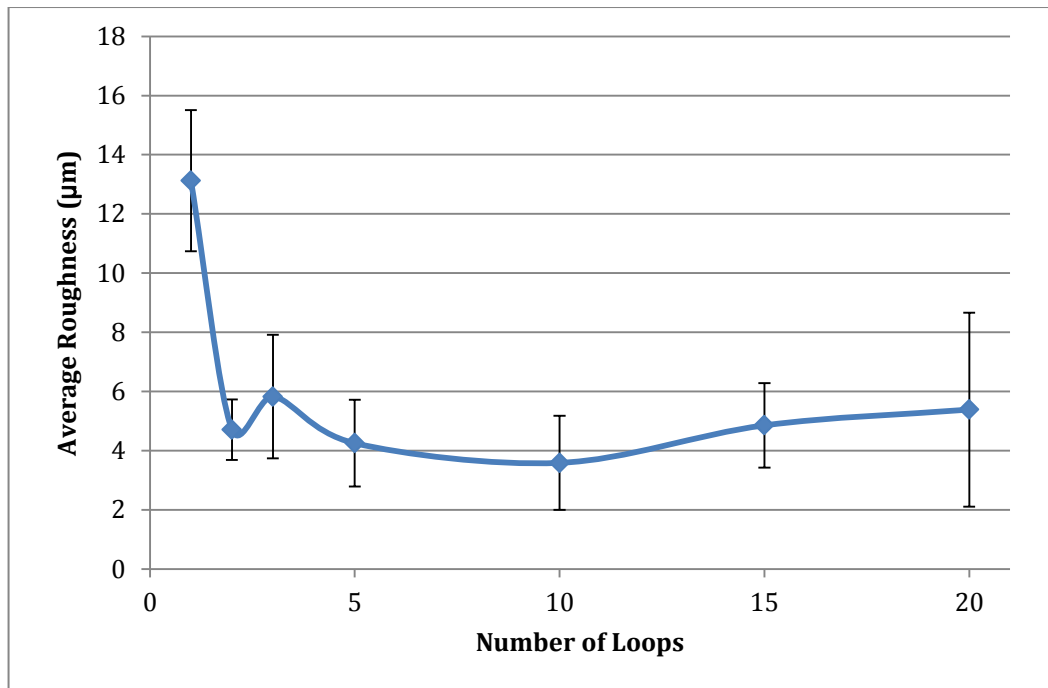


Figure 8-4: Impact of number of loops on the average roughness (Ra) of the surface within the larger sub-region (D) which is defined as shown in Figure 8-1. Surface roughness appear to be greatly improved by the use of a second loop but further loops appear to offer no roughness improvement. The error bars indicate 95% confidence level.

The next thing to examine is the impact of the number of loops on the surface roughness at the bottom of the channels. Figure 8-4 shows the average roughness of sub-region D. The data suggests that there is merit in terms of surface roughness to having at least two loops. There is a significant drop in roughness between one loop and two loops. However, additional loops appear to offer no value in regards to improved surface smoothness. It is also important to note that additional loops do not detract from the roughness either, so if additional loops are required for increased depth there is no apparent detrimental effect on roughness. Figure 8-5 demonstrates similar results for roughness along x and y-planes. The increased roughness in the y direction, when compared to the x direction,

could be a result of the ablation technique; a series of lines cut parallel to the x-axis. This technique leads to slight peaks and troughs between each line.

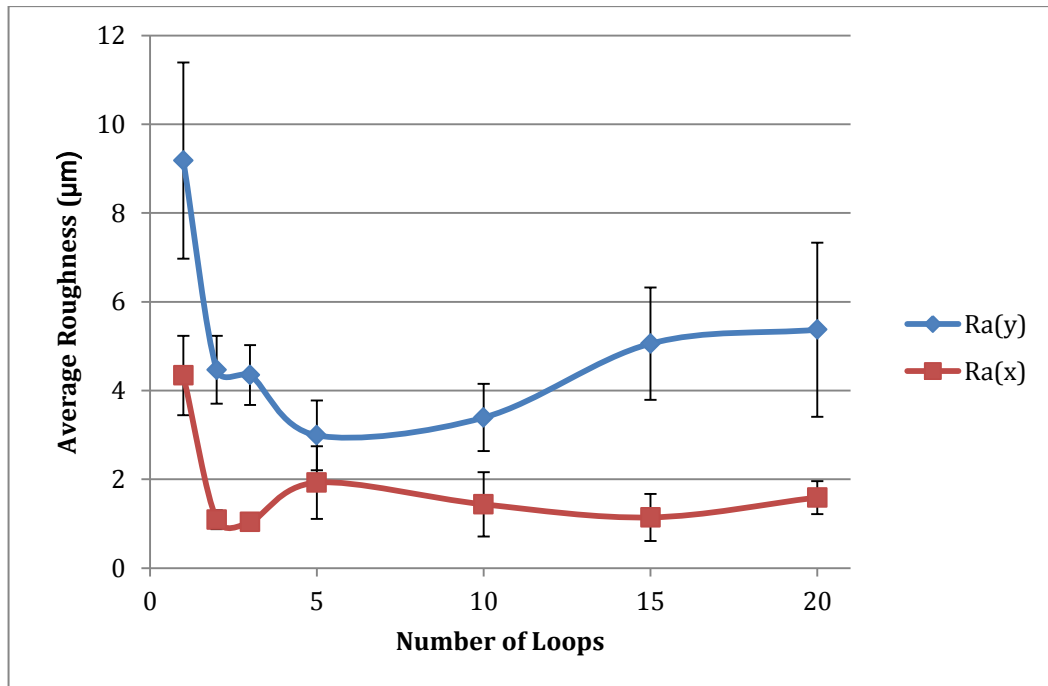


Figure 8-5: Impact of ablation loops on the average surface roughness along x and y-planes taken from points A, B and C as defined in Figure 8-1. The roughness appears to be greater in the y-plane, likely due to the laser ablation technique. The error bars indicate 95% confidence level.

8.2.2 Machining Speed

Tests were run to examine the impact of machining speed on laser ablation, where only one loop was used as the speed was varied. When analysing the results, the data for 1B (1mm min^{-1}) was excluded due to a machining error as shown in Figure 8-6.

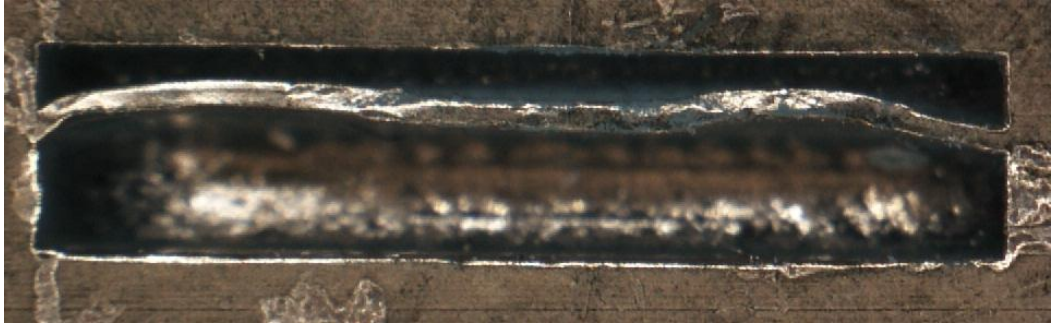


Figure 8-6: Photomicrograph of laser ablated channel 1B (machining speed 1mm min^{-1}) showing a machining error. Part of the channel was missed in the ablation process due to an emergency stop during the process consequently this channel was omitted from presented results.

Again, the impact on channel depth was investigated. The speed was varied from 1mm min^{-1} up to 50mm min^{-1} and peak depth measurements taken, the results of which are shown in Figure 8-7.

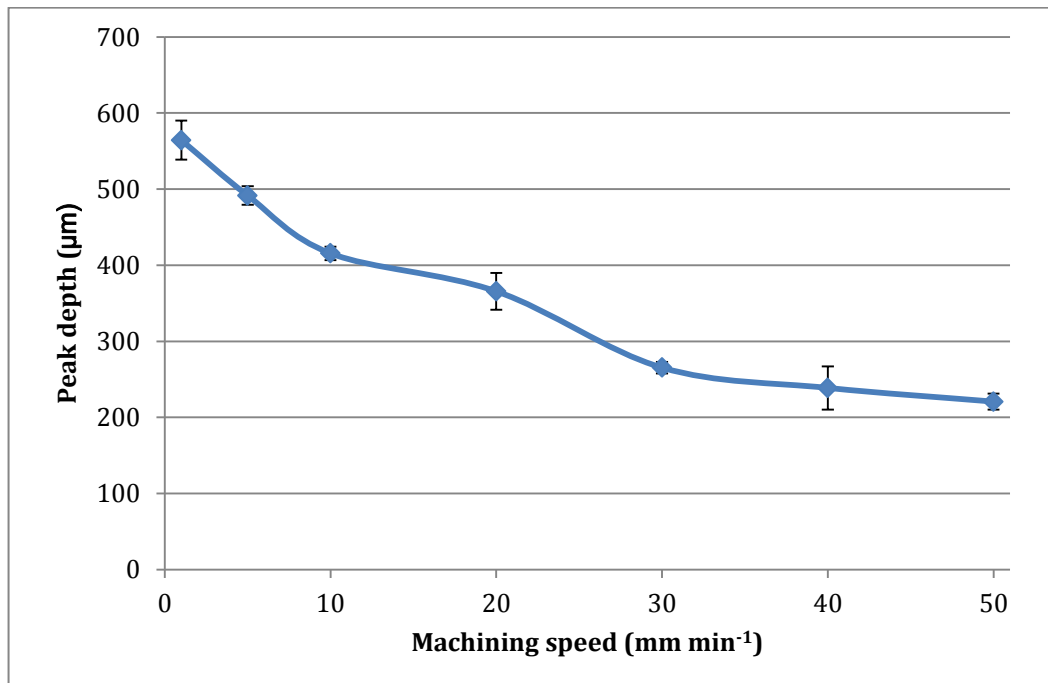


Figure 8-7: Peak depth of laser ablated channels as machining speed varies. It appears that greater depths can be achieved at slower machining speeds. Error bars indicate 95% confidence levels.

It can be seen from Figure 8-7 that increasing the machining speed leads to a reduction of the peak depth. There is a suggestion from this data that as the machining speed increases, the amount of depth lost for each increase is reduced, indicated by the decreasing gradient of the curve. This is demonstrated more clearly when using the depth measurements found from taking measurements at points A, B and C, as shown in Figure 8-8.

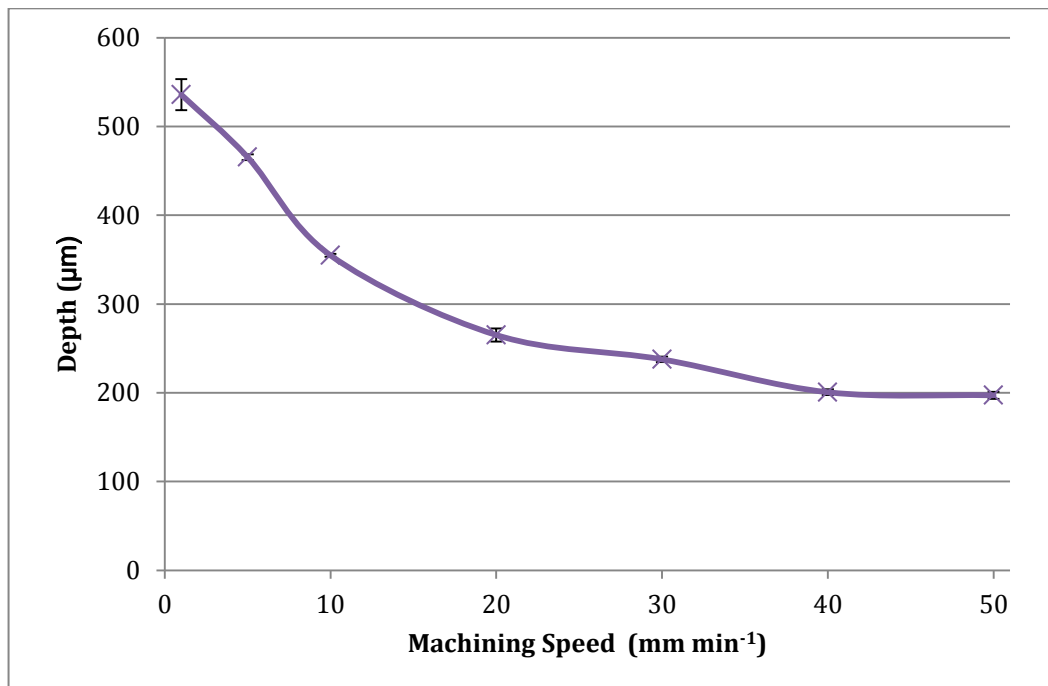


Figure 8-8: Average channel depth as femtosecond laser machining speed is varied. Interferometer measurements taken at points A, B and C as defined in Figure 8-1. Shows that depth is reduced as speed increases. There appear to be diminishing reductions as the speed increases up to 40 mm min⁻¹, beyond which it appears to level out. Error bars indicate the 95% confidence level.

Having shown the impact of machining speed on channel depth the next parameter to investigate was surface roughness. As can be seen in Figure 8-9 there does appear to be some impact with regards to average roughness. It appears that machining at 1 mm min⁻¹ offers the roughest surface although the error for this result is large. This may be due to the slight variation in

output power over time that is exhibited by the femtosecond laser. When milling at a slow speed, this could potentially mean that there is a greater power variation within a certain distance. This power variation would affect the depth, and hence, the surface roughness. The data also suggests that there is an optimum level of surface smoothness at around 10mm min^{-1} . Once error bars are taken into consideration it appears that altering the speed beyond 20mm min^{-1} has little to no impact on the surface roughness.

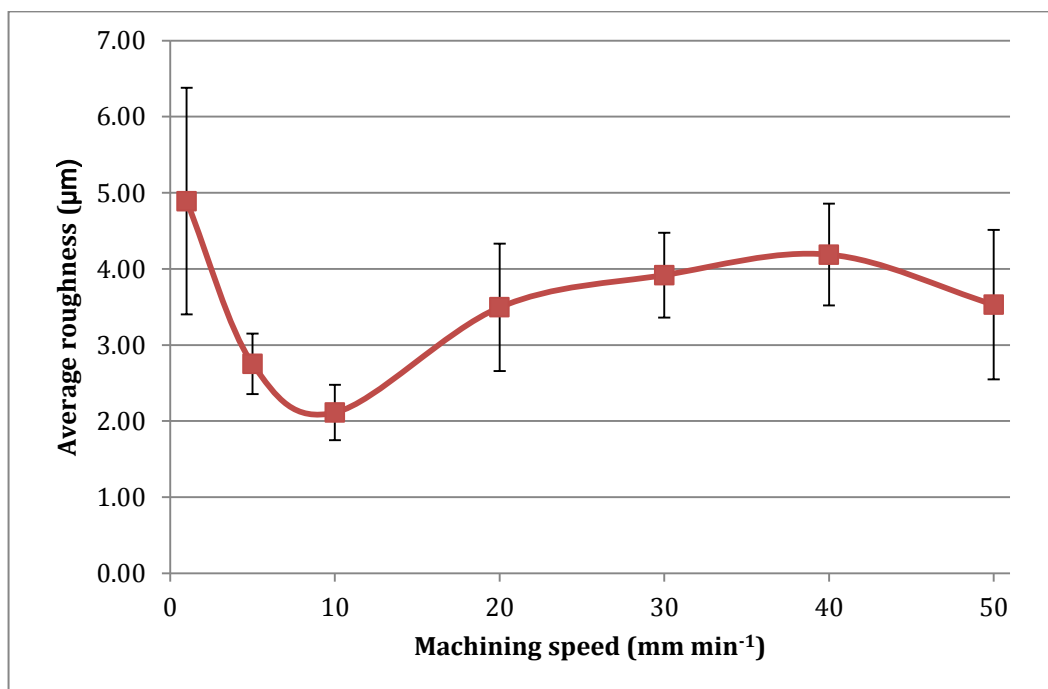


Figure 8-9: Average surface roughness at the bottom of PTFE channels in relation to machining speed of the femtosecond laser. Interferometer roughness measurements taken from sub-regions A, B and C as defined in Figure 8-1. An optimum machining speed for minimal surface roughness appears to be present at $\sim 10\text{mm/s}$. Error bars indicate 95% confidence levels.

8.3 Conclusion

It has been demonstrated that machining speed and number of loops can have a significant impact when femtosecond laser ablating PTFE. This data can, therefore, be used as a guide when determining how to micro-machine

PTFE. The user must determine what trade-offs need to be made by deciding if roughness, depth or time taken are the priorities for a given situation. Although previous studies have investigated laser ablation of polymers such as PTFE they have generally been concerned with investigating the nature of the laser itself. Investigating the impact of properties such as fluence, wavelength and pulse duration on ablation rate [204, 205] whereas the work presented here puts more focus on the machining properties like machining speed and number of loops.